University of Nevada, Reno

Molecular mechanisms underlying cerebral small vessel disease associated with mutations in *COL4A1*

A dissertation submitted in partial fulfillment of the
requirements for the degree of Doctor of Philosophy in
Cellular and Molecular Pharmacology and Physiology

by

Evan T. Yamasaki

Advisor: Dr. Scott Earley

May 2023

THE GRADUATE SCHOOL

We recommend that the dissertation
prepared under our supervision by

Evan Yamasaki

entitled

Molecular mechanisms underlying cerebral small vessel disease associated with mutations in COL4A1

be accepted in partial fulfillment of the
requirements for the degree of

DOCTOR OF PHILOSOPHY

Scott Earley, Ph.D.
Advisor

Yumei Feng Earley, M.D., Ph.D.
Committee Member

Robert D. Harvey, Ph.D.
Committee Member

Brain Perrino, Ph.D.
Committee Member

Bradley Ferguson, Ph.D.
Graduate School Representative

Markus Kemmelmeier, Ph.D., Dean
Graduate School

May, 2023

ABSTRACT

Cerebral small vessel diseases (cSVDs) are the leading cause of stroke and vascular dementia, but the underlying pathogenic mechanisms are unknown. Humans and mice with autosomal dominant mutations in the collagen-encoding gene *COL4A1* present with brain pathology that typifies cSVD. Data in this thesis reveals divergent pathogenic mechanisms in two *Col4a1* mutant mouse models and offers viable therapeutic strategies for treating related cSVDs. *Col4a1*^{G1344D} cSVD was associated with the loss of myogenic tone due to blunted pressure-induced smooth muscle cell (SMC) depolarization. Dysregulation of membrane potential was linked to impaired Ca^{2+}-dependent activation of transient receptor potential melastatin 4 (TRPM4) channels caused by disruption in sarcoplasmic reticulum (SR) Ca^{2+} signaling. Deficits were prevented by treating mice with 4-phenylbutyrate, a compound that promotes the trafficking of misfolded proteins from the SR, suggesting accumulation of mutant collagen in the SR contributes to the pathogenesis. The fundamental defect in *Col4a1*^{G394V} cSVD was the depletion of phosphatidylinositol 4,5 bisphosphate (PIP_2), a necessary cofactor for TRPM4 and inwardly-rectifying K^+ (K_{IR}) channels, in vascular SMCs and endothelial cells. This caused a loss of myogenic tone and neurovascular coupling contributing to cSVD. PIP_2 depletion was linked to increased phosphoinositide 3-kinase (PI3K) activity acting downstream of transforming growth factor-beta (TGF-β) receptors. Restoring PIP_2 by blocking PI3K or TGF-β receptors restored myogenic tone, neurovascular coupling, and memory function. Differences in pathogenic mechanisms between mutations within the same gene highlight the diverse causes and the need for specific treatments of cSVDs.

Table of Contents

List of Tables

Chapter 2:

List of Figures

Chapter 1:

Chapter 2:

Chapter 3:

Chapter 4:

CHAPTER 1: LITERATURE REVIEW

INTRODUCTION

Cerebral small vessel diseases (cSVDs) are the leading cause of stroke and vascular cognitive impairment, contributing to around 50% of all dementia cases (1-4). cSVDs are a heterogeneous group of disorders that affect small arteries, arterioles, venules, and capillaries within the brain that cause infarctions, microbleeds, and hemorrhages in the white and/or gray matter that damage the cerebral parenchyma (5). The majority of cSVDs are sporadic and are attributable to a mix of genetic and environmental factors, among which age and hypertension are the most significant contributors (6). Due to an incomplete understanding of the underlying pathophysiology, there are no specific preventative or therapeutic approaches for cSVDs. To unravel these mechanisms, multiple research groups are studying cSVDs caused by variations in a single gene. An improved understanding of these monogenic forms of the disease may offer insights into the mechanisms underlying the more common sporadic forms and present specific therapeutic targets (7-9). Mutations in the genes encoding collagen type IV collagen alpha 1 (*COL4A1*) and alpha 2 (*COL4A2*) cause Gould syndrome, an autosomal dominant multisystem disorder that includes cSVD and other defects (9, 10). How *COL4A1* and *COL4A2* mutations cause cSVD is unclear. The aim of the research described here is to determine the molecular mechanisms that underly *COL4A1*-related cSVD by studying $Col4a1^{G1344D}$ and $Col4a1^{G394V}$ mutant mouse models.

To understand the pathogenesis of cSVDs, we must first understand how cerebral vessels meet the unique challenges of supplying nutrients and oxygen to the brain. Hence, cerebral vascular physiology is described in the first section, and what is known about the causes of cSVDs is discussed in the second.

CEREBRAL VASCULAR PHYSIOLOGY

The brain makes up a small fraction of total body mass, but it is the largest source of energy consumption – accounting for ~20% of total oxygen and glucose metabolism (11, 12). Neurons lack significant energy reserves, which makes them highly dependent on an uninterrupted supply of energy substrates provided by the circulation (13). Neuronal activity consumes the majority of the energy needed in the brain (14). Localized regions with greater neuronal activity require more energy substrates, but due to the fixed volume limitations of the skull, a global increase in cerebral blood flow is not possible. These unique characteristics make normal brain function dependent on temporal and spatial control of blood flow tightly regulated by the cerebral circulation.

VASCULAR ANATOMY OF THE BRAIN

The brain is a highly perfused organ. Blood enters the cranium through two pairs of large arteries: the right and left internal carotid and vertebral arteries. The internal carotid arteries primarily feed the anterior circulation. The vertebral arteries join to form the basilar artery at the base of the cerebellum and represent the primary suppliers of blood to the posterior regions (15). The basilar artery and internal carotid arteries also feed a fully connected ring of intermediate communicating arteries called the circle of Willis. Three major arteries - the anterior, middle, and posterior cerebral arteries - branch off from the circle of Willis in pairs to supply different regions of the cerebrum (Figure 1A). The anterior cerebral arteries supply blood to areas along the interhemispheric fissure, including portions of the frontal lobe and the superomedial parietal lobes (15). The middle cerebral arteries provide blood to parts of the frontal, temporal, and parietal lobes, making them the largest and most complex of the major cerebral arteries (15). Middle cerebral artery occlusion is a common cause of ischemic stroke and often carries a severe prognosis (16). The posterior cerebral arteries supply the temporal, occipital, and a portion of the inferior parietal lobes (15). These major arteries further divide into progressively smaller arteries along the surface of the brain, which are collectively termed pial arteries. Parenchymal arterioles branch from pial arteries at right angles, penetrating the brain within the Virchow-Robin space to perfuse the subsurface microcirculation (Figure 1B).

Pial arteries differ from parenchymal arterioles. Pial arteries have two or three circumferentially oriented layers of smooth muscle cells (SMCs), while parenchymal arterioles only have one (17). Parenchymal arterioles depolarize and constrict to lower levels of intravascular pressure compared to pial arteries (18). This is partly due to differences in K^+ channel activity that act as negative feedback elements limiting depolarization and constriction (19, 20). Additionally, parenchymal arterioles respond differently to vasoconstrictors like angiotensin II due to differences in angiotensin II receptor type 1 total and subtype expression (21). Pial arteries form a collateral network that can compensate for occlusion, but parenchymal arteries do not, and occlusion results in significant reductions in flow and tissue damage (22).

Downstream of arteries and arterioles is the capillary bed of the brain, a dense network of intercommunicating vessels composed of specialized endothelial cells (ECs) (Figure 1B). The capillary network in the human brain is immense - it is estimated to be ~400 miles in length, with one capillary endothelial cell for every neuron (23, 24). Capillaries serve as the primary site of oxygen and metabolite exchange. Unlike other vascular beds, brain capillaries are non-fenestrated and are part of a unique structure called the blood-brain barrier (BBB). The BBB is formed by interlocking tight junctions between ECs supported by pericytes, astrocytes, and basement membranes, which enforce the transcellular transport of molecules between the blood and the parenchyma of the brain. The BBB allows the diffusion of gaseous molecules and small lipophilic agents, but the movement of hydrophilic molecules across the barrier requires specific EC transporters (25).

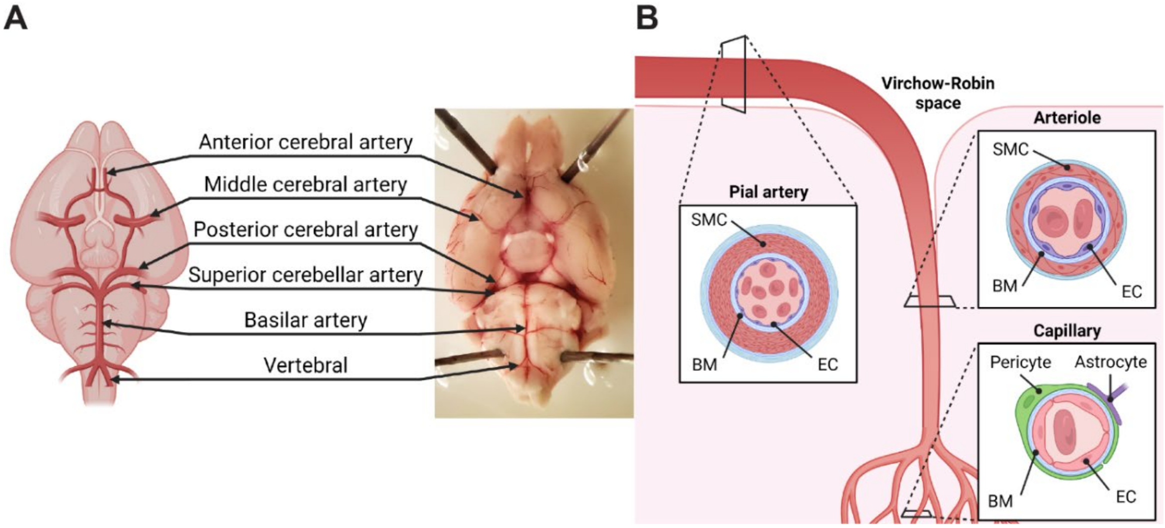

Figure 1. Anatomy of the cerebral circulation. (A) Anatomy of the pial arteries on the dorsal surface of a mouse brain. Adapted from Wenceslau *et al.* (26) (B) Illustration of the transition of surface pial arteries to penetrating arterioles and then to brain capillaries showing the difference in wall structure from multiple layers of smooth muscle cells (SMCs) to none. A monolayer of ECs lines the lumen of vessels at all branches. Pericytes, astrocytes, and the basement membrane (BM) support ECs to form the neurovascular unit and blood-brain barrier.

BASEMENT MEMBRANES

Basement membranes are a specialized type of extracellular matrix (ECM) that provide structural support, modulate cell signaling pathways, and participate in other activities in a tissue-specific manner (27). The basement membrane of the cerebral vasculature is a sheet-like structure that encircles the abluminal side of all blood vessels, lining the basal aspect of all ECs (28). This structure is critical for angiogenesis during development, vascular homeostasis, and maintenance of the BBB (29). The primary constituents of basement membranes are collagen IV, laminin, heparan sulfate proteoglycans (HSPGs), and nidogen (Figure 2) (30).

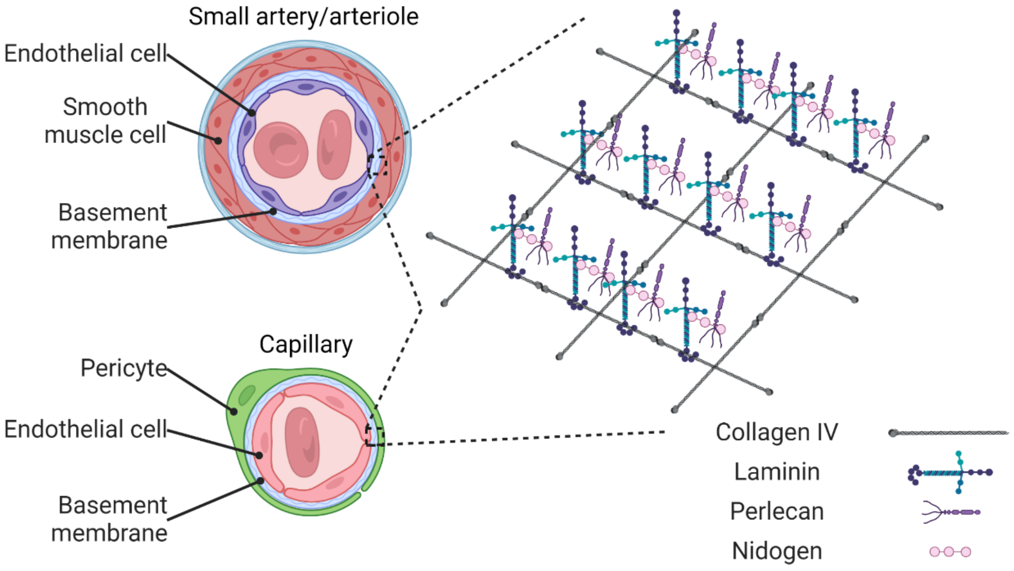

Figure 2. Cerebrovascular basement membrane. Illustration showing the location of the basement membrane in brain vessels and the proposed interactions of major extracellular matrix proteins that compose the basement membrane.

The collagen IV family members are characterized by their ability to form a covalently bonded sheet-like network. Mammals have six genetically distinct collagen IV chains encoded by three pairs of paralogous genes, collagen type IV alpha 1-6 (*COL4A1-6*) (31). The cerebrovascular basement membrane consists of heterotrimers composed of two COL4A1 and one COL4A2. These proteins can be separated into three domains: a short N-terminal 7S domain, a long triple helical collagenous domain, and a C-terminal globular noncollagenous (NC1) domain (32, 33). The 7S domain is involved in intermolecular crosslinking and macromolecular organization (31). The collagenous domain constitutes the majority of the protein composed of long stretches of Gly-X-Y repeats, where X and Y represent variable amino acids. Triple helical domains are periodically interrupted by various regions that serve other functions (34). The NC1 domains are the site of molecular recognition that initiate the assembly of heterotrimers (35).

The biosynthesis of collagen IV is a complex process involving multiple co- and posttranslational modifications catalyzed by various enzymes within the endoplasmic/sarcoplasmic reticulum (ER/SR). These modifications include hydroxylation of proline and lysine residues, glycosylation of hydroxylsine residues, and the addition of oligosaccharides. These processes occur prior to heterotrimerzation; additional modifications occur after assembly (31). Loss of enzymes that carry out these processes, such as prolyl 4-hydroxylase or the chaperone heat shock protein 47, disrupt the basement membrane due to altered collagen IV biosynthesis (36, 37). Upon molecular assembly in the ER/SR, type IV collagens are secreted from the cell and incorporated into the ECM. Basement membrane collagenous networks are formed by uniting two NC1 trimers, four 7S domains, and lateral collagenous domain associations to create a “chicken-wire” or “spider-like” configuration that provides a molecular scaffold for other ECM proteins (Figure 2) (38, 39).

Beyond providing mechanical stability and a foundation for other ECM proteins, collagen IV can regulate a variety of biological processes, including cell adhesion, migration, survival, proliferation, and homeostasis through direct interaction with the cells surrounding the basement membrane, including vascular SMCs and ECs (40-42). Collagen IV physically interacts with cell surface receptors, including integrins and discoidin domain receptors, through multiple binding sites within the triple helical and NC1 domains (31).

In addition to a collagen IV network, basement membranes have a laminin network that serves various biological functions, including cell adhesion, differentiation, and basement membrane integrity (43, 44). Laminins are cross-shaped heterotrimeric glycoproteins containing α, β, and γ chains (45). Five distinct α-chains (α1-5), four β-chains (β1-4), and three γ-chains (γ1-3) that have been discovered (46); these chains non-randomly assemble into 16 potential trimeric laminin isoforms (46, 47). The α-subunits are responsible for cell surface adhesion and receptor interactions, while the β- and γ- subunits primarily play structural roles (48). Laminin- α4β1γ1 (411) and -511 are the major isoforms found in the vessel wall (49, 50). Deletion of laminin α4 or α5 subunits leads to disruption of vascular development, defective BBB integrity, intracerebral hemorrhage (ICH), and embryonic lethality due to disrupted interactions with integrins (51-54).

Nidogens link the collagen IV and laminin networks (55). Nidogen-1 and -2 are highly homologous glycoproteins found in all basement membranes and are composed of three globular domains (G1, G2, G3) connected by a linker and a rod segment (56). The G3 domain of nidogen-1 binds with high affinity to laminin γ-chain, while the G2 domain binds to collagen IV as well as the HSPG perlecan (56-58). It is presumed that nidogen-2 binds to ECM components via the same domains as nidogen-1 based on structural similarities and comparable binding activities of nidogen-1 and -2 (59, 60).

There are three major basement membrane HSPGs: perlecan, agrin, and collagen type XVIII. Perlecan and agrin are the most abundant HSPGs in cerebrovascular basement membranes (61). HSPGs are critical to basement membrane integrity and bind to various ligands primarily via the heparin sulfate chain (62). Heparin-binding ligands include growth factors, cytokines, enzymes, enzyme inhibitors, and ECM proteins (63). Basement membrane HSPGs can regulate cell signaling by acting as a reservoir for growth factors and chemokines, like the transforming growth factor-β family and controlling their activation and presentation to cells (64).

Together, the basement membrane proteins form a network that provides more than structural support. The basement membrane can bind to cell-surface receptors and regulate the distribution, activation, and presentation of soluble growth factors, such as TGF-β, to initiate intracellular transduction responses that control cell and vascular homeostasis (65, 66). Disruption of the vascular basement membrane is associated with multiple pathologies, including stroke, Alzheimer's' disease, and cSVDs however the mechanisms are not well established (29). Cerebrovascular dysfunction often precedes brain injury in these diseases (67, 68), suggesting basement membrane defects may disrupt essential mechanisms like cerebral blood flow autoregulation to cause disease.

CEREBRAL AUTOREGULATION AND MYOGENIC RESPONSE

A global increase in cerebral blood flow in response to elevations in cardiac output would damage the brain by causing it to compress against the enclosing skull. Fortunately, specialized autoregulatory mechanisms maintain constant cerebral blood flow during fluctuations in cardiac output and arterial blood pressure. For humans, nonhuman primates, and many commonly used laboratory animals, cerebral autoregulation maintains nearly constant cerebral blood flow when mean arterial pressure (MAP) is between ~50-150 mmHg (Figure 3) (69, 70). Within this autoregulatory range, arterial diameter, and hence vascular resistance, is adjusted in proportion to MAP to maintain constant blood flow. Outside of the autoregulatory range, cerebral blood flow passively fluctuates with arterial blood pressure. Blood flow may become insufficient at MAPs below ~50 mmHg, leading to cerebral ischemia and irreversible brain damage. On the other end of the spectrum, autoregulation fails if MAP exceeds ~150 mmHg, and the resulting forced dilation of cerebral pial arteries damages downstream parenchymal arterioles and capillaries (71). Thus, loss of cerebral autoregulation under pathological conditions leaves the brain vulnerable to ischemia, microvascular injury, disruption of the BBB, and intracerebral hemorrhage.

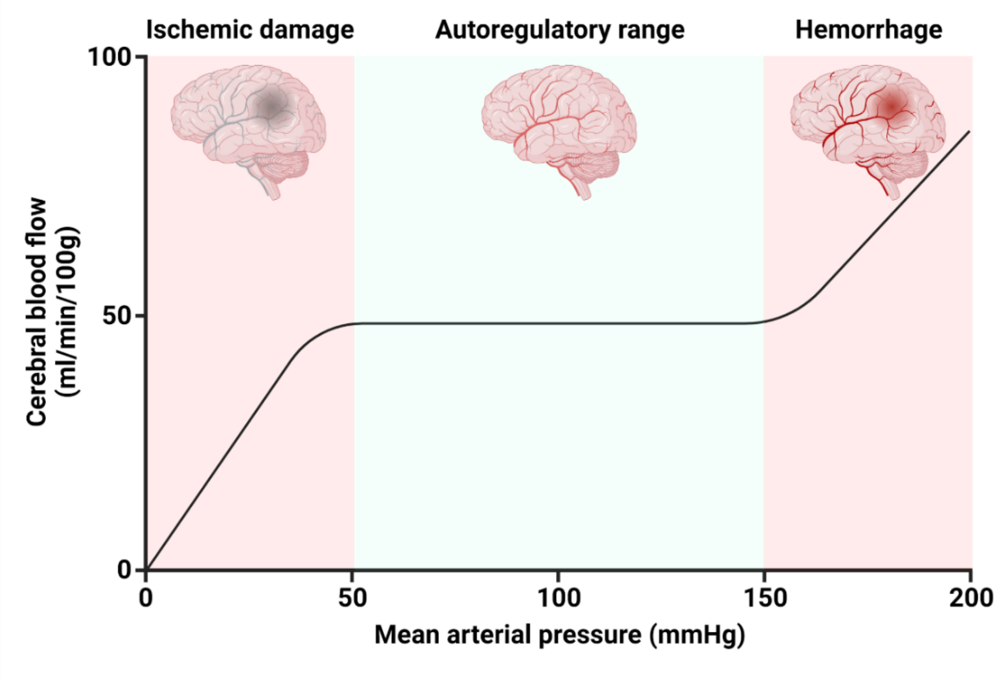

Figure 3. Cerebral autoregulation. Autoregulation curve showing plateau of cerebral blood flow versus mean arterial pressure between 50 to 150 mmHg.

Smooth muscle, or myogenic, influences are fundamental and the predominant contributor to cerebral autoregulation, as demonstrated by experiments showing that denervated and endothelium-denuded vessels maintain pressure-induced vasoconstriction (72). The intrinsic property of SMCs from arteries and arterioles to constrict in response to increases in intraluminal pressure and relax to decreases in pressure is termed “myogenic tone” or the “myogenic response.” Despite initially being characterized by Bayliss in 1902 (73), the mechanisms that control the myogenic response have been unveiled only recently (74). The current theory is that the myogenic response is regulated by a “push/pull” relationship between vasoconstrictor and vasodilator mechanisms, which are both controlled by highly localized Ca^{2+} release from the sarcoplasmic reticulum (SR).

Elevation in intraluminal pressure causes the depolarization of the plasma membranes of vascular SMCs (75), which in turn stimulates Ca^{2+} influx through voltage-dependent $Ca_V1.2$ channels (VDCCs) (76). A global rise in cytosolic [Ca^{2+}] leads to the activation of myosin light chain kinase, myosin light chain phosphorylation, increased cross-bridge cycling, and actomyosin force generation culminating in vasoconstriction (77). Our laboratory (78) demonstrated that mechanical stretch of the plasma membrane stimulates the generation of inositol triphosphate (IP_3) by phospholipase C (PLC) and the release of Ca^{2+} from the SR through IP_3 receptors (IP_3R) that activates functionally coupled plasmalemmal monovalent cation-selective, Ca^{2+}-activated transient receptor potential melastatin 4 (TRPM4) channels. TRPM4 channel activation allows an influx of Na^+, which depolarizes the membrane. A subsequent study by our lab showed that the inherently mechanosensitive G-protein coupled receptor angiotensin II receptor type I was the primary sensor of intraluminal pressure that activated PLC (79). TRPC6 and Ca^{2+}-activated Cl^- channel TMEM16A (encoded by and referred to as *ANO1*) acting downstream of G-protein coupled receptors are also involved in pressure-induced depolarization of cerebral arteries (74). TRPC6, a Ca^{2+}-permeable nonselective cation channel, is activated by PLC-mediated diacylglycerol production, causing an influx of Na^+ and Ca^{2+} that works in conjunction with TRPM4 channels to depolarize the membrane in response to pressure (78, 80). Ca^{2+} influx from TRPC6 can activate ANO1 causing Cl^- efflux, further enhancing pressure-induced depolarization (Figure 4) (81).

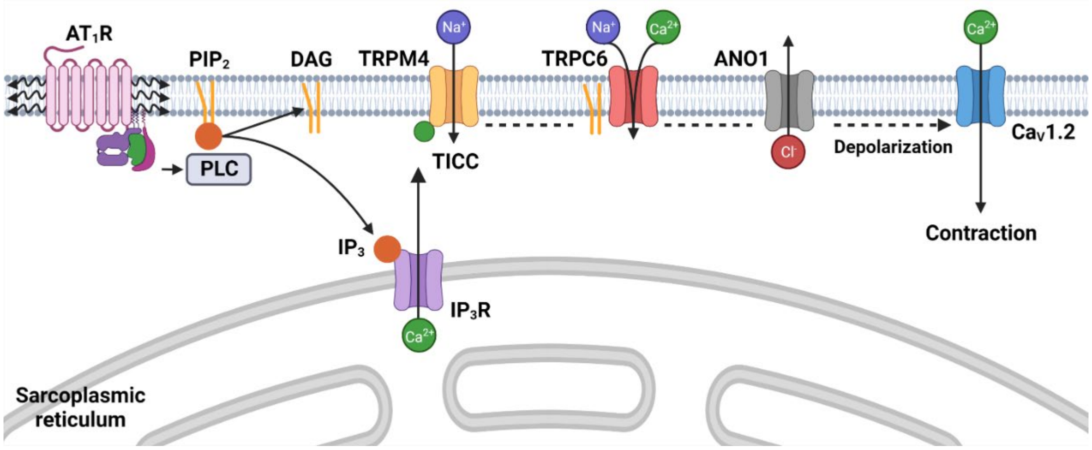

Figure 4. Postulated mechanisms for pressure-induced depolarization and vasoconstriction. Membrane stretch activates angiotensin II receptor type 1 (AT_1R) linked to phospholipase C (PLC). PLC cleaves phosphatidylinositol 4,5-bisphosphate (PIP_2) into diacylglycerol (DAG) and inositol triphosphate (IP_3). IP3 activates IP3 receptors on the sarcoplasmic reticulum that release Ca^{2+} to initiate Na^+ influx through transient receptor potential melastatin 4 (TRPM4) channels. DAG stimulates TRPC6 activity, causing Na^+ and Ca^{2+} influx. Local Ca^{2+} signals from TRPC6 trigger Cl^- efflux through Ca^{2+}-activated Cl^- channel Anoctamin-1 (ANO1). Na^+ and Ca^{2+} influx and Cl^- efflux depolarize the smooth muscle cell membrane activating voltage-dependent, L-type calcium channel ($Ca_V1.2$), causing a global increase in cytosolic calcium that increases contraction.

Potassium channels counteract pressure-induced depolarization. Activation of K^+ channels leads to K^+ efflux and hyperpolarization because the equilibrium potential for K^+ is more negative than the resting potential of SMCs. Vascular SMCs express large conductance (BK) calcium-activated, voltage-gated (K_V), inwardly-rectifying (K_{IR}), and ATP-sensitive K^+ channels (82). The most significant negative feedback regulator of pressure-induced depolarization are BK channels, but K_V channels also play a role (Figure 5). K_V family members are expressed in vascular SMCs with varying half-maximal activation voltages (83-85). K_V channels are active at the resting membrane potential of vascular SMCs, with depolarization further increasing K_v channel activity. These properties make K_V channels regulators of resting membrane potential and contribute to negative feedback of pressure-induced depolarization (86). The Ca^{2+}-

activated potassium (K_{Ca}) channel family is comprised of three subfamilies: small conductance (SK), intermediate conductance (IK), and BK channels. K_{Ca} channels are activated by membrane depolarization and calcium. SK and IK channels are not present in contractile vascular SMCs (20, 87). A signaling pathway formed by BK channels on the plasma membrane and type 2 ryanodine receptors (RyR2) on the SR opposes TRPM4-mediated membrane depolarization and myogenic vasoconstriction. Pressure-induced depolarization, activation of VDCCs, and subsequent increases in global intracellular Ca^{2+} concentration lead to increased activity of Ca^{2+}-sensitive RyR2 clusters on the SR, causing SR Ca^{2+} release in a transient focal Ca^{2+} signal known as a Ca^{2+} spark (88). Ca^{2+} sparks activate nearby BK channels on the plasma membrane, generating macroscopic outward K^+ currents, called spontaneous transient outward currents (STOCs), that hyperpolarize the plasma membrane (88, 89). The balance of TRPM4-mediated depolarization and BK channel hyperpolarization is the principal dictator of myogenic reactivity in cerebral arteries (Figure 6).

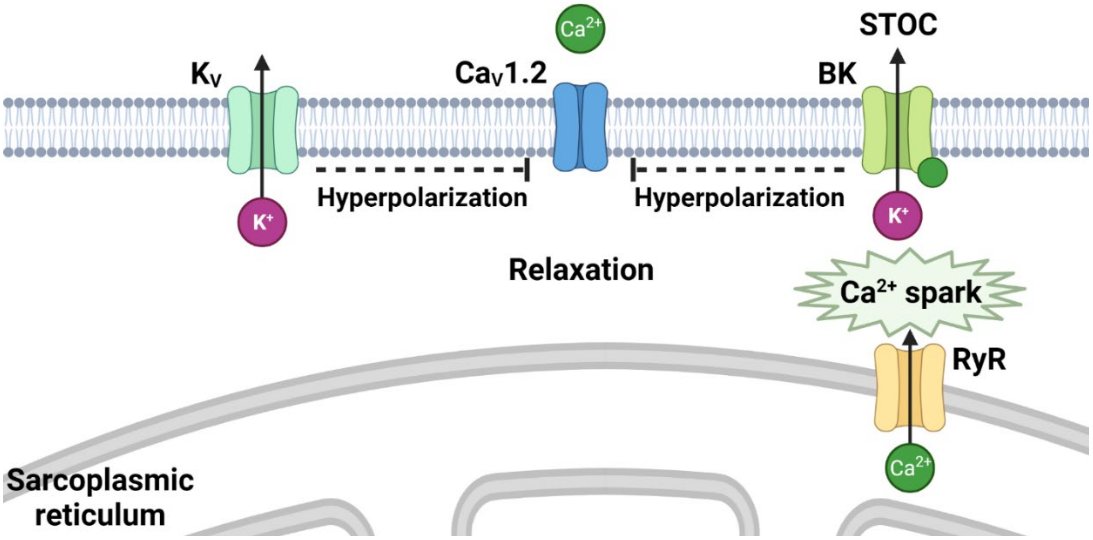

Figure 5. Ion channels that contribute to negative-feedback regulation of myogenic tone. Pressure-induced depolarization activates voltage-gated (K_V) and large-conductance Ca^{2+}-activated potassium (BK) channels causing K^+ efflux, limiting membrane depolarization closing voltage-dependent Ca^{2+} channels ($Ca_V1.2$). BK channels are also activated by Ca^{2+} release from the SR through ryanodine receptor (RyR) clusters; this Ca^{2+} spark activates functionally coupled BK channels causing macroscopic outward K^+ currents called spontaneous transient outward currents (STOCs).

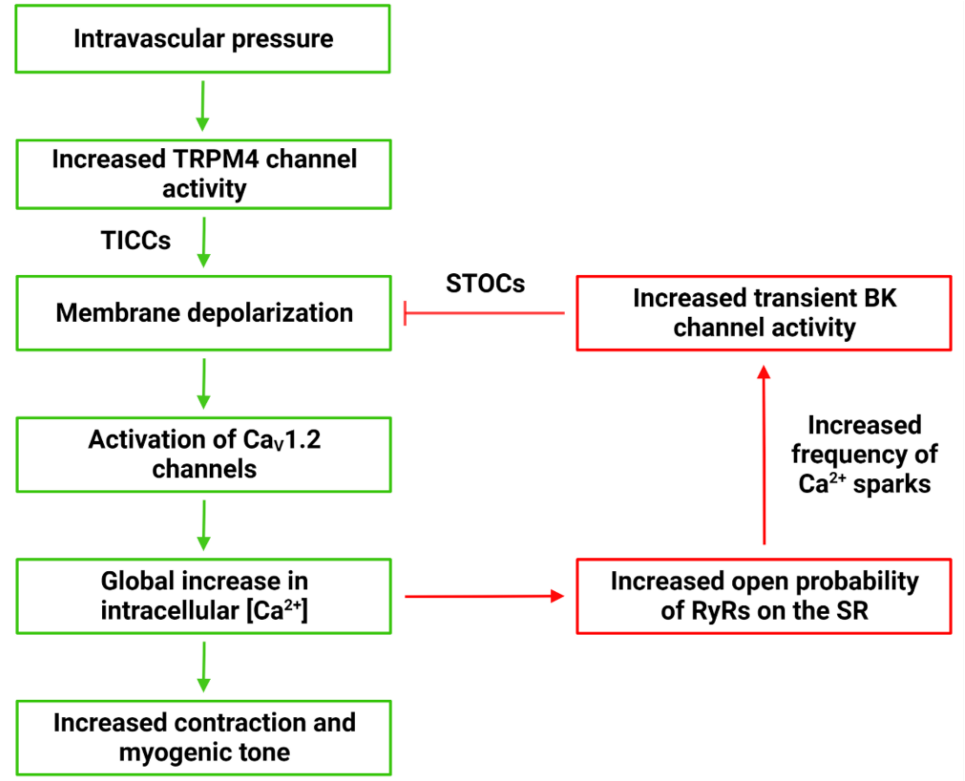

Figure 6. Myogenic pressure-induced depolarization and negative feedback signaling pathway. Increases in intravascular pressure stretch the plasma membrane of vascular smooth muscle cells, indirectly activating transient receptor potential melastatin 4 (TRPM4) channels. Na^{2+} influx through TRPM4 channels, termed transient inward cation currents (TICCs), depolarize the membrane activating voltage-dependent, L-type Ca^{2+} channels ($Ca_V1.2$), leading to a global increase in cytosolic Ca^{2+} and vasoconstriction. Global increases in Ca^{2+} generate localized, transient Ca^{2+}-induced Ca^{2+} release events from the sarcoplasmic reticulum through ryanodine receptor (RyR) clusters; this Ca^{2+} spark activates functionally coupled Ca^{2+}-activated large conductance potassium (BK) channels generating macroscopic K^+ efflux currents called spontaneous transient outward currents (STOCs) that hyperpolarize the membrane.

NEUROVASCULAR COUPLING

Neurons within the brain lack significant energy reserves and metabolic substrates must be delivered to the most active regions of the brain to match demand in real-time through increases in blood flow. This response is termed functional hyperemia (90). However, due to the enclosing cranium's fixed volume, increasing global blood flow to the brain to meet metabolic demands is not possible. Neurovascular coupling (NVC) rapidly and precisely directs blood flow to the most active regions of the brain through communication between active neurons and the cerebral microvasculature. During NVC, active neurons trigger the dilation of upstream parenchymal arterioles and pial arteries to increase regional blood supply (91). NVC and functional hyperemia are fundamental to healthy brain function. Dysregulation of NVC contributes to cognitive decline in normal aging and disease, including vascular dementia and Alzheimer's disease (92-95). The mechanisms underlying increases in regional blood flow following heightened neuronal activity are not completely understood.

It has been proposed that the release of glutamate during neurotransmission binds to $G_{q/11}$ protein-linked metabotropic glutamate receptors (mGluR) on perisynaptic astrocytic processes, thereby stimulating Ca^{2+}-dependent signaling pathways that lead to the release of vasodilatory substances from astrocytic endfeet acting directly on the smooth muscle of parenchymal arterioles (96-98). Several recent studies have challenged this model of NVC. One account observed a lack of mGluR expression in astrocytes after postnatal week 3, suggesting this pathway is absent in adults (99). Another group reported that astrocytic Ca^{2+} signals occurred after the vasodilatory response (100), while others could not observe astrocytic Ca^{2+} signals (101, 102). These conflicting reports suggest an incomplete model of NVC.

A new paradigm has emerged, highlighting the extensive capillary network as a sensory web that detects neuronal activity and orchestrates the dilation of upstream arterioles (103). The capillary network intertwines every brain region, placing neurons no further than 15 μm from the nearest capillary EC, making them ideal sensors of local neuronal activity throughout the brain (104). Two ion channels present on brain capillary

ECs, transient receptor potential ankyrin 1 (TRPA1) and $K_{IR}2.1$, are critical sensors of neuronal activity and are necessary for NVC (103, 105). TRPA1 channels are activated by reactive oxygen species metabolites that initiate a retrograde propagating intercellular Ca^{2+} wave. These slowly-propagating Ca^{2+} signals are converted to rapidly propagating electrical signals in specialized post-arteriole vascular segments that dilate upstream arterioles (105). $K_{IR}2.1$ channels are activated by increased extracellular K^+ ions, released during neuronal activity, generating a propagating hyperpolarizing electrical signal that causes dilation of upstream parenchymal arterioles (Figure 7) (103). $K_{IR}2.1$ channels on adjacent endothelial cells conduct this signal. Hyperpolarization is rapidly transmitted through myoendothelial gap junctions to SMCs in the upstream arteriole, causing dilation that promotes a hyperemic response in the capillary bed where the K^+ signal originated.

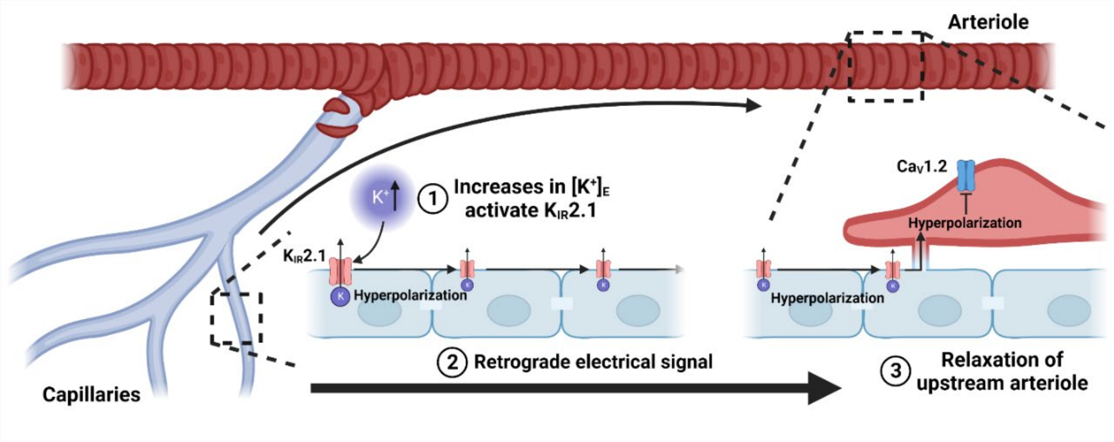

Figure 7. Neurovascular coupling initiated by K_{IR} channels on brain capillary endothelial cells. K^+ ions released by neuronal activity activate inward-rectifier K^+ potassium channel 2.1 ($K_{IR}2.1$) on brain capillary endothelial cells. $K_{IR}2.1$ initiates a regenerative, retrograde hyperpolarizing signal that is transferred to upstream parenchymal arteriole smooth muscle cells via gap junctions. Smooth muscle cell hyperpolarization closes voltage-dependent $Ca_V1.2$ channels leading to relaxation and arteriole dilation.

These NVC paradigms are not mutually exclusive. NVC is essential for healthy brain function and life itself. Thus, it is conceivable that distinct complementary and overlapping mechanisms exist for redundancy. Despite this, NVC is often disrupted in disease states such as stroke, Alzheimer's disease, and cSVD, but the precise molecular mechanisms remain unknown.

CEREBRAL SMALL VESSEL DISEASE

cSVDs are a group of related pathologies with various etiologies that affect the structure and function of small arteries, arterioles, capillaries, and venules of the brain. cSVDs are the leading cause of stroke and vascular dementia, contributing to 25% of strokes and more than 40% of dementias (1, 106). cSVDs cause lesions in the brain that are visualized with magnetic resonance imaging (MRI). Typical radiological features include white matter hyperintensities, dilated perivascular spaces, lacunar infarcts, microbleeds, and ICH (Figure 8) (107-110). Brain lesions and structural changes to the cerebral vasculature precede clinical manifestations of cSVDs, which include stroke, cognitive decline, dementia, psychiatric disorders, abnormal gait, and urinary incontinence (106, 111-113). Aging is the most significant risk factor for cSVDs. White matter hyperintensities are present in less than 5% of individuals younger than 50 years, increasing to nearly 100% for people 90 years and older (114). The prevalence of cerebral microbleeds increases from 6.5% for people between 45-50 years to ~36% for people 80 years and older (115). The number of people affected by cSVDs and vascular dementia is expected to rise exponentially due to a growing population of aged individuals. Hypertension, diabetes, hyperlipidemia, and smoking are also significant risk factors (116). There are no effective treatments or methods to resolve or prevent cSVDs because the underlying pathogenic mechanisms remain poorly understood.

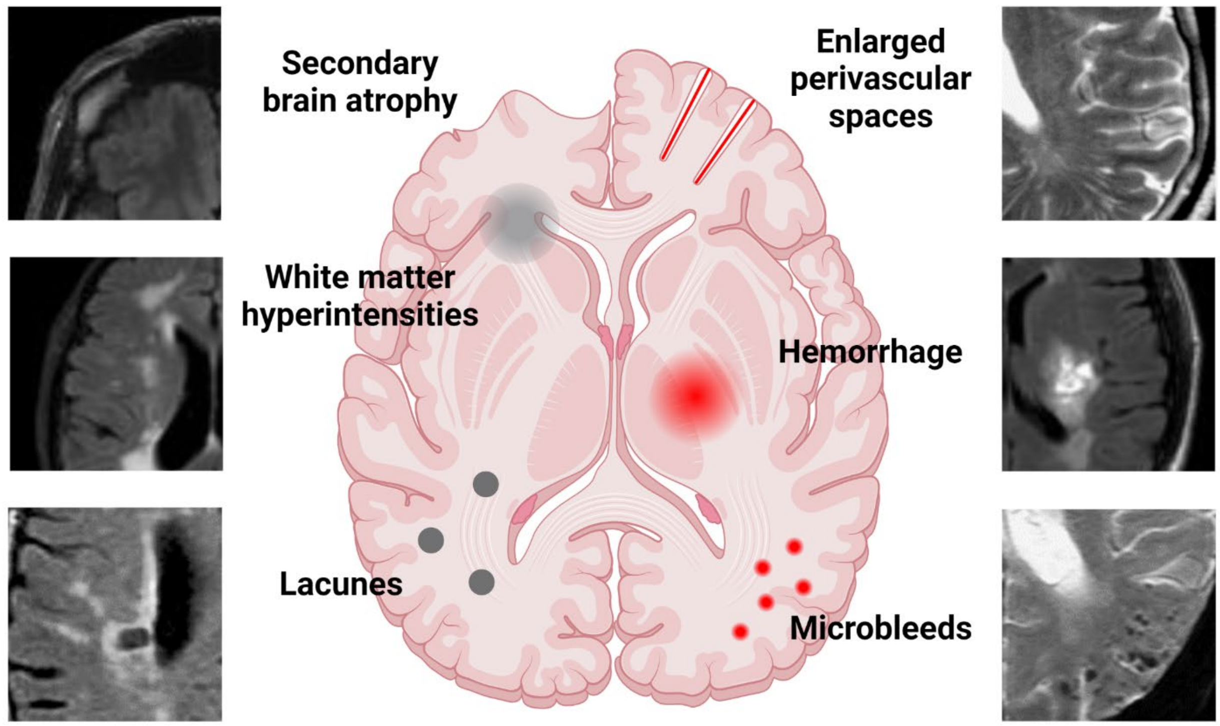

Figure 8. Neuroimaging features of cerebral small vessel diseases. Typical brain abnormalities associated with cSVDs. MRI images are adapted from Shi *et al.* (117) and Lemmens *et al.* (118).

TYPES OF CSVDS

Various classification systems have been created to typify cSVDs based on MRI markers, clinical features, and etiopathogenesis (106, 119). However, the most common forms of cSVDs can generally be broken down into amyloidal and non-amyloidal cSVDs. Amyloid-related cSVD is associated with sporadic and hereditary cerebral amyloid angiopathy (CAA), a chronic degenerative disease caused by progressive deposition of β-amyloid in the walls of cortical and leptomeningeal small arteries, arterioles, and capillaries (106). CAA and Alzheimer’s disease frequently co-occur, presumably because β-amyloid is pathogenic in both (120, 121). The two disorders differ in brain injury mechanisms. The exact mechanism of Alzheimer's disease is unclear, but most theories center around the neurotoxicity of β-amyloid (122). CAA-related brain injuries arise from blood vessel dysfunction. In severe forms of CAA, blood vessels become dilated and disrupted, with focal wall fragmentation leading to microbleeds and hemorrhage (123). The incidence of CAA is primarily associated with age, becoming as frequent as 50% in individuals over 90 years of age (124). Non-amyloidal cSVDs are a broader category with a variety of etiologies. These forms include age-related, vascular risk factor related, or degenerative microangiopathy cSVDs (106, 119). This thesis will focus on non-amyloidal cSVDs, the most prevalent forms of cSVDs (106). Despite sharing radiological and clinical features, the pathogenesis of sporadic non-amyloidal cSVDs is heterogeneous.

Current knowledge of the pathogenesis of sporadic non-amyloidal cSVDs

The most common pathological changes associated with sporadic non-amyloidal cSVDs are arteriosclerosis and endothelial dysfunction. Here we will discuss how these changes contribute to typical brain abnormalities observed in cSVDs.

Cerebral arteriosclerosis, or the thickening and hardening of the walls of arteries in the brain, is a consequence of aging caused by phenotypic switching of vascular SMCs leading to hypertrophy, rearrangement of SMCs, and remodeling of the ECM (125). This leads to diminished compliance, reduced elasticity, increased arterial stiffness, and elevated susceptibility to hemorrhagic and ischemic stroke (126). Cerebral myogenic autoregulation protects downstream fragile cerebral microvessels from excessive pressure by dampening high-pressure waves (127, 128). Arteriosclerosis and aging impair cerebral myogenic autoregulation leading to the transmission of higher pressures to the cerebral microcirculation, which contributes to microvascular damage and pathogenesis of some forms of cSVD (129, 130). Hypertrophic inward remodeling narrows the vessel lumen and increases stiffness, decreasing vasodilatory capacity and increasing susceptibility to occlusion, ultimately resulting in hypoperfusion (131, 132). Chronic hypoperfusion causes white matter injury, lacunar strokes, brain atrophy, and memory impairment (133).

Cerebrovascular EC dysfunction is another cause of non-amyloidal cSVDs. Vascular ECs line the luminal surface of all vessels playing an active role in vascular reactivity and the BBB. Arterial ECs produce nitric oxide (NO), which diffuses to and relaxes SMCs to cause vasodilation. NO is essential for the local control of CBF (134). Endothelial dysfunction reduces NO release, leading to pathological vasoconstriction and impaired blood flow. Severe and persistent endothelial dysfunction in the brain results in tissue ischemia and neuronal damage. Decreased NO in patients with cSVD could be due to increases in the endogenous NO synthase inhibitor, asymmetric dimethylarginine (ADMA). ADMA was shown to be significantly elevated in the plasma of patients with cSVD, and the level of ADMA correlated with the level of cognitive impairment (135).

Cerebrovascular ECs are integral to the BBB. BBB integrity is disrupted in patients with cSVD with permeability proportional to white matter hyperintensity burden and cognitive impairment (136-139). An additional study showed that BBB permeability was higher in normal-appearing white matter surrounding hyperintensities than in other ordinary white matter, suggesting that increased BBB permeability precedes the onset of white matter hyperintensities (140). Although evidence supports the concept that BBB breakdown plays a role in the formation of white matter hyperintensities, it is not observed in all patients with white matter hyperintensities (141), further emphasizing the diversity of cSVDs. The interaction between endothelium-dependent regulation of CBF and BBB breakdown in cSVD and whether they jointly contribute to disease progression is unclear. However, decreases in CBF can cause BBB breakdown (142). Two potential mechanisms by which this may occur are decreases in shear stress caused by hypoperfusion leading to the downregulation of tight junction proteins (143) and/or nitrosylation or nitrosation of tight junction proteins due to increased NO production (25).

Although current studies demonstrate that arteriosclerosis, endothelial dysfunction, and BBB disruption play a role in sporadic non-amyloid cSVDs, they do not provide a causal mechanism. The uncertain pathogenesis of cSVDs combined with the sporadic nature of the disease hinders the progress of understanding the molecular mechanisms that might lead to effective therapies. Monogenic forms of cSVD recapitulate clinical, radiological, and histopathological features of sporadic cSVDs. Studying monogenic forms of cSVDs may provide essential insights into the pathogenic mechanisms of all cSVDs.

MONOGENIC FORMS OF CSVD

The majority of cSVD cases are thought to result from the interaction of multiple genetic variants and environmental factors, but there are also monogenic inherited cSVDs, including cerebral autosomal dominant arteriopathy with subcortical infarcts and leukoencephalopathy (CADASIL), cerebral autosomal recessive arteriopathy with subcortical infarcts and leukoencephalopathy (CARASIL), and collagen type IV mutation related cSVDs (COL4A1/COL4A2) (144). Monogenic/familial forms of non-amyloidal cSVD share many pathological and clinical features of sporadic cSVDs. Investigation of monogenic forms of cSVDs is a promising approach to unveil underlying pathogenic mechanisms and discover novel treatments for monogenic and sporadic cSVDs.

CADASIL

CADASIL is the most common monogenic form of cSVD (145, 146). CADASIL is caused by mutations in *NOTCH3* (147). *NOTCH3* encodes a transmembrane receptor that undergoes proteolytic cleavage to release its extracellular domain and an intracellular fragment, which translocates to the nucleus to act as a transcription factor of genes involved in vascular SMC differentiation, angiogenesis, and response to injury (148). NOTCH3 is primarily expressed in vascular SMCs and pericytes and is required for the maturation and function of small vessels (149). The extracellular domain of NOTCH3 contains 34 epidermal growth factor repeats (EGFR). Each EGFR includes six cysteine residues that form three pairs of disulfide bonds to maintain normal NOTCH3 confirmation. All CADASIL *NOTCH3* mutations occur in exons 2-24, which encode the 34 EGFR, resulting in an odd number of EGFR cystine residues leaving an unpaired cysteine (150, 151). Unpaired cysteines create abnormal disulfide bridges with other NOTCH extracellular domains, which cause aggregation and formation of granular osmiophilic material (GOM), a pathological hallmark of CADASIL (152, 153). CADASIL causes thickening of the vascular wall and luminal stenosis of small cortical vessels. Histological studies revealed vascular SMC degeneration and NOTCH3 extracellular domain accumulation in the tunica media with increased accumulation of ECM proteins (154, 155).

CADASIL mutations likely act through a gain-of-function mechanism rather than decreased canonical NOTCH3 function (156). Patients with nonsense or null *NOTCH3* mutations do not exhibit the hallmarks of CADASIL (157). Transgenic mouse studies also support the hypothesis of toxic gain-of-function properties of mutant NOTCH3. Mice harboring human *NOTCH3* with p.Arg90Cys, p.Arg169Cys, or p.Cys428Ser mutations exhibited CADASIL-like pathological changes, NOTCH3 extracellular domain accumulation, and GOM deposition (158). Transgenic CADASIL mouse models have detectable white matter lesions at 12 months of age with diminished myogenic tone and impaired functional hyperemia appearing as early as six months (68, 159). This suggests that cerebrovascular defects precede and contribute to the pathogenesis of CADASIL cSVD.

Impaired myogenic tone in cerebral parenchymal arterioles from CADASIL mice was linked to abnormal hyperpolarization due to the upregulation of voltage-gated K^+ channels at the plasma membrane of SMCs (160). Increases in plasmalemmal Kv channels were linked to elevated tissue inhibitor of metalloproteinase 3 (TIMP3) activity (161). TIMP3 regulates the activity of a broad spectrum of metalloproteinases that release growth factors to control endocytosis of Kv channels (161-163). Notably, TIMP3 forms a complex with the extracellular domain of NOTCH3 and has been shown to accumulate around GOMs (162). Parenchymal arterioles are the last defense of capillaries from the disruptive effects of acute fluctuations in arterial pressure. Therefore, a decrease in myogenic tone increases the susceptibility of downstream capillaries to pressure overload. In addition, loss of myogenic tone diminishes vasodilatory reserve and impairs functional hyperemia.

$K_{IR}2.1$-based capillary-to-arteriole dilation is also impaired in CADASIL mice (164). Dabertrand et al. (164) show that these mice have diminished capillary EC $K_{IR}2.1$ current that is rescued by adding exogenous phosphatidylinositol 4,5-bisphosphate (PIP_2). PIP_2 physically interacts with $K_{IR}2.1$ channels to modulate activity, and phospholipid depletion reduces channel activity (165). Additionally, exogenous PIP_2 was able to restore *ex vivo* propagated vasodilation and *in vivo* functional hyperemia in CADASIL mice, suggesting that reduced levels of PIP_2 are integral to the pathogenesis of CADASIL cSVD. PIP_2 depletion in CADASIL mice was linked to diminished PIP_2 synthesis due to reduced ATP levels in capillary ECs (166).

These reports were the first insight into the molecular basis of cerebrovascular dysfunction associated with CADASIL cSVD. They also provide proof of concept for the therapeutic potential of PIP_2 replacement. However, it remains to be seen if this molecular pathway is specific to the CADASIL cSVD model or if it is shared with some forms of sporadic cSVDs. Interestingly, PIP_2 depletion has been reported to be involved in the pathology of the 5xFAD mouse model of Alzheimer's disease, providing evidence that PIP_2 deficiency is involved in multiple types of cSVDs (167).

CARASIL

CARASIL is an autosomal recessive monogenic cSVD characterized by early-onset leukoencephalopathy, alopecia, and lumbago (168). Pathogenic mutations in high-temperature requirement A serine peptidase 1 (*HTRA1*) cause CARASIL (169). Heterozygous HTRA1 pathogenic variants, known as *HTRA1*-cSVD, have also been noted (170). *HTRA1*-cSVD shares radiological and clinical features with classical CARASIL, but symptoms are milder and have a delayed onset. Post-mortem histology of CARASIL patients revealed extensive SMC loss, fibrous thickening of the intima, and fractured internal elastic lamina of arteries and arterioles (171). GOMs are not observed in patients with CARASIL, distinguishing it from CADASIL (172, 173).

The loss of HTRA1 protease activity is associated with CARASIL pathogenesis (169). HTRA1 is a serine protease that forms trimers and relies on an allosteric mechanism to regulate the proteolytic activity, which accounts for the dominant negative effects that lead to *HTRA1*-cSVD (174, 175). All CARASIL-associated HTRA1 missense mutations occur near or within the trypsin-like serine protease domain (169, 176) suggesting the loss of HTRA1 protease activity underlies pathogenesis.

HTRA1 modulates transforming growth factor-β (TGF-β) signaling (177). TGF-β signaling is implicated in many cellular functions, including regulating tissue homeostasis and repair, immune and inflammatory responses, ECM deposition, and cell differentiation (178). CARASIL-associated HTRA1 mutations lead to an increase in TGF-β signaling that causes increased synthesis of ECM proteins with consequent vascular fibrosis (179). CARASIL patients have increased ECM protein fibronectin, versican, and hyaluronan in the walls of cerebral arterioles (169, 180). These findings indicate that increased TGF-β signaling plays a critical role in the pathogenesis of CARASIL cSVD.

TGF-β signaling is extensively regulated by a balance of its unique synthesis pathway, sequestration, and activation mechanisms (66, 181). TGF-β is synthesized as a homodimeric proprotein cleaved by a proprotein convertase into a latency-associated peptide (LAP) and TGF-β ligand during post-translational processing (66). The LAP forms a noncovalent complex with the TGF-β ligand and a latent TGF-β-binding protein, which is secreted from the cell as a large latent complex and sequestered by the ECM in an inactive state (66). Serine proteases, matrix metalloproteinases, or acidic microenvironments within the ECM can activate the TGF-β complex. There are two proposed mechanisms for how HTRA1 downregulates TGF-β signaling. The more commonly reported mechanism involves HTRA1-mediated cleavage of the TGF-β complex or TGF-β receptors in the extracellular space (177, 182, 183). Alternatively, another group suggests that degradation of TGF-β proprotein in the ER is initiated by HTRA1 post-translational processing (180).

Although the exact mechanism by which HTRA1 downregulates TGF-β under physiological conditions is unclear, there is substantial evidence that HTRA1-linked disinhibition of TGF-β signaling underlies the molecular basis of CARASIL.

COL4A1* AND *COL4A2

As discussed above, heterotrimers of two COL4A1 and one COL4A2 polypeptides make up type IV collagen, a major component of basement membranes in nearly all organs, including the cerebral vasculature. Pathogenic mutations in *COL4A1* and *COL4A2* cause a rare autosomal dominant multisystem disorder that manifests the hallmarks of cSVD (9, 184). cSVD-related insults include micro- and macrohemorrhages, white matter hyperintensities, enlarged perivascular spaces, and lacunar ischemic strokes (9, 10, 184, 185). Other features of *COL4A1* and *COL4A2* mutations include porencephaly, ocular dysgenesis, renal defects, and myopathy (185).

The majority of pathogenic *COL4A1* and *COL4A2* mutations are missense mutations that result in a substitution of a glycine residue within the collagenous domain Gly-X-Y repeats (185). There are multiple pathways by which *COL4A1* and *COL4A2* mutations could cause disease (Figure 9). A deficiency of normal heterotrimers could lead to compromised basement membranes that perturb function. However, mice heterozygous for *Col4a1 and Col4a2* null alleles are viable with no overt phenotype suggesting pathogenicity is due to antimorphic or neomorphic effects of mutant trimers (186). COL4A1 and COL4A2 are translated in the ER/SR, where they interact with resident proteins to ensure proper folding, post-translational modification, and heterotrimer assembly prior to secretion (31). Pathogenic mutations in *COL4A1* and *COL4A2* result in intracellular accumulation, leading to activation of ER stress and subsequent activation of the unfolded protein response (187-189). Prolonged ER/SR stress can eventually trigger cell death, oxidative stress, and/or inflammation (190, 191). Treating *Col4a1* and *Col4a2* mutant mice with the FDA-approved chemical chaperone sodium 4-phenylbutyrate to promote the secretion of misfolded collagen IV and reduced ICH (189, 192-195). These findings support that ER/SR stress plays a critical role in the pathogenesis of some forms of *COL4A1* and *COL4A2*-related cSVDs, as well as provide a proof of concept of a potential therapy for some cSVDs.

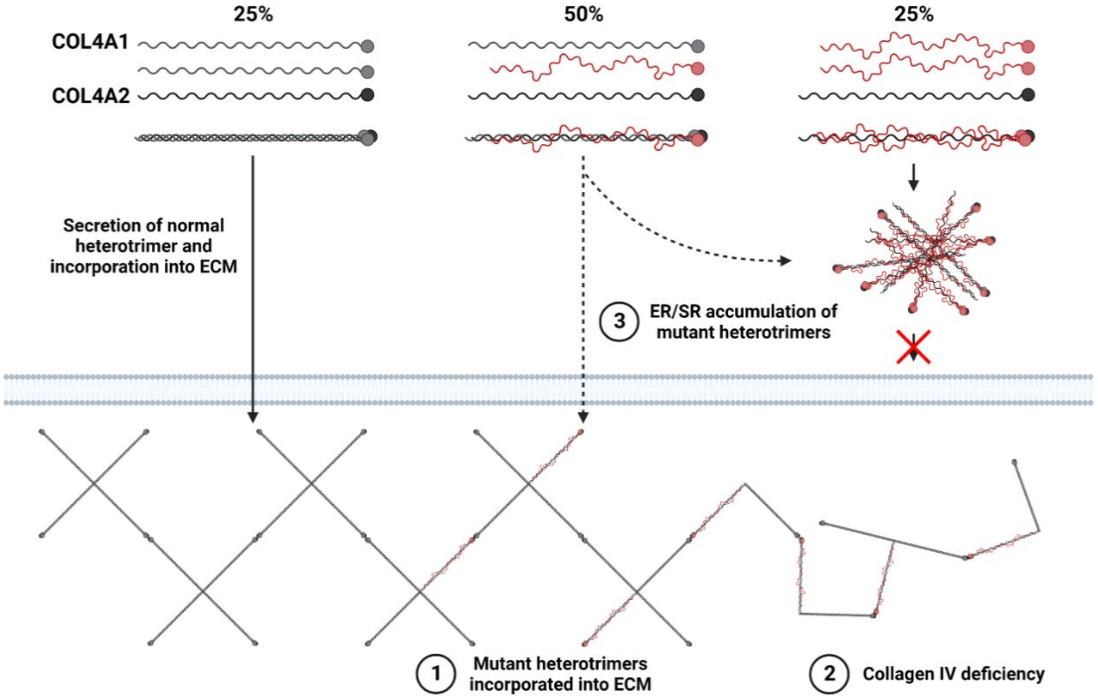

Figure 9. Potential sites for pathogenic insults in collagen IV biosynthesis pathway. Assuming random assembly within the endoplasmic/sarcoplasmic reticulum of cells heterozygous for *COL4A1* mutations, 25% of heterotrimers will be normal, and 75% would be abnormal (cells heterozygous for *COL4A2* mutations would produce 50% normal and abnormal). Normal heterotrimers would be secreted from the cell to be incorporated into the extracellular matrix (ECM), while abnormal ones tend to accumulate intracellularly. This leads to three potential sites for pathogenic insults: any mutant trimers that are secreted can disrupt ECM functional stability, decreased amount

of normal heterotrimers can lead to extracellular collagen IV deficiency, and/or intracellular accumulation causes ER/SR stress that disrupts cell function. Adapted from Kuo *et al.* 2012 (185).

The cytotoxic effects of intracellular accumulation of misfolded collagen IV cannot account for all pathogenic mutations. Allelic heterogeneity exists between *Col4a1* mutations with respect to the location of the mutation within the triple-helical domain. Mutations nearer to the carboxy terminus have severe intracellular accumulation of COL4A1 and COL4A2, while pathogenic mutations near the amino terminus, like $Col4a1^{G394V}$, have no intracellular accumulation (189). This observation suggests that the presence of mutant heterotrimers in the basement membrane contributes to the pathogenesis of some forms of COL4A1 and COL4A2-related cSVDs. Mutant heterotrimers compromising the structure and/or function of the basement membrane is a postulated mechanism. Mutant heterotrimers likely disrupt the basement membrane’s ability to regulate cell function via integrin or soluble growth factor-mediated cell signaling. Supporting this, Gould and colleagues recently showed that integrin and TGF-β signaling contributes to the pathogenesis of COL4A1-related ocular dysgenesis and myopathy (196, 197).

Further support that disruption of integrin signaling plays a role in the pathogenesis of *COL4A1* mutations comes from patients with hereditary angiopathy, nephropathy, and cramps (HANAC) syndrome. HANAC syndrome is caused by mutations in *COL4A1* exons 24 and 25 that occur near an integrin-binding domain (198, 199). Patients present with cSVD in addition to aneurysms in the carotid siphon (200). Other vascular phenotypes include retinal arteriolar tortuosities with repeated retinal hemorrhages. The majority of HANAC syndrome mutations are collagenous domain glycine mutations, so disruptions to basement membrane structure and/or cytotoxicity due to intracellular collagen IV heterotrimer accumulation may also play a role in the pathogenesis of HANAC syndrome (198, 201).

In addition to cSVDs caused by collagenous domain glycine mutations, mutations in or around the miR-29 microRNA binding site within the 3’ untranslated region of *COL4A1* causes an ischemic cSVD called pontine autosomal dominant microangiopathy and leukoencephalopathy (PADMAL) (202). Clinical manifestations of PADMAL include lesions predominantly in the pons with rare microbleeds (203). This is distinct from *COL4A1* missense glycine mutations and CADASIL, where lesions are mainly localized to subcortical regions. Mutations that disrupt the *COL4A1* miR-29 binding site upregulates expression leading to increased ECM deposition within the walls of small cerebral vessels, causing fibrosis (202).

Together these reports emphasize the diversity of cSVDs. Even within the same genes, mutations can cause cSVD through different mechanisms. Further investigations into animal models are critical for the development of specific therapeutic strategies for both COL4A1 cSVDs as well as some forms of sporadic cSVDs. COL4A1 cSVDs have been linked to ER stress and disruption of basement membrane function through the incorporation of mutant type IV collagen heterotrimers, but the exact pathophysiological mechanisms and how they impact cerebrovascular processes remain incompletely understood.

This dissertation focuses on identifying the molecular mechanisms contributing to cSVD in mice with missense mutations in *Col4a1* at amino acid 394 (*Col4a1*$^{+/G394V}$) and 1344 (*Col4a1*$^{+/G1344D}$). The second chapter describes our investigations of *Col4a1*$^{+/G1344D}$ mice. We found that these mice exhibit age-dependent ICH and brain lesions associated with a loss of myogenic vasoconstriction. Myogenic tone was lost due to impaired pressure-induced depolarization caused by decreased Ca^{2+}-dependent activation of TRPM4 channels and disrupted SR Ca^{2+} signaling. Treating *Col4a1*$^{+/G1344D}$ mice with 4-phenylbutyrate, a compound that promotes the trafficking of misfolded proteins, prevented these defects. This suggests that *Col4a1*^{G1344D} mutations prevent the secretion of mutant heterotrimers, causing them to accumulate in the SR and disrupting fundamental Ca^{2+} signaling processes. In the third chapter, we report that *Col4a1*$^{+/G394V}$ mice also have age-dependent impairment of the myogenic response associated with a significant decrease in depolarizing TRPM4 currents. However, decreased vascular SMC PIP_2 levels, a necessary cofactor for TRPM4 activity, was the cause of decreased TRPM4 activity. Inhibition of phosphatidylinositol-3-kinase (PI3K), an enzyme that reduces PIP_2 bioavailability by converting it to phosphatidylinositol (3,4,5)-trisphosphate (PIP_3) restored myogenic tone. Selective block of TGF-β receptors had the same effect. In the fourth chapter, we found that *Col4a1*$^{+/G394V}$ mice had age-related defects in capillary-to-arteriole dilation, functional hyperemia in the brain, and memory. This was due to depleted PIP_2 in arterial and capillary ECs leading to the loss of $K_{IR}2.1$ channel activity. PI3K and TGF-β receptor inhibition restored capillary-to-arteriole dilation, suggesting hyperactivity of TGF-β signaling pathways that stimulate PI3K to deplete PIP_2 is the fundamental defect in *Col4a1*$^{+/G394V}$ mice. Longitudinal treatment with PI3K inhibitors improved NVC and memory function in *Col4a1*$^{+/G394V}$ mice. In conclusion, the body of work presented here describes two distinct and novel age-dependent mechanisms for cSVD and provides proof-of-concept evidence for viable therapeutic strategies.

CHAPTER 2: DEFECTIVE CA^{2+}- DEPENDENT ACTIVATION OF TRPM4 CHANNELS CONTRIBUTES TO AGE-RELATED CEREBRAL SMALL VESSEL DISEASE IN *COL4A1* MUTANT MICE

Evan Yamasaki[1], Pratish Thakore[1], Sher Ali[1], Alfredo Sanchez Solano[1], Xiaowei Wang[2], Xiao Gao[3,4], Cassandre Labelle-Dumais[2], Myriam M. Chaumeil[3,4], Douglas B. Gould[2,5], and Scott Earley[1*]

[1]Department of Pharmacology, Center for Molecular and Cellular Signaling in the Cardiovascular System, University of Nevada, Reno School of Medicine, Reno, NV 89557-0318, USA

[2]Department of Ophthalmology, UCSF School of Medicine, San Francisco, CA 94158, USA

[3]Department of Physical Therapy and Rehabilitation Science, UCSF School of Medicine, San Francisco, CA 94143, USA

[4]Department of Radiology and Biomedical Imaging, UCSF School of Medicine, San Francisco, CA 94143, USA

[5]Department of Anatomy, Institute for Human Genetics, Cardiovascular Research Institute, Bakar Aging Research Institute, UCSF School of Medicine, San Francisco, CA 94158, USA

Keywords: *COL4A1*, collagen, cerebral small vessel diseases, basement membrane, myogenic tone, TRPM4, IP$_3$R, Calcium, Ca^{2+}, ER Stress, SR Stress, ion channels.

[*]Corresponding author

Address Correspondence To: Scott Earley, Ph.D.
University of Nevada, Reno School of Medicine
Manville Health Sciences Building, Room 8
MS-0318
Reno, NV 89557-0318, USA
Phone: (775) 784-4117
Fax: (775) 784-1620
Email: searley@med.unr.edu

ABSTRACT

Humans and mice with mutations in *COL4A1* and *COL4A2* manifest radiological and clinical hallmarks of cerebral small vessel disease (cSVD), but the pathogenic mechanisms are unknown. Here we report that mice with a missense mutation in *Col4a1* at amino acid 1344 (*Col4a1*$^{+/G1344D}$) exhibit age-dependent intracerebral hemorrhage (ICH), brain lesions detected by magnetic resonance imaging, and memory deficits. This pathology was associated with the loss of myogenic vasoconstriction, a vascular response essential for autoregulation of cerebral blood flow. Electrophysiological analyses showed that the loss of myogenic constriction resulted from blunted pressure-induced smooth muscle cell (SMC) membrane depolarization. Further, we found that dysregulation of membrane potential was associated with impaired Ca^{2+}-dependent activation of transient receptor potential melastatin 4 (TRPM4) cation channels and disruptions in sarcoplasmic reticulum (SR) Ca^{2+} signaling. Treating *Col4a1*$^{+/G1344D}$ mice with 4-phenylbutyrate, a compound that promotes the trafficking of misfolded proteins and alleviates SR stress, averted the loss of myogenic tone, prevented ICH, and reduced memory defects. We conclude that alterations in SR Ca^{2+} handling that impair TRPM4 channel activity results in dysregulation of SMC membrane potential and loss of myogenic tone which contributes to age-related cSVD in *Col4a1*$^{+/G1344D}$ mice.

Graphical Abstract

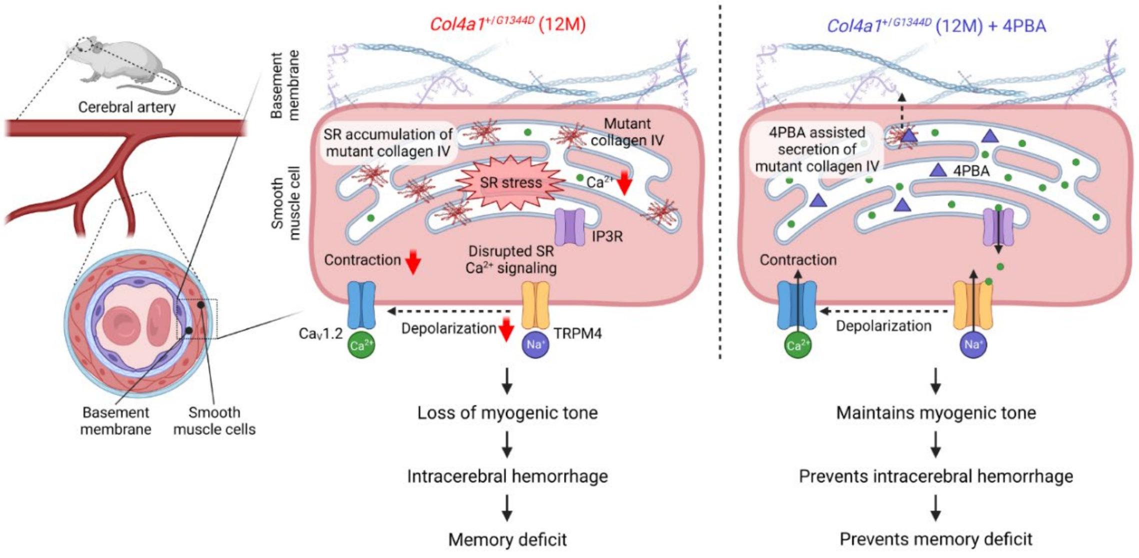

INTRODUCTION

Cerebral small vessel diseases (cSVDs) are a group of related pathologies that damage tiny arteries, arterioles, venules, and capillaries in the brain. These diseases are a major cause of stroke and, after Alzheimer's disease, the second leading cause of adult cognitive impairment and dementia (106, 204). The underlying pathogenic mechanisms of cSVDs remain largely unknown, and no specific treatment options exist. Sporadic and familial forms of cSVD share clinical and radiological features, including white matter hyperintensities, dilated perivascular spaces, lacunar infarcts, microbleeds, and intracerebral hemorrhages (ICHs) (107-110). Individuals with Gould syndrome, a rare multisystem disorder caused by autosomal dominant mutations in collagen IV alpha 1 (*COL4A1*) and alpha 2 (*COL4A2*), manifest these hallmarks of cSVD (9, 10, 184). The majority of pathogenic *COL4A1* and *COL4A2* mutations substitute critical glycine (G) residues within triple helical domains (195). These mutations impair the secretion of heterotrimers of COL4A1 and COL4A2 [$\alpha1\alpha1\alpha2$(IV)] which can lead to endoplasmic reticulum (ER) stress and/or disrupt the structure and function of basement membranes (187-189). However, it is not known how collagen defects and associated ER stress cause cSVD. An allelic series of *Col4a1* and *Col4a2* mutations demonstrate pathological heterogeneity (189). For the current study, we investigated the pathogenesis of *Col4a1*-associated cSVD using mice with a missense mutation that changes the G residue at amino acid position 1344 to aspartate (D). These animals, designated *Col4a1*$^{+/G1344D}$, model the most common type of mutation that occurs in humans and develop cSVD pathology that is more severe compared with others in the allelic series (189, 195).

Distinctive attributes of the cerebral vasculature serve the unique requirements of the brain. For example, cerebral arteries and arterioles exhibit graded constriction in response to changes in intravascular pressure. This vital autoregulatory process, known as the vascular myogenic response, protects downstream capillary beds from potentially harmful increases in perfusion pressure when cardiac output is elevated during exercise or other stimuli (71). The myogenic response is intrinsic to vascular smooth muscle cells (SMCs) and requires the coordinated activity of several ion channels. Increases in intraluminal pressure activate transient receptor potential melastatin 4 (TRPM4) channels, allowing an influx of Na^+ ions that depolarizes the plasma membrane to increase voltage-dependent Ca^{2+} inflow through Cav1.2 Ca^{2+} channels and engage the contractile apparatus (205, 206). Pressure-induced membrane depolarization is balanced by hyperpolarizing currents conducted by several K^+-permeable ion channels, including large-conductance Ca^{2+} activated K^+ (BK) channels, voltage-dependent K^+ (K_V) channels, and others (82, 88, 207). The interplay of depolarizing and hyperpolarizing currents controls the resting membrane potential of SMCs and maintains cerebral arteries in a state of partial contraction. BK and TRPM4 channels require high levels of intracellular Ca^{2+} for activation and, under native conditions, are stimulated by Ca^{2+} released from the sarcoplasmic reticulum (SR) through ryanodine receptors (RyRs) and inositol triphosphate receptors (IP_3Rs), respectively (88, 208). Impairment of the myogenic response has been implicated in many types of cerebrovascular disease, including familial cSVD associated with cerebral autosomal dominant arteriopathy with subcortical infarcts and leukoencephalopathy (CADASIL) caused by mutations in *NOTCH3* (160). However, the impact of *Col4a1* mutations on the myogenic response and how this affects neuronal pathology is not known.

Here, we report that *Col4a1*$^{+/G1344D}$ mice exhibit age-dependent loss of myogenic tone that is associated with spontaneous intracerebral hemorrhage (IHC), brain lesions detected by susceptibility-weighted magnetic resonance imaging (SWI), and defects in spatial working and recognition memory. The deficit in myogenic tone resulted from diminished stretch-induced activation of TRPM4 channels and impaired pressure-induced SMC membrane depolarization. We also found that subcellular and global Ca^{2+} signals generated by releasing Ca^{2+} from the SR through RyRs and IP_3Rs were disrupted in SMCs from aged *Col4a1*$^{+/G1344D}$ mice. Treating *Col4a1*$^{+/G1344D}$ mice with 4-phenylbutyrate (4PBA), a small molecule with chaperone properties that improves the secretion of misfolded proteins and diminishes ER/SR stress (189, 192-195, 209), attenuated the loss of myogenic tone, largely protected mice from ICH, and diminished memory deficits. These data suggest that SR stress in SMCs from *Col4a1*$^{+/G1344D}$ mice causes disruptions in intracellular Ca^{2+} signaling, stretch-induced activation of TRPM4 channels, pressure-induced SMC membrane potential depolarization, and myogenic constriction. Our data also suggest that these defects contribute to spontaneous ICH and memory defects. Thus, the findings of this study reveal a novel age-dependent mechanism of cSVD and identify 4PBA or other chaperone drugs as a potential treatment option.

RESULTS

Col4a1$^{+/G1344D}$ mice exhibit age-dependent pathology

All studies utilized *Col4a1*$^{+/G1344D}$ mice or *Col4a1*$^{+/+}$ littermates as controls. Amino acid 1344 is part of a triple helical domain near the C-terminus (Figure 1A). To investigate age-related aspects of cSVD pathology, mice were studied at 3 and 12 months (M) of age, representing the young adult and middle-age stages of life, respectively. Male and female mice were used throughout the study, and no sex-specific differences were detected.

Spontaneous ICH is a highly penetrant and consequential manifestation of *Col4a1* mutations (210). ICH severity was measured in brain sections from *Col4a1*$^{+/+}$ and *Col4a1*$^{+/G1344D}$ mice stained with Prussian blue. In young adults, ICH was not detected in *Col4a1*$^{+/+}$ mice, but small punctate Prussian blue staining was present in brain sections from *Col4a1*$^{+/G1344D}$ mice (Figure 1B and C). Middle-aged *Col4a1*$^{+/+}$ mice did not exhibit ICH, but brain sections from 12 M-old *Col4a1*$^{+/G1344D}$ mice displayed large areas of Prussian blue staining mainly localized to the subcortical regions (Figure 1D and E). The total area of Prussian blue staining in 12 M-old *Col4a1*$^{+/G1344D}$ mice was nearly 20-fold more extensive than in 3 M-old mutants (1.9% vs. 0.1% of brain area, respectively), indicating that the severity of spontaneous ICH increases dramatically with age.

cSVDs are often diagnosed in individuals by radiological findings including brain lesions (117). Brain lesions were measured in 12 M-old *Col4a1*$^{+/+}$ and *Col4a1*$^{+/G1344D}$ mice *in vivo* using SWI. Middle-aged *Col4a1*$^{+/+}$ mice did not exhibit SWI-detectable brain lesions, but brains from age-matched *Col4a1*$^{+/G1344D}$ mice had multiple lesions, mainly localized to the thalamus (Figure 1F-I). The number, total volume, and localization of brain lesions detected with SWI are consistent with ICH detected with Prussian blue staining.

Col4a1$^{+/G1344D}$ mice exhibit age-dependent declines in memory function

To evaluate the impact of *Col4a1* mutations on memory function, *Col4a1*$^{+/+}$ and *Col4a1*$^{+/G1344D}$ mice were subjected to the Y-maze spontaneous alternation behavioral assay (Figure 2A). This test was designed to detect defects in short-term spatial working memory (211). 3 M-old *Col4a1*$^{+/+}$ and *Col4a1*$^{+/G1344D}$ mice performed similarly in this test with no significant differences in spontaneous alternation, the maximum number of alternations, or total distance traveled (Figure 2B-D). In contrast, the alternation index of 12 M-old *Col4a1*$^{+/G1344D}$ mice was significantly reduced compared to age-matched *Col4a1*$^{+/+}$ animals (Figure 2E). There were no significant differences in the maximum number of alternations or distance moved (Figure 2F and G).

To test longer-term spatial reference memory, *Col4a1*$^{+/+}$ and *Col4a1*$^{+/G1344D}$ mice were subjected to the Y-maze novel arm behavioral assay (Figure 2H) (211). 3 M-old *Col4a1*$^{+/+}$ and *Col4a1*$^{+/G1344D}$ mice performed equally in this test, with no significant differences in the time spent or the number of entries in the novel arm (Figure 2I-K). However, the time spent and the number of entries in the novel arm of 12 M-old *Col4a1*$^{+/G1344D}$ mice was significantly lower than age-matched *Col4a1*$^{+/+}$ animals (Figure 2L-N). These data suggest that *Col4a1*$^{+/G1344D}$ mice exhibit age-dependent deficits in short-term and long-term memory.

Diminished pressure-induced constriction of cerebral arteries from middle-aged Col4a1$^{+/G1344D}$ mice is due to impaired SMC membrane depolarization.

To better understand the underlying causes of ICH and memory deficits in *Col4a1*$^{+/G1344D}$ mice, we used *ex vivo* pressure myography to study the myogenic response of cerebral arteries (26). Vasoconstriction in response to stepwise increases in intraluminal pressure (from 5 to 120 mmHg) was evaluated by measuring the active steady-state luminal diameter of cannulated cerebral arteries bathed in standard physiological saline solution at each pressure. This procedure was then repeated using a Ca^{2+}-free bathing solution to determine the passive response to pressure, and myogenic tone was calculated as the difference in active versus passive diameter normalized to the passive diameter. The myogenic tone of cerebral arteries isolated from 3 M-old *Col4a1*$^{+/+}$ and *Col4a1*$^{+/G1344D}$ mice did not differ (Figure 3A and B). However, cerebral arteries from 12 M-old *Col4a1*$^{+/G1344D}$ mice barely constricted in response to pressure and had significantly lower levels of myogenic tone than those from age-matched *Col4a1*$^{+/+}$ mice (Figure 3C and D). These data demonstrate that cerebral arteries from *Col4a1*$^{+/G1344D}$ mice lose myogenic tone with age.

SMCs in the vascular wall depolarize in response to increases in intraluminal pressure (75). Depolarization of the plasma membrane increases voltage-dependent Ca^{2+} influx to trigger muscular contraction and vasoconstriction (75, 76). To determine if the loss of myogenic tone in middle-aged *Col4a1*$^{+/G1344D}$ mice was associated with impaired pressure-induced depolarization, we recorded the membrane potentials of SMCs in intact cerebral arteries using intracellular microelectrodes. At a low intraluminal pressure (20 mmHg), the membrane potential of SMCs in cerebral arteries from 3 M-old *Col4a1*$^{+/+}$ and *Col4a1*$^{+/G1344D}$ mice did not differ (Figure 3E and F). Increasing intraluminal pressure to physiological levels (80 mmHg) depolarized the SMC membrane potential in arteries from both groups to the same extent (Figure 3E and F). When vessels from 12 M-old animals were investigated, SMC membrane potential did not differ between

Col4a1$^{+/+}$ and *Col4a1*$^{+/G1344D}$ when arteries were pressurized to 20 mmHg (Figure 3G and H). However, when intraluminal pressure was increased to 80 mmHg, the depolarization of SMCs in cerebral arteries from *Col4a1*$^{+/G1344D}$ mice was significantly blunted compared with controls (Figure 3G and H). These data suggest that cerebral arteries from 12 M-old *Col4a1*$^{+/G1344D}$ mice lose myogenic tone because pressure-induced SMC membrane depolarization is impaired.

Age-related declines in BK and TRPM4 channel activity in SMCs from Col4a1$^{+/G1344D}$ ***mice.***

Changes in ion channel activity could account for impaired pressure-induced SMC depolarization in arteries from *Col4a1*$^{+/G1344D}$ mice. We used patch-clamp electrophysiology to compare the activity of hyperpolarizing K_V and BK channels and depolarizing TRPM4 channels in native SMCs from control and *Col4a1*$^{+/G1344D}$ mice.

Elevated SMC K_V channel current density is responsible for diminished myogenic tone in cerebral arteries from CADASIL cSVD mice (160). To determine if this mechanism accounts for the loss of myogenic tone in cerebral arteries from middle-aged *Col4a1*$^{+/G1344D}$ mice, we measured K_V currents in freshly isolated SMCs. K_V currents were recorded using the amphotericin B perforated patch-clamp configuration to maintain the integrity of intracellular signaling cascades. Whole-cell currents were evoked by applying voltage steps from -60 to +60 mV from a holding potential of -80 mV in the presence of selective BK channel blocker paxilline (1 µM). The voltage step protocol was repeated in the presence of K_V channel blocker 4-aminopyridine (5 mM), and K_V current amplitude was determined at each potential by subtraction. We found that K_V current amplitudes did not differ between SMCs from 12 M-old *Col4a1*$^{+/+}$ and *Col4a1*$^{+/G1344D}$ mice at all applied command potentials (Supplemental Figure 1A and B).

The activity of BK channels in cerebral artery SMCs under native conditions is driven by the transient release of Ca^{2+} ions through RyRs on the SR into restricted subcellular microdomains proximal to the plasma membrane (212). These signaling events, known as Ca^{2+} sparks, activate clusters of BK channels on the plasma membrane to generate large-amplitude spontaneous transient outward currents (STOCs) (88, 207). We utilized the amphotericin B perforated patch-clamp configuration to measure STOCs in cerebral artery SMCs from 3 M-old *Col4a1*$^{+/+}$ and *Col4a1*$^{+/G1344D}$ mice over a range of command potentials (-60-0 mV) and saw no significant difference in STOC frequency or amplitude (Figure 4A-C). However, the frequency and amplitude of STOCs were significantly lower in cerebral artery SMCs from 12 M-old *Col4a1*$^{+/G1344D}$ mice compared with age-matched controls (Figure 4D-F). To determine if decreases in STOCs result from changes in gene expression, we utilized ddPCR to measure transcript levels of *Kcnma1* (BK subunit α), *Kcnmb1 (*BK subunit $\beta1$), and *Ryr2* (ryanodine receptor 2). No differences in mRNA expression levels were detected (Supplemental Figure 2).

Reduced BK channel activity depolarizes the SMC membrane potential and increases contractility (89). Thus, diminished BK channel activity in SMCs from 12 M-old *Col4a1*$^{+/G1344D}$ mice cannot account for impaired pressure-induced membrane depolarization.

TRPM4 is a Ca^{2+}-activated, nonselective monovalent cation channel required for pressure-induced SMC depolarization and the development of myogenic tone in cerebral arteries (78, 205, 206, 213). Over the membrane potential range of SMCs in the vascular wall under physiological conditions (-60 to -30 mV), TRPM4 channels conduct inward Na^+ currents that depolarize the plasma membrane in response to increases in intraluminal pressure (205, 214). Patch-clamp electrophysiology was used to determine if TRPM4 activity is diminished in *Col4a1*$^{+/G1344D}$ mice. We assessed channel function and availability in freshly isolated cerebral artery SMCs using the conventional whole-cell patch-clamp configuration with a high [Ca^{2+}] intracellular solution to directly activate TRPM4. Currents were recorded as voltage ramps (-100 to +100 mV) were applied. Voltage ramps were repeated in the presence of TRPM4 blocker 9-phenanthrol (30 µM) (205), and TRPM4 currents were isolated by subtraction. Prior studies using ion substitution protocols have shown that Ca^{2+}-activated, 9-phenanthrol currents recorded using these methods are carried by Na^{+} ions, providing substantial evidence that these are *bona fide* TRPM4 currents (206). We found that the amplitudes of whole-cell TRPM4 currents recorded from cerebral artery SMCs did not differ between *Col4a1*$^{+/+}$ and *Col4a1*$^{+/G1344D}$ mice at 3 and 12 M of age (Figure 4G-J). These data indicate that the collagen mutation studied here has no direct effects on TRPM4 channel function and does not impair the trafficking of channel protein to the plasma membrane.

TRPM4 channels in SMCs are activated by a signal transduction cascade initiated by angiotensin II type 1 receptors (AT$_1$Rs) (21, 79, 215, 216). Activation of Gq protein-coupled AT$_1$Rs stimulates phospholipase C (PLC), leading to the cleavage of phosphatidylinositol 4,5-bisphosphate (PIP$_2$) into diacylglycerol and inositol triphosphate (IP$_3$). IP$_3$ stimulates Ca^{2+} release from the SR through IP$_3$Rs to transiently activate TRPM4 channels (78, 79, 208). AT$_1$Rs are directly activated by the stretch of the plasma membrane in a manner independent of their ligand and are a critical mechanosensor in SMCs (21, 79, 215, 216). To measure the activity of TRPM4 channels in response to mechanical force, we patch-clamped SMCs in the amphotericin B perforated patch configuration and applied negative pressure (-20 mmHg) through the patch pipet to stretch the plasma membrane. Stretch-induced transient inward cation currents (TICCs) evoked in this manner are blocked by 9-phenanthrol and abolished by knockdown of TRPM4 expression (205, 208). Stretch-activated TICC activity in SMCs from 3-M old *Col4a1*$^{+/+}$ and *Col4a1*$^{+/G1344D}$ (Figure 4K and L) did not differ. In contrast, stretch-induced TICC activity in SMCs from 12 M-old *Col4a1*$^{+/G1344D}$ mice was significantly lower than that of age-matched *Col4a1*$^{+/+}$ mice (Figure 4M and N). To determine if altered gene expression underlies the reduction in TICC activity, we utilized ddPCR to measure transcript levels of *Trpm4* (TRPM4)*, Itpr1* (IP_3 receptor 1)*,* and *Itpr2* (IP_3 receptor 2) in cerebral arteries from 12 M-old *Col4a1*$^{+/+}$ and *Col4a1*$^{+/G1344D}$ mice. No differences in mRNA copy number were observed (Supplemental Figure 2). These data suggest that blunted pressure-induced SMC depolarization and impaired myogenic tone result from diminished stretch-induced activation of TRPM4 channels.

Defective intracellular Ca^{2+} signaling in cerebral artery SMCs from middle-aged Col4a1$^{+/G1344D}$ mice.

Ca^{2+} released from the SR drives BK and TRPM4 channel activity in cerebral artery SMCs (88, 208). Therefore, we investigated the possibility that these vital SR Ca^{2+} signaling pathways are disrupted in SMCs from 12 M-old *Col4a1*$^{+/G1344D}$ mice. Freshly isolated SMCs were loaded with the Ca^{2+}-sensitive fluorophore Fluo-4 AM and imaged using high-speed, high-resolution spinning disk confocal microscopy. Spontaneous Ca^{2+} sparks were present in SMCs isolated from 3 M-old *Col4a1*$^{+/+}$ and *Col4a1*$^{+/G1344D}$ mice. The frequency, amplitude, duration, rise time, and decay rate did not differ between groups (Figure 5A-C). Spontaneous Ca^{2+} sparks were also present in SMCs isolated from both groups of middle-aged mice. No significant differences in Ca^{2+} spark amplitude, duration, rise time, and decay rate were observed, but notably, Ca^{2+} spark frequency was significantly lower in SMCs from 12 M-old *Col4a1*$^{+/G1344D}$ mice (Figure 4D-

F). Diminished Ca^{2+} spark frequency likely accounts for decreased STOC frequency in SMCs from middle-aged *Col4a1* mutant mice.

Fluo-4 AM-loaded SMCs were challenged with a ryanodine receptor agonist, caffeine (10 mM), to investigate how RyR function was affected by the *Col4a1*$^{+/G1344D}$ mutation (217). Ca^{2+} signals arising from intracellular release were isolated from Ca^{2+} influx events by acutely removing Ca^{2+} from the extracellular solution immediately before recording. Caffeine-evoked global increases in cytosolic [Ca^{2+}] did not differ between SMCs from young adult *Col4a1*$^{+/+}$ and *Col4a1*$^{+/G1344D}$ mice (Figure 5G and H). In contrast, caffeine-induced global Ca^{2+} signals were smaller in amplitude in SMCs from 12 M-old *Col4a1*$^{+/G1344D}$ mice than in controls (Figure 5I and J). These data indicate that the release of SR Ca^{2+} from RyRs is impaired in the SMCs of *Col4a1*$^{+/G1344D}$ mice in an age-dependent manner.

Fluo-4 AM loaded-SMCs were also treated with the G_q protein-coupled thromboxane A2 receptor agonist U46619 to investigate IP_3R-mediated Ca^{2+} signaling. U46619-induced (100 nM) Ca^{2+} signals did not differ between cerebral artery SMCs from 3 M-old *Col4a1*$^{+/+}$ and *Col4a1*$^{+/G1344D}$ mice (Figure 5K and L). In contrast, Ca^{2+} signals induced by U46619 were smaller in amplitude in SMCs from 12 M-old *Col4a1*$^{+/G1344D}$ mice compared to controls (Figure 5M and N). These data suggest that the release of SR Ca^{2+} from IP_3Rs is also impaired in the SMCs of *Col4a1*$^{+/G1344D}$ mice in an age-dependent manner. RyRs and IP_3Rs share the same SR Ca^{2+} source (218). Impairment of Ca^{2+} release through both receptors suggests that the SR [Ca^{2+}] of SMCs from middle-aged *Col4a1*$^{+/G1344D}$ mice is lower than that of corresponding controls. Diminished SR Ca^{2+} levels could account for diminished STOC and TICC activity and decreased Ca^{2+} spark frequency.

4PBA prevents age-related loss of myogenic tone, spontaneous ICH, and spatial working memory deficits in Col4a1$^{+/G1344D}$ mice.

Col4a1$^{+/G1344D}$ mice display increased intracellular accumulation of misfolded α1α1α2(IV) collagen, which causes ER/SR stress in collagen-producing cells (187, 189). The chemical chaperone 4PBA facilitates the trafficking of misfolded mutant proteins and reduces ER/SR stress (219). To investigate a potential link between impaired collagen secretion and the pathology of *Col4a1*$^{+/G1344D}$ mice, 4PBA (50 mM) was added to the drinking water of mutant and control animals from birth (postnatal day 0).

We found that age-related loss of myogenic tone was prevented by treating *Col4a1*$^{+/G1344D}$ mice with 4PBA (Figure 6A and B). Spontaneous ICH in middle-aged *Col4a1*$^{+/G1344D}$ mice treated with 4PBA was 4-fold lower than untreated *Col4a1*$^{+/G1344D}$ mice and did not differ from 4PBA-treated control mice (Figure 6C and D). These data suggest that 4PBA significantly diminishes the age-dependent myogenic tone defect and ICH in *Col4a1*$^{+/G1344D}$ mice. Finally, using the spontaneous alteration Y-maze assay, we found that although the mean alternation index of middle-aged *Col4a1*$^{+/G1344D}$ mice treated with 4PBA was slightly lower than 4PBA treated control mice, it was significantly higher than untreated *Col4a1*$^{+/G1344D}$ mice (Figure 6E). The maximum number of alternations and distance moved did not differ between 4PBA-treated 12 M-old *Col4a1*$^{+/G1344D}$ and *Col4a1*$^{+/+}$ and untreated *Col4a1*$^{+/G1344D}$ mice (Figure 6F and G). These data indicate that 4PBA treatment largely mitigates deficits in spatial working memory. We conclude that age-related loss of myogenic tone, ICH, and memory defects in *Col4a1*$^{+/G1344D}$ mice can be prevented or attenuated by treatment with 4PBA, linking the mutant's brain pathology with impaired secretion of misfolded collagen molecules and/or ER/SR stress.

DISCUSSION

Despite the enormous impact of the disease, the molecular pathogenesis of cSVD is essentially unknown. Here we utilized the *Col4a1*$^{+/G1344D}$ mouse model of Gould syndrome to investigate how this monogenic form of cSVD damages small arteries in the brain during aging. Our findings show that these mice exhibit pathological changes with age that include the loss of myogenic tone, high levels of spontaneous ICH, brain lesions, and memory defects. Electrophysiology experiments revealed that the loss of myogenic tone is associated with diminished pressure-induced SMC depolarization and decreased activities of BK and TRPM4 channels. In addition, we found that fundamental RyR- and IP_3R-dependent Ca^{2+} signaling pathways are disrupted in SMCs from middle-aged *Col4a1*$^{+/G1344D}$ mice, likely due to a reduction in SR Ca^{2+} levels. Treating *Col4a1*$^{+/G1344D}$ mice with the chemical chaperone 4PBA negated the loss of myogenic tone, prevented spontaneous ICH, and reduced deficits in spatial working memory. We conclude that the age-dependent cSVD pathogenesis of *Col4a1*$^{+/G1344D}$ mice results from defects in SMC SR function that lead to reduced Ca^{2+} store load and disrupted intracellular Ca^{2+} signaling. Defects in subcellular Ca^{2+} signals diminish TRPM4 channel activity, disrupting membrane potential regulation and impeding pressure-induced constriction of cerebral arteries. These findings reveal a novel mechanism of age-dependent cSVD.

The myogenic response is a vital autoregulatory mechanism that protects delicate capillaries in the brain from pressure overload during increases in cardiac output and transient increases in perfusion associated with exercise, stress, and other stimuli (71). Loss of myogenic tone is observed in the CADASIL model of familial cSVD (68, 160). Notably, Dabertrand *et al*. linked the loss of myogenic tone in the CADASIL model with blunted pressure-induced SMC membrane potential depolarization and connected the defect in membrane potential regulation with increased surface expression of K_V channels and elevated hyperpolarizing K^+ current density (160). Our study uncovered a different ion channel defect in the SMCs of *Col4a1*$^{+/G1344D}$ cSVD mice – Kv currents did not differ from controls but stretch-induced TRPM4 cation channel activity was greatly diminished. This defect was not due to reduced *Trpm4* expression, gross defects in channel function, or the number of channels available for activation on the plasma membrane. Instead, our data suggest that activation of TRPM4 by Ca^{2+} released from the SR through IP_3Rs was faulty in middle-aged *Col4a1*$^{+/G1344D}$ mice. The release of SR Ca^{2+} from RyRs was also impaired in SMCs from mutant mice, disrupting the Ca^{2+} spark – BK channel Ca^{2+} signaling pathway and diminishing STOC frequency. STOCs act as a negative feedback regulator to SMC pressure-induced membrane depolarization and contraction (220). However, because SMC pressure-induced membrane depolarization is impaired in middle-aged *Col4a1*$^{+/G1344D}$ mice, the STOC pathway is not engaged and has minimal influence on membrane potential. The impairment of multiple Ca^{2+} signaling modalities in mutant SMCs suggests that SR Ca^{2+} handling is defective. This concept is supported by a prior study showing that a ~16% decrease in SR [Ca^{2+}] diminished STOC frequency by 70% (221). Another study showed that depletion of SR [Ca^{2+}] to less than 80% of normal completely abolished IP_3R-mediated Ca^{2+} release (222). In many types of cells, store-operated Ca^{2+} entry (SOCE) is protective against decreases in ER/SR [Ca^{2+}] (223). However, SOCE is virtually undetectable in native, contractile vascular SMCs, promoting their susceptibility to pathogenic SR Ca^{2+} depletion (224-226). We conclude that disrupted pressure-induced SMC depolarization and loss of myogenic tone in middle-aged *Col4a1*$^{+/G1344D}$ mice are due to impaired activation of TRPM4 by Ca^{2+} released from the SR.

Protein synthesis and folding occurs within the SR (227). *Col4a1*$^{+/G1344D}$ mice display impaired secretion and increased intracellular accumulation of collagen α1α1α2(IV), presumably due to the misfolding of mutant protein (189). Retention of misfolded proteins causes ER/SR stress (228). Our data showed that treatment with 4PBA, a molecular chaperone that promotes the secretion of misfolded proteins, prevented the loss of myogenic tone, attenuated spontaneous ICH, and diminished impairment of spatial working memory, suggesting that ER/SR stress contributes to the pathology of middle-aged *Col4a1*$^{+/G1344D}$ mice. One of the pathological manifestations of ER/SR stress is the depletion of Ca^{2+} stores (229). Yamato *et al.* (230) demonstrated that tunicamycin-induced ER stress promotes RyR-mediated ER Ca^{2+} leak, potentially due to increased reactive oxygen species (ROS) production that depleted ER Ca^{2+} store load. Steady-state free Ca^{2+} levels in the ER/SR are maintained by the release of Ca^{2+} into the cytosol through RyRs and IP_3Rs, mobile and stationary Ca^{2+}-binding proteins in the SR lumen, and transport of Ca^{2+} from the cytosol into the SR by sarco/endoplasmic reticulum ATPase (SERCA) enzymes (218), and any of these processes can be potentially impacted by ER/SR stress in *Col4a1*$^{+/G1344D}$ mice. Future investigations into possible links between SMC SR stress and Ca^{2+} handling defects in other genetic and sporadic forms of cSVD may reveal new therapeutic options.

This study showed that *Col4a1*$^{+/G1344D}$ mice display spontaneous ICH and memory deficits by middle age, reminiscent of the age-dependent effects of sporadic cSVDs in humans. Our findings also indicate that dysregulation of critical SMC Ca^{2+} signaling mechanisms and TRPM4 channel activity is a central feature of cerebrovascular dysfunction in this model. The pathology of *Col4a1*$^{+/G1344D}$ mice is significantly attenuated by treatment with 4PBA, supporting the concept that promoting the secretion of misfolded proteins and/or reducing SR stress may be a viable treatment strategy for some forms of cSVD.

MATERIALS AND METHODS

Chemical and reagents: All chemicals and other reagents were obtained from Sigma-Aldrich, Inc. (St. Louis, MO, USA) unless otherwise specified.

Animals: Young adult (3M) and middle-aged (12M) male and female littermate *Col4a1*$^{+/+}$ and *Col4a1*$^{+/G1344D}$ mice were used in this study. The *Col4a1*^{G1344D} mutation was backcrossed to C57BL/6J mice for over 20 generations (231). Animals were maintained in individually ventilated cages (≤5 mice/cage) with *ad libitum* access to food and water in a room with controlled 12-hour light and dark cycles. All animal care procedures and experimental protocols involving animals complied with the National Institutes of Health (NIH) *Guide for the Care and Use of Laboratory Animals* and were approved by the Institutional Animal Care and Use Committees at the University of Nevada, Reno, and University of California, San Francisco.

Histological analysis: Isoflurane anesthetized mice were transcardially perfused with ice-cold phosphate-buffered saline (PBS) followed by ice-cold 4% paraformaldehyde (Fisher, Waltham, MA, USA) in PBS. Brains were postfixed with 4% paraformaldehyde for 24 hours at 4°C, cryoprotected in 30% sucrose in PBS, and embedded in optimal cutting temperature compound (Fisher). Coronal cryosections (35 µm) regularly spaced (500 µm) along the rostrocaudal axis were stained with a Prussian blue and nuclear fast red stain kit (Abcam, Cambridge, UK) following the manufacture's protocol. Images were acquired with a BZ-X700 microscope using BZ-X Viewer 1.3.0.5 software and stitched with BZ-X Analyzer 1.3.0.3 software (Keyence, Osaka, Japan). The percentage of brain area with Prussian blue staining for each section was calculated with ImageJ software (v2.3.0/1.53f; NIH, Bethesda, MD, USA). Hemorrhage severity was expressed as the average percentage of hemosiderin surface area on ~21 sections for each brain.

***In vivo* magnetic resonance imaging:** All *in vivo* magnetic resonance (MR) experiments were conducted on a 14.1 Tesla vertical MR system (Agilent Technologies, Palo-Alto, CA) equipped with 100 G/cm gradients and a single tuned millipede ^{1}H proton coil ($Ø_I$ = 40 mm). For each imaging session, mice were anesthetized using isoflurane (1-1.5% in O_2) and positioned in a dedicated craddle maintaining constant anesthesia and placed in the MR bore; respiration and temperature were continuously monitored during all acquisitions to ensure animal well-being and data reproducibility. Susceptibility weighted imaging (SWI) was performed to acquire high-resolution images of the mouse brain, using the following parameters: gradient-echo scheme, field of view (FOV) = 20 x 20 mm^2, matrix = 256 x 256, 16 slices, 0.4 mm slice thickness, 0.1 mm interslice gap, number of averages = 16, echo time (TE)/repetition time (TR) = 4.60/140ms, flip angle = 10 degrees. T2-weighted (T2W) images were also acquired in a fast-spin-echo scheme to evaluate brain anatomical structures, using the same FOV geometry as SWI and the following parameters: number of averages = 8, TE/TR = 21.38/2500ms, flip angle = 90 degrees. The fast-spin-echo based T2W imaging is less sensitive to distortion artifacts caused by B_0 inhomogeneity than SWI, and is thus used for the atlas-based brain structure registration as described below.

Hypointense lesions corresponding to ICH were quantified based on manual segmentation of the SWI images using an in-house software. To investigate the number of and distribution of hypointense SWI lesions across the brain, an open-sourced atlas-based imaging data analysis pipeline (AIDAmri) (232) was customized to register T2W brain images to the Allen Brain Reference Atlas (233). Based on the registration result, the normalized lesion volumes for each brain region were summed up across all animals and an intra-group region-wise volumetric analysis was performed.

Y-Maze behavioral assessment: Memory function was assessed using the Y-maze (Maze Engineers, Skokie, IL, USA) using two different configurations.

The spontaneous alternation behavioral assay was used to assess short-term spatial working memory (211). Mice were placed into one of the three arms of maze (start arm) and were allowed to explore all three arms for 10 minutes. Session videos were recorded and analyzed using Ethovision XT software (version 16.0.1536, Noldus Information Technology, Leesburg, VA, USA). Spontaneous alternation was evaluated by scoring the order of entries into each arm during the 10-minute recording period. Spontaneous alternation was calculated as spontaneous alternation (%) = [number of spontaneous alternations/max alternation] × 100, where the spontaneous alternation is defined as the number consecutive entries into each arm of the maze in any order without any repeats, and the max alternation is the total number of alternations possible (max alternation = total number of arm entries – 2).

The novel arm configuration was used to evaluate longer-term spatial reference memory (211). This test was performed across 2 days. On day one, mice were placed into one of the three arms of maze (start arm) and were allowed to explore only two of the arms for 10 minutes (training trial). On day two, the test trial was conducted with the closed arm opened which served as the novel arm. Mice were returned into the maze via the same start arm and were allowed to explore all three arms for 10 minutes. Session videos were recorded and analyzed using Ethovision XT software, and the time spent in the novel arm and entries into the novel arm were measured.

Isolation of cerebral arteries and SMCs: Mice were euthanized by decapitation under isoflurane anesthesia. Cerebral arteries were carefully isolated from the brain in Ca^{2+}-free Mg^{2+} physiological saline solution (Mg^{2+}-PSS) consisting of 140 mM NaCl, 5 mM

KCl, 2 mM $MgCl_2$, 10 mM HEPES, and 10 mM glucose (pH 7.4, adjusted with NaOH), with 0.5% bovine serum albumin (BSA). Native SMCs for patch-clamp experiments were obtained by initially digesting isolated arteries in 1 mg/mL papain (Worthington Biochemical Corporation, Lakewood, NJ, USA), 1 mg/mL dithiothreitol (DTT), and 10 mg/mL BSA in Ca^{2+}-free PSS at 37°C for 12 minutes, followed by a 14-minute incubation with 1 mg/mL type II collagenase (Worthington Biochemical Corporation). A single-cell suspension was prepared by washing digested arteries three times with Mg^{2+}-PSS and triturating with a fire-polished glass pipette. All cells used for this study were freshly dissociated on the day of experimentation.

Pressure myography: The current best practices guidelines for pressure myography experiments were followed (26). Arteries were mounted between two glass cannulas (outer diameter, 40–50 μm) in a pressure myograph chamber (Living Systems Instrumentation, St Albans City, VT, USA) and secured by a nylon thread. Intraluminal pressure was controlled using a servo-controlled peristaltic pump (Living Systems Instrumentation), and preparations were visualized with an inverted microscope (Accu-Scope Inc., Commack, NY, USA) coupled to a USB camera (The Imaging Source LLC, Charlotte, NC, USA). Changes in luminal diameter were assessed using IonWizard software (version 7.2.7.138; IonOptix LLC, Westwood, MA, USA). Arteries were bathed in warmed (37°C), oxygenated (21% O_2, 6% CO_2, 73% N_2) PSS (119 mM NaCl, 4.7 mM KCl, 21 mM $NaHCO_3$, 1.17 mM $MgSO_4$, 1.8 mM $CaCl_2$, 1.18 mM KH_2PO_4, 5 mM glucose, 0.03 mM EDTA) at an intraluminal pressure of 5 mmHg. Following equilibration for 15 min, intraluminal pressure was increased to 110 mmHg, and vessels were stretched to their approximate *in vivo* length, after which pressure was reduced back to 5 mmHg for an additional 15 min. Vessel viability was assessed for each preparation by evaluating vasoconstriction response to high extracellular [K^+] PSS, made isotonic by adjusting the [NaCl] (60 mM KCl, 63.7 mM NaCl). Arteries that showed less than 10% constriction in response to elevated [K^+] were excluded from further investigation.

Myogenic tone was assessed by raising the intraluminal pressure stepwise from 5 mmHg to 120 mmHg in 20 mmHg increments (5-20 mmHg for the first step). The active diameter was obtained by allowing vessels to equilibrate for at least 5 minutes at each pressure or until a steady-state diameter was reached. Following completion of the pressure-response study, intraluminal pressure was lowered to 5 mmHg, and arteries were superfused with Ca^{2+}-free PSS supplemented with EGTA (2 mM) and the voltage-dependent Ca^{2+} channel blocker diltiazem (10 μM) to inhibit SMC contraction, after which passive diameter was obtained by repeating the stepwise increase in intraluminal pressure. Myogenic tone at each pressure step was calculated as myogenic tone (%) = [1 – (active lumen diameter/passive lumen diameter)] × 100.

Membrane potential: For measurements of SMC membrane potential, cerebral arteries were isolated, cannulated, and viability confirmed as described. SMC membrane potential was recorded from intact pressurized arteries at intraluminal pressures of 20 mmHg and 80 mmHg. SMCs were impaled through the adventitia with glass intracellular microelectrodes (100-200 MΩ) backfilled with 3M KCl. Membrane potential was recorded using an Electro 705 amplifier (World Precision Instruments, Sarasota, FL, USA). Analog output from the amplifier was recorded using Ionwizard software (version 7.5.1.162; IonOptix). Criteria for acceptance of membrane potential recordings were 1) an abrupt negative deflection of potential as the microelectrode was advanced into a cell; 2) stable membrane potential for at least 30 seconds, and 3) an abrupt change in the potential to ~0 mV after the electrode was retracted from the cell.

Electrophysiological recordings: Enzymatically-isolated native SMCs were transferred to a recording chamber (Warner Instruments, Holliston, MA, USA) and allowed to adhere to glass coverslips for 20 minutes at room temperature. Recording electrodes (3–5 MΩ) were pulled on a model P-87 micropipette puller (Sutter Instruments, Novato, CA, USA) and polished using a MF-830 MicroForge (Narishige Scientific Instruments Laboratories, Long Island, NY, USA). Currents were recorded at room temperature using an Axopatch 200B amplifier (Molecular Devices, Sunnyvale, CA, USA) equipped with an Axon CV 203BU headstage and Digidata 144A digitizer (Molecular Devices) for all patch-clamp electrophysiology experiments. Clampex and Clampfit (version 10.2; Molecular Devices) were used for data acquisition and analysis.

The bathing solution composition for perforated-patch recordings of Kv currents, STOCs, and TICCs was 134 mM NaCl, 6 mM KCl, 1 mM $MgCl_2$, 2 mM $CaCl_2$, 10 mM HEPES, and 10 mM glucose (pH 7.4, adjusted with NaOH). The patch pipette solution contained 110 mM K-aspartate, 1 mM $MgCl_2$, 30 mM KCl, 10 mM NaCl, 10 mM HEPES, and 5 μM EGTA (pH 7.2, adjusted with KOH). Amphotericin B (200 μM) was included in the pipette solution to gain electrical access. Whole-cell K^+ currents were recorded using a step protocol (-60 to +60 mV in 10 mV, 250 ms steps) from a holding potential of -80 mV. The BK channel blocker paxilline (1 μM) was included in the bath solution when Kv currents were recorded. Whole-cell K^+ currents were recorded in the absence and presence of K_V channel blocker 4-aminopyridine (5 mM), and the Kv component was determined by subtraction. Summary current-voltage (I-V) plots were generated using values obtained from the last 50 ms of each step. STOCs were recorded from SMCs voltage-clamped over a range of membrane potentials (-60 to 0 mV; 10 mV steps). TICCs were recorded from SMCs voltage-clamped at -70 mV; membrane stretch was delivered by applying negative pressure through the recording electrode using a pressure clamp system (HSPC-1; ALA Scientific Instruments Inc., Farmingdale, NY, USA). TICC activity was calculated as the sum of the open channel probability (NP_o) of multiple open states of 1.75 pA (234).

Whole-cell TRPM4 currents were recorded in a bath solution consisting of 156 mM NaCl, 1.5 mM $CaCl_2$, 10 mM glucose, 10 mM HEPES, and 10 mM TEACl (pH 7.4, adjusted with NaOH). The patch pipette solution contained 156 mM CsCl, 8 mM NaCl, 1 mM $MgCl_2$, 10 mM HEPES (pH 7.4, adjusted with NaOH), and a free Ca^{2+} concentration of 200 µM, adjusted using the appropriate amount of $CaCl_2$ and EGTA, as determined with Max-Chelator software (WEBMAXC standard, available at https://somapp.ucdmc.ucdavis.edu/pharmacology/bers/maxchelator/webmaxc/webmaxcS.htm. Whole-cell cation currents were evoked by applying 400 ms voltage ramps from -100 to +100 mV from a holding potential of -60 mV. Voltage ramps were repeated every 2 s for 300 s. The selective TRPM4 inhibitor 9-phenanthrol (30 µM) was applied after peak TRPM4 current was recorded (~100 s). Whole-cell TRPM4 current amplitude was expressed as the 9-phenanthrol-sensitive current at +100 mV.

Quantitative droplet digital PCR: Total RNA was extracted from isolated cerebral arteries by homogenization in TRIzol reagent (Invitrogen, Waltham, MA, USA), followed by purification using a Direct-zol RNA microprep kit (Zymo Research, Irvine, CA, USA) with on-column DNAse treatment. RNA concentration was determined using an RNA 6000 Pico Kit run on a Bioanalyzer 2100 running Agilent 2100 Expert Software (B.02.11; Agilent Technologies, Santa Clara, CA, USA). RNA was converted to cDNA using iScript cDNA Supermix (Bio-Rad, Hercules, CA, USA). Quantitative droplet digital PCR (ddPCR) was performed using QX200 ddPCR EvaGreen Supermix (Bio-Rad), custom-designed primers (Supplementary Table 1), and cDNA templates. Generated droplet emulsions were amplified using a C100 Touch Thermal Cycler (Bio-Rad), and the fluorescence intensity of individual droplets were measured using a QX200 Droplet Reader (Bio-Rad) running QuantaSoft (version 1.7.4; Bio-Rad). Analysis was performed using QuantaSoft Analysis Pro (version 1.0596; Bio-Rad).

Ca^{2+} imaging: Images were acquired using an iXon 897 EMCCD camera (Andor; 16 × 16 µm pixel size) coupled to a spinning-disk confocal head (CSU-X1; Yokogawa) with a 100× oil-immersion objective (Olympus; NA 1.45) at an acquisition rate of 33 frames per second (fps). Custom software (SparkAn; https://github.com/vesselman/SparkAn) provided by Dr. Adrian D. Bonev (University of Vermont) was used to analyze the properties of Ca^{2+} sparks and whole-cell RyR and IP_3R Ca^{2+} signals.

To image Ca^{2+} sparks, a suspension of freshly isolated SMCs was placed in a glass-bottom 35 mm dish, and cells were allowed to adhere to the glass coverslip for 20 min at room temperature. SMCs were then loaded with the Ca^{2+}-sensitive fluorophore, Fluo-4-AM (1 µM; Invitrogen), in the dark for 20 minutes at room temperature in Mg^{2+}-PSS. Cells were subsequently washed three times with Ca^{2+}-containing PSS and incubated at room temperature for 20 min in the dark to allow sufficient time for Fluo-4 de-esterification. The threshold for Ca^{2+} spark detection was defined as local increases in fluorescence ≥ 0.2 $\Delta F/F_0$.

To image RyR and IP_3R Ca^{2+} signals, SMCs were plated and loaded with Fluo-4-AM as stated above, but immediately before imaging, cells were washed three times and imaged in Mg^{2+}-PSS to eliminate signals resulting from the influx of Ca^{2+}. Caffeine (10 mM) or U46619 (100 nM; Enzo Biochem, Farmingdale, NY) were applied to the bath.

4PBA treatment: Mice were provided with 4-phenylbutyrate (4PBA; 50 mM; Scandinavian Formulas Inc., Sellersville, PA, USA) from birth in drinking water that was refreshed weekly as described previously (194).

Statistical analysis: All summary data are presented as means ± SEM. Statistical analyses were performed, and graphs were constructed using Prism version 9.3.1 (GraphPad Software, San Diego, CA, USA). The value of n refers to the number of cells for patch-clamp electrophysiology and Ca^{2+} imaging experiments, number of arteries for pressure myography and membrane potential experiments, and number of animals for histological analyses, magnetic resonance imaging, Y-maze, and ddPCR experiments. Statistical analyses were performed using unpaired Student’s t-tests and one-way and two-way analysis of variance (ANOVA). A P value < 0.05 was considered statistically significant for all analyses.

Grant support: This study was supported by grants from the National Institutes of Health (NHLBI R35HL155008, R01HL091905, R01HL137852, R01HL139585, R01146054 and R01HL122770, and NIGMS P20GM130459 to S.E. and NINDS RF1NS110044 and R33NS115132 to M.M.C, D.B.G, and S.E. ; The Transgenic Genotyping and Phenotyping Core at the COBRE Center for Molecular and Cellular Signaling in the Cardiovascular System, University of Nevada, Reno, is maintained by a grant from NIH/NIGMS (P20GM130459 Sub#5451), as is the High Spatial and Temporal Resolution Imaging Core at the COBRE Center for Molecular and Cellular Signaling in the Cardiovascular System, University of Nevada, Reno (P20GM130459 Sub#5452). The UCSF Department of Ophthalmology is supported by P30EY002162 and an unrestricted grant from Research to Prevent Blindness.

Author contributions: S.E. and D.B.G. initiated and supervised the project. S.E. designed the experiments. E.Y. performed brain histology, pressure myography, sharp electrode and patch-clamp electrophysiology, Ca^{2+} imaging, and ddPCR experiments. X.W. and X.G. performed magnetic resonance imaging experiments. S.A. and A.S.S. performed patch-clamp electrophysiology experiments. P.T. performed pressure myography and Y-maze experiments. C.L.D. performed animal colony management. E.Y., S.A., A.S.S., P.T., X.G., and S.E. analyzed the data. E.Y. and S.E. drafted the manuscript and prepared the figures. E.Y., C.L.D, M.M.C., D.B.G., and S.E. revised the manuscript.

Competing interests: The authors declare that they have no competing interests.

Data and materials availability: All data needed to evaluate the conclusions in the paper are present in the paper or the Supplementary Materials

FIGURES

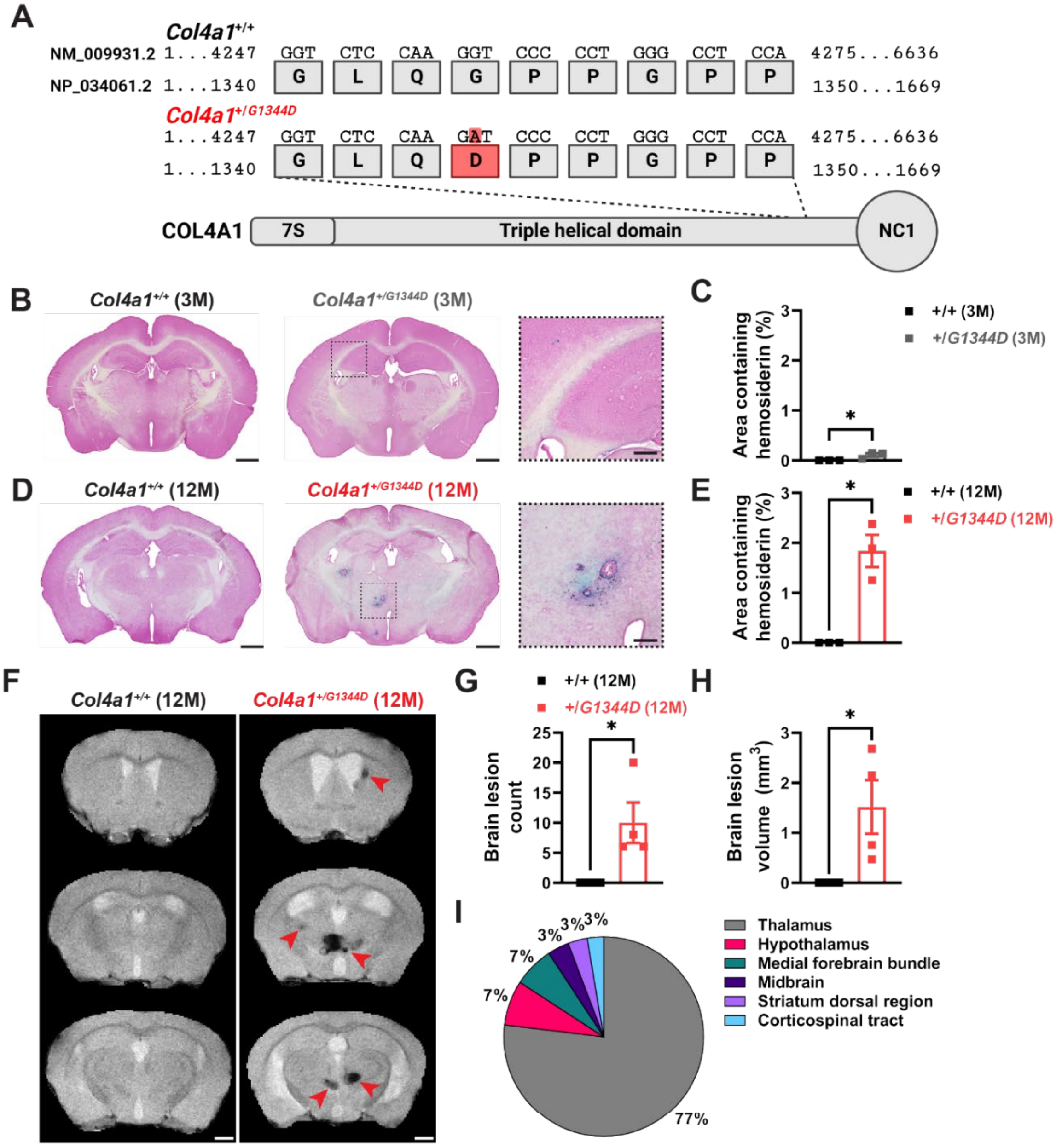

Figure 1. Col4a1$^{+/G1344D}$ mice exhibit age-dependent pathologies. (A) Schematic representation of the *Col4a1* point mutation that leads to *Col4a1^{G1344D}*. (B) Intracerebral hemorrhage (ICH) was assessed using Prussian blue staining. Representative images of brain sections from 3M-old *Col4a1$^{+/+}$* and *Col4a1$^{+/G1344D}$* mice stained with Prussian blue. (C) Summary data presented as percentage of brain area with Prussian blue staining in brain sections (500 µm intervals). N = 3 animals per group. *P ≤ 0.05, unpaired t-test. (D) Representative images of brain sections from 12 M-old *Col4a1$^{+/+}$* and *Col4a1$^{+/G1344D}$* mice stained with Prussian blue. (E) Summary data presented as percentage of brain

area with Prussian blue staining in brain sections (500 µm intervals). N = 3 animals per group. *$P \leq 0.05$, unpaired t-test. (F) Brain lesions were evaluated *in vivo* using high field susceptibility-weighted magnetic resonance imaging (SWI). Representative SWI images from 12M-old *Col4a1*$^{+/+}$ and *Col4a1*$^{+/G1344D}$ mice. Red arrow heads highlight hypointense pixels that indicate hemorrhagic lesions. Quantification of (G) the number of lesions and (H) the total volume of lesions detected by SWI. N = 4 animals per group. *$P \leq 0.05$, unpaired t-test. (I) Region-wise volumetric distribution of lesions detected by SWI from 12M-old *Col4a1*$^{+/G1344D}$ mice. Scale bars = 1 mm. Inset scale bars = 250 µm.

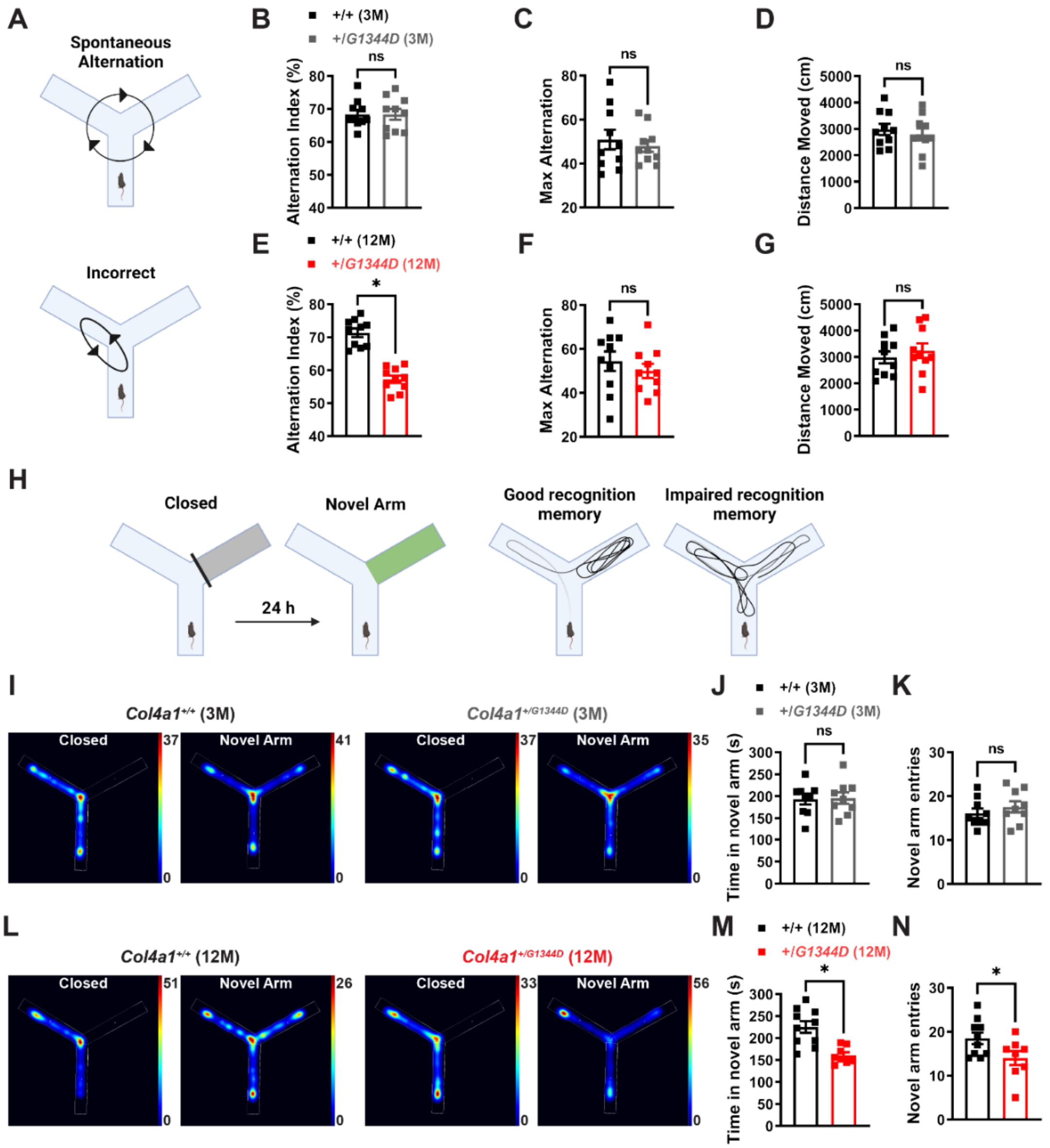

Figure 2. Col4a1$^{+/G1344D}$ mice have age-dependent decline in memory function. (A) Illustration of Y-maze spontaneous alternation behavior assay showing examples of a correct (top) and incorrect (bottom) spontaneous alternation. Summary data of (B) alternation index, (C) max number of alternations reflecting exploratory activity, and (D) total distance moved during spontaneous alternation Y-maze task of 3 M-old *Col4a1*$^{+/+}$ and *Col4a1*$^{+/G1344D}$ mice. N = 10 animals per group. ns = not significant, unpaired t-test. (E) Summary data of alternation index, (F) max number of alternations, and (G) total distance moved during spontaneous alternation Y-maze task of 12 M-old *Col4a1*$^{+/+}$ and *Col4a1*$^{+/G1344D}$ mice. N =10 animals per group. *P ≤ 0.05, ns = not significant, unpaired t-test. (H) Illustration of Y-maze novel arm procedure. (I) Heatmaps showing the time (s) that 3 M-old *Col4a1*$^{+/+}$ and *Col4a1*$^{+/G1344D}$ mice spent in areas of the Y-maze during the novel arm assay. (J) Summary data of dwell time and (K) entries into the novel arm. N =

9 animals per group. ns = not significant, unpaired t-test. (L) Heatmaps showing the time (s) that 12 M-old *Col4a1*$^{+/+}$ and *Col4a1*$^{+/G1344D}$ mice spent in areas of the Y-maze during the novel arm assay. (M) Summary data of dwell time and (N) entries into the novel arm. N = 8 or 10 animals per group. *P ≤ 0.05, unpaired t-test.

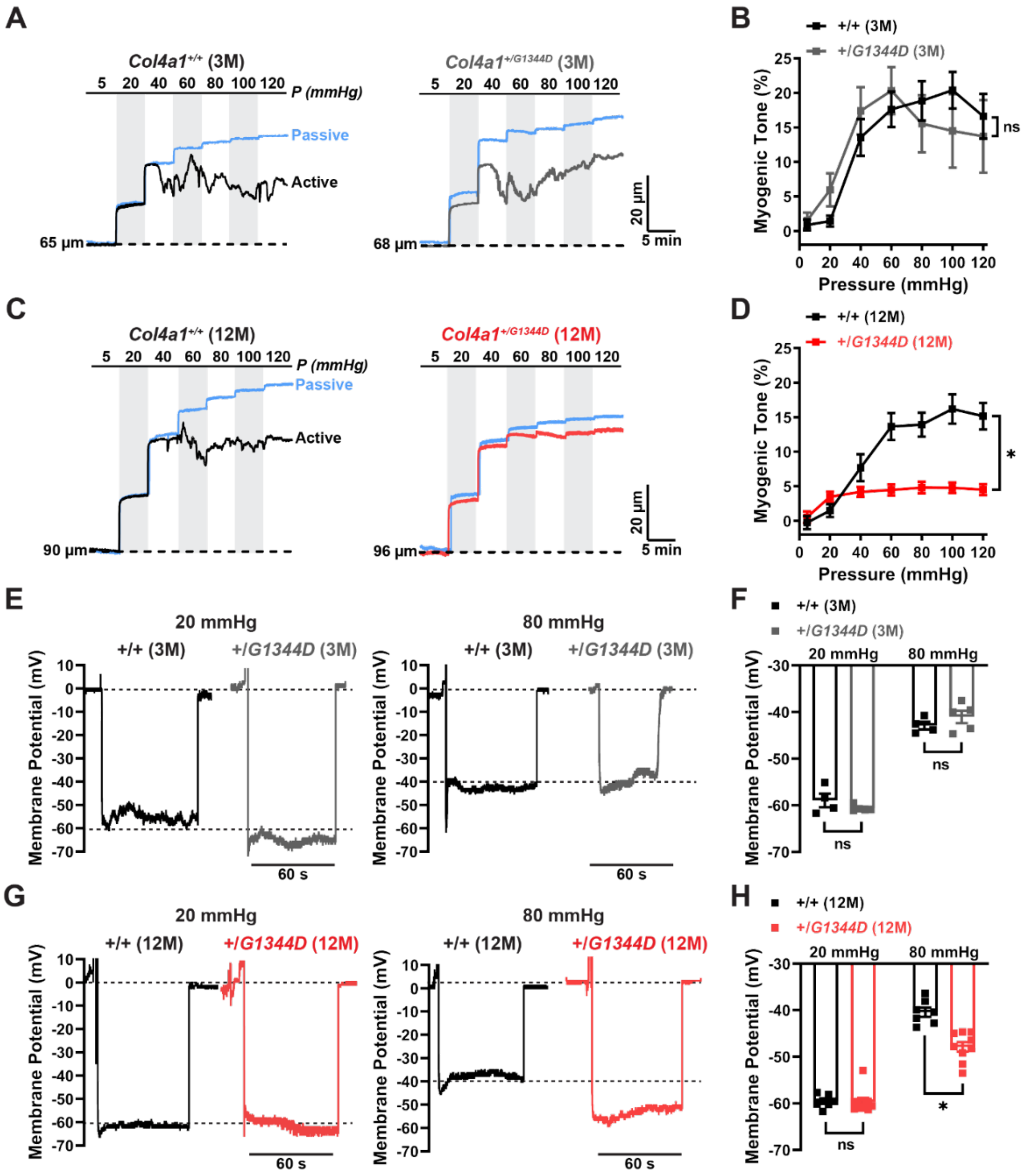

Figure 3. Cerebral arteries from Col4a1$^{+/G1344D}$ mice have age-dependent loss of myogenic tone and pressure induced depolarization. (A) Representative recordings of the inner diameter of isolated cerebral arteries from 3 M-old *Col4a1*$^{+/+}$ and *Col4a1*$^{+/G1344D}$ mice showing the myogenic response to increases in pressure (active) and the dilation of the same arteries when extracellular Ca^{2+} has been removed (passive). (B) Summary data of myogenic tone as a function of intraluminal pressure. n = 5-10 vessels from 5 or 6 animals per group. ns = not significant, two-way ANOVA. (C) Representative recordings of the inner diameter of isolated cerebral arteries from 12 M-old *Col4a1*$^{+/+}$ and *Col4a1*$^{+/G1344D}$ mice. (D) Summary data of myogenic tone as a function of intraluminal pressure. n = 13 vessels from 6 or 9 animals per group. *$P \leq 0.05$, two-

way ANOVA. (E) Representative membrane potential (mV) recordings of smooth muscle cells (SMCs) in pressurized cerebral arteries isolated from 3 M-old *Col4a1*$^{+/+}$ and *Col4a1*$^{+/G1344D}$ mice at 20 mmHg and 80 mmHg intraluminal pressure. (F) Summary data showing membrane potential of SMCs in pressurized cerebral arteries at 20 mmHg and 80 mmHg intraluminal pressure. n = 4-5 vessels from 3 or 4 animals per group. ns = not significant, unpaired t-test. (G) Representative membrane potential recordings of SMCs in pressurized cerebral arteries isolated from 12 M-old *Col4a1*$^{+/+}$ and *Col4a1*$^{+/G1344D}$ mice at 20 mmHg and 80 mmHg intraluminal pressure. (H) Summary data showing membrane potential of SMCs in pressurized cerebral arteries at 20 mmHg and 80 mmHg intraluminal pressure. n = 7-9 vessels from 5 or 6 mice per group. $^*P \leq 0.05$, unpaired t-test.

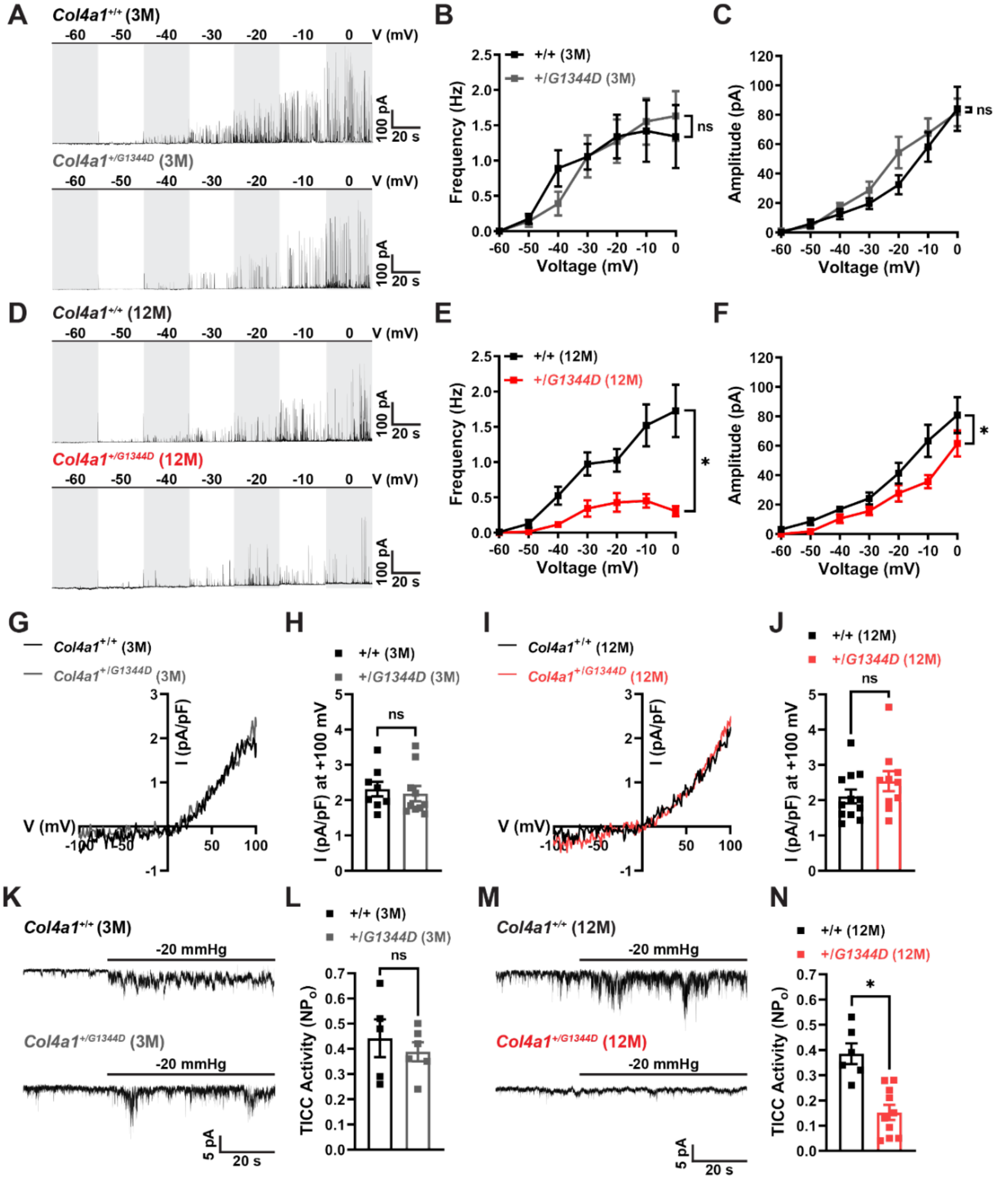

Figure 4. Age-dependent decrease in physiological BK and TRPM4 channel activity in Col4a1$^{+/G1344D}$ mice. (A) Representative traces of spontaneous transient outward currents (STOCs) in freshy isolated cerebral artery smooth muscle cells (SMCs) from 3 M-old *Col4a1*$^{+/+}$ and *Col4a1*$^{+/G1344D}$ mice over a range of membrane potentials (-60 to 0 mV). Summary data showing STOC frequency (B) and amplitude (C) at each command potential. n = 8-12 cells from 5 animals per group. ns = not significant, two-way ANOVA. (D) Representative traces of STOCs in cerebral artery SMCs from 12 M-old *Col4a1*$^{+/+}$ and *Col4a1*$^{+/G1344D}$ mice. Summary data showing STOC frequency (E) and

amplitude (F) at each command potential. n = 12 cells from 5 animals per group. *P ≤ 0.05, two-way ANOVA. (G) Representative I-V plots of whole-cell patch-clamp TRPM4 current recordings during voltage ramps (-100 to 100 mV) in cerebral artery SMCs from 3 M-old *Col4a1*$^{+/+}$ and *Col4a1*$^{+/G1344D}$ mice. Currents were evoked by including 200 µM free Ca^{2+} in the intracellular solution and the TRPM4 portion of the current was determined with the addition of TRPM4 blocker 9-phenanthrol (30 µM). (H) Summary of whole-cell TRPM4 current density at +100 mV. n = 8-10 cells from 3 or 4 animals per group. ns = not significant, unpaired t-test. (I) Representative I-V plots of whole-cell patch-clamp TRPM4 current recordings in cerebral artery SMCs from 12 M-old *Col4a1*$^{+/+}$ and *Col4a1*$^{+/G1344D}$ mice. (J) Summary of whole-cell TRPM4 current density at +100 mV. n = 10-12 cells from 4 animals per group. ns = not significant, unpaired t-test. (K) Representative traces of transient inward cation currents (TICCs) evoked by applying negative pressure (-20 mmHg) to stretch the plasma membrane of voltage-clamped (-70 mV) cerebral artery SMCs isolated from 3 M-old *Col4a1*$^{+/+}$ and *Col4a1*$^{+/G1344D}$ mice. (L) Summary data of TICC activity. n = 5-6 cells from 3 animals per group. ns = not significant, unpaired t-test. (M) Representative traces of TICCs in cerebral artery SMCs isolated from 12 M-old *Col4a1*$^{+/+}$ and *Col4a1*$^{+/G1344D}$ mice. (N) Summary data of TICC activity. n = 8-10 cells from 4 or 5 animals per group. *P ≤ 0.05, unpaired t-test.

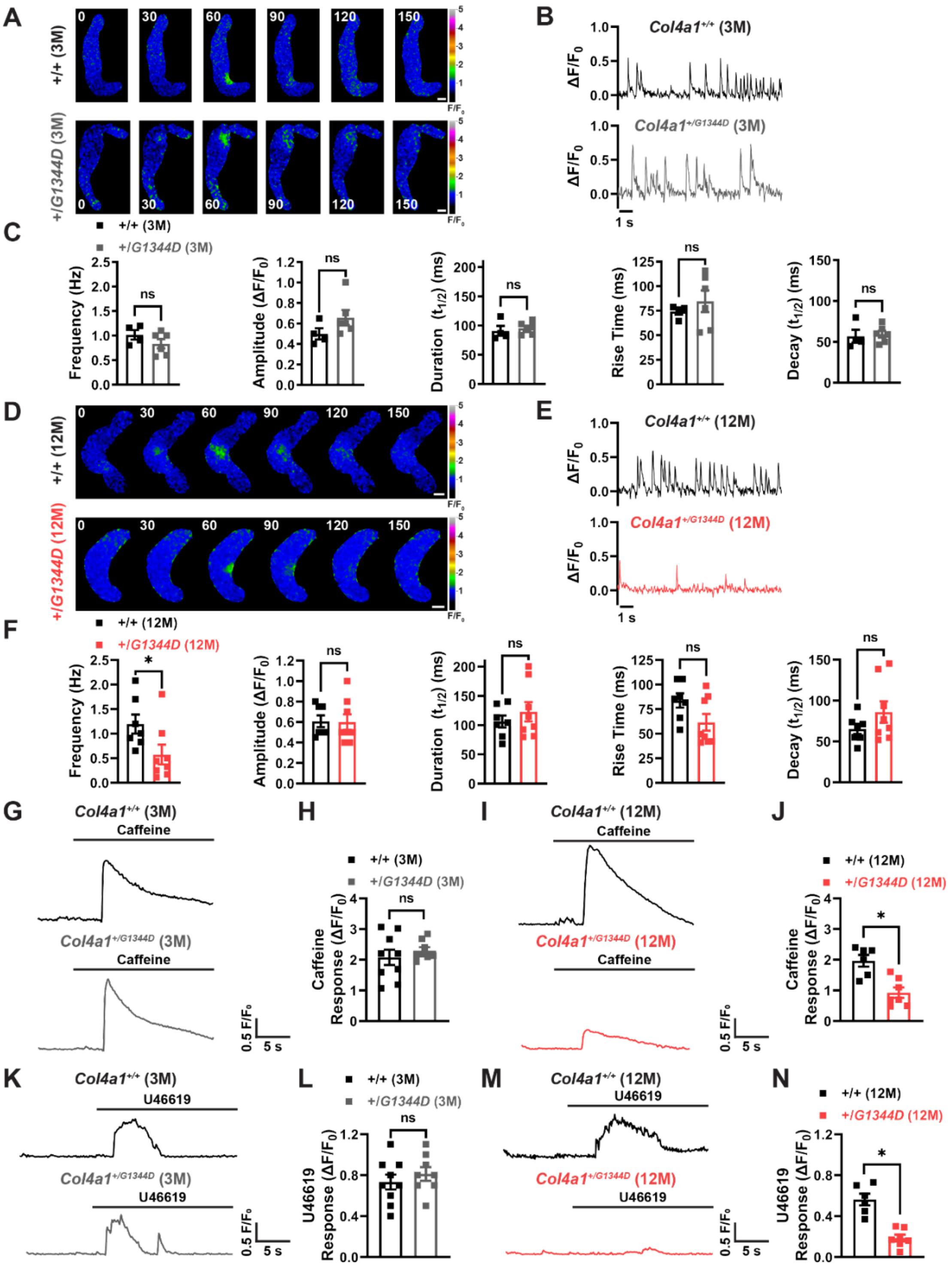

Figure 5. Col4a1$^{+/G1344D}$ mice have altered sarcoplasmic reticulum Ca^{2+} signaling. (A) Representative time-course spinning disk confocal images exhibiting Ca^{2+} spark events in Fluo-4-AM loaded cerebral artery smooth muscle cells (SMCs) from 3 M-old *Col4a1*$^{+/+}$ and *Col4a1*$^{+/G1344D}$ mice. Time = milliseconds, scale bar = 5 µm. (B)

Representative traces of Ca^{2+} spark events in cerebral artery SMCs isolated from 3 M-old *Col4a1*$^{+/+}$ and *Col4a1*$^{+/G1344D}$ mice presented as changes in fractional fluorescence ($\Delta F/F_0$) vs. time. (C) Summary data showing Ca^{2+} spark frequency, amplitude, duration, rise time, and decay. n = 4-6 cells from 3 animals per group. ns = not significant, unpaired t-test. (D) Representative time-course images exhibiting Ca^{2+} spark events in cerebral artery SMCs from 12 M-old *Col4a1*$^{+/+}$ and *Col4a1*$^{+/G1344D}$. Time = milliseconds, scale bar = 5 µm. (E) Representative traces of Ca^{2+} spark events in cerebral artery SMCs isolated from 12 M-old *Col4a1*$^{+/+}$ and *Col4a1*$^{+/G1344D}$ mice presented $\Delta F/F_0$ vs. time. (F) Summary data showing Ca^{2+} spark frequency, amplitude, duration, rise time, and decay. n = 7-8 cells from 3 or 4 animals per group. $^*P \leq 0.05$, ns = not significant, unpaired t-test. (G) Representative traces showing whole cell changes in F/F_0 in response to caffeine (10 mM) in Fluo-4-AM loaded cerebral artery SMCs from 3 M-old *Col4a1*$^{+/+}$ and *Col4a1*$^{+/G1344D}$ mice. (H) Summary data of the $\Delta F/F_0$ in response to caffeine. n = 8-9 cells from 3 animals per group. ns = not significant, unpaired t-test. (I) Representative traces showing whole cell changes in F/F_0 in response to caffeine in SMCs from 12 M-old *Col4a1*$^{+/+}$ and *Col4a1*$^{+/G1344D}$ mice. (J) Summary data of the $\Delta F/F_0$ in response to caffeine. n = 6-7 cells from 3 animals per group. $^*P \leq 0.05$, unpaired t-test. (K) Representative traces showing whole cell changes in F/F_0 in response to U46619 (100 nM) in Fluo-4-AM loaded cerebral artery SMCs from 3 M-old *Col4a1*$^{+/+}$ and *Col4a1*$^{+/G1344D}$ mice. (L) Summary data of the $\Delta F/F_0$ in response to U46619. n = 8-9 cells from 3 animals per group. ns = not significant, unpaired t-test. (M) Representative traces showing whole cell changes in F/F_0 in response to U46619 in SMCs from 12 M-old *Col4a1*$^{+/+}$ and *Col4a1*$^{+/G1344D}$ mice. (N) Summary data of the $\Delta F/F_0$ in response to U46619. n = 6-7 cells from 3 animals per group. $^*P \leq 0.05$, unpaired t-test.

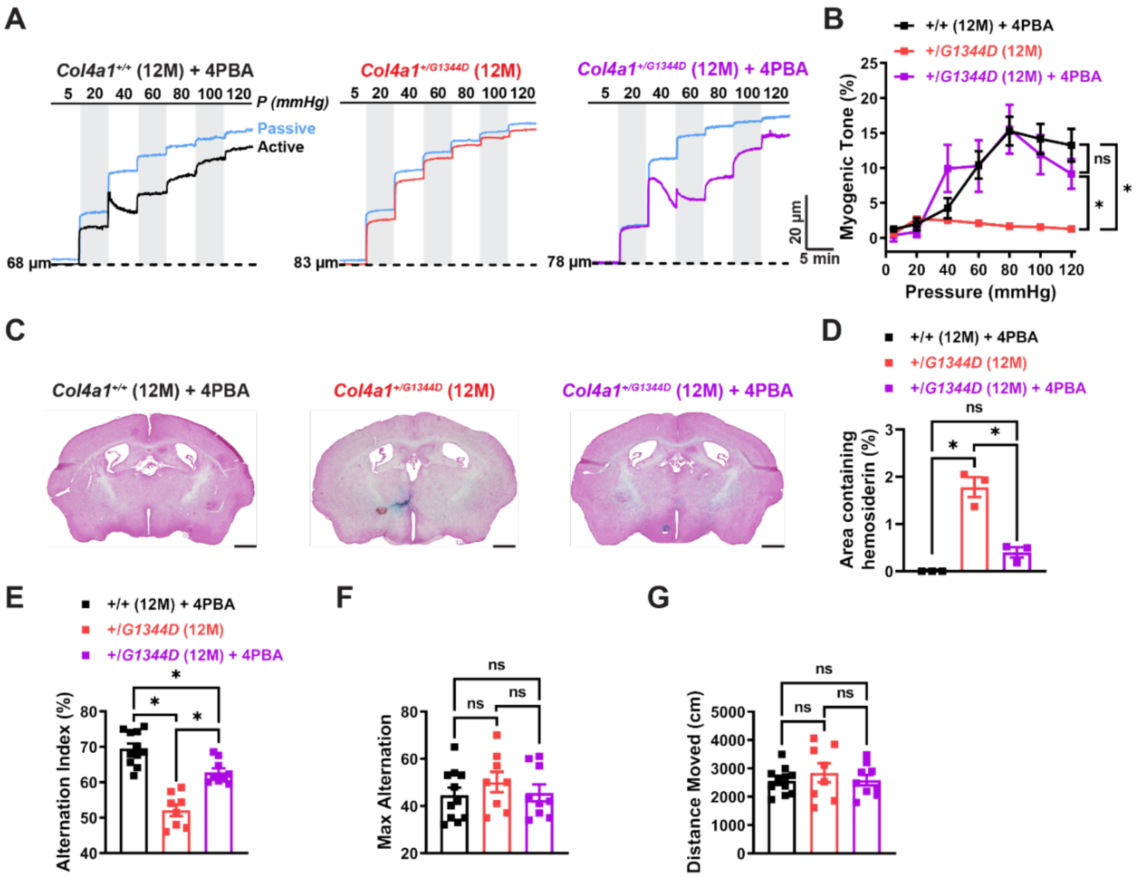

Figure 6. 4PBA prevents age-related cerebrovascular dysfunction. (A) Representative recordings of the inner diameter of isolated cerebral arteries from 4PBA treated 12 M-old *Col4a1*$^{+/+}$ and *Col4a1*$^{+/G1344D}$ and untreated *Col4a1*$^{+/G1344D}$ mice showing the myogenic response to increases in pressure (active) and the dilation of the same arteries when extracellular Ca^{2+} has been removed (passive). (B) Summary data of myogenic tone as a function of intraluminal pressure. n = 6 or 9 vessels from 3 or 5 mice. *P ≤ 0.05, ns = not significant, two-way ANOVA. (C) Representative images of Prussian blue stained brain sections from 4PBA treated 12 M-old *Col4a1*$^{+/+}$ and *Col4a1*$^{+/G1344D}$ and untreated *Col4a1*$^{+/G1344D}$ mice. Scale bar = 1 mm. (D) Summary data presented as percentage of brain area with Prussian blue staining in brain sections (500 µm intervals). N = 3 animals per group. *P ≤ 0.05, ns = not significant, one-way ANOVA. Short-term spatial working memory of 4PBA treated 12 M-old *Col4a1*$^{+/+}$ and *Col4a1*$^{+/G1344D}$ mice and untreated *Col4a1*$^{+/G1344D}$ mice was assessed by spontaneous alternation in the Y-maze; (E) summary data of alternation index, (F) max number of alternations reflecting exploratory activity, and (G) total distance moved during spontaneous alternation Y-maze task. N = 9, 8, or 11 animals per group. *P ≤ 0.05, ns = not significant one-way ANOVA.

Supplemental Figures

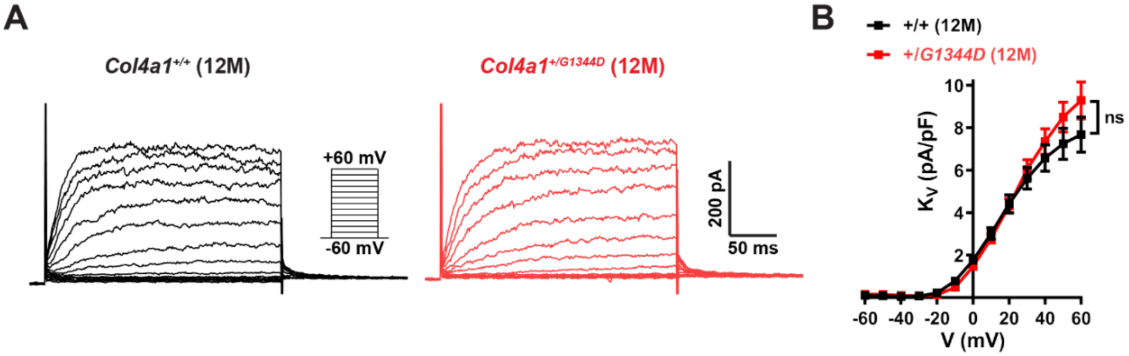

Supplemental Figure 1. Loss of myogenic tone and impaired depolarization is not attributable to increased K_V currents. (A) Representative recording of 4-aminopyridine (5 mM)-sensitive K_V currents in freshy isolated cerebral artery smooth muscle cells from 12 M-old *Col4a1*$^{+/+}$ and *Col4a1*$^{+/G1344D}$ mice. Currents were elicited by applying voltage pulses (250 ms) from -60 to +60 mV in 10 mV steps with BK channel blocker paxilline (1 μM). (B) Summary data of K_V current at each command potential, normalized to cell capacitance. n = 10-11 cells from 3 animals per group. ns = not significant, two-way ANOVA.

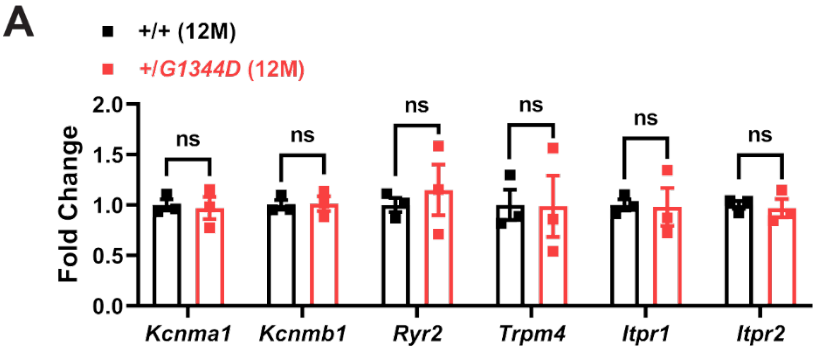

Supplemental Figure 2. mRNA expression of STOC and TICC pathway components. mRNA transcript levels of genes involved in the spontaneous transient outward current (*Kcnma1, Kcnmb1, Ryr2)* and transient inward cation current (*Trpm4, Itpr1, Itpr2*) pathways in isolated cerebral arteries from 12 M-old *Col4a1*$^{+/+}$ and *Col4a1*$^{+/G1344D}$ mice measured by ddPCR and presented as fold change over control mice. n = 3 animals per group. ns = not significant, unpaired t-test.

Supplemental Table 1. Primers used for quantitative ddPCR.

Gene	**Forward primer (5’-3’)**	**Reverse primer (5’-3’)**
Kcnma1	GCTTAAGCTCCTGATGATAGCC	AAGGTGGTTCCCAGGGTTAA
Kcnmb1	ATGGGCCATGCTGTATCACA	TGTCCAGGTTCCTGGGGATATA
Ryr2	TGGAGGACATGCATCCAACA	TCCTATGCCTGACAAGAACTCC
Trpm4	AGGGCTCTTGTGAAAGCCTG	TCCCCACGGAAAAGTTCAC
Itpr1	AACGTGGGCCACAACATCTA	CCAGGTTTCAGCATGGTTTGAA
Itpr2	CCTCAAGACAACCTGCTTCA	TGATGTGCTCCTCAAAGGAC

CHAPTER 3: FAULTY TRPM4 CHANNELS UNDERLIE AGE-DEPENDENT CEREBRAL VASCULAR DYSFUNCTION IN GOULD SYNDROME

Evan Yamasaki[1], Sher Ali[1], Alfredo Sanchez Solano[1], Pratish Thakore[1], Megan Smith[2], Xiaowei Wang[2], Cassandre Labelle-Dumais[2], Douglas B. Gould[2,3], and Scott Earley[1*]

[1]Department of Pharmacology, Center for Molecular and Cellular Signaling in the Cardiovascular System, University of Nevada, Reno School of Medicine, Reno, Nevada, 89557-0318, USA

[2]Departments of Ophthalmology, Institute for Human Genetics, UCSF School of Medicine, San Francisco, CA 94158, USA

[3]Department of Anatomy, Institute for Human Genetics, Cardiovascular Research Institute, Bakar Aging Research Institute, UCSF School of Medicine, San Francisco, CA 94158, USA

Keywords: *COL4A1*, collagen, cerebral small vessel diseases, basement membrane, myogenic tone, PIP_2, PI3K, TGF-β, ion channels.

[*]Corresponding author

Address Correspondence To:
Scott Earley, Ph.D.
University of Nevada, Reno School of Medicine
Manville Health Sciences Building, Room 8
MS-0318
Reno, NV 89557-0318, USA
Phone: (775) 784-4117
Fax: (775) 784-1620
Email: searley@med.unr.edu

ABSTRACT

Gould syndrome is a rare multisystem disorder resulting from autosomal dominant mutations in the collagen-encoding genes *COL4A1* and *COL4A2.* Human patients and *Col4a1* mutant mice display brain pathology that typifies cerebral small vessel diseases (cSVDs), including white matter hyperintensities, dilated perivascular spaces, lacunar infarcts, microbleeds, and spontaneous intracerebral hemorrhage. The underlying pathogenic mechanisms are unknown. Using the *Col4a1*$^{+/G394V}$ mouse model, we found that vasoconstriction in response to internal pressure – the vascular myogenic response – is blunted in cerebral arteries from middle-aged (12 months old) but not young adult (3 months old) animals, revealing age-dependent cerebral vascular dysfunction. The defect in the myogenic response was associated with a significant decrease in depolarizing cation currents conducted by TRPM4 (transient receptor potential melastatin 4) channels in native cerebral artery smooth muscle cells (SMCs) isolated from mutant mice. The minor membrane phospholipid phosphatidylinositol 4,5 bisphosphate (PIP_2) is necessary for TRPM4 activity. Dialyzing SMCs with PIP_2 and selective blockade of phosphoinositide 3-kinase (PI3K), an enzyme that converts PIP_2 to phosphatidylinositol (3,4,5)-trisphosphate (PIP_3), restored TRPM4 currents. Acute inhibition of PI3K activity and blockade of transforming growth factor-beta (TGF-β) receptors also rescued the myogenic response, suggesting that hyperactivity of TGF-β signaling pathways stimulates PI3K to deplete PIP_2 and impair TRPM4 channels. We conclude that age-related cerebral vascular dysfunction in *Col4a1*$^{+/G394V}$ mice is caused by the loss of depolarizing TRPM4 currents due to PIP_2 depletion, revealing a novel, age-dependent mechanism of cSVD.

Significance Statement

Cerebral small vessel diseases (cSVDs) are a group of related idiopathic and familial pathologies that cause stroke, intracerebral hemorrhage (ICH), and cognitive decline. The underlying mechanisms are poorly understood, and no effective treatment options exist. Here, we investigated a mouse that models a form of cSVD caused by a mutation in the gene encoding type collagen IV alpha1 (COL4A1) to better understand the pathogenesis of the disease. We found that impairment of transient receptor potential melastatin 4 (TRPM4) cation channels disrupted the ability of cerebral arteries from middle-aged mutant animals to constrict in response to physiological levels of intraluminal pressure. Vascular function was restored by acute inhibition of phosphoinositide 3-kinase and transforming growth factor-beta receptors, potentially identifying new therapeutic targets.

Graphical Abstract

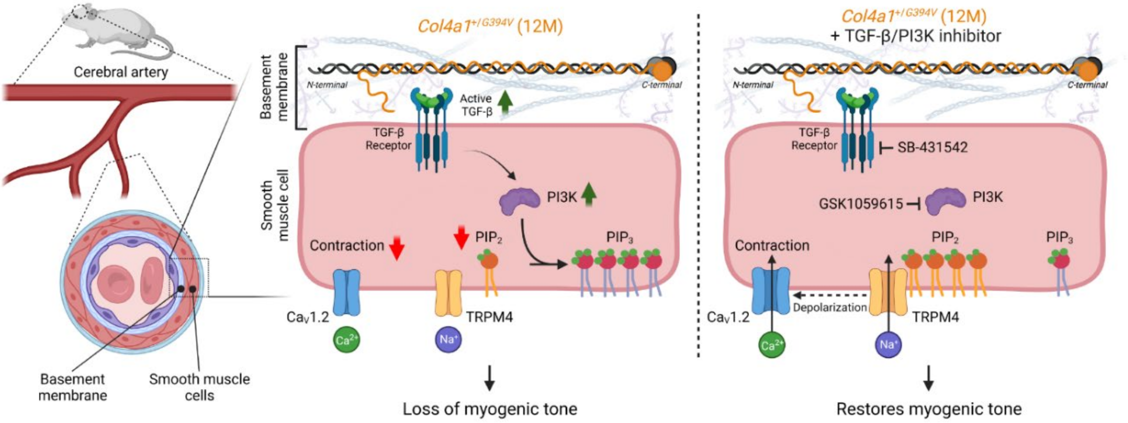

INTRODUCTION

Cerebral small vessel diseases (cSVDs) are a group of familial and sporadic pathologies afflicting the blood vessels in the brain. cSVDs are a major cause of vascular contributions to cognitive impairment and dementia (VCID), second only to Alzheimer's disease as the most common form of dementia in adults (1). VCID and cSVDs are more prevalent in the elderly and are expected to overburden health care systems globally as the world's population ages (235). Idiopathic and familial forms of the disease have been described, but the pathogenesis remains poorly understood and specific treatment options are not available. Mutations in the genes encoding type IV collagen alpha 1 (COL4A1) and alpha 2 (COL4A2) cause Gould syndrome, an autosomal dominant multisystem disorder that encompasses all the hallmarks of cSVDs, including white matter hyperintensities, intracerebral hemorrhage (ICH), lacunes, and microinfarcts (9, 10). How *COL4A1* and *COL4A2* mutations cause cSVD and related brain defects are not known. Studies using a murine allelic series of *Col4a1* and *Col4a2* mutations show allelic heterogeneity with a position effect whereby mutations closer to the carboxyl terminus of the triple helical domain are associated with increased ICH severity (195, 236). These findings suggest that the mechanisms underlying cSVD associated with Gould syndrome are heterogeneous and complex. Here, we sought to elucidate the molecular links between a specific *Col4a1* mutation and cerebrovascular dysfunction.

COL4A1 and COL4A2 form a heterotrimer [α1α1α2(IV)] that is a fundamental component of all basement membranes. Collagen α1α1α2(IV) is secreted to the extracellular space, where it polymerizes into networks that are further cross-linked with other basement membrane components. COL4A1 and COL4A2 proteins are composed of a long triple helical domain flanked by 7S and NC1 domains at the amino and carboxyl termini, respectively (31). The triple helical regions consist of long stretches of G-X-Y repeats characteristic of all collagens. Glycine (G) is required at every third amino acid as the absence of a side chain allows it to fit into the core of the triple helix (237). The vast majority of pathogenic *COL4A1* and *COL4A2* mutations are missense mutations of one of these highly conserved glycine residues (210, 238, 239). Such mutations are thought to drive three potential adverse outcomes: diminishment of normal collagen α1α1α2(IV) in basement membranes; secretion and incorporation of mutant collagen α1α1α2(IV) that disrupts the functional integrity of the basement membrane; and intracellular retention of misfolded collagen α1α1α2(IV) molecules that cause ER/SR stress in collagen-producing cells (185). *Col4a1* mutant mice display striking position-dependent heterogeneity in trafficking defects, with diminishing export and increased intracellular retention of collagen α1α1α2(IV) associated with mutations closer to the carboxyl terminus of the protein (189). For the current study, we used mice heterozygous for a point mutation in *Col4a1* in which the G residue at position 394 (relatively near the amino terminus) had been replaced by valine (V). *Col4a1*$^{+/G394V}$ mice traffic collagen α1α1α2(IV) out of cells relatively efficiently (189), suggesting that the pathology of these animals is independent of ER/SR stress and that structural and/or functional imperfections in the basement membrane is the primary defect.

Autoregulation of blood flow in the brain is maintained in part by the vascular myogenic response, a process that sustains partial constriction of arteries and arterioles in response to intraluminal pressure (71). The myogenic response maintains near-constant blood flow within the microcirculation during beat-to-beat fluctuations in the force of perfusion, thereby preventing tissue ischemia during transient drops in pressure and protecting delicate capillary beds during temporary increases in pressure (71). Several types of cerebrovascular disease disrupt this process, including familial cSVD associated with cerebral autosomal dominant arteriopathy with subcortical infarcts and leukoencephalopathy (CADASIL) (160). The effects of *Col4a1* mutations on the myogenic tone of cerebral arteries are not known. Signaling pathways intrinsic to vascular smooth muscle cells (SMCs) forming the walls of arteries and arterioles generate the myogenic response (71). Increases in intraluminal pressure activate TRPM4 (transient receptor potential melastatin 4) channels, allowing an influx of Na^+ ions that depolarize the SMC plasma membrane to initiate Ca^{2+} influx through voltage-gated Ca^{2+} channels and engage contractile pathways (78, 205, 206). The depolarizing effects of TRPM4 channels are balanced by hyperpolarizing K^+ currents primarily conducted by voltage-dependent K^+ (Kv) channels, large-conductance Ca^{2+} activated K^+ (BK) channels, and inwardly-rectifying K^+ (K_{IR}) channels (88, 207). In the CADASIL mouse model, increased Kv channel current density in SMCs accounts for diminished myogenic tone (160). The electrophysiological properties of SMCs from *Col4a1* mutant mice have not been reported.

Here, we show that the myogenic response of cerebral pial arteries from *Col4a1*$^{+/G394V}$ mice was dramatically impaired in an age-dependent manner. In contrast to CADASIL models, K^+ currents in SMCs from *Col4a1*$^{+/G394V}$ mice were not increased compared to controls. Instead, we found that the loss of myogenic tone was associated with decreased activity of inward Na^+ currents conducted by TRPM4 channels. TRPM4 currents were restored by supplying exogenous phosphatidylinositol 4,5 bisphosphate (PIP_2), a minor membrane phospholipid that is a necessary co-factor for TRPM4 activity (240, 241), and by selective blockade of phosphoinositide 3-kinase (PI3K), an enzyme that depletes PIP_2 by converting it to phosphatidylinositol (3,4,5)-trisphosphate (PIP_3).

Further, inhibition of PI3K activity and blockade of upstream transforming growth factor-beta (TGF-β) receptors rescued myogenic tone in arteries from 12 months (M)-old mutant mice. We conclude that age-dependent cerebral vascular dysfunction in *Col4a1*$^{+/G394V}$ mice is caused by the loss of depolarizing TRPM4 currents due to PIP_2 depletion. Conversion of PIP_2 to PIP_3 by PI3K, acting downstream of TGF-β receptors, accounts for diminished PIP_2 levels in SMCs. Our findings reveal a novel mechanism of age-dependent cerebral vascular dysfunction and identify PI3K and TGF-β receptors as novel therapeutic targets for some forms of cSVDs.

RESULTS

Cerebral arteries from middle-aged Col4a1$^{+/G394V}$ mice fail to generate myogenic tone.

Mutant mice used for this study harbor a point mutation in the gene sequence that results in the substitution of G for V at position 394 of the polypeptide (Figure 1A). Mice that were 3 (young adult) or 12 (middle-aged) months (M) old were included in our study design. Both male and female mice were used for all experiments, and no sex-specific differences were detected. Histological examination of Prussian blue-stained brain sections showed that the brains of 3 M-old *Col4a1*$^{+/G394V}$ mice (Figure 1B) lacked ICH, but loss of brain tissue resulting from hemorrhagic events and evidence of spontaneous ICH was present in brains from 12 M-old *Col4a1*$^{+/G394V}$ mice (Figures 1C).

Established pressure myography techniques (26) were used to investigate the development of spontaneous myogenic tone in cerebral pial arteries from *Col4a1*$^{+/G394V}$ mice. Initially, changes in the diameters of cannulated cerebral arteries were recorded as intraluminal pressure was increased in a stepwise manner from 5 to 140 mmHg, and the luminal diameter during active muscular contraction was recorded at each pressure. After this challenge, the pressure was returned to 5 mmHg, vessels were superfused with a Ca^{2+}-free solution, and changes in diameter in response to increases in pressure were again recorded to determine the passive response – the diameter in the absence of muscular contraction. Myogenic tone was calculated as the difference in active versus passive diameter normalized to the passive diameter. Arteries from 3 M-old mice from both groups began to constrict when pressures within the physiological range (i.e., 40 mmHg and above) were applied, and myogenic tone did not differ (Figure 1D and E). In addition, vasoconstriction in response to application of a high concentration of extracellular K^+ (60 mM) was applied to collapse K^+ gradients and directly depolarize SMC plasma membranes did not differ between cerebral arteries from 3 M-old control and mutant mice (Figure 1F). In contrast, arteries isolated from 12 M-old *Col4a1*$^{+/G394V}$ mice barely constricted across all levels of applied pressure, and myogenic tone was significantly lower compared to 12 M-old *Col4a1*$^{+/+}$ littermates (Figure 1G and H). These data demonstrate that cerebral arteries from *Col4a1*$^{+/G394V}$ mice lose the ability to develop myogenic tone during aging. Vasoconstriction in response to elevated [K^+] did not differ between 12 M-old *Col4a1*$^{+/+}$ and *Col4a1*$^{+/G394V}$ mice (Figure 1I), indicating that voltage-dependent Ca^{2+} influx and fundamental contractile mechanisms were not grossly impaired in 12 M-old *Col4a1*$^{+/G394V}$ mice. Passive dilation of cerebral arteries in response to increases in intraluminal pressure did not differ between 12 M-old *Col4a1*$^{+/+}$ and *Col4a1*$^{+/G394V}$ mice (Figure 1 – figure supplement 1), indicating that changes in vascular compliance do not account for impaired myogenic tone in mutant mice. The myogenic tone of cerebral arteries in which endothelial cell function had been disrupted by the passage of air through the lumen was also assessed. Pressure-induced constriction was significantly less in endothelium-denuded arteries from 12 M-old *Col4a1*$^{+/G394V}$ compared to *Col4a1*$^{+/+}$ littermates (Figure 1- figure supplement 2), demonstrating that that impaired myogenic tone in these animals is due to SMC dysfunction.

Loss of myogenic tone in cerebral arteries from middle-aged Col4a1$^{+/G394V}$ mice is not attributable to increases in SMC K^{+} channel currents.

Impaired myogenic tone in cerebral arteries from CADASIL cSVD mice is due to elevated Kv current density in SMCs (160). To determine if this mechanism also accounts for impaired myogenic tone in 12 M-old *Col4a1*$^{+/G394V}$ mice, we measured K^{+} channel currents in cerebral artery SMCs using patch-clamp electrophysiology. To record Kv currents, freshly-isolated SMCs were patch-clamped in the amphotericin B perforated configuration in the presence of the selective BK channel blocker paxillin (1 μM), and voltage-dependent currents were evoked by the application of a series of voltage steps from -60 to +60 mV from a holding potential of -80 mV. The voltage step protocol was repeated in the presence of the Kv channel blocker 4-aminopyridine (5 mM), and Kv current amplitude was determined at each potential by subtraction. We found that Kv current amplitude did not differ between SMCs from *Col4a1*$^{+/+}$ and *Col4a1*$^{+/G394V}$ mice at any applied membrane potentials (Figure 2A and B). These data indicate that the mechanisms that impair myogenic tone in 12 M-old *Col4a1*$^{+/G394V}$ mice differ from the CADASIL cSVD model.

BK channel activity has a powerful hyperpolarizing effect on the SMC membrane potential that could account for the lack of myogenic tone in cerebral arteries from 12 M-old *Col4a1*$^{+/G394V}$ mice (88, 207). Under physiological conditions, Ca^{2+} sparks - transient, localized Ca^{2+} signals generated by the release of Ca^{2+} from the SR into the cytosol through RyRs - activate clusters of BK channels on the plasma membrane to produce large-amplitude spontaneous transient outward currents (STOCs) (88). We compared

BK channel activity between SMCs from 12 M-old *Col4a1*$^{+/+}$ and *Col4a1*$^{+/G394V}$ mice using the amphotericin B perforated patch-clamp configuration. We found that the frequency and amplitude of STOCs recorded over a range of command potentials (-60 to 0 mV) did not differ between groups, indicating that elevated BK channel activity does not account for the loss of myogenic tone in 12 M-old *Col4a1*$^{+/G394V}$ mice (Figure 2C-E).

An increase in K_{IR} channel activity could also account for the loss of myogenic tone in 12 M-old *Col4a1*$^{+/G394V}$ mice. Conventional whole-cell patch-clamp electrophysiology was used to measure K_{IR} current density in cerebral artery SMCs from 12 M-old *Col4a1*$^{+/+}$ and *Col4a1*$^{+/G394V}$ mice. K_{IR} currents were evoked by applying a high concentration of K^+ (60 mM) to the bath solution during voltage ramps (-100 to +20 mV). Voltage ramps were repeated in the presence of the selective K_{IR} channel blocker $BaCl_2$ (10 μM), and K_{IR} current amplitude was determined by subtraction. K_{IR} current density was significantly smaller in SMCs from 12 M-old *Col4a1*$^{+/G394V}$ mice compared with *Col4a1*$^{+/+}$ animals (Figure 2F and G). However, decreases in K^+ current density depolarize the SMC plasma membrane and increase vasoconstriction. Therefore, loss of K_{IR} channel activity does not account for the diminished myogenic tone of cerebral arteries from 12 M-old *Col4a1*$^{+/G394V}$ mice.

TRPM4 currents are diminished in cerebral artery SMCs from middle-aged Col4a1$^{+/G394V}$ mice.

TRPM4 channel activity is necessary for pressure-induced SMC depolarization and the development of myogenic tone in cerebral arteries (78, 205, 206). TRPM4 channels are activated by high intracellular [Ca^{2+}], selective for monovalent cations (i.e., Na^+ and K^+), and impermeant to Ca^{2+} ions (213, 242). Patch-clamp electrophysiology was used to determine if TRPM4 activity was diminished in SMCs from 12 M-old

Col4a1$^{+/G394V}$ mice. SMCs were patch-clamped in the conventional whole-cell configuration with a high [Ca^{2+}] intracellular solution to activate TRPM4 channels directly. Currents were recorded as voltage ramps (-100 to +100 mV) were applied, and the ramp protocol was repeated in the presence of the TRPM4 blocker 9-phenanthrol (30 µM). The TRPM4 component of the whole-cell current was determined by subtraction. Ion substitution studies have demonstrated that Ca^{2+}-activated, 9-phenanthrol-sensitive currents recorded in this manner are carried by Na^{+} ions (206, 213, 242). These currents were also blocked by the recently described (243, 244) selective TRPM4 inhibitor 4-chloro-2-(2-(naphthalene-1-yloxy) acetamido) benzoic acid (NBA), providing substantial evidence that these are *bona fide* TRPM4 currents (Figure 3 – figure supplement 1). We found that conventional whole-cell TRPM4 currents recorded from SMCs from 3 M-old mice did not differ between mutants and controls (Figure 3A and B). In contrast, whole-cell TRPM4 currents were significantly blunted in SMCs from 12 M-old *Col4a1*$^{+/G394V}$ mice compared with controls (Figure 3C and D).

In additional experiments designed to study the activity of TRPM4 channels under near-physiological conditions, TRPM4-dependent transient inward cation currents (TICCs) were recorded from SMCs using an intracellular solution that minimally disrupted intracellular Ca^{2+} signaling (245). We found that TICCs recorded from SMCs from 3 M-old mice did not differ between groups (Figure 3E and F). In contrast, TICC activity and amplitude were significantly lower in SMCs from 12 M-old *Col4a1*$^{+/G394V}$ mice compared with *Col4a1*$^{+/+}$ animals (Figure 3G and H). Prior studies used ion substitution to show that TICCs are Na^{+} currents and are inactivated by down-regulation of TRPM4 expression (245, 246). TICCs were also inhibited by NBA (Figure 3 – figure supplement 1), providing further evidence that these currents depend on TRPM4 activity. These findings suggest that diminished TRPM4 channel activity accounts for the loss of myogenic tone in cerebral arteries from middle-aged *Col4a1*$^{+/G394V}$ mice.

Impaired TRPM4 activity is restored by exogenous PIP$_2$.

Diminished TRPM4 activity in SMCs from 12 M-old *Col4a1*$^{+/G394V}$ mice could result from decreased *Trpm4* expression. However, we used droplet digital PCR (ddPCR) to show the number of *Trpm4* transcripts in cerebral arteries from 12 M-old *Col4a1*$^{+/+}$ and *Col4a1*$^{+/G394V}$ mice were not different (Figure 4A). We therefore investigated dysregulation of TRPM4 activity using patch-clamp electrophysiology.

The activities of TRPM4 and K_{IR} channels are diminished in SMCs from 12 M-old *Col4a1*$^{+/G394V}$ mice. Both channels require PIP$_2$ for activity (240, 241), suggesting that PIP$_2$ depletion could underlie the defects. We tested this idea by adding exogenous PIP$_2$ to the intracellular solution during patch-clamp electrophysiology experiments. We found that when diC8-PIP$_2$ (10 μM) was added to the intracellular solution, conventional whole-cell TRPM4 currents (Figure 4B and C) and TICCs recorded from cerebral artery SMCs from 12 M-old *Col4a1*$^{+/G394V}$ mice (Figure 4D and E) were restored to the levels recorded from age-matched *Col4a1*$^{+/+}$ mice. Supplying PIP$_2$ via the intracellular solution also increased K_{IR} current density in SMCs from *Col4a1*$^{+/G394V}$ mice to the level of control animals (Figure 4F and G). These data suggest that PIP$_2$ levels are lower in SMCs from 12 M-old *Col4a1*$^{+/G394V}$ mice compared to age-matched *Col4a1*$^{+/+}$ mice, leading to diminished TRPM4 and K_{IR} channel activity.

Inhibition of PI3K and TGF-β receptors rescues myogenic tone.

The steady-state level of PIP$_2$ is controlled by the relative activities of biosynthesis and removal pathways (Figure 5A). PIP$_2$ is produced through sequential

ATP-dependent phosphorylation of phosphatidylinositol (PI) by the enzymes phosphatidylinositol 4-kinase (PI4K) and phosphatidylinositol-4-phosphate 5 kinase (PIP5K). Prior studies report that diminished levels of ATP underlie decreased synthesis of PIP_2 and reduced K_{IR} channel activity in brain capillary endothelial cells from CADASIL and 5xFAD Alzheimer's disease mice (164, 167). We measured ATP levels in freshly-isolated cerebral artery SMCs from 12 M-old control and *Col4a1*$^{+/G394V}$ mice using a combined luciferase/fluorescence assay that demonstrated a broad dynamic range and high sensitivity (Figure 5 –figure supplement 1). SMC ATP levels did not differ between 12 M-old control and *Col4a1*$^{+/G394V}$ mice (Figure 5B), suggesting that PIP_2 synthesis is not limited by ATP availability in the mutant animals. We next considered pathways that remove or modify PIP_2. One of the ways that PIP_2 levels can be reduced is by PI3K-induced phosphorylation to PIP_3. To investigate this possibility, we treated SMCs with the potent and selective PI3K inhibitor GSK1059615 (10 nM) (247) and found that whole-cell TRPM4 currents and TICCs recorded from SMCs isolated from 12 M-old *Col4a1*$^{+/G394V}$ were restored to control levels by PI3K inhibition (Figure 5C and D). These data indicate that elevated PI3K activity accounts for diminished PIP_2 levels and decreased TRPM4 currents in SMCs from 12 M-old *Col4a1*$^{+/G394V}$ mice.

Deficient TRPM4 channel activity in SMCs from 12 M-old *Col4a1*$^{+/G394V}$ mice is repaired by blocking PI3K. Therefore, we used pressure myography to determine if the PI3K pathway is also linked to the loss of myogenic tone in cerebral arteries from 12 M-old *Col4a1*$^{+/G394V}$ mice. Arteries were studied before and after incubation with GSK1059615 (10 nM) for 30 min. This treatment slightly increased the contractility of arteries from 12 M-old *Col4a1*$^{+/+}$ mice, but differences in myogenic tone did not reach statistical significance (Figure 5E). In contrast, blockade of PI3K dramatically increased the contractility of cerebral arteries from 12 M-old *Col4a1*$^{+/G394V}$ mice. Myogenic tone within the physiological range (40 to 100 mmHg) was significantly elevated and restored to the levels observed for arteries from control animals (Figure 5F). However, at higher levels of intraluminal pressure (120 and 140 mmHg), myogenic tone was not improved by PI3K inhibition (Figure 5F). These data suggest that elevated PI3K activity in cerebral arteries from 12 M-old *Col4a1*$^{+/G394V}$ mice blunts the development of myogenic tone over a physiologically relevant range of pressures. Higher pressures, such as those encountered during systemic hypertension, override the rescue effect of PI3K inhibition.

Data presented so far support a model in which elevated PI3K activity decreases SMC PIP_2 levels and TRPM4 activity to impair the development of myogenic tone in cerebral arteries from 12 M-old *Col4a1*$^{+/G394V}$ mice. But how does a point mutation in *Col4a1* lead to elevated PI3K activity? Basement membranes sequester and regulate the bioavailability of extracellular regulatory proteins and growth factors and release these substances in response to environmental cues. One of these factors, TGF-β, can stimulate PI3K activity (248). We therefore investigated the effects of acute TGF-β receptor blockade on the development of myogenic tone. Myogenic tone was measured in cerebral arteries from 12 M-old control and *Col4a1*$^{+/G394V}$ mice before and after treatment (30 min) with SB-431542 (1 µM), a potent and selective inhibitor of TGF-β type I receptors (249). The effects of this treatment were strikingly similar to the impact of PI3K blockade. The contractility of arteries from *Col4a1*$^{+/+}$ mice was slightly increased in the presence of SB-431542, but the difference in myogenic tone was not statistically significant (Figure 5G). The myogenic tone of arteries from 12 M-old *Col4a1*$^{+/G394V}$ mice was enhanced at pressures in the normal range for non-hypertensives, but myogenic tone was not improved at higher pressure levels (Figure 5H). These data suggest that blockade of TGF-β receptors restores myogenic tone to arteries from *Col4a1*$^{+/G394V}$ mice at normal pressure levels, but the myogenic response remains impaired at hypertensive pressure. Addition of GSK1059615 to arteries treated with SB-431542 did not further increase myogenic tone in arteries from either 12 M-old *Col4a1*$^{+/G394V}$ or control mice (Figure 5 – figure supplement 2), suggesting that PI3K activity acts downstream of TGF-β receptors. In control experiments, we found that DMSO, the vehicle for both GSK1059615 and SB-431542, had no effect on the myogenic tone of cerebral vessels from either group (Figure 5 – figure supplement 3).

DISCUSSION

Autosomal dominant mutations in *COL4A1* and *COL4A2* cause cSVD and related brain injuries, including ICH, porencephaly, and white matter lesions (9, 10), but the mechanistic underpinnings of this pathology are unknown. Here, we investigated how a specific point mutation in *Col4a1* damages small arteries in the brain during aging. Our findings show that the vascular myogenic response, a process that is vital for the autoregulation of cerebral blood flow, was deficient in cerebral arteries from middle-aged, but not young adult*,* *Col4a1*$^{+/G394V}$ mice. Electrophysiological analysis of SMCs from these animals revealed that the loss of myogenic tone was associated with diminished activity of TRPM4 cation channels. TRPM4 currents were rescued by dialyzing SMCs with PIP_2 or by preventing the conversion of PIP_2 to PIP_3 by blocking PI3K. Our data also show that inhibition of PI3K or TGF-β receptors restored the myogenic tone of cerebral arteries from middle-aged *Col4a1*$^{+/G394V}$ mice. We conclude that the loss of myogenic tone in arteries from 12 M-old *Col4a1*$^{+/G394V}$ mice is due to pathological overstimulation of TGF-β receptors that drives increased PI3K activity to deplete PIP_2 and diminish cation influx through TRPM4 channels. Loss of TRPM4's depolarizing influence decreases voltage-dependent Ca^{2+} influx to reduce SMC contractility and myogenic vasoconstriction. These findings reveal a novel age-dependent mechanism of cSVD.

Disrupted PIP_2 metabolism has emerged as a leading pathogenic process in multiple types of cSVDs (250). In prior studies, PIP_2 deficits were shown to reduce K_{IR} channel activity in brain capillary endothelial cells and impair somatosensory-induced functional hyperemia in CADASIL cSVD and 5xFAD familial Alzheimer's disease mice (164, 167). Here, we demonstrated that pathologically lowered PIP_2 levels in SMCs disrupts TRPM4 cation channels and impairs the development of myogenic tone in cerebral arteries from middle-aged *Col4a1*$^{+/G394V}$ mice. Interestingly, K_{IR} channel activity and PIP_2 levels were not altered in SMCs and cerebral arterial endothelial cells from CADASIL and 5xFAD mice (164, 167), suggesting cellular heterogeneity in PIP_2 defects in different types of cSVD. The effects of cSVDs on PIP_2 levels in other types of cells involved in cerebral blood flow regulation, such as pericytes, microglia, and astrocytes, have not been reported, but such data may be enlightening. Diminished intracellular ATP levels and impaired PIP_2 synthesis reportedly account for the deficit in brain capillary endothelial cells (164, 167). However, ATP levels in SMCs from *Col4a1*$^{+/G394V}$ mice did not differ from controls. Instead, our data indicate that elevated PI3K activity and conversion of PIP_2 to PIP_3 is responsible for the deficit. Thus, although multiple forms of cSVDs may share PIP_2 insufficiency as a core pathogenic mechanism, the pathways to depletion differ. Pharmacological manipulation of PIP_2 may prove to be a breakthrough treatment option for multiple types of cSVDs. Further investigations into fluctuations of brain vascular PIP_2 levels during normal aging and sporadic forms of cSVDs are essential.

Elevated TGF-β signaling has been shown to contribute to the ocular pathogenesis of *Col4a1* mutant mice (197). Acute block of TGF-β receptors repaired defective myogenic tone of cerebral arteries from middle-aged *Col4a1*$^{+/G394V}$ mice, implicating this pathway in the deficiency. Our findings also suggest that TGF-β acts upstream of PI3K in *Col4a1*$^{+/G394V}$ mice. A prior report shows that TGF-β receptors bind the ubiquitin ligase TNF receptor-associated factor 6 (TRAF6) (251). When activated, TRAF6 stimulates Lys^{63}-linked ubiquitylation of the p85α (regulatory) subunit of PI3K, activating the catalytic subunit and increasing the conversion of PIP_2 to PIP_3 (251). Disrupted TGF-β signaling is also associated with cerebral autosomal recessive arteriopathy with subcortical infarcts and leukoencephalopathy (CARASIL), a familial form of cSVD that is caused by mutations in *HTRA1* (169). *HTRA1* encodes a serine protease localized to the extracellular matrix (ECM) that normally contributes to the restraint of TGF-β signaling, and CARASIL-causing mutations disinhibit these pathways (169). It is not known if elevated TGF-β signaling associated with CARASIL also increases PI3K activity to deplete PIP_2 and disrupt ion channel activity, but this outcome is possible and potentially exciting. It is also not known how *COL4A1* mutations increase TGF-β signaling. The production and maturation of TGF-β and activation of corresponding signaling cascades are complex processes, suggesting several possibilities for the defect. TGF-β ligand and latency-associated protein (LAP) are expressed as single pre-pro precursor polypeptides that form homodimers and are subsequently cleaved by proteases during post-translational processing (66). The ligand dimer non-covalently associates with LAP, this complex is covalently attached to latent TGF-β-binding protein (LTBP), and the entire assembly is secreted from the cell and sequestered by the extracellular matrix (ECM) as an inactive complex (66). TGF-β ligand is liberated to bind its receptors and initiate signaling cascades by several stimuli, including activation of integrins and/or modification of the ECM by metalloproteases (66). Any of these processes could be affected by *Col4a1* mutations in a way that increases TGF-β bioavailability. For example, it is conceivable that defects in the structure of the basement membrane associated with the incorporation of mutant collagen, in conjunction with the insults of normal aging, impair the sequestration of the TGF-β-LAP complex in 12 M-old *Col4a1*$^{+/G394V}$ mice, leading to increased availability, activation of the cognate signaling cascades and, ultimately, vascular dysfunction.

Even within monogenetic forms of familial cSVD, the pathogenic mechanisms and impacts of the disease widely vary. For example, *Col4a1*$^{+/G498V}$ mutant mice displayed cSVD-like pathology in young adult animals together with hypermuscularity and elevated pressure-induced contractility of pericyte-ensheathed transitional vascular segments bridging capillaries and arterioles in the retinal vasculature (252, 253). Here we show that cerebral vascular dysfunction in *Col4a1*$^{+/G394V}$ mice is observed from middle age and involves the loss of pressure-induced constriction of cerebral arteries caused by faulty TRPM4 cation channels in SMCs. These and other examples show that cSVDs are a cluster of related disorders with similar outcomes arising from different processes rather than a single, monolithic disease. Accordingly, a targeted, precision medicine-based approach may be the best strategy for developing effective therapeutics for cSVDs and associated dementias.

MATERIALS AND METHODS

Chemical and reagents: Unless otherwise specified, chemicals and other reagents were obtained from Sigma-Aldrich, Inc. (St. Louis, MO, USA).

Animals: Young adult (3 M-old) and middle-aged (12 M-old) male and female littermate *Col4a1*$^{+/+}$ and *Col4a1*$^{+/G394V}$ mice were used in this study. The *Col4a1*^{G394V} mutation was backcrossed to C57BL/6J mice for over 20 generations (189, 231). Animals were maintained in individually ventilated cages (≤5 mice/cage) with *ad libitum* access to food and water in a room with controlled 12-hour light and dark cycles. All animal care procedures and experimental protocols involving animals complied with the NIH *Guide for the Care and Use of Laboratory Animals* and were approved by the Institutional Animal Care and Use Committees at the University of Nevada, Reno, and UCSF. Mice were euthanized by decapitation and exsanguination under isoflurane anesthesia (Baxter Healthcare, Deerfield, IL, USA). Brains were isolated and placed in ice-cold Ca^{2+}-free physiological saline solution (Mg-PSS, containing140 mM NaCl, 5 mM KCl, 2 mM $MgCl_2$, 10 mM HEPES, and 10 mM glucose (pH 7.4, NaOH), supplemented with 0.5% bovine serum albumin.

Brain Histological Analysis: Anesthetized mice were transcardially perfused with PBS, followed by 4% paraformaldehyde (Fisher, Waltham, MA, USA) dissolved in PBS. Whole brain images were acquired using a digital camera (Sony α6000; Sony, Tokyo, Japan). Brains were postfixed in 4% paraformaldehyde for 24 hours, cryoprotected in 30% sucrose in PBS, and embedded in optimal cutting temperature compound (Fisher). Coronal cryosections (35 µm) regularly spaced (500 µm) along the rostrocaudal axis were stained with a Prussian blue and Nuclear Fast Red stain kit (Abcam, Cambridge, UK). Images were acquired with a BZ-X700 microscope using BZ-X Viewer 1.3.0.5 software and stitched with BZ-X Analyzer 1.3.0.3 software (Keyence, Osaka, Japan).

Isolation of cerebral arteries and SMCs: Cerebral pial arteries (middle cerebral, posterior cerebral, and superior cerebellar) were gently removed from the brain and washed in Mg-PSS. Native SMCs for patch-clamp experiments were obtained by initially digesting isolated arteries in 1 mg/mL papain (Worthington Biochemical Corporation, Lakewood, NJ, USA), 1 mg/mL dithiothreitol (DTT), and 10 mg/mL BSA in Mg-PSS at 37°C for 12 min, followed by a 14-min incubation with 1 mg/mL type II collagenase (Worthington Biochemical Corporation). A single-cell suspension was prepared by washing digested arteries three times with Mg-PSS and triturating with a fire-polished glass pipette. All cells used for this study were freshly dissociated on the day of experimentation.

Pressure myography: The current best practices guidelines for pressure myography experiments were followed (254). Arteries were mounted between two glass cannulas (outer diameter, 40–50 μm) in a pressure myograph chamber (Living Systems Instrumentation, St Albans City, VT, USA) and secured by a nylon thread. Intraluminal pressure was controlled using a servo-controlled peristaltic pump (Living Systems Instrumentation). Preparations were visualized with an inverted microscope (Accu-Scope Inc., Commack, NY, USA) coupled to a USB camera (The Imaging Source LLC, Charlotte, NC, USA). Changes in luminal diameter were assessed using IonWizard software (version 7.2.7.138; IonOptix LLC, Westwood, MA, USA). Arteries were bathed in warmed (37°C), oxygenated (21% O_2, 6% CO_2, 73% N_2) PSS (119 mM NaCl, 4.7 mM KCl, 21 mM $NaHCO_3$, 1.17 mM $MgSO_4$, 1.8 mM $CaCl_2$, 1.18 mM KH_2PO_4, 5 mM glucose, 0.03 mM EDTA) at an intraluminal pressure of 5 mmHg. Following equilibration for 15 min, intraluminal pressure was increased to 110 mmHg, and vessels were stretched to their approximate *in vivo* length, after which pressure was reduced back to 5 mmHg for an additional 15 min. Vessel viability was assessed for each preparation by evaluating vasoconstrictor responses to high extracellular [K^+] PSS, made isotonic by adjusting the [NaCl] (60 mM KCl, 63.7 mM NaCl). Arteries that showed less than 10% constriction in response to elevated [K^+] were excluded from further investigation.

Myogenic tone was assessed by raising the intraluminal pressure stepwise from 5 mmHg to 20 mmHg and then to 140 mmHg in 20 mmHg increments. The active diameter was obtained by allowing vessels to equilibrate for at least 5 minutes at each pressure or until a steady-state diameter was reached. Following completion of the pressure-response study, intraluminal pressure was lowered to 5 mmHg, and arteries were superfused with Ca^{2+}-free PSS supplemented with EGTA (2 mM) and the voltage-dependent Ca^{2+} channel blocker diltiazem (10 μM) to inhibit SMC contraction, after which passive diameter was obtained by repeating the stepwise increase in intraluminal pressure. Myogenic tone at each pressure step was calculated as myogenic tone (%) = [1 – (active lumen diameter/passive lumen diameter)] × 100. For some experiments, the endothelium was disrupted by passing air bubbles through the lumen as previously described (254).

Electrophysiological recordings: Enzymatically isolated native SMCs were transferred to a recording chamber (Warner Instruments, Hamden, CT, USA) and allowed to adhere to glass coverslips for 15 minutes at room temperature. Recording electrodes (3–5 MΩ) were pulled and polished. Currents were recorded at room temperature using an Axopatch 200B amplifier (Molecular Devices, Sunnyvale, CA, USA) equipped with an Axon CV 203BU headstage and Digidata 1440A digitizer (Molecular Devices) for all patch-clamp electrophysiology experiments.

The bathing solution composition for perforated-patch whole-cell recordings of K_V currents and STOCs was 134 mM NaCl, 6 mM KCl, 1 mM $MgCl_2$, 2 mM $CaCl_2$, 10 mM

HEPES, and 10 mM glucose at pH 7.4 (NaOH). The pipette solution contained 110 mM K-aspartate, 1 mM $MgCl_2$, 30 mM KCl, 10 mM NaCl, 10 mM HEPES, and 50 µM EGTA at pH 7.2 (KOH). Amphotericin B (200 µg/mL) was included in the pipette solution of all perforated-patch recordings to allow electrical access. Perforation was deemed acceptable if series resistance was less than 50 MΩ. Whole-cell K^+ currents were recorded using a step protocol (-60 to +60 mV in 10 mV, 250 ms steps) from a holding potential of -80 mV. The BK channel blocker paxilline (1 µM) was included in the bath solution when Kv currents were recorded. Whole-cell K^+ currents were recorded in the absence and presence of 4-aminopyridine (5 mM), and the Kv component was determined by subtraction. Summary current-voltage (I-V) plots were generated using values obtained from the last 50 ms of each step. STOCs, produced by the efflux of K^+ through BK channels, were recorded from SMCs voltage-clamped at a range of membrane potentials (-60 to 0 mV).

Conventional whole-cell patch-clamp electrophysiology was used to measure Ba^{2+}-sensitive K_{IR} currents in isolated cerebral artery SMCs. Currents were recorded by voltage-ramp protocol (-100 mV to +20 mV for 3000 ms) from the holding potential of -30 mV. Voltage ramps were repeated every 10 s for 300 s. The composition of external bathing solution was: 80 or 134 mM NaCl, 60 or 6 mM KCl, 1 mM $MgCl_2$, 10 mM HEPES, 10 mM glucose and 2 mM $CaCl_2$ (PH 7.4). The pipette solution was of the following composition: 5 mM NaCl, 35 mM KCl, 100 mM K-gluconate, 1 mM $CaCl_2$, 0.5 mM $MgCl_2$, 10 mM HEPES, 10 mM EGTA, 2.5 mM Na_2- ATP, and 0.2 mM GTP (pH 7.2). The Kir channel currents were activated by increasing the extracellular K^+ concentration from 6 to 60 mM (replacing Na^+) and blocked using Ba^{2+} (10 µM).

Whole-cell TRPM4 currents were recorded in a bath solution consisting of 156 mM NaCl, 1.5 mM $CaCl_2$, 10 mM glucose, 10 mM HEPES, and 10 mM TEACl (pH 7.4, adjusted with NaOH). The patch pipette solution contained 156 mM CsCl, 8 mM NaCl, 1 mM $MgCl_2$, 10 mM HEPES (pH 7.4, adjusted with NaOH), and a free Ca^{2+} concentration of 200 µM, adjusted using the appropriate amount of $CaCl_2$ and EGTA, as determined with Max-Chelator software (WEBMAXC standard, available at https://somapp.ucdmc.ucdavis.edu/pharmacology/bers/maxchelator/webmaxc/webmaxcS.htm). Whole-cell cation currents were evoked by applying 400 ms voltage ramps from -100 to +100 mV from a holding potential of -60 mV. Voltage ramps were repeated every 2 s for 300 s. The selective TRPM4 inhibitor 9-phenanthrol (30 µM) or NBA (3 µM) was applied after peak TRPM4 current was recorded (~60 s). Whole-cell TRPM4 current amplitude was expressed as the 9-phenanthrol or NBA-sensitive current at +100 mV.

TICCs were recorded using modified whole-cell patch-clamp conditions as described in our previous publication (245). The bath solution contained 140 mM NaCl, 5 mM CsCl, 2 mM $CaCl_2$, 1 mM $MgCl_2$, 10 mM glucose, and 10 mM HEPES (pH 7.4, adjusted with NaOH). The pipette solution contained 20 mM CsCl, 87 mM K-aspartate, 1 mM $MgCl_2$, 5 mM MgATP, 10 mM EGTA, and 10 mM HEPES (pH 7.2, adjusted with CsOH). Cells were voltage-clamped at -70 mV, and TICC activity was calculated as the sum of the open channel probability (NP_o) of multiple open states of 1.75 pA (234).

***Isolation of RNA and ddPCR*:** Total RNA was extracted from isolated cerebral arteries by homogenization in TRIzol reagent (Invitrogen, Waltham, MA), followed by purification using a Direct-zol RNA microprep kit (Zymo Research, Irvine, CA) with on-column DNAse treatment. RNA concentration was determined using an RNA 6000 Pico Kit run on a Bioanalyzer 2100 using Agilent 2100 Expert Software (B.02.11; Agilent

Technologies, Santa Clara, CA). RNA was converted to cDNA using iScript cDNA Supermix (Bio-Rad, Hercules, CA). Quantitative droplet digital PCR (ddPCR) was performed using QX200 ddPCR EvaGreen Supermix (Bio-Rad), cDNA templates, and custom-designed primers for *Trpm4* (NM_175130.4): 5’-TTCACGTACTCTGGCCGAAA-3’ (sense) and 5’-CGGGTAACGAGACTGTACACA-3’ (antisense). Generated droplet emulsions were amplified using a C100 Touch Thermal Cycler (Bio-Rad), and the fluorescence intensities of individual droplets were measured using a QX200 Droplet Reader (Bio-Rad) running QuantaSoft (version 1.7.4; Bio-Rad). Analysis was performed using QuantaSoft Analysis Pro (version 1.0596; Bio-Rad).

Measurement of [ATP] in SMCs: Cerebral artery SMCs were prepared by enzymatic digestion. The cell suspension was passed through a 70 µm cell strainer (VWR, Radnor, PA, USA) to remove large debris, and the viable SMC concentration was determined by manual count using a hemocytometer and Trypan Blue staining. The intracellular [ATP] was determined by lysing the cells and quantifying luminescence produced by luciferase-induced conversion of ATP to light using the CellTiter-Glo Assay 3D (Promega, WI, USA). Approximately 5000 SMCs were added to each reaction. To further ensure equal input of SMCs, the CellTiter-Glo 3D Assay was multiplexed with CellTox Green Assay (Promega), a fluorescent dye that selectively and quantitatively binds double-stranded DNA. Dye fluorescence is directly proportional to DNA concentration and the number of cells in each assay. ATP concentration (luminescence) was normalized to the number of cells (fluorescence) to determine intracellular ATP per cell. Luminescence and fluorescence ($485_{Ex}/538_{Em}$) were measured using a FlexStation 3 (Molecular Devices, San Jose, CA, USA). A serial tenfold dilution of ATP (1 nM to 1 µM; 80 µl contains 8^{-14} to 8^{-11} moles of ATP, respectively) was measured to calibrate the linear working range of ATP detection. Data were expressed as the ratio of ATP luminescence/DNA fluorescence.

Statistical analysis: All summary data are presented as means ± SEM. Statistical analyses were performed, and graphs were constructed using Prism version 9.3.1 (GraphPad Software, San Diego, CA, USA). The value of n refers to the number of cells for patch-clamp electrophysiology experiments and arteries for myography experiments. Statistical analyses were performed using unpaired Student's t-tests or two-way analysis of variance (ANOVA). A P-value < 0.05 was considered statistically significant for all analyses.

Grant Support: This study was supported by grants from the National Institutes of Health (NHLBI R35155008 and NIGMS P20GM130459 to S.E.; NINDS R01NS096173 to D.B.G.; and NINDS RF1NS110044 and R33NS115132 to D.B.G and S.E.). The Transgenic Genotyping and Phenotyping Core and the High Spatial and Temporal Resolution Imaging Core at the COBRE Center for Molecular and Cellular Signaling in the Cardiovascular System, University of Nevada, Reno are maintained by grants from NIH/NIGMS (P20GM130459 Sub#5451 and P20GM130459 Sub#5452). The University of California, San Francisco Department of Ophthalmology is supported by a Vision Core grant NEI P30EY002162, and by an unrestricted grant from Research to Prevent Blindness, New York, NY.

Author contributions: S.E. and D.B.G. initiated and supervised the project. S.E. designed the experiments. E.Y. performed brain histology, pressure myography, patch-clamp electrophysiology, ATP assays, and ddPCR experiments. S.A. and A.S.S. performed patch-clamp electrophysiology experiments. P.T. performed pressure myography experiments. M.S., X.W., and C.L.D. performed brain histology and animal colony management. E.Y., S.A., A.S.S., P.T., and S.E. analyzed the data. E.Y. and S.E. drafted the manuscript and prepared the figures. E.Y., C.L.D., D.B.G., and S.E. revised the manuscript.

Competing interests*:* The authors declare that they have no competing interests.

Data and materials availability: All data needed to evaluate the conclusions in the paper are present in the paper or the Supplementary Materials

FIGURES

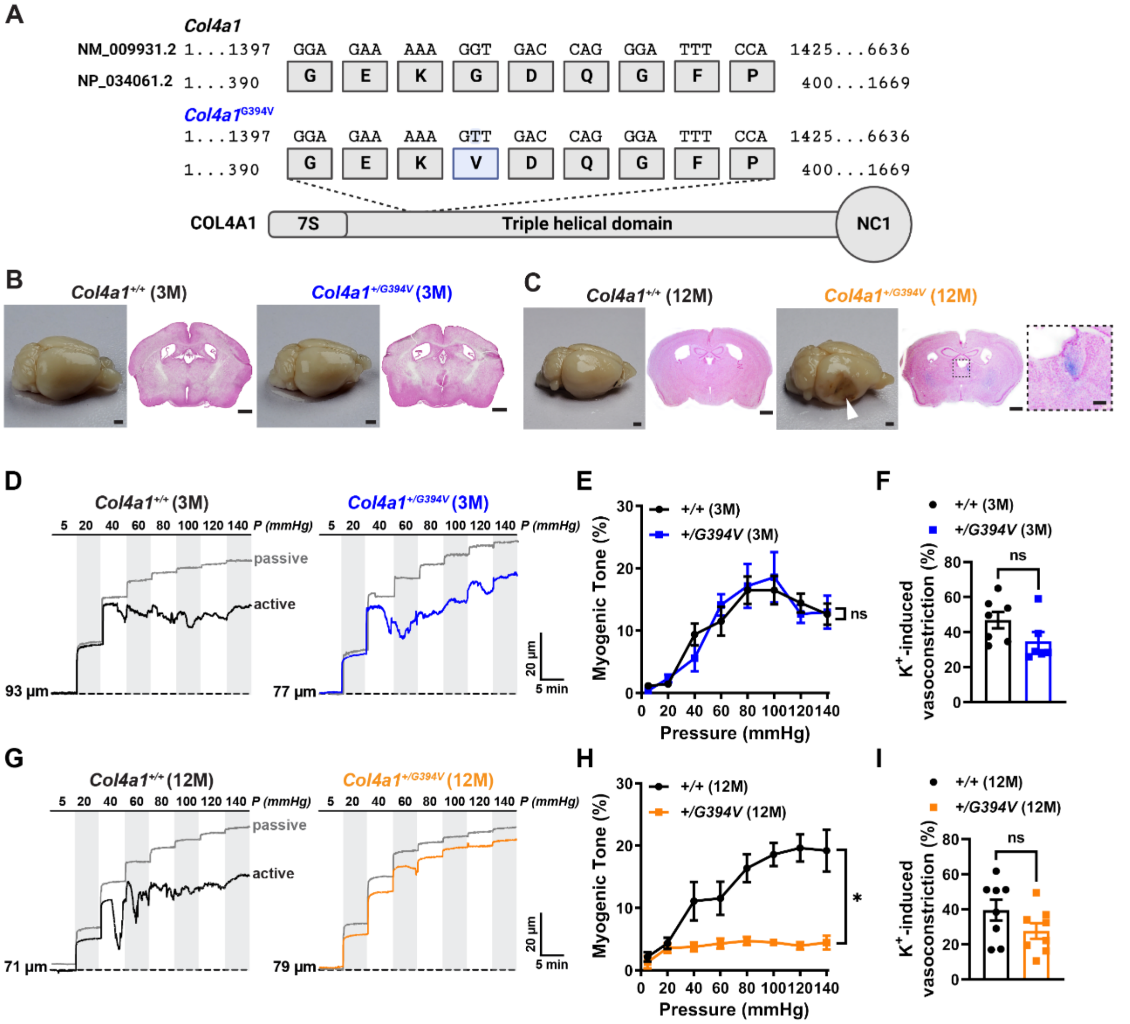

Figure 1. Cerebral arteries from 12 M-old Col4a1*$^{+/G394V}$ *mice fail to develop myogenic tone. (A) Schematic representation of COL4A1 showing the position of the *Col4a1*^{G394V} mutation. (B and C) Representative images of perfusion-fixed brains and coronal brain sections stained with Prussian blue and Nuclear Fast Red from 3 M-old (B) and 12 M-old (C) *Col4a1*$^{+/+}$ and *Col4a1*$^{+/G394V}$ mice. Arrowhead indicates a region with loss of brain tissue secondary to a hemorrhagic event. Enlarged region in the inset shows an example of spontaneous ICH. Scale = 1 mm. Inset scale = 200 µm. Representative of 4 mice per group. (D) Typical recordings of the inner diameter of isolated cerebral arteries from 3 M-old *Col4a1*$^{+/+}$ *and Col4a1*$^{+/G394V}$ mice showing the myogenic response to increases in intraluminal pressure (active) and the dilation of the same arteries when extracellular Ca^{2+} has been removed (passive). (E) Summary of myogenic tone, expressed as mean ± SEM, as a function of intraluminal pressure. n = 6-7 arteries from 6 animals per group. ns = not significant, two-way ANOVA. (F) Summary data showing vasoconstriction of isolated cerebral arteries from 3 M-old *Col4a1*$^{+/+}$ *and Col4a1*$^{+/G394V}$ mice in response to 60 mM KCl. n = 6-7 arteries from 6 animals per group. ns = not significant, unpaired t-test. (G) Representative traces of the myogenic response

and passive diameter of isolated cerebral arteries from 12 M-old *Col4a1*$^{+/+}$ *and Col4a1*$^{+/G394V}$ mice. (H) Summary of myogenic tone expressed as mean ± SEM as a function of intraluminal pressure. n = 8 arteries from 5 or 6 animals per group. *P<0.05, two-way ANOVA. (I) Summary data showing vasoconstriction of isolated cerebral arteries from 12 M-old *Col4a1*$^{+/+}$ *and Col4a1*$^{+/G394V}$ mice in response to 60 mM KCl. n = 8 arteries from 5 or 6 animals per group. ns = not significant, unpaired t-test.

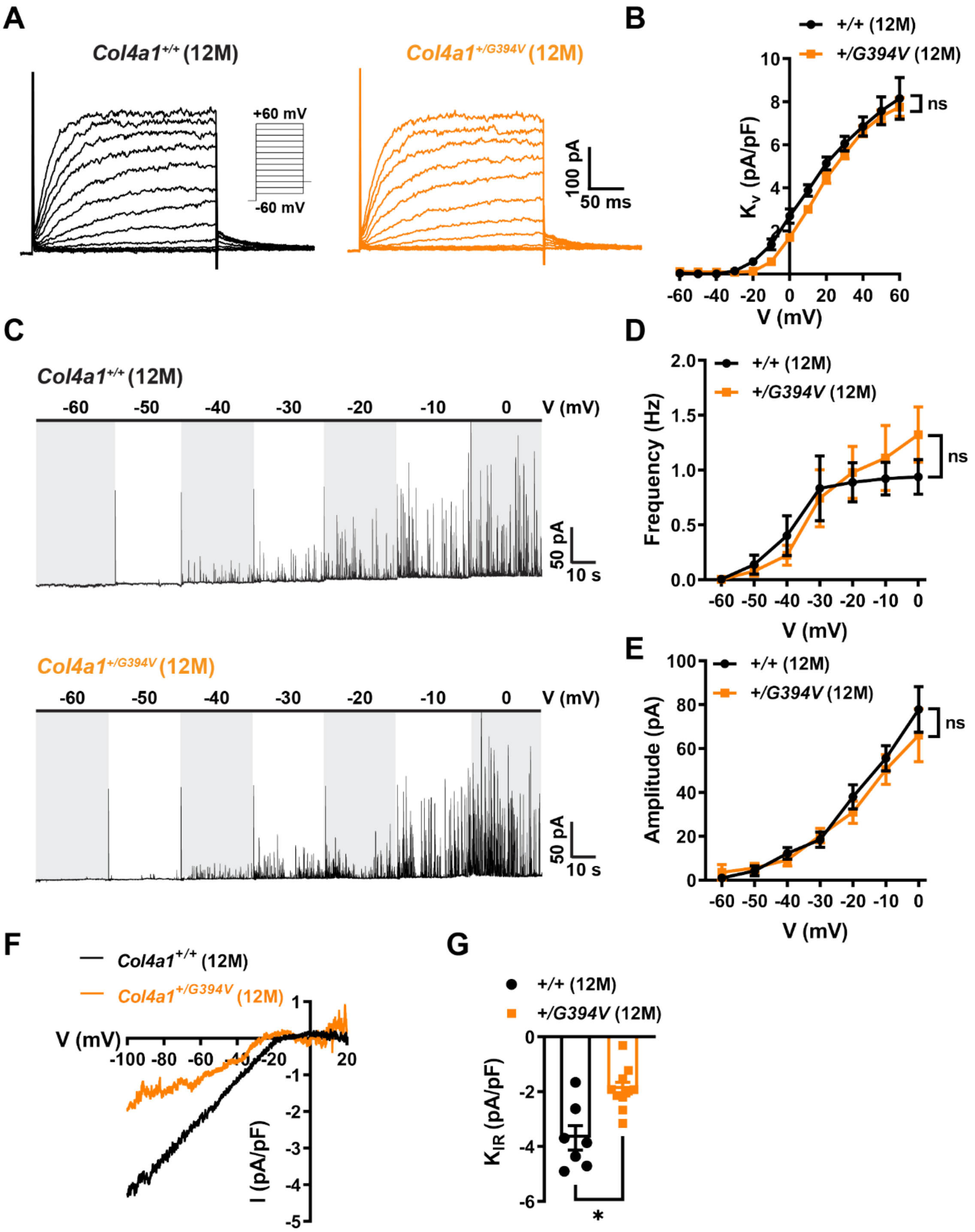

Figure 2. Loss of myogenic tone in cerebral arteries from middle-aged Col4a1$^{+/G394V}$ mice is not attributable to increased SMC K$^+$ channel currents. (A) Example recording of 4-aminopyridine (5 mM)-sensitive Kv currents elicited by application of voltage pulses (250 ms) from -60 to + 60 mV in the presence of the BK channel blocker paxilline (1 μM). (B) Summary data of K_V current at each command potential, normalized to cell capacitance (pA/pF). n = 8-10 cells from 3 animals per

group. ns = not significant, two-way ANOVA. (C) Representative traces of STOCs recorded over a series of membrane potentials (-60 to 0 mV). (D and E) Summary data for STOC frequency (D) and amplitude (E) at each command potential. n = 11-14 cells from 6 or 7 animals per group. ns = not significant, two-way ANOVA. (F) Representative recording of $BaCl_2$-sensitive K_{IR} whole-cell currents evoked by adding 60 mM KCl to the bath as voltage ramps (-100 to +20 mV) were applied. (G) Summary data of K_{IR} current amplitude recorded at -100 mV and normalized to cell capacitance (pA/pF). n = 7-10 cells from 4 or 6 animals per group. *P<0.05, unpaired t-test.

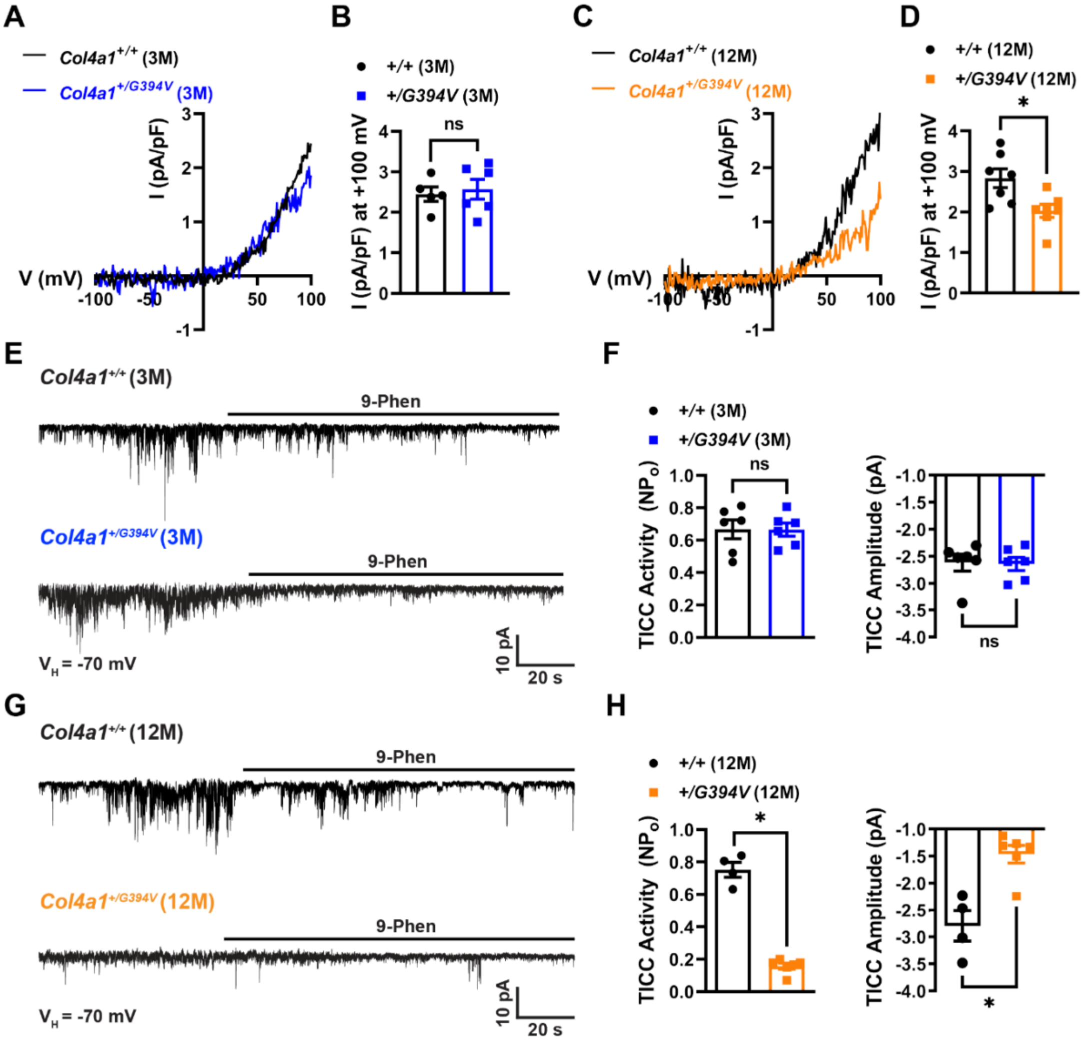

Figure 3. TRPM4 currents are diminished in cerebral artery SMCs from 12 M-old Col4a1$^{+/G394V}$ mice. (A) Typical I-V plots of whole-cell TRPM4 currents in SMCs from 3 M-old mice produced as voltage ramps (-100 to +100 mV) were applied. Currents were evoked by including 200 μM free Ca^{2+} in the intracellular solution. (B) Summary of TRPM4 current amplitude at +100 mV normalized to cell capacitance. n = 5-6 cells from 4 or 5 animals per group. ns = not significant, unpaired t-test. (C) Representative I-V plots of whole-cell TRPM4 currents in SMCs from 12 M-old mice. (D) Summary of TRPM4 current amplitude at +100 mV normalized to cell capacitance in 12 M-old mice. n = 7 cells from 5 animals per group. *P<0.05, unpaired t-test. (E) Typical recordings of whole-cell TICCs in SMCs from 3 M-old mice voltage-clamped at -70 mV. TICCs were inhibited by the TRPM4 blocker 9-phenanthrol (30 μM). (F) Summary of total TICC activity and amplitude. n = 6 cells from 3 animals per group. ns = not significant, unpaired t-test. (G) Representative recordings of TICCs in SMCs from 12 M-old mice. (H) Summary of total TICC activity and amplitude. n = 4-6 cells from 3 animals per group. *P<0.05, unpaired t-test.

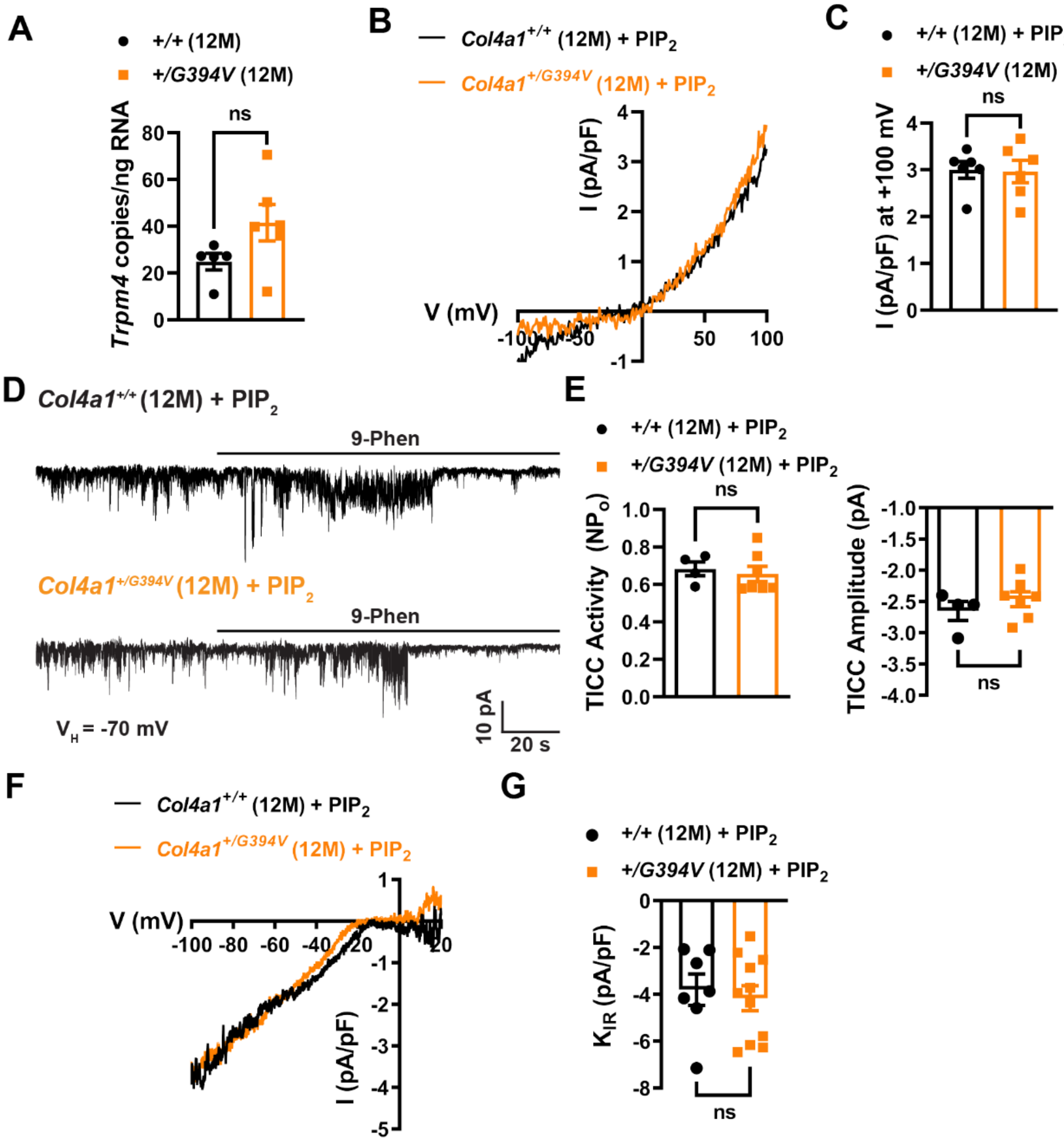

Figure 4. Impaired TRPM4 activity is restored by exogenous PIP$_2$. (A) ddPCR assay for *Trpm4* mRNA (as transcript copies/ng total RNA) in cerebral arteries. n = 5 or 6 animals. ns = not significant, unpaired t-test. (B) Typical recordings of whole-cell TRPM4 currents in SMCs from 12 M-old *Col4a1*$^{+/+}$ and *Col4a1*$^{+/G394V}$ mice with diC8-PIP$_2$ (10 μM) added to the intracellular solution. (C) Summary of TRPM4 current amplitude at +100 mV, normalized to cell capacitance (pA/pF). n = 6 cells from 4 animals per group. ns = not significant, unpaired t-test. (D) Representative recordings of TICCs in SMCs from 12 M-old *Col4a1*$^{+/+}$ and *Col4a1*$^{+/G394V}$ mice with diC8-PIP$_2$ (10 μM) added to the intracellular solution. (E) Summary of total TICC activity and amplitude. n = 4-7 cells from 3 or 4 animals per group. ns = not significant, unpaired t-test. (F) Representative recording of BaCl$_2$-sensitive K$_{IR}$ whole-cell currents recorded in SMCs from 12 M-old animals with diC8-PIP$_2$ (10 μM) added to the intracellular solution. (G) Summary data of K$_{IR}$ current amplitude recorded at -100 mV and normalized to cell capacitance (pA/pF). n= 7-11 cells from 3 animals per group. ns = not significant, unpaired t-test.

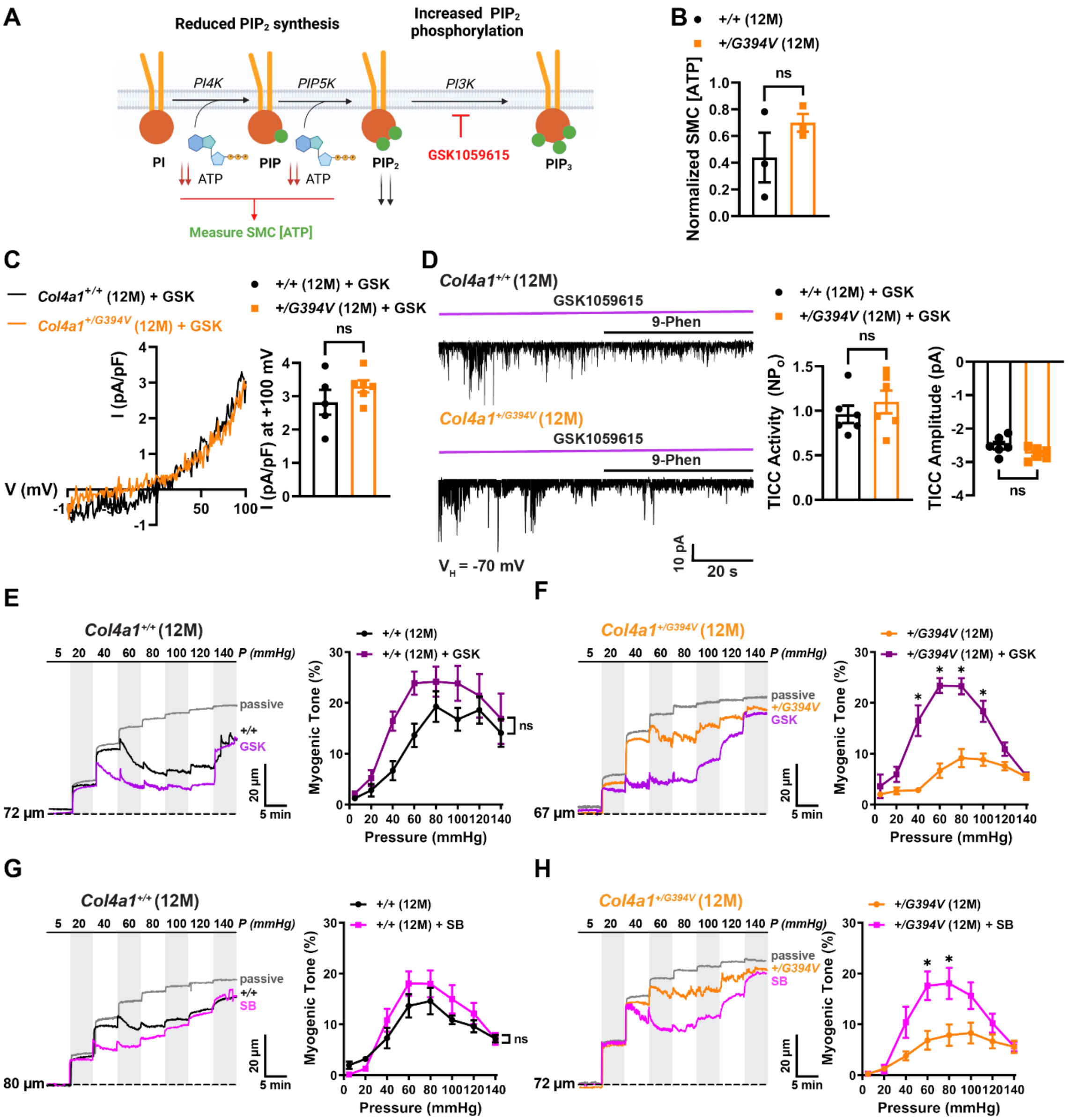

Figure 5. Inhibition of PI3K and TGF-β receptors rescues myogenic tone. (A) PIP$_2$ synthesis and removal pathways. (B) Normalized SMC [ATP]. n = 3 animals per group. ns = not significant, unpaired t-test. (C) Typical recordings and summary data of whole-cell TRPM4 currents in SMCs from 12 M-old *Col4a1*$^{+/+}$ and *Col4a1*$^{+/G394V}$ mice treated with the PI3K blocker GSK1059615 (10 nM). Inhibition of PI3K activity with GSK1059615 (10 nM) restores whole-cell TRPM4 currents in SMCs from 12 M-old *Col4a1*$^{+/G394V}$ mice to the level of controls. n = 5-6 cells from 3 or 4 animals per group. ns = not significant, unpaired t-test. (D) Inhibition of PI3K activity with GSK1059615 (10 nM) restores TICC activity and amplitude recorded from SMCs from 12 M-old *Col4a1*$^{+/G394V}$ mice to the level of controls. n= 6 cells from 4 animals per group. ns = not significant, unpaired t-test. (E and F) Representative traces (E) and summary data (F) of the myogenic response of cerebral arteries from 12 M-old *Col4a1*$^{+/+}$ and *Col4a1*$^{+/G394V}$ mice before and after blocking PI3K with GSK1059615 (10 nM, 30 min). n = 6 arteries from 4 or 5 animals per

group, *P<0.05, ns = not significant, 2-way ANOVA. (G and H) Representative traces (G) and summary data (H) of the myogenic response of cerebral arteries from 12 M-old *Col4a1*$^{+/+}$ and *Col4a1*$^{+/G394V}$ mice before and after blocking TGF-β receptors with SB-431542 (1 μM, 30 min). n = 5-6 arteries from 3 animals per group, *P<0.05, ns = not significant, 2-way ANOVA.

Supplemental Figures

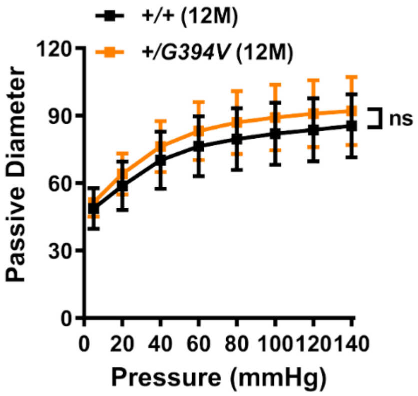

Figure 1 - figure supplement 1. Passive diameter of cerebral arteries from 12 M-old Col4a1$^{+/G394V}$ mice. Summary data of the passive diameter of cerebral arteries expressed as as a function of intraluminal pressure. n = 8 arteries from 5 or 6 animals per group. ns = not significant, two-way ANOVA.

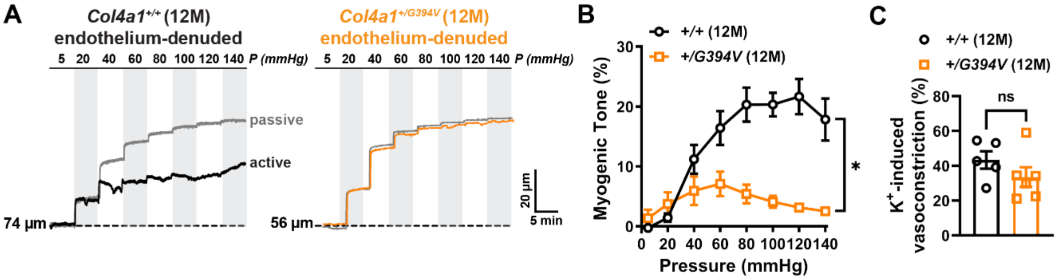

Figure 1 - figure supplement 2. Endothelium-denuded cerebral arteries from 12 M-old Col4a1$^{+/G394V}$ mice fail to develop myogenic tone. (A) Typical recordings of the inner diameter of endothelium-denuded cerebral arteries from 12 M-old *Col4a1$^{+/+}$ and Col4a1$^{+/G394V}$* mice in response to step-wise increases in intraluminal pressure when Ca^{2+} is present (active) and when extracellular Ca^{2+} has been removed (passive). (B) Summary of myogenic tone expressed as mean ± SEM as a function of intraluminal pressure. n = 5 or 6 arteries from 3 animals per group. *P<0.05, two-way ANOVA. (C) Summary data showing vasoconstriction of endothelium-denuded isolated cerebral arteries from 12 M-old *Col4a1$^{+/+}$ and Col4a1$^{+/G394V}$* mice in response to KCl (60 mM). n = 5 or 6 arteries from 3 animals per group. ns = not significant, unpaired t-test.

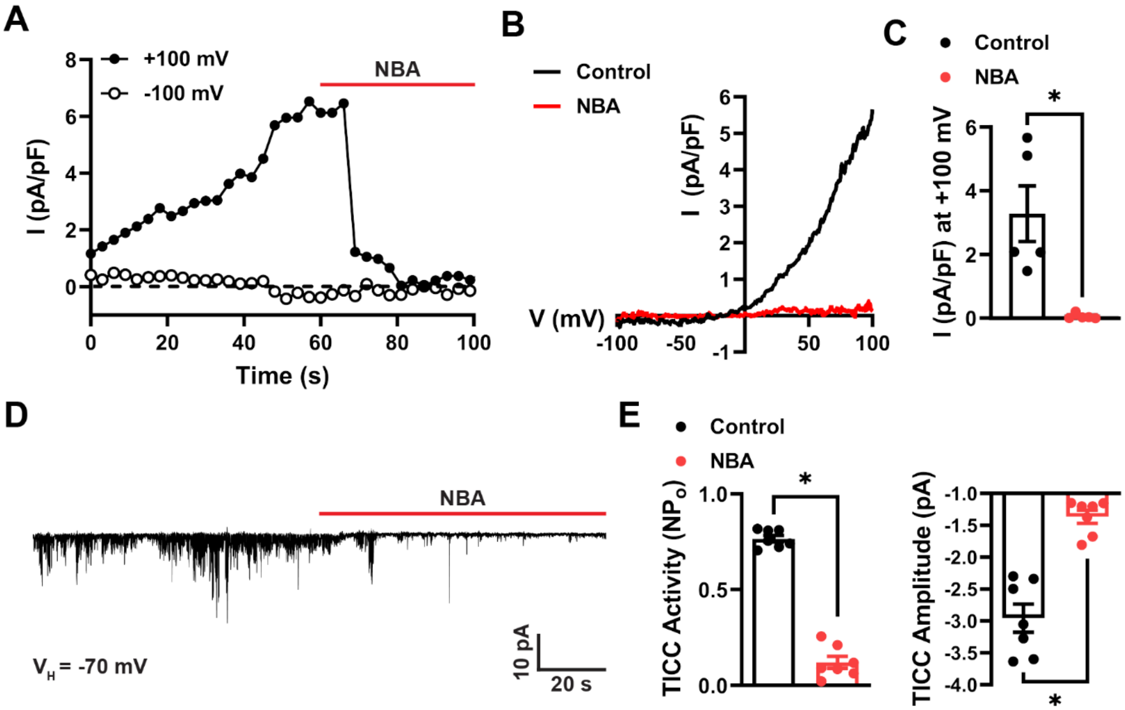

Figure 3 - figure supplement 1. TRPM4 inhibitor NBA blocks whole-cell Ca^{2+}-activated currents and TICCs. (A) Representative time course of a conventional whole-cell patch-clamp recording of a SMC from a 3 M-old *Col4a1*$^{+/+}$ mouse showing an outwardly rectifying cation current activated by 200 μM free Ca^{2+} in the intracellular solution as voltage ramps (-100 to +100 mV) were applied. This current was abolished by the selective TRPM4 inhibitor 4-chloro-2-(2-(naphthalene-1-yloxy) acetamido) benzoic acid (NBA; 3 μM). (B) I-V plots for experiment shown in (A) in the presence and absence of NBA. Currents were obtained after peak current stabilized (~60s after break-in). (C) Summary of current amplitude at +100 mV normalized to cell capacitance. n = 5 cells from 4 animals. *P<0.05, unpaired t-test. (D) Typical recordings of whole-cell TICC in a SMCs a 3 M-old *Col4a1*$^{+/+}$ mouse. V_H = -70 mV. TICCs were inhibited by NBA (3 μM). (E) Summary of TICC activity and amplitude in the presence and absence of NBA. n = 7 cells from 3 animals. *P<0.05, unpaired t-test.

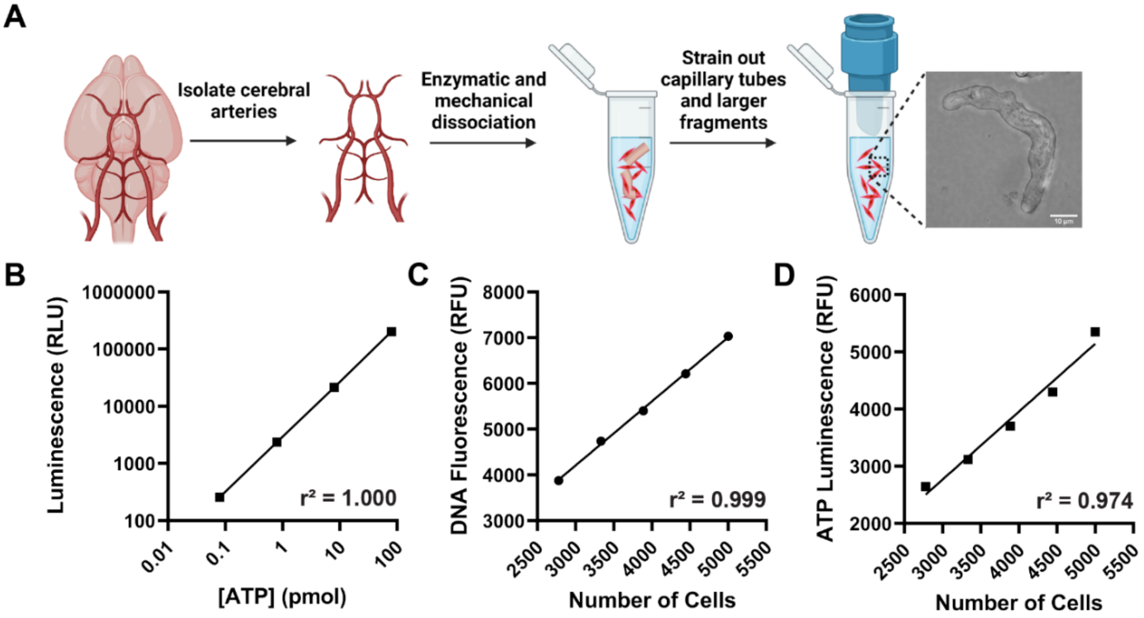

Figure 5 - figure supplement 1. ATP assay validation. (A) Preparation of SMCs for ATP assay. (B) Relative luminescence units (RLU) are directly proportional to the [ATP] over four orders of magnitude (0.08 to 80 pmol) (r^2 = 1.00). (C) DNA fluorescence (relative fluorescence units, RFU) as a function of cell number (r^2 = 0.99). (D) ATP luminescence (RLU) as a function of cell number (r^2 = 0.97).

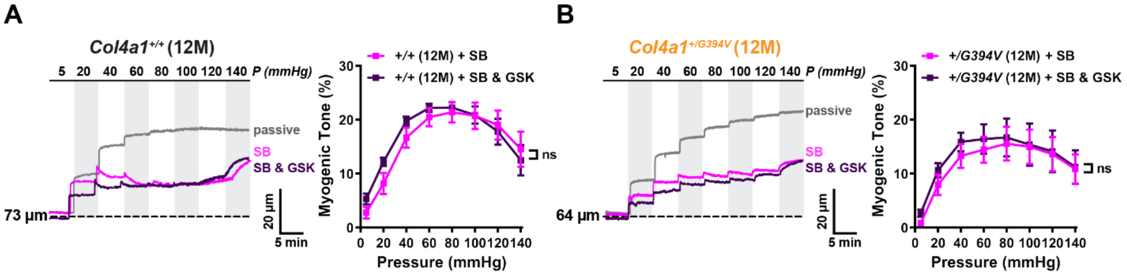

Figure 5 - figure supplement 2. Myogenic tone with SB-431542 and GSK1059615. (A and B) Representative traces and summary data of the myogenic response of cerebral arteries from 12 M-old *Col4a1*$^{+/+}$ (A) and *Col4a1*$^{+/G394V}$ (B) mice after first blocking TGF-β receptors with SB-431542 (1 µM, 30 min) and then blocking both TGF-β receptors and PI3K with the addition of GSK1059615 (10 nM, 30 min). Combined blockade did not have an additive effect. n = 5 or 6 arteries from 3 animals per group. *P<0.05, ns = not significant, 2-way ANOVA.

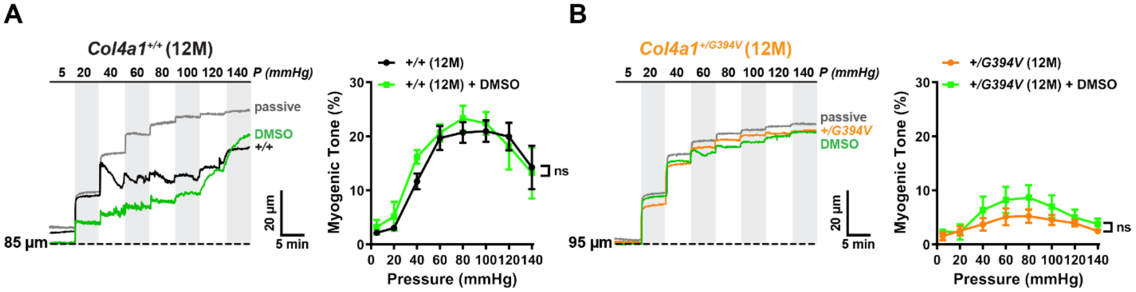

Figure 5 - figure supplement 3. Vehicle control experiments. (A and B) Representative traces and summary data of the myogenic response of cerebral pial arteries from 12 M-old *Col4a1*$^{+/+}$ (A) and *Col4a1*$^{+/G394V}$ (B) mice before and after treating arteries with DMSO (0.01%), the vehicle for GSK1059615 and SB-431542 (30 min). n = 4-6 arteries from 4 or 5 animals per group. ns = not significant, 2-way ANOVA.

CHAPTER 4: PHOSPHATIDYLINOSITOL-3-KINASE INHIBITION RESCUES AGE-DEPENDENT DEFECTS IN NEUROVASCULAR COUPLING AND COGNITIVE IMPAIRMENT IN A GENETIC MODEL OF CEREBRAL SMALL VESSEL DISEASE

Pratish Thakore[1†], Evan Yamasaki[1†], Sher Ali[1†], Alfredo Sanchez Solano[1], C. Labelle-Dumais[2], Xiao Gao[3,4], Myriam M. Chaumeil[3,4], Douglas B. Gould[2], and Scott Earley[1*]

[1]Department of Pharmacology, Center for Molecular and Cellular Signaling in the Cardiovascular System University of Nevada, Reno School of Medicine; Reno, Nevada, 89557-0318, USA

[2]Department of Ophthalmology and Anatomy, Institute for Human Genetics, University of California San Francisco School of Medicine; San Francisco, CA 94143, USA

[3]Department of Physical Therapy and Rehabilitation Science, UCSF, San Francisco USA

[4]Department of Radiology and Biomedical Imaging, UCSF, San Francisco USA

***Corresponding author:** Email: searley@med.unr.edu

[†]These authors contributed equally to this work.

***Address Correspondence To**: Scott Earley, Ph.D.
University of Nevada, Reno School of Medicine
Manville Health Sciences Building, Room 8
MS-0318
Reno, NV, 89557-0318, USA
Phone: (775) 784-4117
Fax: (775) 784-1620
Email: searley@med.unr.edu

ABSTRACT

Neurovascular coupling (NVC), a vital physiological process that rapidly and precisely directs localized blood flow to the most active regions of the brain, is accomplished in part by the vast network of cerebral capillaries acting as a sensory web capable of detecting increases in neuronal activity and orchestrating the dilation of upstream parenchymal arterioles. Here, we report a *Col4a1* mutant mouse model of cerebral small vessel disease (cSVD) had age-dependent defects in capillary-to-arteriole dilation, functional hyperemia in the brain, and memory. The fundamental defect in aged mutant animals was the depletion of the minor membrane phospholipid phosphatidylinositol 4,5 bisphosphate (PIP_2) in brain capillary endothelial cells, leading to the loss of inwardly rectifier K^+ (Kir2.1) channel activity. Blocking phosphatidylinositol-3-kinase (PI3K), an enzyme that diminishes the bioavailability of PIP_2 by converting it to phosphatidylinositol (3,4,5)-trisphosphate (PIP_3), restored Kir2.1 channel activity, capillary-to-arteriole dilation, and functional hyperemia. In longitudinal studies, chronic PI3K inhibition also improved the memory function of aged *Col4a1* mutant mice. Our data suggest that PI3K inhibition is a viable therapeutic strategy for treating defective NVC and cognitive impairment associated with cSVD.

Graphical Abstract

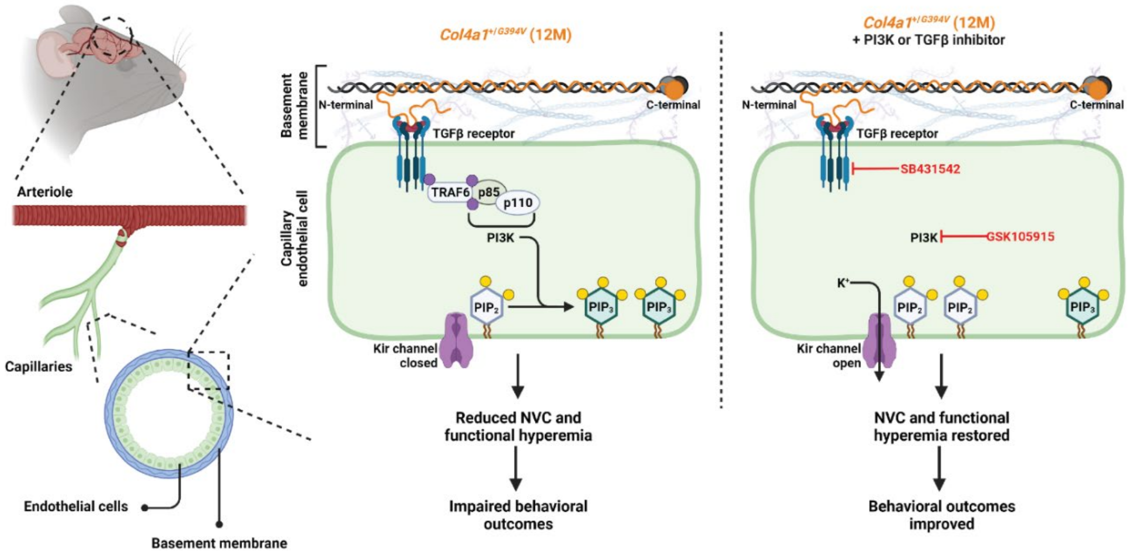

INTRODUCTION

A group of familial and idiopathic pathologies known as cerebral small vessel diseases (cSVDs) are a leading cause of vascular dementia known as vascular contributions to cognitive impairment and dementia (VCID) (255), and is second only to Alzheimer's disease as the most common cause of cognitive impairment in adults (256, 257). The global impact of cSVDs is massive and rapidly growing as the world's population ages (235), but little is currently known about the pathogenesis of the disease, and no specific treatments exist. Brain atrophy, lacunes, enlarged perivascular spaces, intracerebral hemorrhages (ICH), white matter hyperintensities, and microinfarcts detected by magnetic resonance imaging (MRI) are clinical signs of irreversible brain damage brought on by cSVDs (117). cSVDs also impair functional hyperemia, a crucial physiological process in which local blood flow is swiftly and precisely diverted to the most active brain regions (90, 258-260). Dysregulation of cerebral blood flow contributes to vascular dementia (255), but it is not known if resolution of this impairment can delay or reverse cognitive decline. Autosomal dominant mutations in the genes encoding collagen type IV alpha 1 (COL4A1) and alpha 2 (COL4A2) cause an inherited form of cSVD as part of a multisystem disorder now called Gould syndrome (196, 261-263). In this study, we used *Col4a1* mutant mice to elucidate the molecular events that disrupt functional hyperemia in this type of cSVD and applied these findings to repair the deficit.

Functional hyperemia is accomplished by a collection of physiological processes called neurovascular coupling (NVC). During NVC, active neurons trigger the dilation of upstream pial arteries and parenchymal arterioles supplying the brain, boosting blood flow to fulfill regional metabolic demands (91). The underlying mechanisms have been intensely studied for decades, and although accumulated findings support several leading hypotheses (264-266), much remains unknown. A new paradigm has emerged envisioning the vast cerebral capillary network as a sensory web capable of detecting increases in neuronal activity and orchestrating the dilation of upstream parenchymal arterioles (103). In this arrangement, substances released from nearby active neurons and/or astrocytic endfeet stimulate brain capillary endothelial cell (EC) receptors to generate retrograde propagating vasodilator signals that travel against the flow of blood and dilate upstream arterioles. Two types of ion channels present on brain capillary ECs, inward-rectifying K^+ (Kir2.1) channels, and transient receptor potential ankyrin 1 (TRPA1) cation channels, are critical sensors of neuronal activity and are necessary for NVC and functional hyperemia in the brain (103, 105). Kir2.1 channels are activated by K^+ ions released during neuronal activity and initiate rapid retrograde propagating electrical signals that ultimately dilate upstream arterioles and increase blood flow to meet neuronal demand (103, 267, 268). TRPA1 channels are activated by reactive oxygen species metabolites and stimulate propagating intercellular Ca^{2+} waves that dilate upstream arterioles (105). Capillary-to-arteriole dilation is impaired in the CADASIL (Cerebral Autosomal Dominant Arteriopathy with Sub-cortical Infarcts and Leukoencephalopathy) cSVD mouse model (164), but the impact of *Col4a1* mutations on NVC coupling is unknown.

Here, we report that Kir2.1 channel activity in ECs of cerebral arteries and brain capillaries from *Col4a1* mutant mice is lost during aging. K^+-induced capillary-to-arteriole dilation was absent in vascular preparations from 12-month (M)-old mutant animals, resulting in impaired functional hyperemia in the somatosensory cortex and memory deficits. Reduced Kir2.1 channel activity was due to diminished phosphatidylinositol 4,5 bisphosphate (PIP_2), a minor membrane phospholipid that is an essential co-factor for Kir2.1 activity (269, 270). Kir2.1 channel activity was restored by blocking phosphoinositide 3-kinase (PI3K) activity, an enzyme that converts PIP_2 to phosphatidylinositol (3,4,5)-trisphosphate (PIP_3). Capillary-to-arteriole dilation was repaired by blocking PI3K and transforming growth factor-β (TGF-β) receptors, suggesting that overactive TGF-β signaling drives PI3K in aged *Col4a1* mutant mice. Chronic treatment of mutant mice with a PI3K antagonist restored Kir2.1 channel activity and capillary-to-arteriole dilation, improved functional hyperemia, and largely resolved memory deficits. Our findings reveal a novel age-dependent mechanism of impaired NVC associated with cSVD and identify PI3K as a potential therapeutic target for treating vascular cognitive impairment and dementia.

RESULTS

Age-dependent loss of Kir2.1 channel activity and capillary-to-arteriole dilation in Col4a1$^{+/G394V}$ mice.

Mutant mice used for this study harbor a point mutation in one copy of the *Col4a1* gene that results in the substitution of valine (V) for glycine (G) at position 394 of the COL4A1 polypeptide (*Col4a1*$^{+/G394V}$) (189). Wild type littermates were used as controls for all experiments. Both male and female mice were studied, and no sex-specific differences were observed. Age is the most critical risk factor for cSVD and vascular dementia (1, 271). Therefore, we used *Col4a1*$^{+/G394V}$ and control mice at 3 and 12 M of age, representing young adulthood and middle age, respectively, throughout this study. *In vivo* susceptibility-weighted magnetic resonance imaging (SWI) was performed to identify possible brain lesions. No hypointense lesions were detected on any SWI images from 12 M-old *Col4a1*$^{+/+}$ and *Col4a1*$^{+/G394V}$ mice (Fig. 1- supplement 1A), demonstrating that this mutation does not induce magnetic resonance (MR)-detectable hemorrhagic lesions. Volumetric analysis of the T2-weighted (T2W) images showed that the ventricle/brain ratio was not significantly different between 12 M-old *Col4a1*$^{+/+}$ and *Col4a1*$^{+/G394V}$ mice (Fig. 1- supplement 1B), further demonstrating that these mutant mice do not present obvious brain damage.

Using whole-cell patch clamp electrophysiology, we first investigated how Kir2.1 currents in freshly isolated brain capillary ECs (Fig. 1A) were affected by *Col4a1*^{G394V} mutation. Kir2.1 channels were activated by increasing the [K$^+$] of the bath solution to 60 mM, and currents were recorded as voltage ramps (-100 to +40 mV) were applied. The selective Kir channel blocker $BaCl_2$ (10 μM) was used to isolate the current. Kir2.1 current densities in brain capillary ECs from young adult mice did not differ between mutant and control (Fig. 1B) but were significantly reduced in brain capillary ECs from 12 M-old *Col4a1*$^{+/G394V}$ mice compared with aged-matched control animals (Fig. 1C). We then utilized an innovative *ex vivo* cerebral microvascular preparation in which parenchymal arteriole segments with intact capillary branches were isolated from the brain, cannulated and pressurized (103, 105) to determine if loss of Kir2.1 channel activity translated into impaired capillary-to-arteriole dilation. Capillaries were stimulated by locally applying pulses (7 seconds; 10 psi) of KCl (10 mM) dissolved in artificial cerebral spinal fluid (aCSF) using a micropipette attached to a picospritzer (Fig. 1D). Focal application of K$^+$ to the capillary beds of 3 M-old *Col4a1*$^{+/+}$ and *Col4a1*$^{+/G394V}$ mice produced robust, reversible, and reproducible dilations of the upstream arterioles (Fig. 1E and F). The addition of the nitric oxide donor sodium nitroprusside (SNP) to the tissue bath maximally dilated arterioles from both groups (Fig. 1G). Similar responses were observed when tissues from 12 M-old control mice were used (Fig. 1H and I). In contrast, focal application of K$^+$ onto capillaries from 12 M-old *Col4a1*$^{+/G394V}$ mice did not dilate upstream arterioles. However, SNP produced maximal dilation, demonstrating the viability of the preparation (Fig. 1J). These results show that the age-dependent impairment of Kir2.1 current activity in brain capillary ECs from *Col4a1*$^{+/G394V}$ mice eliminates capillary-to-arteriole dilation.

We also investigated the effects of the *Col4a1* mutation on Kir2.1 channel activity in the ECs that line cerebral arteries (arteriolar ECs) (Fig. 1- supplement 2A) and found that these currents did not differ for 3 M-old mice but were blunted in 12 M-old *Col4a1*$^{+/G394V}$ animals compared to age-matched controls (Fig. 1- supplement 2B and C). Prior studies show that cerebral arteries dilate when [K$^+$] is raised from 3 mM to between 8 and 20 mM because increased Kir2.1 channel activity hyperpolarizes the membrane potential of vascular smooth muscle cells (160, 272). Higher [K$^+$] (greater than 30 mM) collapses the gradient, causing membrane depolarization and vasoconstriction. To determine the functional consequence of reduced Kir2.1 channel activity in arteriolar ECs from *Col4a1* mutants, we used standard pressure myography techniques (254) to investigate the effects of increasing [K$^+$] on vasomotor responses of isolated cerebral arteries. We found that raising the external [K$^+$] from 3 mM to a range of 8 to 20 mM dilated cerebral arteries from 12-M old control animals but had no effect on arteries from 12 M-old *Col4a1*$^{+/G394V}$ mice (Fig. 1 – supplement 2D and E). In contrast, vasoconstriction in response to higher [K$^+$] (30 and 60 mM) did not differ between 12 M-old *Col4a1*$^{+/G394V}$ and control mice (Fig. 1 – supplement 2F). These results demonstrate that age-dependent loss of Kir2.1 currents in arteriolar ECs from *Col4a1*$^{+/G394V}$ mice impairs K$^+$-induced vasodilation. In addition, our data show that fundamental voltage-dependent contractile mechanisms are not grossly affected.

Age-dependent impairment of functional hyperemia in Col4a1$^{+/G394V}$ mice.

The effects of the *Col4a1*^{G394V} mutation on brain hemodynamics *in vivo* were investigated using the thinned-skull laser Doppler flowmetry method to measure blood flow changes in the somatosensory cortex in response to stimulating whiskers for 1, 2, or 5 seconds (s) (Fig. 2A and B) (105, 273, 274). Stimulating contralateral whiskers for 1 s reproducibly increased blood flow in the somatosensory cortex of 3 M-old mice, with no differences in the amplitude, latency, or kinetics of the response between control and mutant mice (Fig. 2C to H). The magnitude of blood flow increases in response to 1 s stimulation were significantly blunted in 12 M-old *Col4a1*$^{+/G394V}$ mice compared to age-matched controls (Fig. 2I and J). In addition, the latency of the blood flow response was increased, and the rise and decay rates were diminished in 12 M-old mutant mice (Fig. 2K to N). Similar outcomes were observed for the 2 s (Fig. 2 – supplement 1), and 5 s (Fig. 2O to Z) stimulation protocols – no differences were detected in 3 M-old mice, but a blunted increases in blood flow, increased latency, and decreased rise rate and decay rate was detected for 12 M-old *Col4a1*$^{+/G394V}$ mice compared with controls. In addition, the duration of the blood flow increase was reduced in 12-M old mutant mice compared with controls in the 5 s stimulation protocol. Stimulation of ipsilateral whiskers failed to produce any change in the blood flow (Fig. 2 – supplement 2). These results demonstrate that loss of brain EC Kir2.1 channel activity and capillary-to-arteriole dilation is associated with impaired functional hyperemia in 12 M-old *Col4a1*$^{+/G394V}$ mice *in vivo*.

Age-dependent memory deficits in Col4a1*$^{+/G394V}$ *mice.

Impaired NVC is associated with deficiencies in spatial working and recognition memory (211, 275). Here, the spontaneous alternation behavioral assay was used to determine if *Col4a1*$^{+/G394V}$ mice develop memory deficits. Mice were freely allowed to explore all three arms of a Y-shaped maze for 10 minutes, and their consecutive entries into each of the arms were recorded and reported as % alternation (Fig. 3A) (276, 277). Spontaneous alternation, the maximum number of alternations, and the total distance moved did not differ between 3 M-old *Col4a1*$^{+/G394V}$ and controls (Fig. 3B to D). However, spontaneous alternation was significantly diminished for 12 M-old *Col4a1*$^{+/G394V}$ mice compared with age-matched controls (Fig. 3E), suggesting deficits in spatial working memory. The maximum alternation and total distance moved did not differ between 12 M-old mutant and control mice, indicating that impaired mobility does not account for reduced alternation (Fig. 3F and G).

A second behavioral assay, the novel arm test, was also used to evaluate recognition memory function in mutant mice. This task is driven by the innate curiosity of mice to explore previously unvisited areas (278, 279). Initially, mice were allowed to explore a Y-maze for 10 minutes with one arm of the maze blocked. After 24 hours, the mice were allowed to explore the maze for 10 minutes with all arms open (Figure 3H). Mice with normal recognition memory spend more time exploring the novel arm than those explored on the previous day. The dwell time and the number of entries in the novel arm did not differ between 3 M-old *Col4a1*$^{+/G394V}$ and control mice (Figure 3I to K). In contrast, 12 M-old *Col4a1*$^{+/G394V}$ mice spent significantly less time and had fewer entries into the novel arm compared with age-matched controls (Figure 3L to N). These data provide further evidence of age-dependent memory deficits in *Col4a1*$^{+/G394V}$ mice.

PIP$_2$ depletion reduces Kir2.1 currents in 12 M-old Col4a1$^{+/G394V}$ mice.

Kir2.1 channels require PIP$_2$ for activity (269, 270), and prior studies reported that pathogenic loss of PIP$_2$ diminished Kir2.1 channel activity in brain capillary ECs from CADASIL cSVD mice and 5xFAD familial Alzheimer’s disease mice (164, 167).

Therefore, we investigated the possibility that PIP_2 depletion also reduces Kir2.1 current density in ECs from 12 M-old *Col4a1*$^{+/G394V}$ mice. When exogenous diC8-PIP_2 (10 μM) was included in the intracellular solution during whole-cell patch-clamp experiments, Kir2.1 current density in arteriolar ECs (Fig. 4A) and brain capillary EC (Fig. 4B) did not differ between 12 M-old control and age-matched *Col4a1*$^{+/G394V}$ mice, suggesting that PIP_2 depletion is responsible for Kir2.1 current deficiencies in the mutant mice. The steady-state amount of PIP_2 present in the inner leaflet of the plasma membrane is determined by the relative rates of PIP_2 synthesis and degradation. PIP_2 is synthesized by the sequential action of phosphatidylinositol 4-kinase (PI4K), an enzyme that converts phosphatidylinositol (PI) to phosphatidylinositol 4-phosphate (PIP), and phosphatidylinositol 4-phosphate 5-kinase (PIP5K), which converts PIP to PIP_2. PI4K and PIP5K activity require high levels of ATP (i.e., the K_M of PI4K for ATP is ~0.4 to 1 mM) (Fig. 4 – supplement 1A) (280-282). PIP_2 deficiency in capillary ECs from CADASIL mice was attributed to reduced ATP levels and diminished synthesis (164). We measured ATP in isolated brain capillaries using a luciferase-based assay and found that ATP levels did not differ between 12 M-old *Col4a1*$^{+/G394V}$ and control mice (Fig. 4 – supplement 1B), suggesting that PIP_2 synthesis is not impaired by lack of ATP in *Col4a1* mutants. Hydrolysis of PIP_2 by phospholipase C (PLC) to form inositol trisphosphate (IP_3) and diacylglycerol (DAG) diminishes steady-state PIP_2 levels (Fig. 4 – supplement 1C) (283). However, blocking PLC activity with U73122 (10 μM) did not restore Kir2.1 currents in capillary ECs from 12 M-old *Col4a1*$^{+/G394V}$ mice, suggesting that PIP_2 depletion does not result from elevated levels of PLC activity (Fig. 4 – supplement 1D). PIP_2 bioavailability is reduced when the enzyme phosphatidylinositol-4, 5-bisphosphate 3-kinase (PI3K) phosphorylates it to PIP_3 (Fig. 4C). When PI3K was blocked using the selective inhibitor GSK1059615 (10 nM), Kir2.1 currents in capillary ECs from 12 M-old

Col4a1$^{+/G394V}$ mice were restored to control levels (Fig. 4D), suggesting that PIP_2 depletion in mutant mice results from elevated PI3K activity.

To determine if elevated PI3K activity is also responsible for cerebral microvascular dysfunction in mutant mice, capillary-to-arteriole dilation was assessed before and after treatment with GSK1059615 (10 nM, 30 min). This treatment had no effect on preparations from 12 M-old control animals (Fig. 4E and F). In contrast, PI3K block fully restored K^+-induced dilation of upstream arterioles from 12 M-old *Col4a1*$^{+/G394V}$ mice (Figure 4G and H). These data suggest that elevated PI3K activity is responsible for the loss of capillary-mediated dilation in *Col4a1* mutant mice.

Blocking TGF-β receptors restores capillary-to-arteriole dilation in Col4a1$^{+/G394V}$ *mice.*

We next investigated the drivers of PI3K activity in *Col4a1* mutants. Activation of TGF-β receptors can stimulate PI3K activity through a non-canonical signaling pathway involving the TRAF6 ubiquitin ligase (284, 285). Elevated TGF-β signaling contributes to pathology in other *Col4a1* mutant mouse models (197, 286). To test if increased TGF-β signaling disrupts NVC, we measured capillary-to-arteriole dilation before and after treatment with the selective TGF-β receptor blocker SB431542 (1 μM, 30 min). This treatment had no effect on tissue from control mice (Fig. 5A and B), but blockade of TGF-β receptors fully restored capillary-to-arteriole dilation in preparations from 12 M-old *Col4a1*$^{+/G394V}$ mice (Fig. 5C and D). In control studies, we found that the vehicle for GSK1059615 and SB431542 (0.01% v/v DMSO) did not affect capillary-to-arteriole dilation (Fig. 5 – supplement 1) or maximal vasodilation in response to SNP (Fig. 5 –

supplement 2). These data suggest that hyperactive TGF-β signaling drives PI3K activity in *Col4a1* mutants to disrupt cerebral microvascular function.

Chronic PI3K inhibition restores Kir2.1 currents, K^+-induced dilation, functional hyperemia, and memory deficits in 12 M-old Col4a1$^{+/G394V}$ mice.

To determine if chronic inhibition of PI3K could resolve deficits in functional hyperemia and memory in mutant mice, 12 M-old *Col4a1*$^{+/G394V}$ and control mice were injected subcutaneously with GSK1059615 (10 mg/kg) or vehicle each day for 28 days (Figure 6A). At the end of the treatment, we found that Kir2.1 currents in brain capillary ECs from *Col4a1*$^{+/G394V}$ mice injected with GSK1059615 were fully restored to control levels, whereas vehicle treatment had no effect (Fig. 6B). GSK1059615 treatment fully restored capillary-to-arteriole dilation in *ex vivo* microvascular preparations from *Col4a1*$^{+/G394V}$ mice (Fig. 6C and D). These data demonstrate that defects in brain capillary EC Kir2.1 channel function and associated microvascular vasomotor dysfunction can be restored by chronic PI3K blockade.

GSK1059615 treatment also increased the magnitude of blood flow increases in the somatosensory cortex induced whisker stimulation (1 s) in *Col4a1*$^{+/G394V}$ mice compared to vehicle-treated animals (Fig. 6E and F). The latency and rise rates of the blood flow response were also improved (Fig. 6G to J). Similar outcomes were observed for 2 s and 5 s stimulation protocols (Fig. 6 – supplement 1). In control studies, stimulation of ipsilateral whiskers failed to produce any change in the blood flow (Fig. 6 – supplement 2). These data demonstrate that chronic PI3K inhibition can restore functional hyperemia in *Col4a1*$^{+/G394V}$ mice.

In a longitudinal study, we found that GSK1059615 treatment significantly improved the Y-maze spontaneous alternation behavior of 12 M-old *Col4a1*$^{+/G394V,}$

whereas vehicle-treated mutant mice did not improve. The performance of GSK1059615-treated *Col4a1*$^{+/G394V}$ mice did not differ from that of age-matched control animals (Fig. 6K). Interestingly, GSK1059615 treatment reduced the maximum number of alternations (Fig. 6L) and the total distance moved (Fig. 6M) for control and mutant mice. This unexpected side effect of prolonged GSK1059615 administration may be related to fatigue symptoms reported by cancer patients treated with PI3K inhibitors (287). Despite this potential limitation, our data identify PI3K inhibition as a novel therapeutic strategy for treating cognitive impairment associated with some forms of cSVD.

DISCUSSION

Brain injuries and loss of fundamental blood flow control mechanisms due to cSVDs are significant causes of adult dementia. The brain pathology of *Col4a1*$^{+/G394V}$ cSVD mice used in this investigation was mild compared to other models, but NVC and functional hyperemia were significantly impaired. Thus, these animals allow the effects of impaired vascular control to be investigated independently of severe brain damage. Aged mutants performed worse than control mice in behavioral tests of working and recognition memory, suggesting that defects in cerebral blood flow control mechanisms are a primary cause of cognitive impairment in these animals. The fundamental defect leading to impaired NVC was the loss of Kir2.1 channel activity in brain capillary and arterial ECs due to PIP_2 depletion. Accordingly, chronic PI3K blockade rescued Kir2.1 currents, NVC, functional hyperemia, and improved memory function in mutant mice, providing evidence that cognitive impairment associated with cSVD can be resolved by improving blood flow regulation in the brain.

Missense mutations in *COL4A1* and *COL4A2* that alter G residues in collagen triple helices are the most common cause of Gould syndrome (210, 238, 239). Such mutations prevent the proper assembly of collagen chains, potentially leading to intracellular retention, ER stress, and disrupting basement membranes to cause cSVD and other pathologies (185). The impact of specific disease-causing point mutations is highly variable and position dependent. Notably, spontaneous ICH is less severe for mutations nearer to the amino terminus, such as the *Col4a1*^{G394V} mutation, and more severe for mutations closer to the carboxyl terminus (195, 236). Consistent with this finding, *Col4a1*$^{+/G394V}$ mice did not show overt cerebral pathology in MRI scans, however capillary-mediated NVC and functional hyperemia were impaired in an age-dependent manner. The age dependence of this pathology may be related to the unique properties of collagen. Collagens are extraordinarily durable - the *in vivo* half-life of collagen I, present in ligaments and tendons, is more than 100 years (288). The turnover rate of the [α1α1α2(IV)] collagen IV protomer is not precisely known, but an early study reported that the half-life of “vascular collagen” in rat aorta and mesenteric arteries was ~70 days (289). Further, collagen synthesis peaks during later embryonic development and growth as basement membranes form and then markedly decreases with age (290, 291). Our data suggest that *Col4a1*$^{+/G394V}$ mice successfully develop and maintain functional basement membranes early in life when collagen production is maximal. We propose that diminishing collagen production and increasing degradation during aging result in a slow degradation of basement membranes over time, eventually leading to defects by middle age. It is conceivable that a similar process could contribute to idiopathic forms of age-related cSVD in humans.

Impaired function of basement membranes underlies several diseases associated with excessive TGF-β signaling. TGF-β is initially synthesized and processed in an inactive form and exported as large latent complexes that covalently bind to the ECM and basement membranes (292-294). Inappropriate release of the TGF-β ligand from these repressing complexes has significant pathological consequences. For example, disinhibition of TGF-β signaling causes CARASIL (cerebral autosomal recessive arteriopathy with subcortical infarcts and leukoencephalopathy), a rare genetic form of cSVD (169). Excessive activation of TGF-β signaling due to ECM disruptions causes Marfan syndrome (MFS) and Loeys-Dietz syndrome (LDS), multisystem genetic diseases that cause many problems, including mitral valve prolapse and aortic aneurysms (295-297). Genetic knockdown of TGF-β receptors and TGF-β-targeting antibodies improves ocular pathogenesis and reduces ICH of *Col4a1*$^{+/\Delta ex41}$ and *Col4a1*$^{+/G1344D}$ mice, suggesting that *Col4a1* mutations increase TGF-β signaling (197, 286). Our findings suggest that elevated TGF-β receptor activity is also responsible for the loss of capillary-to-arteriole dilation in 12 M-old *Col4a1*$^{+/G394V}$ mice. Although our data do not directly show how the *Col4a1*$^{+/G394V}$ mutation elevates TGF-β signaling, the amino acid substitution occurs immediately adjacent to a putative integrin-binding domain (199). Collagen binding integrins have been shown to recruit TCPTP phosphatase that suppress TGF-β signaling by dephosphorylating TGF-β receptors (34, 298), suggesting that elevated TGF-β activity in *Col4a1*$^{+/G394V}$ mutant mice may be caused by compromised integrin-mediated signaling. Blockade of TGF-β signaling is a potential therapeutic approach for treating this form of cSVD and related sporadic forms, but clinical trials of TGF-β receptor inhibitors have so far been disappointing (299).

Altered PIP_2 metabolism has emerged as a central pathogenic mechanism in multiple forms of cerebral microvascular disease. Prior reports show that PIP_2 insufficiency diminishes Kir2.1 channel activity in brain capillary ECs in mouse models of CADASIL cSVD (164) and familial Alzheimer's disease (167). The current data show that the same defect underlies impaired functional hyperemia and memory deficits in *Col4a1*$^{+/G394V}$ mutant mice. The prior studies provide evidence that reduced levels of ATP in brain capillary ECs diminished the production of PIP_2 (164), whereas our findings indicate that increased activity of PI3K decreased PIP_2 bioavailability in *Col4a1*$^{+/G394V}$ mice. Our data suggest that PI3K activity in this model is driven by a signaling pathway downstream of TGF-β receptors (251). We also show that PIP_2 levels and Kir2.1 channel activity are diminished in cerebral arteriolar ECs from 12 M-old *Col4a1* mutant mice. In contrast, these cells are unaffected in CADASIL and 5xFAD animals, demonstrating cellular heterogeneity of PIP_2 depletion mechanisms among the different disease models. Despite these differences, we propose that repairing defective NVC by increasing PIP_2 levels in brain capillary ECs is a viable therapeutic strategy for multiple forms of cerebrovascular disease. We provide proof-of-concept by targeting the PI3K pathway to preserve PIP_2, thereby restoring functional hyperemia and improving memory function in *Col4a1* mutant mice. Several types of PI3K inhibitors are approved by the FDA for use against advanced cancers (287) and could rapidly advance to clinical trials for the treatment of cSVDs.

MATERIALS AND METHODS

Chemical and reagents

Chemicals and other reagents were obtained from Sigma-Aldrich, Inc. (St. Louis, MO, USA) unless otherwise specified.

Animals

Young adult (3 M-old) and middle-aged (12 M-old) male and female littermate *Col4a1*$^{+/+}$ and *Col4a1*$^{+/G394V}$ mice were used in this study. Animals were maintained in individually ventilated cages (<5 mice/cage) with *ad libitum* access to food and water in a room with controlled 12-hour light and dark cycles. All animal care procedures and experimental protocols involving animals complied with the NIH *Guide for the Care and Use of Laboratory Animals* and were approved by the Institutional Animal Care and Use Committees at the University of Nevada, Reno, and the University of California, San Francisco. Arteries for *ex vivo* experimentation were harvested from mice anesthetized with isoflurane (Baxter Healthcare, Deerfield, IL, USA) and euthanized by decapitation and exsanguination. Brains were isolated and placed in ice-cold Ca^{2+}-free physiological saline solution (Mg-PSS; 134 mM NaCl, 5 mM KCl, 2 mM $MgCl_2$, 10 mM HEPES, 10 mM glucose, 0.5% bovine serum albumin, pH 7.4 with NaOH).

In vivo magnetic resonance imaging

All *in vivo* magnetic resonance (MR) experiments were conducted on a 14.1 Tesla vertical MR system (Agilent Technologies, Palo-Alto, CA, USA) equipped with 100G/cm gradients and a single tuned millipede ^{1}H proton coil (ØI = 40mm). For each imaging session, mice were anesthetized using isoflurane (1-1.5% in O2) and positioned in a dedicated cradle maintaining constant anesthesia and placed in the MR bore; respiration and temperature were continuously monitored during all acquisitions to ensure animal well-being and data reproducibility. Susceptibility Weighted Imaging (SWI) was performed to detect the potential presence of hemorrhagic lesions, using the following parameters: gradient-echo scheme, field of view (FOV) = 20 x 20 mm^2, matrix = 256 x 256, 16 slices, 0.4 mm slice thickness, 0.1 mm interslice gap, number of averages = 16, echo time (TE)/ repetition time (TR) = 4.60 / 140 ms, flip angle = 10 degrees. T2-weighted (T2W) images were also acquired in a fast-spin-echo scheme to calculate brain and ventricle volumes, using the same FOV geometry as SWI and the following parameters: number of averages = 8, TE/TR = 21.38 / 2500 ms, flip angle = 90 degrees. For each animal, total brain and ventricles were manually delineated on the T2W images, their volumes calculated, and the ventricle/brain ratio computed.

Isolation of native brain capillary ECs

Individual brain capillary ECs were obtained as previously described (103, 105). Brains were denuded of surface vessels, and two 1 mm-thick were excised and homogenized in artificial cerebrospinal fluid (aCSF; 124 mM NaCl, 3 mM KCl, 2 mM $MgCl_2$, 2 mM $CaCl_2$, 1.25 mM NaH_2PO_4, 26 mM $NaHCO_3$, and 4 mM glucose) using a Dounce homogenizer. The homogenate was filtered through a 70 µM filter, and capillary networks captured on the filter were transferred to a new tube. Individual cells were isolated by enzymatic digestion with 0.5 mg/ml neutral protease and 0.5 mg/ml elastase (Worthington Biochemical Corporation) in endothelial cell (EC) isolation solution (55 mM NaCl, 80 mM Na-glutamate, 6 mM KCl, 2 mM $MgCl_2$, 10 mM glucose, 0.1 mM $CaCl_2$,10 mM HEPES, pH 7.3) for 45 min at 37°C. Following this, 0.5 mg/ml collagenase type I (Worthington Biochemical Corporation) was added, and a second 2-min incubation at 37°C was performed. Digested networks were washed in ice-cold EC isolation solution, then triturated with a fire-polished glass Pasteur pipette to produce individual ECs. All cells used for this study were freshly dissociated on the day of experimentation.

Isolation of cerebral arteriolar ECs

Single arterial ECs were isolated as previously described (103). Cerebral arteries were dissected from mouse brains and washed in Mg-PSS. Arteries were transferred to EC isolation solution supplemented with 0.5 mg/mL neutral protease and 0.5 mg/mL elastase (Worthington Biochemical Corporation, Lakewood, NJ, USA), and incubated for 40 min at 37°C. Following this, 0.5 mg/mL collagenase type I (Worthington Biochemical Corporation) was added for an additional 2 min incubation at 37°C. A single-cell suspension was prepared by washing digested arteries three times with EC isolation solution to remove enzymes and triturating with a fire-polished glass pipette to dissociate cells. All cells used for this study were freshly dissociated on the day of experimentation.

Whole-cell patch-clamp electrophysiology

Enzymatically isolated native ECs were transferred to a recording chamber (Warner Instruments, Hamden, CT, USA) and allowed to adhere to glass coverslips for 15 minutes at room temperature. Pipettes were fabricated from borosilicate glass (1.5 mm outer diameter, 1.17 mm inner diameter; Sutter Instruments, Novato, CA, USA), fire-polished to yield a tip resistance of 3–6 MΩ. Currents were recorded at room temperature using an Axopatch 200B amplifier (Molecular Devices, San Jose, CA, USA) equipped with an Axon CV 203BU headstage and Digidata 1440A digitizer (Molecular Devices) for all patch-clamp electrophysiology experiments. Currents were filtered at 1 kHz and digitized at 10 kHz. Kir2.1 currents were recorded using the conventional whole-cell configuration at a holding potential of -50 mV, with 400 ms ramps from -100 to +40 mV. The external bathing solution was composed of 134 mM NaCl, 6 mM KCl, 1 mM $MgCl_2$, 2 mM $CaCl_2$, 10 mM glucose, and 10 mM HEPES. The composition of the pipette solution was 10 mM NaCl, 30 mM KCl, 10 mM HEPES, 110 mM K^+ aspartate, and 1 mM $MgCl_2$ (pH 7.2). Kir2.1 currents were activated by increasing extracellular [K^+] concentration from 6 to 60 mM ([NaCl] adjusted to maintain isotonic solution) and blocked using $BaCl_2$ (10 μM). All recordings were performed at room temperature. Clampex and Clampfit software (pClamp version 10.2; Molecular Devices) were used for data acquisition and analysis, respectively.

Pressure myography

The current best practices guidelines for pressure myography experiments were followed (254). Pressure myograph experiments were performed on cerebral arteries and parenchymal arteriole-capillary preparations (105).

Surface cerebral arteries were carefully isolated and mounted between two glass cannulas (approximate outer diameter 40–50 μm) in a pressure myograph chamber (Living Systems Instrumentation, St Albans City, VT, USA) and secured by a nylon thread. Intraluminal pressure was controlled using a servo-controlled peristaltic pump (Living Systems Instrumentation), and preparations were visualized with an inverted microscope (Accu-Scope Inc., Commack, NY, USA) coupled to a USB camera (The Imaging Source LLC, Charlotte, NC, USA). Changes in luminal diameter were assessed using IonWizard software (version 7.2.7.138; IonOptix LLC, Westwood, MA, USA). Arteries were bathed in warmed (37°C), oxygenated (21% O_2, 6% CO_2, 73% N_2) PSS (119 mM NaCl, 4.7 mM KCl, 21 mM $NaHCO_3$, 1.17 mM $MgSO_4$, 1.8 mM $CaCl_2$, 1.18 mM KH_2PO_4, 5 mM glucose, 0.03 mM EDTA) at an intraluminal pressure of 5 mmHg. Following equilibration for 15 min, intraluminal pressure was increased to 110 mmHg, and vessels were stretched to their approximate *in vivo* length, after which pressure was reduced back to 5 mmHg for an additional 15 min. Vessel viability was assessed for each preparation by evaluating vasoconstrictor responses to high extracellular [K^+] PSS, made isotonic by adjusting the [NaCl] (60 mM KCl, 63.7 mM NaCl). Arteries that showed less than 10% constriction in response to elevated extracellular [K^+] were excluded from further investigation. Changes in lumen diameter were recorded at different concentrations of extracellular [K^+] (8 to 60 mM, [NaCl] adjusted to maintain isotonic solution). Arteries were pressurized to 20 mmHg and superfused with 10 nM endothelin-1 to induce vasoconstriction. Passive lumen diameter was determined by superfusing vessels Ca^{2+}-free PSS supplemented with EGTA (2 mM) and the voltage-dependent Ca^{2+} channel blocker diltiazem (10 μM) to inhibit SMC contraction. Change in diameter was calculated at each [K^+] concentration as the change in diameter (%) = (change in lumen diameter / passive diameter) × 100.

Parenchymal arterioles with intact capillary segments deriving from the middle cerebral artery were carefully dissected, cannulated, and secured onto a pressure myograph chamber using the same method described above (105). Preparations were bathed in a warmed, oxygenated aCSF solution at an intraluminal pressure of 5 mmHg. Following equilibration for 15 min, intraluminal pressure was increased to 20 mmHg and superfused with 10 nM endothelin-1 to induce vasoconstriction. Localized application of drugs onto the capillary extremities was achieved by placing a micropipette attached to a Picospritzer III (Parker Hannifin, Cleveland, OH, USA) adjacent to capillary segments. Capillaries were stimulated by locally applying a 7 s pulse of aCSF containing elevated [K^+] (10 mM, [NaCl] adjusted to maintain isotonic solution) onto capillary extremities. To determine preparation viability, SNP (10 μM) was superfused into the circulating aCSF.

Changes in lumen diameter were calculated as vasodilation (%) = (change in lumen diameter / baseline diameter) × 100.

Assessment of functional hyperemia in the brain using laser Doppler flowmetry

Functional hyperemia in the brain was assessed essentially as previously described (105). Mice were anesthetized with isoflurane (5% induction, 2% maintenance), the head was immobilized in a stereotaxic frame, and the skull was exposed. The skull of the right hemisphere was carefully thinned using a drill to visualize the surface vasculature of the somatosensory cortex. Isoflurane anesthesia was replaced with combined α-chloralose (50 mg/kg, i.p.) and urethane (750 mg/kg, i.p.) to eliminate confounding vasodilatory effects of isoflurane. Changes in perfusion were assessed via a laser-Doppler flowmetry probe (PeriFlux System PF5000, Perimed AB, Jakobsberg, Sweden) positioned directly above the somatosensory cortex. The contralateral whiskers were stimulated for either 1, 2, or 5 s, and changes in perfusion were recorded. Contralateral whiskers were stimulated three times at 2 min intervals. Ipsilateral whiskers were also stimulated as a control for potential vibration artifacts. Changes in perfusion were calculated as %Δ Blood flow = (perfusion during stimulus / baseline perfusion) × 100. Kinetics of the response, including latency, duration, rise rate, and decay rate, were also obtained and analyzed.

Y-Maze behavioral assay

Memory function was assessed using the Y-maze (Maze Engineers, Skokie, IL, USA) using two different configurations.

The spontaneous alternation behavioral assay was used to assess short-term spatial working memory (211). Mice were placed into one of the three arms of the maze (start arm) and were allowed to explore all three arms for 10 minutes. Session videos were recorded and analyzed using Ethovision XT software (version 16.0.1536, Noldus Information Technology, Leesburg, VA, USA). Spontaneous alternation was evaluated by scoring the order of entries into each arm during the 10-minute recording period. Spontaneous alternation was calculated as alternation index (%) = (number of spontaneous alternations/max alternation) × 100, where the spontaneous alternation is defined as the number of consecutive entries into each arm of the maze in any order without any repeats, and the max alternation is the total number of alternations possible (max alternation = total number of arm entries – 2).

The novel arm configuration was used to evaluate longer-term spatial reference memory (211). This test was performed across 2 days. On day one, mice were placed into one of the three arms of the maze (start arm) and allowed to explore only two arms for 10 minutes (training trial). On day two, the test trial was conducted with the closed arm opened, which served as the novel arm. Mice were returned to the maze via the same start arm and were allowed to explore all three arms for 10 minutes. Session videos were recorded and analyzed using Ethovision XT software, and the time spent in the novel arm and entries into the novel arm were measured and analyzed.

Measurement of [ATP] in brain capillary ECs

The intracellular [ATP] was determined by lysing brain capillary ECs and quantifying luminescence produced by luciferase-induced conversion of ATP to light using the CellTiter-Glo Assay 3D (Promega, Madison, WI, USA). Approximately ~500 ECs were added to each reaction. To further ensure equal input of ECs, the CellTiter-Glo 3D Assay was multiplexed with CellTox Green Assay (Promega), a fluorescent dye that selectively and quantitatively binds double-stranded DNA. Dye fluorescence is directly proportional to DNA concentration and the number of cells in each assay. ATP concentration (luminescence) was normalized to the number of cells (fluorescence) to determine intracellular ATP per cell. Luminescence and fluorescence ($485_{Ex}/538_{Em}$) were measured using a FlexStation 3 (Molecular Devices). A serial tenfold dilution of ATP (1 nM to 1 uM; 80 µl contains 8^{-14} to 8^{-11} moles of ATP, respectively) was measured to calibrate the linear working range of ATP detection. Data were expressed as the ratio of ATP luminescence/DNA fluorescence.

Statistical analysis

All summary data are presented as means ± SEM. Statistical analyses and graphical presentations were performed using GraphPad Prism software (version 9.4.1, GraphPad Software, Inc, USA). The value of n refers to the number of cells for patch-clamp electrophysiology experiments and measurement of [ATP], vessel preparations for myography experiments, and animals used for MRI acquisition, the Y-maze behavioral assays and functional hyperemia assessment. Statistical analyses were performed using Student's paired or unpaired two-tailed t-test, or repeated measures or non-repeated measures two-way analysis of variance (ANOVA) with a Šidák correction for multiple comparisons. A value of $p<0.05$ was considered statistically significant.

Funding

This study was supported by grants from the National Institutes of Health (NHLBI R35155008 and NIGMS P20GM130459 to S.E.; NINDS R01NS096173 to D.B.G.; and NINDS RF1NS110044 and R33NS115132 to D.B.G and S.E.). The Transgenic Genotyping and Phenotyping Core and the High Spatial and Temporal Resolution Imaging Core at the COBRE Center for Molecular and Cellular Signaling in the Cardiovascular System, University of Nevada, Reno are maintained by grants from NIH/NIGMS (P20GM130459 Sub#5451 and P20GM130459 Sub#5452). The University of California, San Francisco Department of Ophthalmology is supported by a Vision Core grant NEI P30EY002162 and an unrestricted grant from Research to Prevent Blindness, New York, NY.

Author contributions

S.E. and D.B.G. initiated and supervised the project. S.E. designed the experiments. X.G. and M.M.C. performed *in vivo* MRI experiments. S.A., E.Y., and A.S.S. performed patch-clamp electrophysiology experiments. E.Y. and P.T. performed myography experiments. P.T. conducted *in vivo* functional hyperemia experiments and performed Y-maze behavioral tests. E.Y. conducted luciferase assay for the measurement of the cellular level of ATP. P.T., E.Y., S.A., and S.E. analyzed the data. P.T. and S.E. wrote the manuscript and prepared the figures. P.T., E.Y., C.L.D., D.B.G., and S.E. revised the manuscript.

Competing interests

The authors declare that they have no competing interests.

Data and materials availability

All data needed to evaluate the conclusions are present in the paper or the Supplementary Materials.

FIGURES

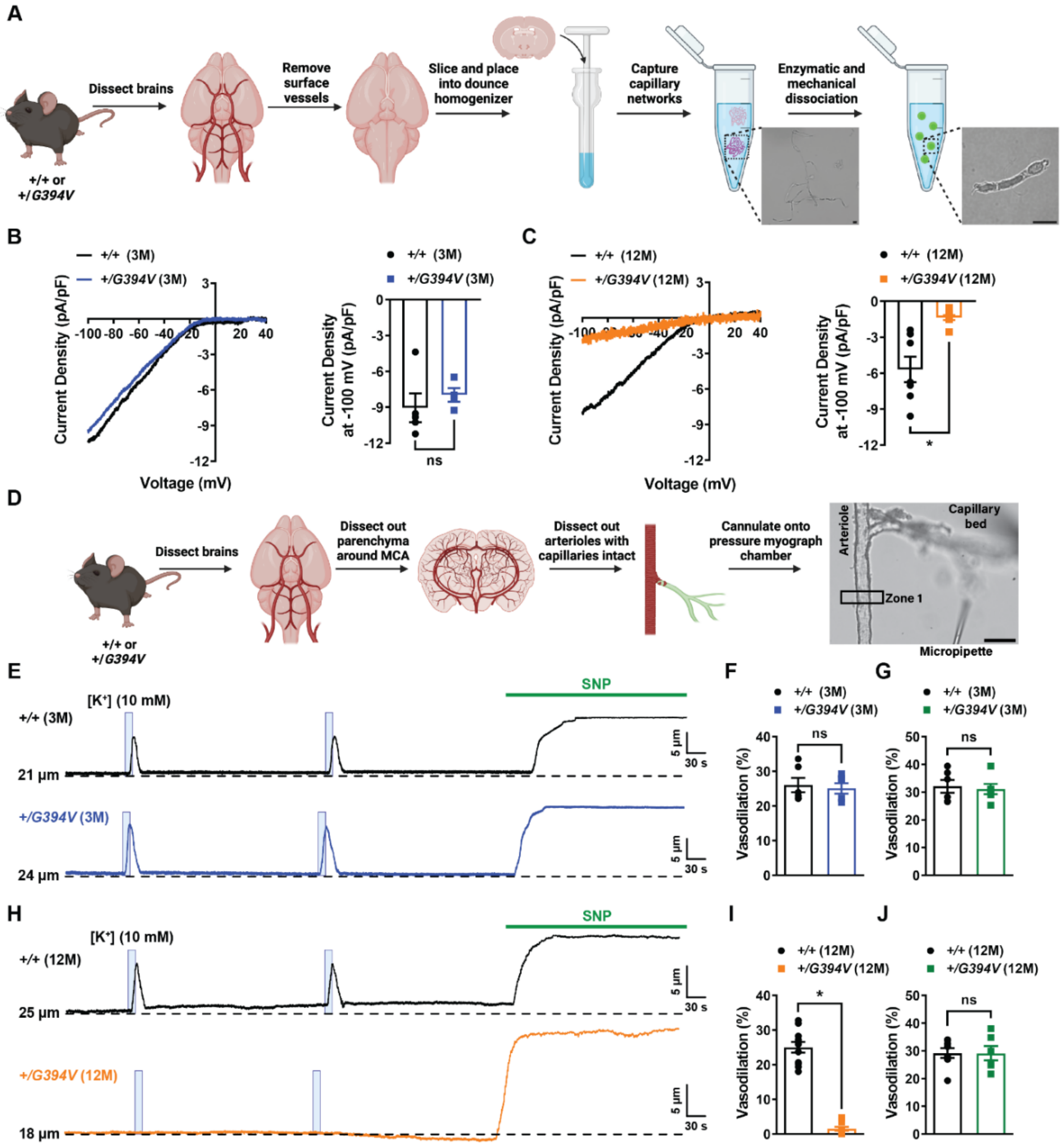

Figure 1. Age-dependent loss of Kir2.1 channel activity and capillary-to-arteriole dilation in Col4a1$^{+/G394V}$ mice. (A) Illustration of the brain capillary EC isolation procedure. Scale bar = 10 µm. (B) Representative I-V traces and summary data showing Kir2.1 current densities in freshly isolated capillary ECs from 3 M-old *Col4a1*$^{+/+}$ and *Col4a1*$^{+/G394V}$ mice (n = 4–5 cells from 4 to 5 animals per group, ns = not significant, unpaired t-test). (C) Representative I-V traces and summary data showing Kir2.1 current densities in freshly isolated capillary ECs from 12 M-old *Col4a1*$^{+/+}$ and *Col4a1*$^{+/G394V}$ mice (n = 7–8 cells from 4 animals per group; *p<0.05, unpaired t-test). (D) Illustration of the microvascular preparation. Parenchymal arterioles with intact capillaries were carefully dissected and cannulated onto a pressure myograph chamber, and compounds of

interest were focally applied to capillary extremities. Scale bar = 50 µm. (E and F) Representative traces (E) and summary data (F) showing K^+ (10 mM, blue box)-induced dilation of upstream arterioles in preparations from 3 M-old *Col4a1*$^{+/+}$ and *Col4a1*$^{+/G394V}$ mice (n = 6 preparations from 3 animals per group, ns = not significant, unpaired t-test). (G) The dilation produced by superfusing SNP (10 µM) in preparations from 3 M-old *Col4a1*$^{+/+}$ and *Col4a1*$^{+/G394V}$ mice (n = 6 preparations from 3 animals per group, ns = not significant, unpaired t-test). (H and I) Representative traces (H) and summary data (I) showing K^+ (10 mM, blue box)-induced dilation of upstream arterioles in preparations from 12 M-old *Col4a1*$^{+/+}$ and *Col4a1*$^{+/G394V}$ mice (n = 11 preparations from 6 to 7 animals per group, *$p<0.05$, unpaired t-test). (J) The dilation produced by superfusing SNP (10 µM) in preparations from 12 M-old *Col4a1*$^{+/+}$ and *Col4a1*$^{+/G394V}$ mice (n = 6–8 preparations from 3 to 5 animals per group, ns = not significant, unpaired t-test).

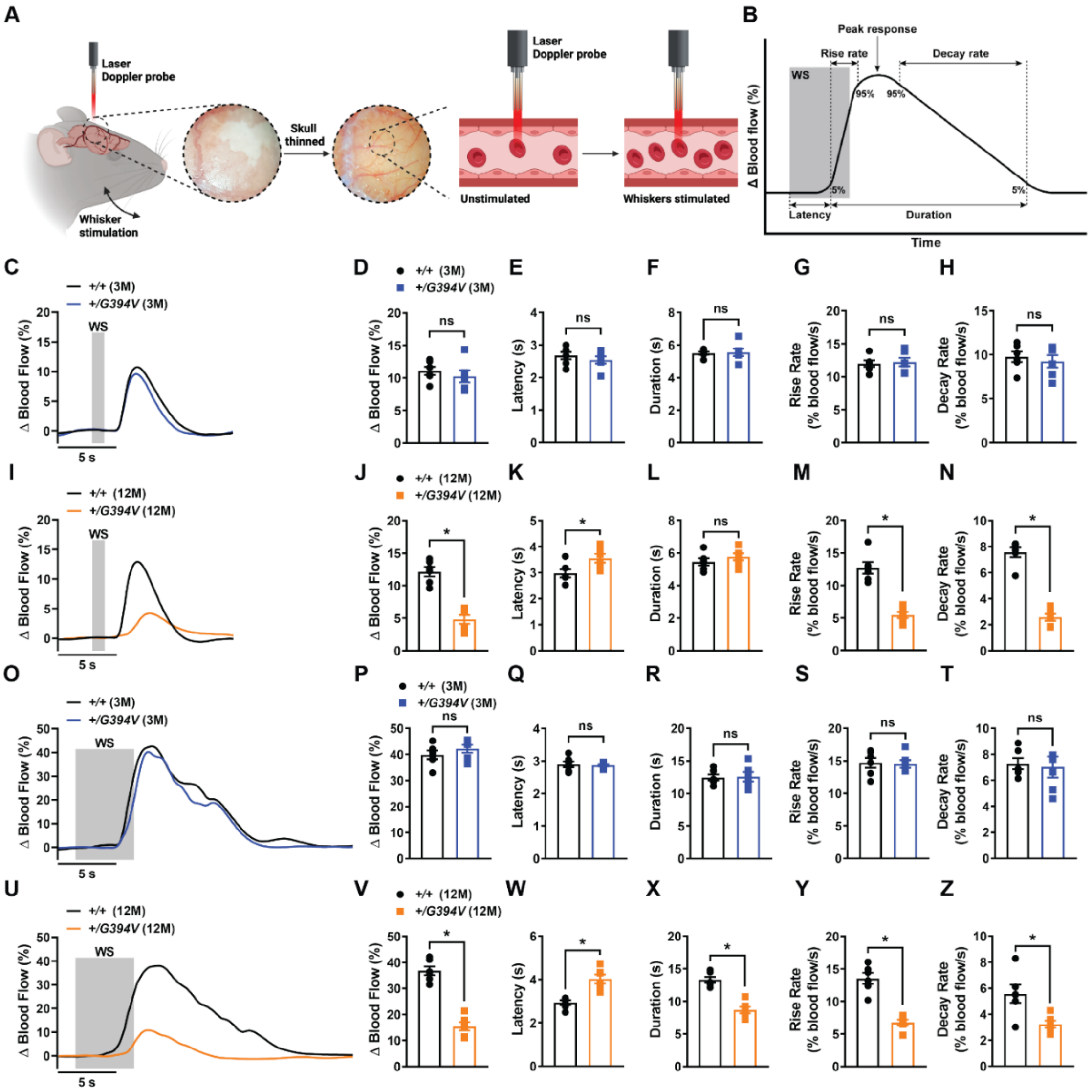

Figure 2. Age-dependent impairment of functional hyperemia in Col4a1$^{+/G394V}$ mice. (A) Illustration demonstrating the functional hyperemia assessment procedure in the mouse somatosensory cortex. (B) Illustration demonstrating the parameters that were analyzed. (C and D) Representative traces (C) and summary data (D) showing the increase in blood flow following 1 s contralateral whisker stimulation (WS) in 3 M-old *Col4a1*$^{+/+}$ and *Col4a1*$^{+/G394V}$ mice (n = 6 animals per group, ns = not significant, unpaired t-test). (E to H) Latency (E), duration (F), rise rate (G), and decay rate (H) were also analyzed (n= 6 animals per group, ns = not significant, unpaired t-test). (I and J) Representative traces (I) and summary data (J) showing the increase in blood flow following 1 s contralateral WS in 12 M-old *Col4a1*$^{+/+}$ and *Col4a1*$^{+/G394V}$ mice (n = 6 animals per group, *p<0.05, unpaired t-test). (K to N) Latency (K), duration (L), rise rate (M), and decay rate (N) were also analyzed (n = 6 animals per group, *p<0.05, ns = not significant, unpaired t-test). (O and P) Representative traces (O) and summary data (P) showing the increase in blood flow following 5 s contralateral WS in 3 M-old *Col4a1*$^{+/+}$ and *Col4a1*$^{+/G394V}$ mice (n = 6 animals per group, ns = not significant, unpaired t-test). (Q to T) Latency (Q), duration (R), rise rate (S), and decay rate (T) were also analyzed (n=

6 animals per group, ns = not significant, unpaired t-test). (U and V) Representative traces (U) and summary data (V) showing the increase in blood flow following 5 s contralateral WS in 12 M-old *Col4a1*$^{+/+}$ and *Col4a1*$^{+/G394V}$ mice (n = 6 animals per group, *p<0.05, unpaired t-test). (W to Z) Latency (W), duration (X), rise rate (Y), and decay rate (Z) were also analyzed (n = 6 animals per group, *p<0.05, unpaired t-test).

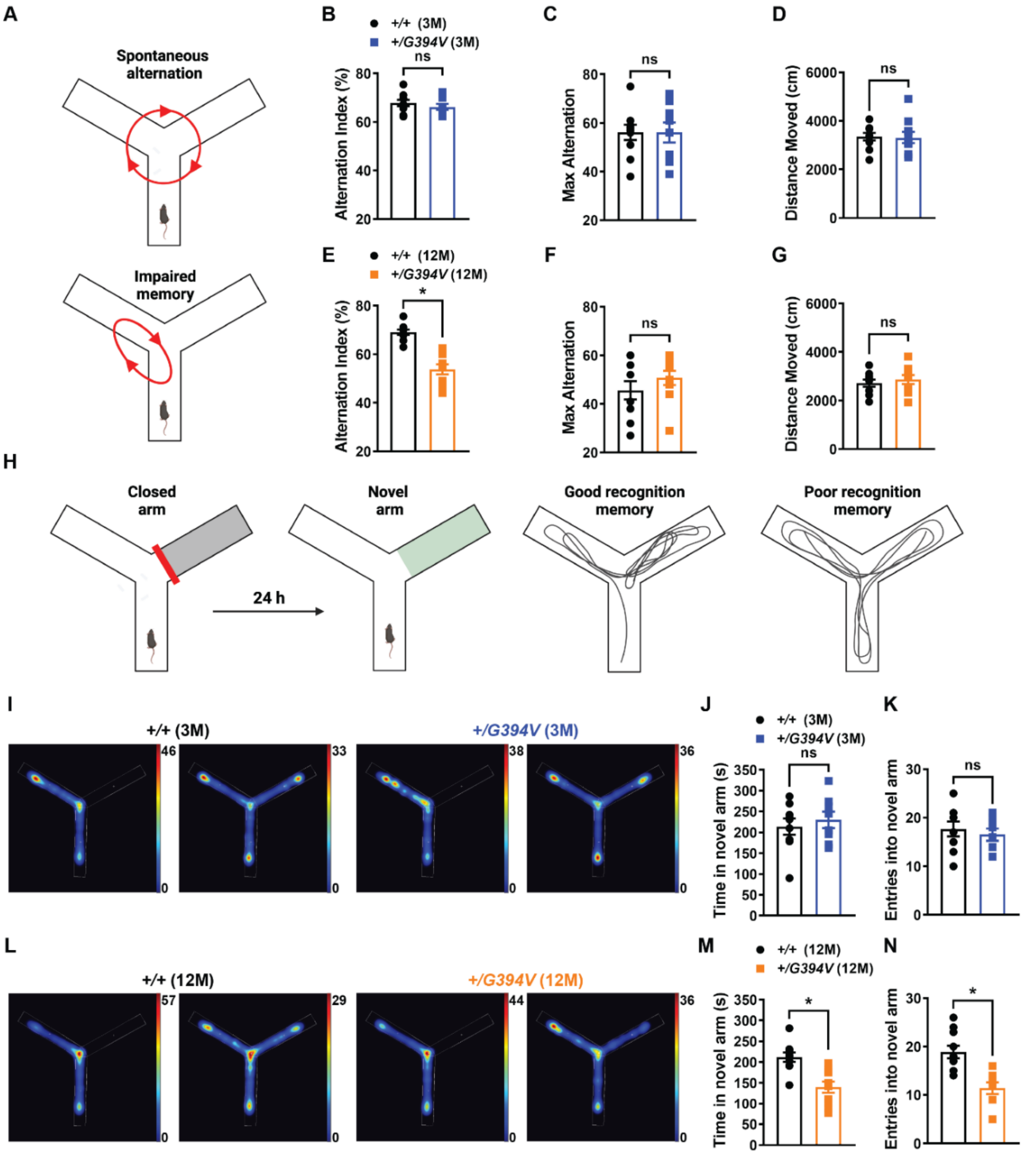

Figure 3. Age-dependent memory deficits in Col4a1$^{+/G394V}$ mice. (A) Illustration of the Y-maze spontaneous alternation behavior assay showing examples of a spontaneous (top) and nonspontaneous (bottom) alternation. (B) Summary data showing alternation index, an indicator spatial working memory, in 3 M-old *Col4a1*$^{+/+}$ and *Col4a1*$^{+/G394V}$ mice (n = 10 animals per group, ns = not significant, unpaired t-test). (C and D) Summary data showing max alternation (C) and distance moved (D), indicative of exploratory activity, in 3 M-old *Col4a1*$^{+/+}$ and *Col4a1*$^{+/G394V}$ mice (n = 10 animals per group, ns = not significant, unpaired t-test). (E) Summary data showing the alternation index of 12 M-old *Col4a1*$^{+/+}$ and *Col4a1*$^{+/G394V}$ mice (n = 10 animals per group, *$p<0.05$, unpaired t-test). (F and G) Summary data showing max alternation (F) and distance moved (G) in 12 M-old *Col4a1*$^{+/+}$ and *Col4a1*$^{+/G394V}$ mice (n = 10 animals per group, ns = not significant,

unpaired t-test). (H) Illustration demonstrating typical and impaired Y-maze novel arm behavior. (I) Representative heatmaps showing the time (s) 3 M-old *Col4a1*$^{+/+}$ and *Col4a1*$^{+/G394V}$ mice spent in areas of the Y-maze during the novel arm test. (J and K) Summary data showing the time spent (J) and entries (K) into the novel arm (n = 8–9 animals per group, ns = not significant, unpaired t-test). (L) Representative heatmaps showing the time (s) 12 M-old *Col4a1*$^{+/+}$ and *Col4a1*$^{+/G394V}$ mice spent in areas of the Y-maze during the novel arm test. (M and N) Summary data showing the time spent (M) and entries (N) into the novel arm (n = 10 animals per group, *p<0.05, unpaired t-test).

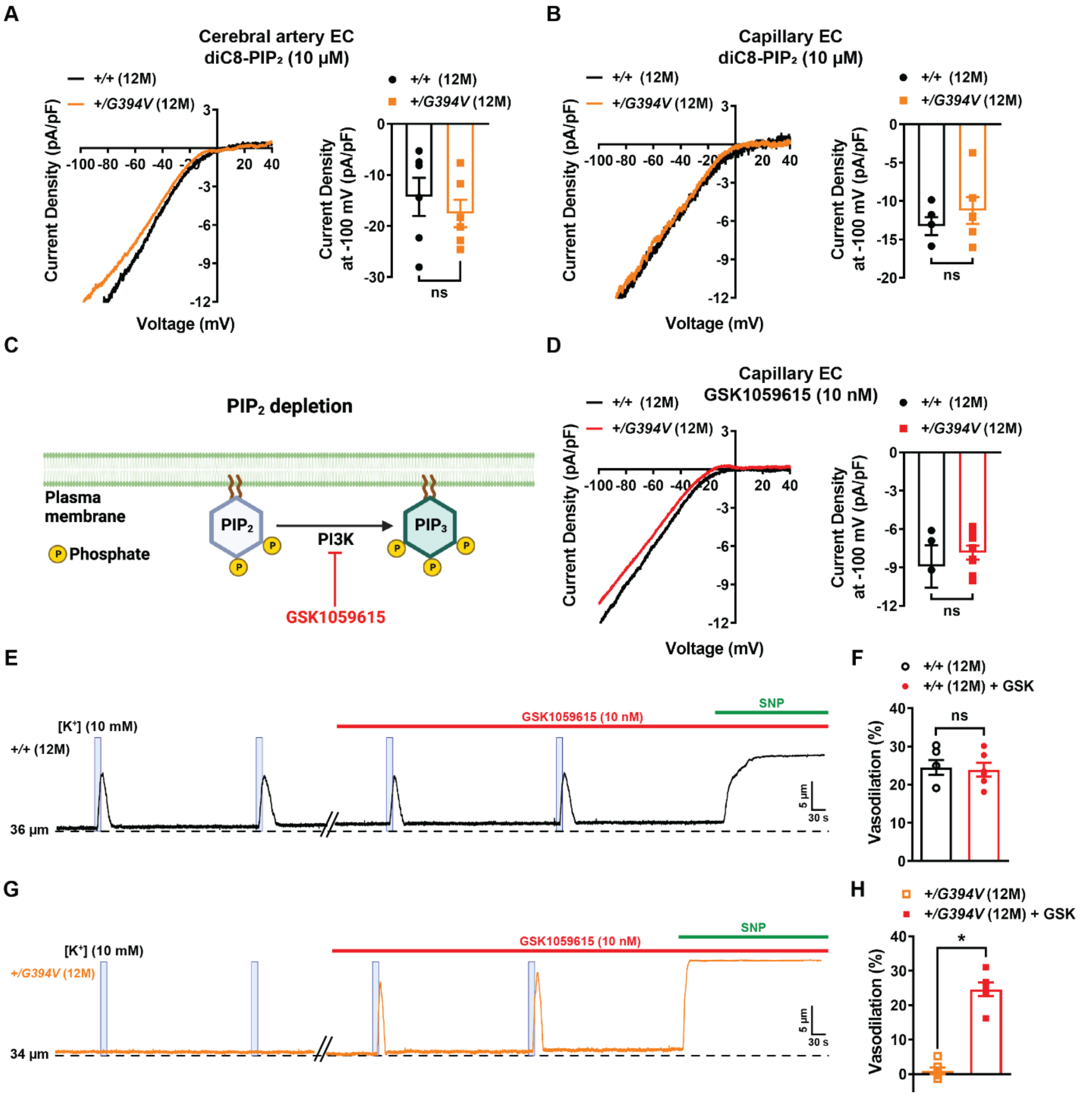

Figure 4. PIP$_2$ depletion reduces Kir2.1 currents in 12 M-old Col4a1$^{+/G394V}$ mice. (A) Representative I-V traces and summary data showing Kir2.1 current densities in freshly isolated cerebral artery ECs from 12 M-old *Col4a1*$^{+/+}$ and *Col4a1*$^{+/G394V}$ mice with internal solution supplemented with diC8-PIP2 (10 µM) (n = 6 cells from 4 animals per group, ns = not significant, unpaired t-test). (B) Representative I-V traces and summary data showing Kir2.1 current densities in freshly isolated brain capillary ECs from 12 M-old *Col4a1*$^{+/+}$ and *Col4a1*$^{+/G394V}$ mice with internal solution supplemented with diC8-PIP2 (10 µM) (n = 5–6 cells from 4 to 5 animals per group, ns = not significant, unpaired t-test). (C) PIP$_2$ depletion pathway. (D) Representative I-V traces and summary data showing Kir2.1 current densities in freshly isolated brain capillary ECs from 12 M-old *Col4a1*$^{+/+}$ and *Col4a1*$^{+/G394V}$ mice treated with the PI3K blocker GSK1059615 (10 nM) (n = 4–8 cells from 3 to 6 animals per group, ns = not significant, unpaired t-test). (E and F) Representative trace (E) and summary data (F) showing K$^+$ (10 mM, blue box)-induced dilation of upstream arterioles in preparations from 12 M-old *Col4a1*$^{+/+}$ mice before and after superfusing the PI3K blocker GSK1059615 (10 nM, 30 min) (n = 6 preparations

from 5 animals per group, ns = not significant, paired t-test). (G and H) Representative trace (G) and summary data (H) showing K^+ (10 mM, blue box)-induced dilation of upstream arterioles in preparations from 12 M-old *Col4a1*$^{+/G394V}$ mice before and after superfusing the PI3K blocker GSK1059615 (10 nM, 30 min) (n = 6 preparations from 5 animals per group, *p<0.05, paired t-test).

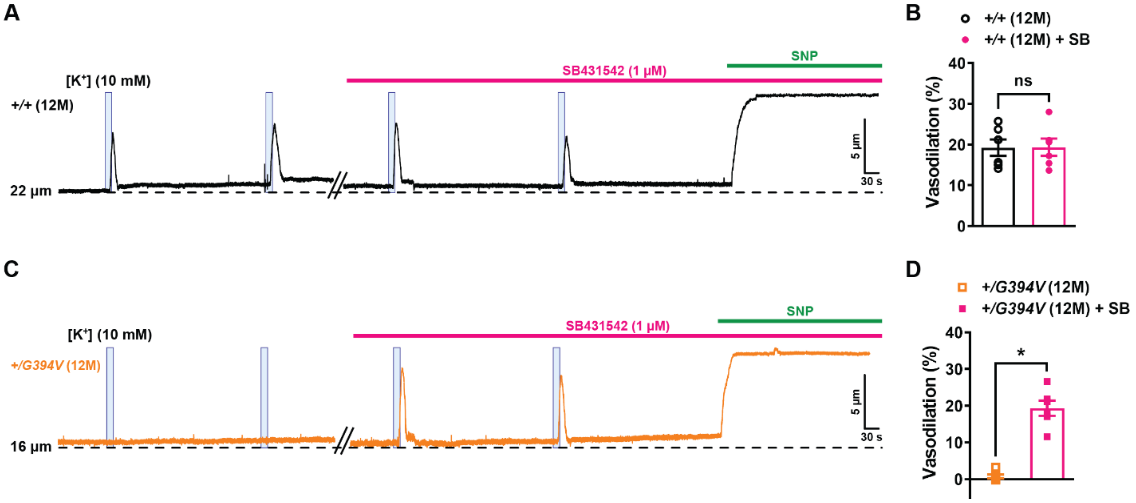

Figure 5. Block of TGF-β receptors repairs capillary-to-arteriole dilation in Col4a1$^{+/G394V}$ mice. (A and B) Representative trace (A) and summary data (B) showing K$^+$ (10 mM, blue box)-induced dilation of upstream arterioles in preparations from 12 M-old *Col4a1*$^{+/+}$ mice before and after superfusing the TGF-β receptor blocker SB431542 (1 µM, 30 min) (n = 6 preparations from 3 animals per group, ns = not significant, paired t-test). (C and D) Representative trace (C) and summary data (D) showing K$^+$ (10 mM, blue box)-induced dilation of upstream arterioles in preparations from 12 M-old *Col4a1*$^{+/G394V}$ mice before and after superfusing the TGF-β receptor blocker SB431542 (1 µM, 30 min) (n = 6 preparations from 4 animals per group, *p<0.05, paired t-test).

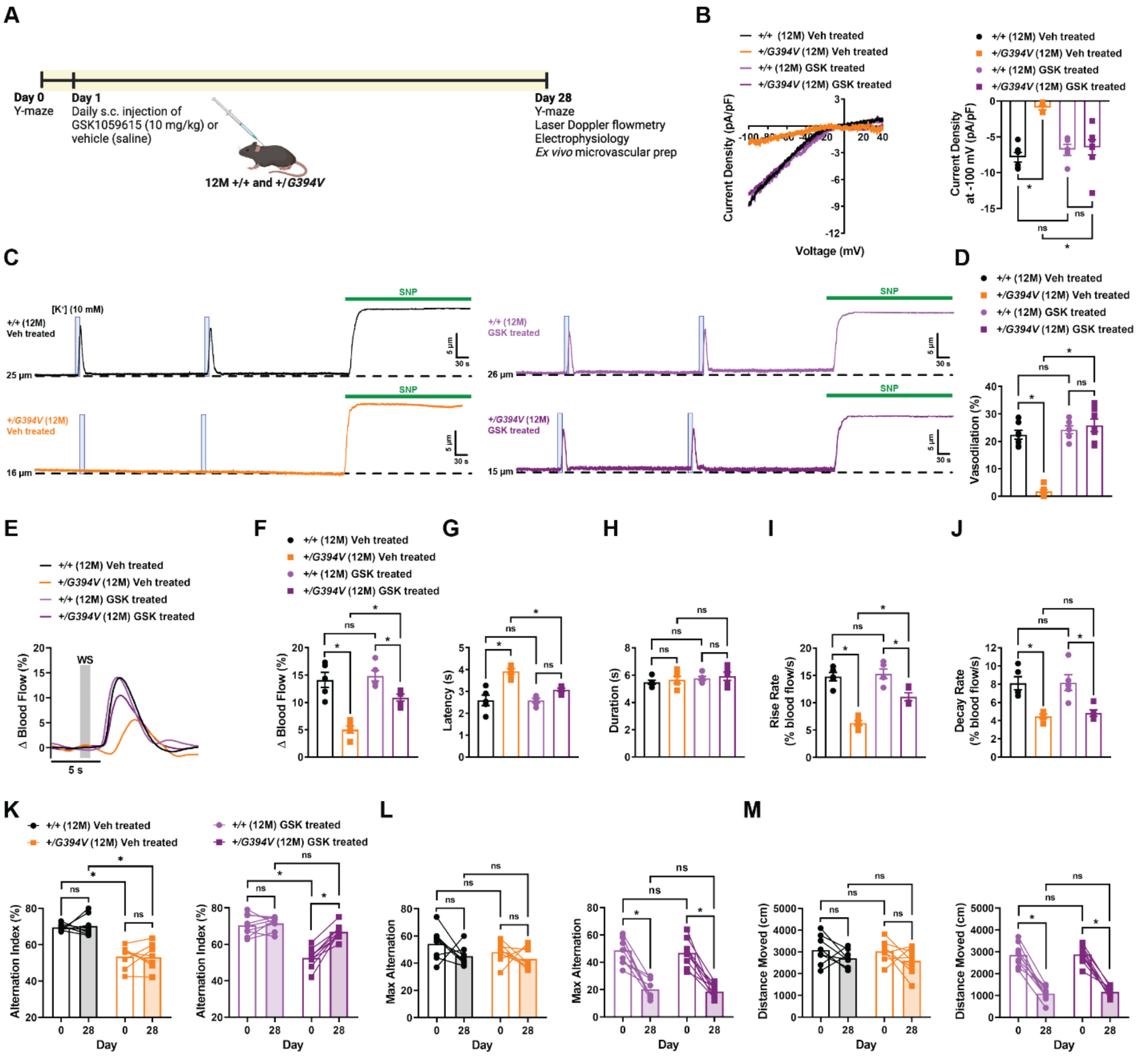

Figure 6. Chronic PI3K inhibition restores Kir2.1 currents, K⁺-induced dilation, functional hyperemia, and memory deficits in 12 M-old Col4a1$^{+/G394V}$ mice. (A) Illustration showing GSK1059615 treatment plan. (B) Representative I-V traces and summary data showing Kir2.1 current densities in freshly isolated capillary ECs from 12 M-old *Col4a1*$^{+/+}$ and *Col4a1*$^{+/G394V}$ mice treated with vehicle (saline) or GSK1059615 (10 mg/kg) for 28 days, s.c. (n = 5–8 cells from 3 to 4 animals per group, *p<0.05, ns = not significant, non-repeated measures two-way ANOVA). (C and D) Representative traces (C) and summary data (D) showing K⁺ (10 mM, blue box)-induced dilation of upstream arterioles in preparations from 12 M-old *Col4a1*$^{+/+}$ and *Col4a1*$^{+/G394V}$ mice treated with vehicle (saline) or GSK1059615 (10 mg/kg) for 28 days, s.c. (n = 6–7 preparations from 3 animals per group, *p<0.05, ns = not significant, non-repeated measures two-way ANOVA). (E and F) Representative traces (E) and summary data (F) showing the increase in blood flow following 1 s contralateral whisker stimulation (WS) in 12 M-old *Col4a1*$^{+/+}$ and *Col4a1*$^{+/G394V}$ mice treated with vehicle (saline) or GSK1059615 (10 mg/kg) for 28 days, s.c. (n = 5 animals per group, *p<0.05, ns = not significant, non-repeated measures two-way ANOVA). (G to J) Latency (G), duration (H), rise rate (I), and decay rate (J) were also analyzed (n= 5 animals per group, *p<0.05, ns = not significant, non-

repeated measures two-way ANOVA). (K) Summary data showing alternation index, an indicator spatial working memory, of 12 M-old *Col4a1*$^{+/+}$ and *Col4a1*$^{+/G394V}$ mice before and after treatment with vehicle (saline) or GSK1059615 (10 mg/kg) for 28 days, s.c. (n = 8–9 animals per group, *p<0.05, ns = not significant, repeated measures two-way ANOVA). (L and M) Summary data showing max alternation (L) and distance moved (M), indicative of exploratory activity, in 12 M-old *Col4a1*$^{+/+}$ and *Col4a1*$^{+/G394V}$ mice before and after treatment with vehicle (saline) or GSK1059615 (10 mg/kg) for 28 days, s.c. (n = 8–9 animals per group, *p<0.05, ns = not significant, repeated measures two-way ANOVA).

Supplemental Figures

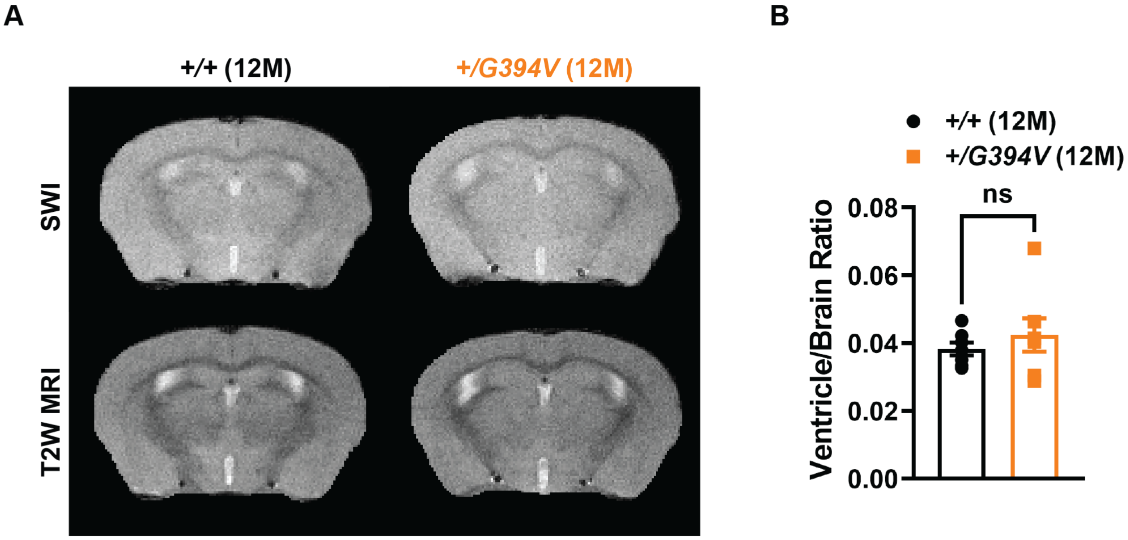

Figure 1 - figure supplement 1. High field magnetic resonance imaging. (A) Representative susceptibility weighted (SWI) and T2 weighted (T2W) MRI images from 12 M-old *Col4a1*$^{+/+}$ and *Col4a1*$^{+/G394V}$ mice. (B) Quantification of ventricle/brain ratio for 12 M-old *Col4a1*$^{+/+}$ and *Col4a1*$^{+/G394V}$ mice (n = 7 animals per group, ns = not significant, unpaired t-test).

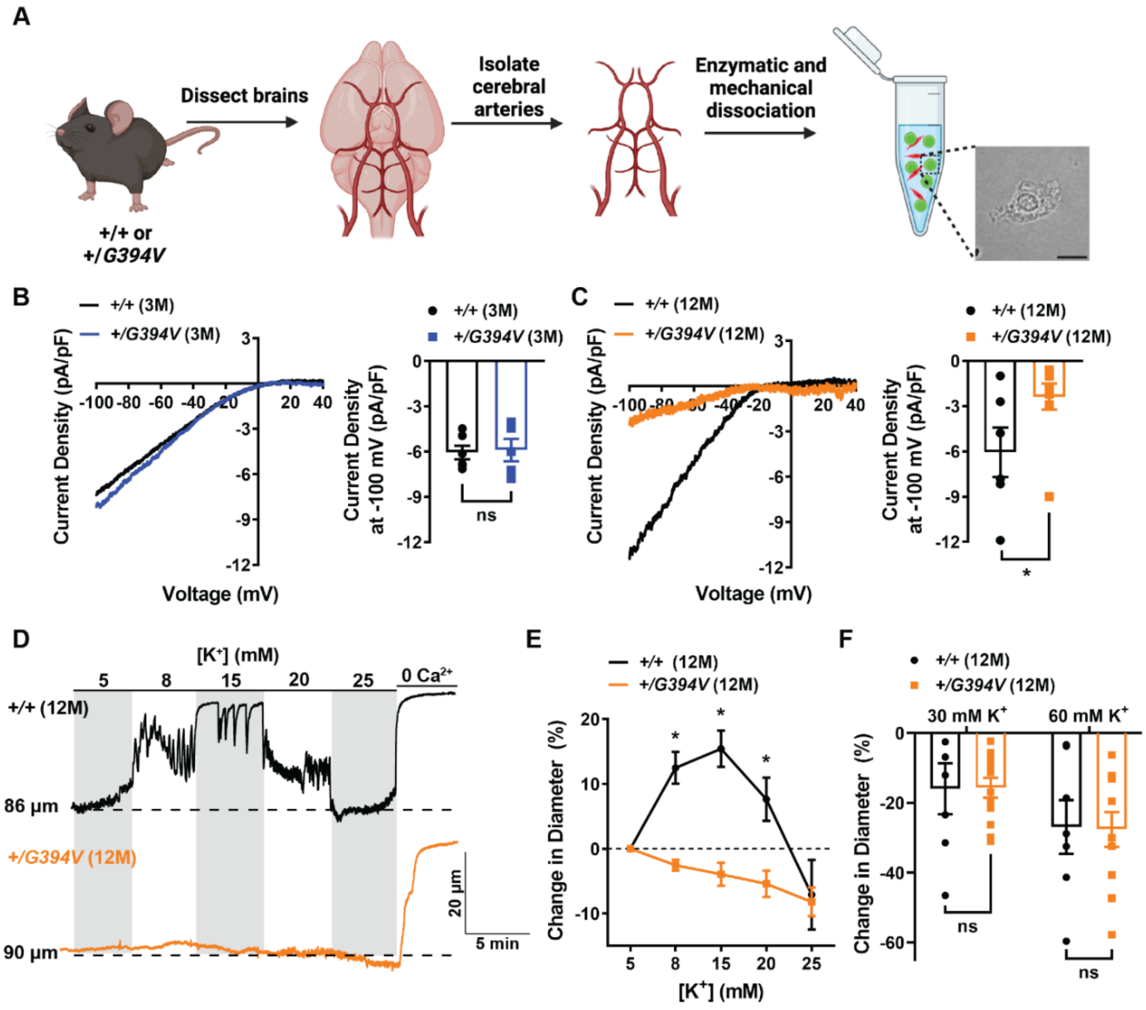

Figure 1 - figure supplement 2. Kir2.1 currents in cerebral artery ECs. (A) Illustration of the cerebral artery EC isolation procedure. Scale bar = 10 µm. (B) Representative I-V traces and summary data showing Kir2.1 current densities in freshly isolated cerebral artery ECs from 3 M-old *Col4a1*$^{+/+}$ and *Col4a1*$^{+/G394V}$ mice (n = 5–6 cells from 5 animals per group, ns = not significant, unpaired t-test). (C) Representative I-V traces and summary data showing Kir2.1 current densities in freshly isolated cerebral artery ECs from 12 M-old *Col4a1*$^{+/+}$ and *Col4a1*$^{+/G394V}$ mice (n = 6–10 cells from 3 to 4 animals per group; *p<0.05, unpaired t-test). (D and E) Representative traces (D) and summary data (E) demonstrating the vasodilator response to raising extracellular [K$^+$] in cerebral arteries from 12 M-old *Col4a1*$^{+/+}$ and *Col4a1*$^{+/G394V}$ mice (n = 9–13 preparations from 6 to 10 animals per group, *p<0.05, non-repeated measures two-way ANOVA). (F) Summary data showing the contractile response to 30 and 60 mM [K$^+$] in cerebral arteries from 12 M-old *Col4a1*$^{+/+}$ and *Col4a1*$^{+/G394V}$ mice (n = 7–12 preparations from 5 to 10 animals per group, ns = not significant, unpaired t-test).

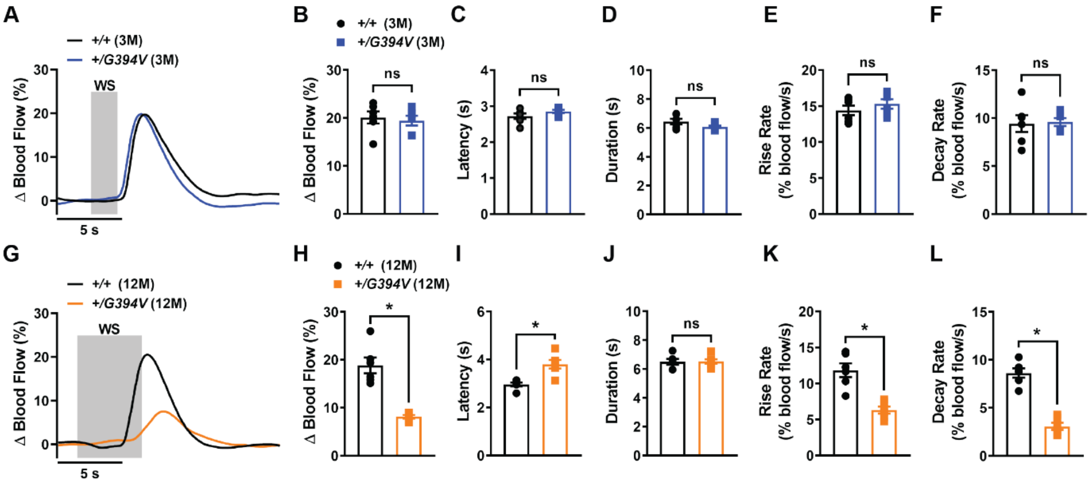

Figure 2 - figure supplement 1. Functional hyperemic response following 2 s whisker stimulation. (A and B) Representative traces (A) and summary data (B) showing the increase in blood flow following 2 s contralateral whisker stimulation (WS) in 3 M-old *Col4a1*$^{+/+}$ and *Col4a1*$^{+/G394V}$ mice (n = 6 animals per group, ns = not significant, unpaired t-test). (C to F) Latency (C), duration (D), rise rate (E) and decay rate (F) were also analyzed (n= 6 animals per group, ns = not significant, unpaired t-test). (G and H) Representative traces (G) and summary data (H) showing the increase in blood flow following 2 s contralateral WS in 12 M-old *Col4a1*$^{+/+}$ and *Col4a1*$^{+/G394V}$ mice (n = 6 animals per group, *p<0.05, unpaired t-test). (I to L) Latency (I), duration (J), rise rate (K) and decay rate (L) were also analyzed (n = 6 animals per group, *p<0.05, ns = not significant, unpaired t-test).

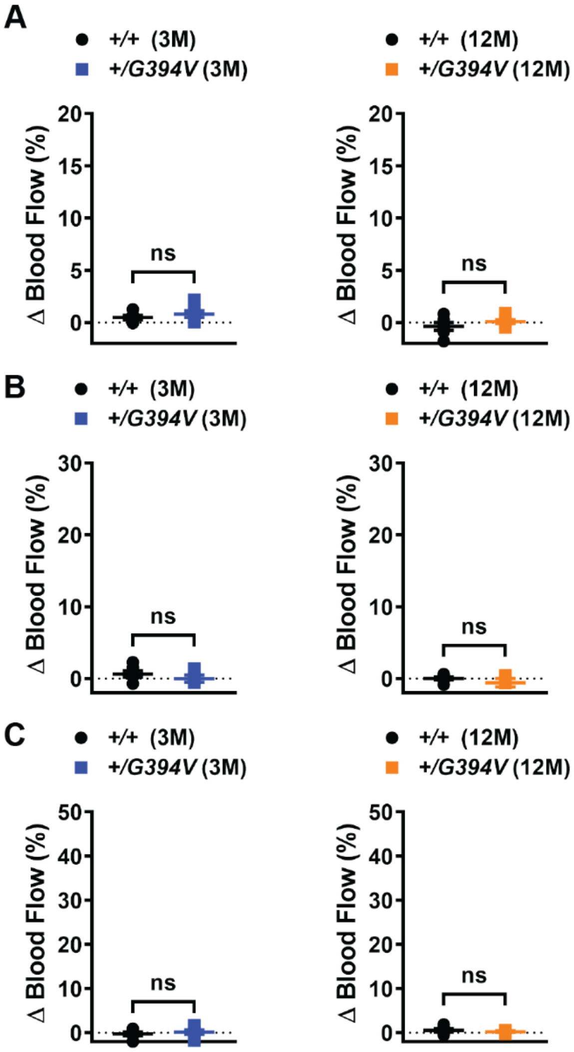

Figure 2 - figure supplement 2. Ipsilateral whisker stimulation. (A to C) Summary data showing no change in blood flow following ipsilateral whisker stimulation for 1 s (A), 2 s (B), and 5 s (C) in 3 M- and 12 M-old *Col4a1*$^{+/+}$ and *Col4a1*$^{+/G394V}$ mice (n = 6 animals per group, ns = not significant, unpaired t-test).

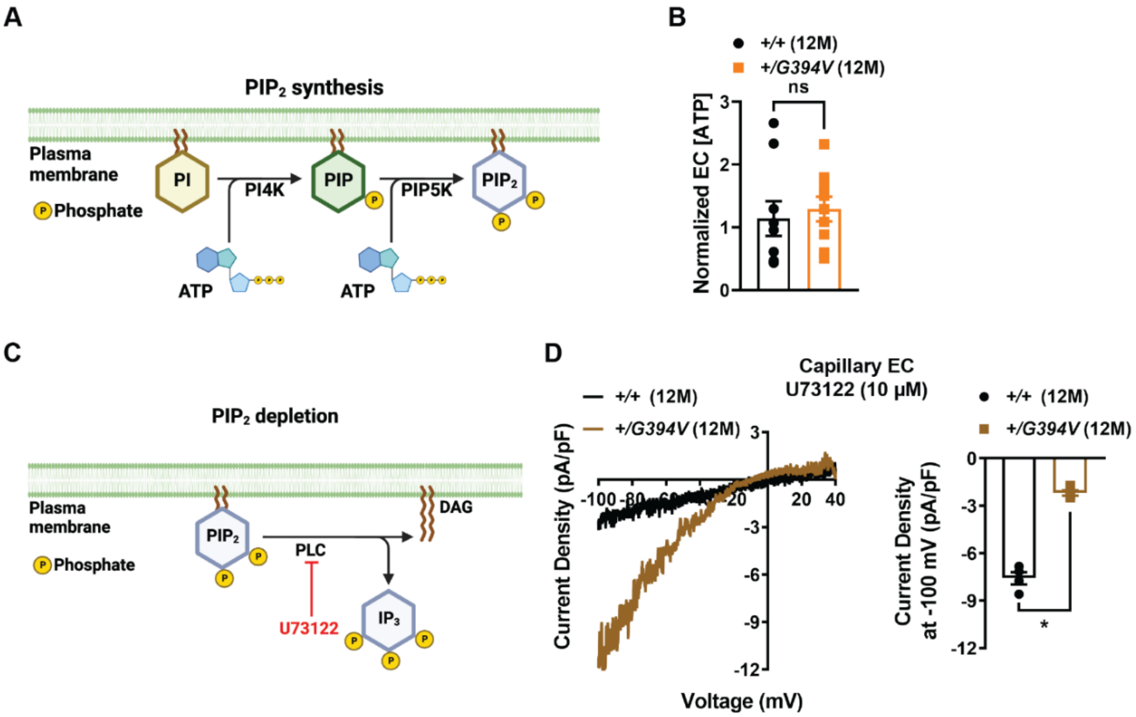

Figure 4 - figure supplement 1. ATP levels in brain capillary ECs. (A) PIP$_2$ synthesis pathway. (B) Summary data showing normalized [ATP] in brain capillary ECs from 12 M-old *Col4a1*$^{+/+}$ and *Col4a1*$^{+/G394V}$ mice. (n = 9 sets of ~500 cells from three mice per group, ns = not significant, unpaired t-test). (C) PIP$_2$ depletion pathway. (D) Representative I-V traces and summary data showing Kir2.1 current densities in freshly isolated brain capillary ECs treated with the PLC inhibitor U73122 (10 μM) from 12 M-old *Col4a1*$^{+/+}$ and *Col4a1*$^{+/G394V}$ mice (n = 4 cells from 3 animals per group, *p<0.05, unpaired t-test).

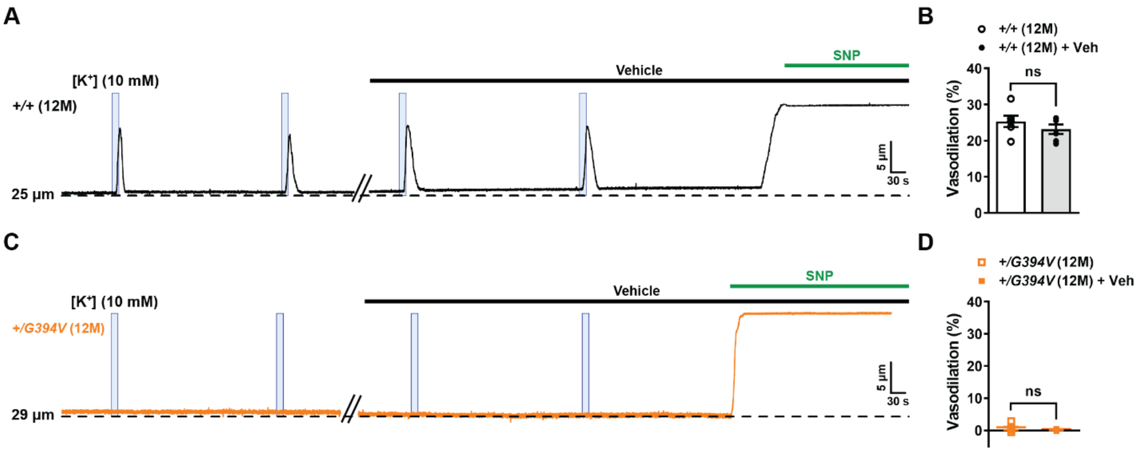

Figure 5 - figure supplement 1. GSK1059615 and SB431542 vehicle response. (A and B) Representative trace (A) and summary data (B) showing K$^+$ (10 mM, blue box)-induced dilation of upstream arterioles in preparations before and after superfusing the vehicle (0.01% v/v DMSO, 30 min) from 12 M-old *Col4a1*$^{+/+}$ mice (n = 6 preparations from 4 animals per group, ns = not significant, paired t-test). (C and D) Representative trace (C) and summary data (D) showing K$^+$ (10 mM, blue box)-induced dilation of upstream arterioles in preparations before and after superfusing the vehicle (0.01% v/v DMSO, 30 min) from 12 M-old *Col4a1*$^{+/G394V}$ mice (n = 6 preparations from 4 animals per group, ns = not significant, paired t-test).

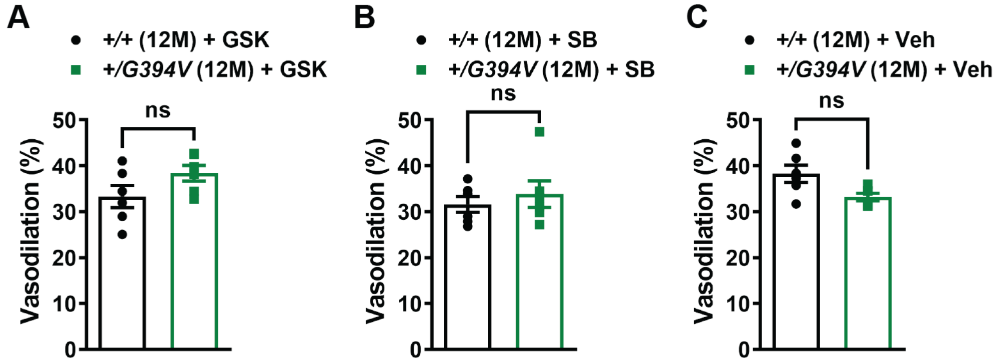

Figure 5 - figure supplement 2. SNP response following GSK1059615, SB431542, and vehicle treatment. (A to C) Summary data showing that the dilation produced by superfusing SNP (10 µM) in the presence of GSK1059615 (10 nM, 30 min) (A), SB431542 (1 µM, 30 min) (B), and vehicle (0.01% v/v DMSO, 30 min) (C) in preparations from 12 M-old *Col4a1*$^{+/+}$ and *Col4a1*$^{+/G394V}$ mice (n = 6 preparations from 3 to 5 animals per group, ns = not significant, unpaired t-test).

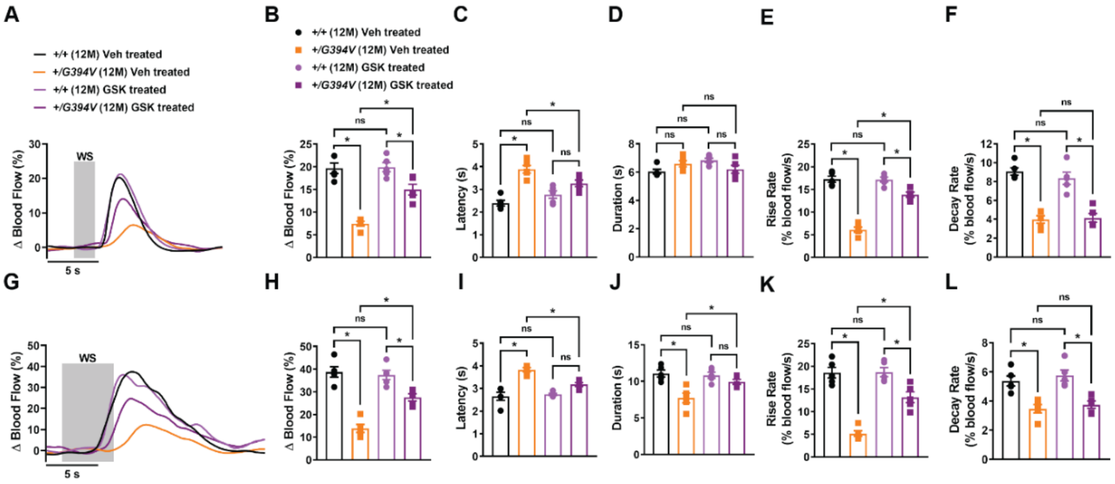

Figure 6 - figure supplement 1. Functional hyperemic response following 2 s and 5 s whisker stimulation in GSK1059615-treated animals. (A and B) Representative traces (A) and summary data (B) showing the increase in blood flow following 2 s contralateral whisker stimulation (WS) in 12 M-old *Col4a1*$^{+/+}$ and *Col4a1*$^{+/G394V}$ mice treated with vehicle (saline) or GSK1059615 (10 mg/kg) for 28 days, s.c. (n = 5 animals per group, *p<0.05, ns = not significant, non-repeated measures two-way ANOVA). (C to F) Latency (C), duration (D), rise rate (E) and decay rate (F) were also analyzed (n= 5 animals per group, *p<0.05, ns = not significant, non-repeated measures two-way ANOVA). (G and H) Representative traces (G) and summary data (H) showing the increase in blood flow following 5 s contralateral WS in 12 M-old *Col4a1*$^{+/+}$ and *Col4a1*$^{+/G394V}$ mice treated with vehicle (saline) or GSK1059615 (10 mg/kg) for 28 days, s.c. (n = 5 animals per group, *p<0.05, ns = not significant, non-repeated measures two-way ANOVA). (I to L) Latency (I), duration (J), rise rate (K) and decay rate (L) were also analyzed (n= 5 animals per group, *p<0.05, ns = not significant, non-repeated measures two-way ANOVA).

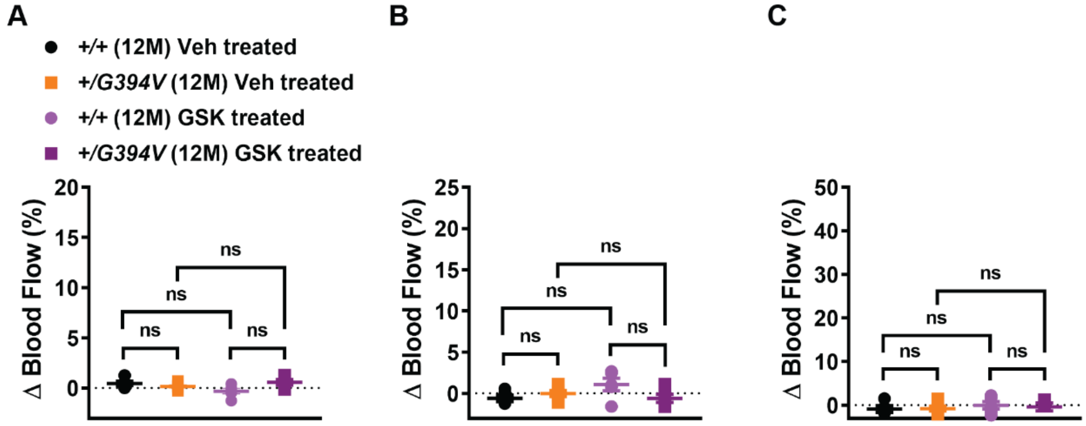

Figure 6 - figure supplement 2. Ipsilateral whisker stimulation in GSK1059615 treated animals. (A to C) Summary data showing no change in blood flow following ipsilateral whisker stimulation for 1 s (A), 2 s (B), and 5 s (C) in 12 M-old Col4a1$^{+/+}$ and Col4a1$^{+/G394V}$ mice treated with vehicle (saline) or GSK1059615 (10 mg/kg) for 28 days, s.c. (n = 5 animals per group, ns = not significant, non-repeated measures two-way ANOVA).

CHAPTER 5: SUMMARY AND FUTURE DIRECTIONS

MUTATIONS IN *COL4A1* CAUSE CSVD THROUGH DIVERGENT MECHANISMS

Clinical presentations and the pathogenicity of *COL4A1* mutations vary with the location of the mutation (239). We used *Col4a1*$^{+/G1344D}$ and *Col4a1*$^{+/G394V}$ cSVD mice to determine the impact of *Col4a1* mutations on vascular function and the molecular mechanisms underlying *Col4a1*-related cSVDs. We found that both mutations caused cerebrovascular dysfunction in 12-month-old but not 3-month-old animals. Surprisingly, we discovered that fundamentally distinct mechanisms account for *Col4a1*^{G1344D} and *Col4a1*^{G394V}-related cSVD.

Chapter 2 demonstrated that *Col4a1*^{G1344D}-related cSVD was associated with an age-dependent loss of myogenic vasoconstriction in cerebral arteries. Electrophysiological analyses showed that impaired pressure-induced SMC depolarization underlies the failure of myogenic vasoconstriction. Dysregulation of SMC membrane potential was associated with disruption of critical SR Ca^{2+} signaling mechanisms and decreased Ca^{2+}-dependent activation of TRPM4 channels. *In vivo* treatment with the chemical chaperone 4PBA attenuated cerebrovascular pathology in *Col4a1*$^{+/G1344D}$ mice, suggesting that SR accumulation of mutant COL4A1 contributes to the pathogenesis and that therapies that increase the secretion of misfolded proteins may be a viable treatment for some forms of cSVD.

Chapter 3 demonstrates that impaired myogenic vasoconstriction in cerebral arteries also contributes to cSVD in *Col4a1*^{G394V} mice. Loss of myogenic tone was associated with a significant decrease in depolarizing cation currents conducted by TRPM4 channels in vascular SMCs. In this model, the reduction in TRPM4 channel activity was associated with decreased PIP_2, a necessary cofactor of TRPM4 (240, 241), rather than impaired Ca^{2+} signaling. Dialyzing SMCs with PIP_2 or inhibition of PI3K, an enzyme that reduces PIP_2 bioavailability by converting it to PIP_3, restored TRPM4 currents in SMCs from *Col4a1*$^{+/G394V}$ mice. Acute inhibition of PI3K and TGF-β receptors restored myogenic vasoconstriction, suggesting that hyperactivity of the TGF-β signaling pathway stimulates PI3K to deplete PIP_2, thereby reducing TRPM4 channel activity.

Chapter 4 shows that *Col4a1*$^{+/G394V}$ mice also lose capillary-to-arterial dilation, resulting in impaired functional hyperemia in an age-dependent manner. We also show that 12-month-old *Col4a1*$^{+/G394V}$ mice have impaired working and recognition memory, likely due to defects in cerebral blood flow control mechanisms. These defects were attributed to the loss of $K_{IR}2.1$ channel activity in brain arteriole and capillary ECs due to PIP_2 depletion, an essential cofactor for $K_{IR}2.1$ channels (269, 270). The pathway for PIP_2 deficit in ECs was the same as in SMCs - overactive TGF-β signaling drives PI3K activity to reduce PIP_2 levels. Chronic *in vivo* PI3K blockade rescued $K_{IR}2.1$ currents, capillary-to-arterial dilation, functional hyperemia, and improved memory function in *Col4a1*$^{+/G394V}$ mice, providing evidence that cognitive impairment associated with some forms of cSVDs can be resolved by restoring blood flow regulation in the brain.

In summary, the research described in this thesis unveils two novel pathogenic molecular mechanisms of cSVD and demonstrates the viability of targeting these pathways to prevent and treat some forms of cSVDs.

FUTURE DIRECTIONS

Although our findings illuminate novel pathogenic mechanisms underlying *COL4A1*-related cSVDs, much more work remains. Three open questions include: 1) Why is the cerebrovascular pathology of *Col4a1* mutant mice age-related? 2) Why are there drastic intrafamilial variations in the severity of *COL4A1* mutations? 3) Are the molecular mechanisms that cause *Col4a1*^{G1344D} and *Col4a1*^{G394V}-related cSVD relevant to the common forms of sporadic cSVDs?

Age is the most significant risk factor for sporadic cSVDs (6). Determining why cerebrovascular dysfunction is age-dependent in *COL4A1*-related cSVDs could provide insight into the pathogenic mechanisms of idiopathic cSVDs. We found that vascular dysfunction was present in 12 M-old but not 3 M-old *Col4a1*$^{+/G1344D}$ and *Col4a1*$^{+/G394V}$ animals, suggesting that these mice are able to produce functional basement membranes during development, but an unknown mechanism disrupts the ability to maintain them during aging. Vascular collagen has a half-life of 60-70 days (289). This slow turnover in comparison to most proteins may underly the age-dependent defects in *Col4a1*-cSVD models. The effect of *Col4a1*^{G1344D} and *Col4a1*^{G394V} mutations on the turnover rate of vascular collagen is unknown. A feasible consequence would be increased turnover due to decreased stability of mutant collagen IV. Collagen IV producing cells including vascular SMCs would need to increase production to compensate for decreased mutant collagen stability. This in combination with the decline in the ability of cells to handle misfolded proteins during normal aging (300) would exacerbate the amount of mutant proteins in the SR and disrupt SR Ca^{2+} signaling, providing an age-related mechanism for cerebrovascular dysfunction in *Col4a1*$^{+/G1344D}$ mice. In *Col4a1*$^{+/G394V}$ mice, decreased stability of mutant collagen IV would likely lead to increased fragility of the basement membrane. Our data suggest that collagen-producing cells in the cerebral vasculature are able to keep up with increased degradation while animals are young. However, collagen production decreases with normal aging (291, 301) and may not be sufficient to maintain homeostasis in mutant mice over time. We propose that age-related defects in the structure of the basement membrane could lead to dysregulation of TGF-β signaling. Alternatively, if *Col4a1* mutations increase the stability of mutant collagen IV heterotrimers or disrupt the ability of endogenous enzymes (e.g., matrix metalloproteinases) to cleave collagen IV, gradually, the ratio of mutant collagen IV heterotrimers to normal heterotrimers would increase with age. The incorporation of mutant collagens could disrupt TGF-β regulation by disrupting the sequestration of TGF-β ligands, increasing bioavailability.

Understanding how *Col4a1*^{G1344D} and *Col4a1*^{G394V} mutations affect collagen IV stability and turnover is critical. Generating mouse models with tagged *Col4a1* to study turnover has been a hurdle because both the N- and C-terminal ends of the proteins are functional domains that are required for intermolecular crosslinking. Additionally, any modifications within the collagenous domain would disrupt the triple helix producing a nonfunctioning protein. Recently, a novel *Col4a1*-GFP mouse model has been generated with a GFP tag that is cleaved after being translated to create a soluble GFP and a functional COL4A1 polypeptide. This mouse model allows investigators to visualize cells actively producing COL4A1. Crossing these mice with *Col4a1*^{G1344D} or *Col4a1*^{G394V} mice could provide insight into how these mutations affect vascular collagen IV turnover. Specifically, crossing these mice with *Col4a1*^{G1344D} mice would allow us to visualize if there is an increased burden on vascular SMCs to produce COL4A1 to compensate for decreased mutant collagen IV heterotrimer stability that would increase SR stress disrupting SR Ca^{2+} signaling.

Our data and previous reports provide evidence that allelic heterogeneity exists among different *COL4A1* mutations (189, 210). In addition to interfamilial variation of mutations, intrafamilial phenotypic variability also exists. The same C*OL4A1* mutation can severely affect one family member while remaining clinically silent in another (185, 238, 302). In humans, this variation could be due to differences in genetics or other modifiable risk factors linked to cSVDs like hypertension, diabetes, hyperlipidemia, and smoking. However, in mouse models, there is also variable penetrance despite genetic homogeneity and environmental factors being controlled between littermates (195). Studying genetic differences between severely impacted and clinically silent patients or animals may reveal complementary mutations that contribute to the development of cSVD or 'protective' variants that prevent disease development. Understanding the causes of variation in the severity of cSVD phenotypes within the same *COL4A1* mutation can lead to other targets for the prevention and treatment of cSVDs.

We show that alterations in SR Ca^{2+} signaling that impairs TRPM4 channel activity contributes to cSVD in *Col4a1*$^{+/G1344D}$ mice and that PIP_2 depletion downstream of increased TGF-β signaling underlies TRPM4 and K_{IR} channel dysfunction leading to cSVD in *Col4a1*$^{+/G394V}$ mice. However, it is not known if these mechanisms contribute to sporadic forms of cSVD. Aging is the most consequential risk factor for cSVD (6). Determining how aging affects the pathways contributing to *Col4a1* cSVDs may reveal links with sporadic cSVDs. Notably, aging impairs RyR- and IP_3R-mediated Ca^{2+} signaling and Ca^{2+} refilling of the SR in cerebral and mesenteric artery SMCs (303, 304), suggesting there may be similarities between *Col4a1*^{G1344D}-related cSVD and sporadic age-related cSVDs. These investigations have only been carried out in mouse arteries. Further studies are needed to see if this occurs in humans. As mentioned earlier, PIP_2 homeostasis has emerged as a central pathogenic mechanism in multiple forms of cerebrovascular diseases, including CADASIL cSVD (164) and Alzheimer's disease (305). TGF-β signaling increases with age in multiple tissues, including the brain (306, 307). A consequence of increased TGF-β signaling is decreased PIP_2, but the effect of aging on PIP_2 levels in vascular SMC and ECs has not been well studied. Investigation into how aging affects PIP_2 homeostasis and TRPM4 and K_{IR} channel activity could provide further evidence of their role in the pathogenesis of idiopathic cSVDs.

cSVDs are a diverse group of disorders that act through divergent pathogenic pathways. Multiple research groups have attempted to define a convergent mechanism to develop a standardized therapeutic approach. However, this philosophy may be detrimental. Recent advances in identifying pathophysiological mechanisms of familial cSVDs, particularly for COL4A1 mutants, emphasize the heterogeneity of pathogenic mechanisms and the need for a personalized medicine approach.

CONCLUSIONS

Mutations in *COL4A1* cause cSVD through different mechanisms depending on the location of the mutation. $\textit{Col4a1}^{G1344D}$ cSVD is linked to impaired Ca^{2+}-dependent activation of TRPM4 channels due to disrupted SR Ca^{2+} signaling, whereas PIP_2 depletion in cerebral artery SMCs and vascular ECs due to increased PI3K activity driven by hyperactive TGF-β signaling causes cSVD in $\textit{Col4a1}^{+/G394V}$ mice. The divergent pathogenic mechanisms of *COL4A1*-related cSVDs emphasize the need for directed treatments, and these pathways may represent a novel target for the prevention and treatment of certain types of cSVDs.

REFERENCES

1. R. J. Cannistraro *et al.*, CNS small vessel disease: A clinical review. *Neurology* **92**, 1146-1156 (2019).
2. P. B. Gorelick *et al.*, Vascular contributions to cognitive impairment and dementia: a statement for healthcare professionals from the american heart association/american stroke association. *Stroke* **42**, 2672-2713 (2011).
3. J. A. Schneider, Z. Arvanitakis, W. Bang, D. A. Bennett, Mixed brain pathologies account for most dementia cases in community-dwelling older persons. *Neurology* **69**, 2197-2204 (2007).
4. H. H. Dodge *et al.*, Risk of incident clinical diagnosis of Alzheimer's disease-type dementia attributable to pathology-confirmed vascular disease. *Alzheimers Dement* **13**, 613-623 (2017).
5. Q. Li *et al.*, Cerebral Small Vessel Disease. *Cell Transplant* **27**, 1711-1722 (2018).
6. F. Han *et al.*, Prevalence and Risk Factors of Cerebral Small Vessel Disease in a Chinese Population-Based Sample. *J Stroke* **20**, 239-246 (2018).
7. A. Joutel *et al.*, Notch3 mutations in CADASIL, a hereditary adult-onset condition causing stroke and dementia. *Nature* **383**, 707-710 (1996).
8. V. V. Giau, E. Bagyinszky, Y. C. Youn, S. S. A. An, S. Y. Kim, Genetic Factors of Cerebral Small Vessel Disease and Their Potential Clinical Outcome. *Int J Mol Sci* **20** (2019).
9. D. B. Gould *et al.*, Role of COL4A1 in small-vessel disease and hemorrhagic stroke. *N Engl J Med* **354**, 1489-1496 (2006).
10. D. B. Gould *et al.*, Mutations in Col4a1 cause perinatal cerebral hemorrhage and porencephaly. *Science* **308**, 1167-1171 (2005).
11. P. N. Ainslie, P. Brassard, Why is the neural control of cerebral autoregulation so controversial? *F1000Prime Rep* **6**, 14 (2014).
12. P. Mergenthaler, U. Lindauer, G. A. Dienel, A. Meisel, Sugar for the brain: the role of glucose in physiological and pathological brain function. *Trends Neurosci* **36**, 587-597 (2013).
13. M. Belanger, I. Allaman, P. J. Magistretti, Brain energy metabolism: focus on astrocyte-neuron metabolic cooperation. *Cell Metab* **14**, 724-738 (2011).
14. F. Hyder, D. L. Rothman, M. R. Bennett, Cortical energy demands of signaling and nonsignaling components in brain are conserved across mammalian species and activity levels. *Proc Natl Acad Sci U S A* **110**, 3549-3554 (2013).
15. A. Chandra, W. A. Li, C. R. Stone, X. Geng, Y. Ding, The cerebral circulation and cerebrovascular disease I: Anatomy. *Brain Circ* **3**, 45-56 (2017).
16. S. Sada, Y. Reddy, S. Rao, S. Alladi, S. Kaul, Prevalence of middle cerebral artery stenosis in asymptomatic subjects of more than 40 years age group: a transcranial Doppler study. *Neurol India* **62**, 510-515 (2014).

17. M. J. Cipolla, in The Cerebral Circulation. (San Rafael (CA), 2009).
18. M. J. Cipolla, R. Li, L. Vitullo, Perivascular innervation of penetrating brain parenchymal arterioles. *J Cardiovasc Pharmacol* **44**, 1-8 (2004).
19. F. Dabertrand, M. T. Nelson, J. E. Brayden, Acidosis dilates brain parenchymal arterioles by conversion of calcium waves to sparks to activate BK channels. *Circ Res* **110**, 285-294 (2012).
20. R. M. Hannah, K. M. Dunn, A. D. Bonev, M. T. Nelson, Endothelial SK(Ca) and IK(Ca) channels regulate brain parenchymal arteriolar diameter and cortical cerebral blood flow. *J Cereb Blood Flow Metab* **31**, 1175-1186 (2011).
21. E. Yamasaki, P. Thakore, V. Krishnan, S. Earley, Differential expression of angiotensin II type 1 receptor subtypes within the cerebral microvasculature. *Am J Physiol Heart Circ Physiol* **318**, H461-H469 (2020).
22. N. Nishimura, C. B. Schaffer, B. Friedman, P. D. Lyden, D. Kleinfeld, Penetrating arterioles are a bottleneck in the perfusion of neocortex. *Proc Natl Acad Sci U S A* **104**, 365-370 (2007).
23. D. J. Begley, M. W. Brightman, Structural and functional aspects of the blood-brain barrier. *Prog Drug Res* **61**, 39-78 (2003).
24. B. V. Zlokovic, Neurovascular mechanisms of Alzheimer's neurodegeneration. *Trends Neurosci* **28**, 202-208 (2005).
25. R. Daneman, A. Prat, The blood-brain barrier. *Cold Spring Harb Perspect Biol* **7**, a020412 (2015).
26. C. F. Wenceslau *et al.*, Guidelines for the measurement of vascular function and structure in isolated arteries and veins. *Am J Physiol Heart Circ Physiol* **321**, H77-H111 (2021).
27. N. Khalilgharibi, Y. Mao, To form and function: on the role of basement membrane mechanics in tissue development, homeostasis and disease. *Open Biol* **11**, 200360 (2021).
28. A. W. Morris, R. O. Carare, S. Schreiber, C. A. Hawkes, The Cerebrovascular Basement Membrane: Role in the Clearance of beta-amyloid and Cerebral Amyloid Angiopathy. *Front Aging Neurosci* **6**, 251 (2014).
29. M. S. Thomsen, L. J. Routhe, T. Moos, The vascular basement membrane in the healthy and pathological brain. *J Cereb Blood Flow Metab* **37**, 3300-3317 (2017).
30. R. Timpl, Macromolecular organization of basement membranes. *Curr Opin Cell Biol* **8**, 618-624 (1996).
31. J. Khoshnoodi, V. Pedchenko, B. G. Hudson, Mammalian collagen IV. *Microsc Res Tech* **71**, 357-370 (2008).
32. S. L. Hostikka, K. Tryggvason, The complete primary structure of the alpha 2 chain of human type IV collagen and comparison with the alpha 1(IV) chain. *J Biol Chem* **263**, 19488-19493 (1988).

33. R. Soininen, T. Haka-Risku, D. J. Prockop, K. Tryggvason, Complete primary structure of the alpha 1-chain of human basement membrane (type IV) collagen. *FEBS Lett* **225**, 188-194 (1987).
34. P. Vandenberg *et al.*, Characterization of a type IV collagen major cell binding site with affinity to the alpha 1 beta 1 and the alpha 2 beta 1 integrins. *J Cell Biol* **113**, 1475-1483 (1991).
35. J. Khoshnoodi, J. P. Cartailler, K. Alvares, A. Veis, B. G. Hudson, Molecular recognition in the assembly of collagens: terminal noncollagenous domains are key recognition modules in the formation of triple helical protomers. *J Biol Chem* **281**, 38117-38121 (2006).
36. T. Holster *et al.*, Loss of assembly of the main basement membrane collagen, type IV, but not fibril-forming collagens and embryonic death in collagen prolyl 4-hydroxylase I null mice. *J Biol Chem* **282**, 2512-2519 (2007).
37. Y. Matsuoka *et al.*, Insufficient folding of type IV collagen and formation of abnormal basement membrane-like structure in embryoid bodies derived from Hsp47-null embryonic stem cells. *Mol Biol Cell* **15**, 4467-4475 (2004).
38. R. Timpl, H. Wiedemann, V. van Delden, H. Furthmayr, K. Kuhn, A network model for the organization of type IV collagen molecules in basement membranes. *Eur J Biochem* **120**, 203-211 (1981).
39. P. D. Yurchenco, H. Furthmayr, Self-assembly of basement membrane collagen. *Biochemistry* **23**, 1839-1850 (1984).
40. Y. F. Cheng, R. H. Kramer, Human microvascular endothelial cells express integrin-related complexes that mediate adhesion to the extracellular matrix. *J Cell Physiol* **139**, 275-286 (1989).
41. T. J. Herbst, J. B. McCarthy, E. C. Tsilibary, L. T. Furcht, Differential effects of laminin, intact type IV collagen, and specific domains of type IV collagen on endothelial cell adhesion and migration. *J Cell Biol* **106**, 1365-1373 (1988).
42. E. P. Moiseeva, Adhesion receptors of vascular smooth muscle cells and their functions. *Cardiovasc Res* **52**, 372-386 (2001).
43. P. D. Yurchenco, Y. S. Cheng, H. Colognato, Laminin forms an independent network in basement membranes. *J Cell Biol* **117**, 1119-1133 (1992).
44. R. Hallmann *et al.*, Expression and function of laminins in the embryonic and mature vasculature. *Physiol Rev* **85**, 979-1000 (2005).
45. R. Timpl *et al.*, Laminin--a glycoprotein from basement membranes. *J Biol Chem* **254**, 9933-9937 (1979).
46. P. Tunggal, N. Smyth, M. Paulsson, M. C. Ott, Laminins: structure and genetic regulation. *Microsc Res Tech* **51**, 214-227 (2000).
47. M. Aumailley *et al.*, A simplified laminin nomenclature. *Matrix Biol* **24**, 326-332 (2005).
48. P. D. Yurchenco, Basement membranes: cell scaffoldings and signaling platforms. *Cold Spring Harb Perspect Biol* **3** (2011).

49. M. Sixt *et al.*, Endothelial cell laminin isoforms, laminins 8 and 10, play decisive roles in T cell recruitment across the blood-brain barrier in experimental autoimmune encephalomyelitis. *J Cell Biol* **153**, 933-946 (2001).
50. L. F. Yousif, J. Di Russo, L. Sorokin, Laminin isoforms in endothelial and perivascular basement membranes. *Cell Adh Migr* **7**, 101-110 (2013).
51. Z. L. Chen *et al.*, Ablation of astrocytic laminin impairs vascular smooth muscle cell function and leads to hemorrhagic stroke. *J Cell Biol* **202**, 381-395 (2013).
52. M. J. Menezes *et al.*, The extracellular matrix protein laminin alpha2 regulates the maturation and function of the blood-brain barrier. *J Neurosci* **34**, 15260-15280 (2014).
53. J. Thyboll *et al.*, Deletion of the laminin alpha4 chain leads to impaired microvessel maturation. *Mol Cell Biol* **22**, 1194-1202 (2002).
54. N. Smyth *et al.*, Absence of basement membranes after targeting the LAMC1 gene results in embryonic lethality due to failure of endoderm differentiation. *J Cell Biol* **144**, 151-160 (1999).
55. P. D. Yurchenco, J. C. Schittny, Molecular architecture of basement membranes. *FASEB J* **4**, 1577-1590 (1990).
56. J. W. Fox *et al.*, Recombinant nidogen consists of three globular domains and mediates binding of laminin to collagen type IV. *EMBO J* **10**, 3137-3146 (1991).
57. M. Hopf, W. Gohring, E. Kohfeldt, Y. Yamada, R. Timpl, Recombinant domain IV of perlecan binds to nidogens, laminin-nidogen complex, fibronectin, fibulin-2 and heparin. *Eur J Biochem* **259**, 917-925 (1999).
58. A. Ries, W. Gohring, J. W. Fox, R. Timpl, T. Sasaki, Recombinant domains of mouse nidogen-1 and their binding to basement membrane proteins and monoclonal antibodies. *Eur J Biochem* **268**, 5119-5128 (2001).
59. E. Kohfeldt, T. Sasaki, W. Gohring, R. Timpl, Nidogen-2: a new basement membrane protein with diverse binding properties. *J Mol Biol* **282**, 99-109 (1998).
60. K. Salmivirta *et al.*, Binding of mouse nidogen-2 to basement membrane components and cells and its expression in embryonic and adult tissues suggest complementary functions of the two nidogens. *Exp Cell Res* **279**, 188-201 (2002).
61. S. Sarrazin, W. C. Lamanna, J. D. Esko, Heparan sulfate proteoglycans. *Cold Spring Harb Perspect Biol* **3** (2011).
62. J. M. Whitelock, J. Melrose, R. V. Iozzo, Diverse cell signaling events modulated by perlecan. *Biochemistry* **47**, 11174-11183 (2008).
63. P. C. Billings, M. Pacifici, Interactions of signaling proteins, growth factors and other proteins with heparan sulfate: mechanisms and mysteries. *Connect Tissue Res* **56**, 272-280 (2015).
64. C. C. Rider, B. Mulloy, Heparin, Heparan Sulphate and the TGF-beta Cytokine Superfamily. *Molecules* **22** (2017).

65. R. O. Hynes, Integrins: bidirectional, allosteric signaling machines. *Cell* **110**, 673-687 (2002).
66. P. ten Dijke, H. M. Arthur, Extracellular control of TGFbeta signalling in vascular development and disease. *Nat Rev Mol Cell Biol* **8**, 857-869 (2007).
67. R. D. Bell, B. V. Zlokovic, Neurovascular mechanisms and blood-brain barrier disorder in Alzheimer's disease. *Acta Neuropathol* **118**, 103-113 (2009).
68. A. Joutel *et al.*, Cerebrovascular dysfunction and microcirculation rarefaction precede white matter lesions in a mouse genetic model of cerebral ischemic small vessel disease. *J Clin Invest* **120**, 433-445 (2010).
69. N. A. Lassen, Cerebral blood flow and oxygen consumption in man. *Physiol Rev* **39**, 183-238 (1959).
70. J. Claassen, D. H. J. Thijssen, R. B. Panerai, F. M. Faraci, Regulation of cerebral blood flow in humans: physiology and clinical implications of autoregulation. *Physiol Rev* **101**, 1487-1559 (2021).
71. M. J. Davis, M. A. Hill, Signaling mechanisms underlying the vascular myogenic response. *Physiol Rev* **79**, 387-423 (1999).
72. D. W. Busija, D. D. Heistad, Factors involved in the physiological regulation of the cerebral circulation. *Rev Physiol Biochem Pharmacol* **101**, 161-211 (1984).
73. W. M. Bayliss, On the local reactions of the arterial wall to changes of internal pressure. *J Physiol* **28**, 220-231 (1902).
74. M. J. Davis, S. Earley, Y. S. Li, S. Chien, Vascular Mechanotransduction. *Physiol Rev* 10.1152/physrev.00053.2021 (2023).
75. D. R. Harder, Pressure-dependent membrane depolarization in cat middle cerebral artery. *Circ Res* **55**, 197-202 (1984).
76. H. J. Knot, M. T. Nelson, Regulation of arterial diameter and wall [Ca2+] in cerebral arteries of rat by membrane potential and intravascular pressure. *J Physiol* **508 (Pt 1)**, 199-209 (1998).
77. H. Zou, P. H. Ratz, M. A. Hill, Role of myosin phosphorylation and [Ca2+]i in myogenic reactivity and arteriolar tone. *Am J Physiol* **269**, H1590-1596 (1995).
78. A. L. Gonzales *et al.*, A PLCgamma1-dependent, force-sensitive signaling network in the myogenic constriction of cerebral arteries. *Sci Signal* **7**, ra49 (2014).
79. P. W. Pires *et al.*, The angiotensin II receptor type 1b is the primary sensor of intraluminal pressure in cerebral artery smooth muscle cells. *J Physiol* **595**, 4735-4753 (2017).
80. D. G. Welsh, A. D. Morielli, M. T. Nelson, J. E. Brayden, Transient receptor potential channels regulate myogenic tone of resistance arteries. *Circ Res* **90**, 248-250 (2002).
81. Q. Wang, M. D. Leo, D. Narayanan, K. P. Kuruvilla, J. H. Jaggar, Local coupling of TRPC6 to ANO1/TMEM16A channels in smooth muscle cells

amplifies vasoconstriction in cerebral arteries. *Am J Physiol Cell Physiol* **310**, C1001-1009 (2016).
82. W. F. Jackson, Potassium Channels in Regulation of Vascular Smooth Muscle Contraction and Growth. *Adv Pharmacol* **78**, 89-144 (2017).
83. R. H. Cox, Molecular determinants of voltage-gated potassium currents in vascular smooth muscle. *Cell Biochem Biophys* **42**, 167-195 (2005).
84. I. A. Greenwood, S. Ohya, New tricks for old dogs: KCNQ expression and role in smooth muscle. *Br J Pharmacol* **156**, 1196-1203 (2009).
85. A. Moreno-Dominguez, P. Cidad, E. Miguel-Velado, J. R. Lopez-Lopez, M. T. Perez-Garcia, De novo expression of Kv6.3 contributes to changes in vascular smooth muscle cell excitability in a hypertensive mice strain. *J Physiol* **587**, 625-640 (2009).
86. W. F. Jackson, K(V) channels and the regulation of vascular smooth muscle tone. *Microcirculation* **25** (2018).
87. J. Ledoux, M. E. Werner, J. E. Brayden, M. T. Nelson, Calcium-activated potassium channels and the regulation of vascular tone. *Physiology (Bethesda)* **21**, 69-78 (2006).
88. M. T. Nelson *et al.*, Relaxation of arterial smooth muscle by calcium sparks. *Science* **270**, 633-637 (1995).
89. J. E. Brayden, M. T. Nelson, Regulation of arterial tone by activation of calcium-dependent potassium channels. *Science* **256**, 532-535 (1992).
90. C. S. Roy, C. S. Sherrington, On the Regulation of the Blood-supply of the Brain. *J Physiol* **11**, 85-158 117 (1890).
91. C. Iadecola, The Neurovascular Unit Coming of Age: A Journey through Neurovascular Coupling in Health and Disease. *Neuron* **96**, 17-42 (2017).
92. M. Balbi *et al.*, Dysfunction of mouse cerebral arteries during early aging. *J Cereb Blood Flow Metab* **35**, 1445-1453 (2015).
93. M. Fabiani *et al.*, Neurovascular coupling in normal aging: a combined optical, ERP and fMRI study. *Neuroimage* **85 Pt 1**, 592-607 (2014).
94. O. Shabir *et al.*, Assessment of neurovascular coupling and cortical spreading depression in mixed mouse models of atherosclerosis and Alzheimer's disease. *Elife* **11** (2022).
95. X. K. Tong, C. Lecrux, P. Rosa-Neto, E. Hamel, Age-dependent rescue by simvastatin of Alzheimer's disease cerebrovascular and memory deficits. *J Neurosci* **32**, 4705-4715 (2012).
96. D. Attwell *et al.*, Glial and neuronal control of brain blood flow. *Nature* **468**, 232-243 (2010).
97. J. A. Filosa, A. D. Bonev, M. T. Nelson, Calcium dynamics in cortical astrocytes and arterioles during neurovascular coupling. *Circ Res* **95**, e73-81 (2004).
98. J. A. Filosa *et al.*, Local potassium signaling couples neuronal activity to vasodilation in the brain. *Nat Neurosci* **9**, 1397-1403 (2006).
99. W. Sun *et al.*, Glutamate-dependent neuroglial calcium signaling differs between young and adult brain. *Science* **339**, 197-200 (2013).

100. C. H. T. Tran, G. Peringod, G. R. Gordon, Astrocytes Integrate Behavioral State and Vascular Signals during Functional Hyperemia. *Neuron* **100**, 1133-1148 e1133 (2018).
101. K. Nizar *et al.*, In vivo stimulus-induced vasodilation occurs without IP3 receptor activation and may precede astrocytic calcium increase. *J Neurosci* **33**, 8411-8422 (2013).
102. P. Jego, J. Pacheco-Torres, A. Araque, S. Canals, Functional MRI in mice lacking IP3-dependent calcium signaling in astrocytes. *J Cereb Blood Flow Metab* **34**, 1599-1603 (2014).
103. T. A. Longden *et al.*, Capillary K(+)-sensing initiates retrograde hyperpolarization to increase local cerebral blood flow. *Nat Neurosci* **20**, 717-726 (2017).
104. P. S. Tsai, D. Kleinfeld, "In Vivo Two-Photon Laser Scanning Microscopy with Concurrent Plasma-Mediated Ablation Principles and Hardware Realization" in In Vivo Optical Imaging of Brain Function*,* nd, R. D. Frostig, Eds. (Boca Raton (FL), 2009).
105. P. Thakore *et al.*, Brain endothelial cell TRPA1 channels initiate neurovascular coupling. *Elife* **10** (2021).
106. L. Pantoni, Cerebral small vessel disease: from pathogenesis and clinical characteristics to therapeutic challenges. *Lancet Neurol* **9**, 689-701 (2010).
107. J. C. Choi, Genetics of cerebral small vessel disease. *J Stroke* **17**, 7-16 (2015).
108. A. Joutel, F. M. Faraci, Cerebral small vessel disease: insights and opportunities from mouse models of collagen IV-related small vessel disease and cerebral autosomal dominant arteriopathy with subcortical infarcts and leukoencephalopathy. *Stroke* **45**, 1215-1221 (2014).
109. A. Joutel, I. Haddad, J. Ratelade, M. T. Nelson, Perturbations of the cerebrovascular matrisome: A convergent mechanism in small vessel disease of the brain? *J Cereb Blood Flow Metab* **36**, 143-157 (2016).
110. L. C. Rutten-Jacobs *et al.*, Common NOTCH3 Variants and Cerebral Small-Vessel Disease. *Stroke* **46**, 1482-1487 (2015).
111. K. F. de Laat *et al.*, Loss of white matter integrity is associated with gait disorders in cerebral small vessel disease. *Brain* **134**, 73-83 (2011).
112. A. Poggesi *et al.*, Urinary complaints in nondisabled elderly people with age-related white matter changes: the Leukoaraiosis And DISability (LADIS) Study. *J Am Geriatr Soc* **56**, 1638-1643 (2008).
113. X. Xu *et al.*, Cerebral microbleeds and neuropsychiatric symptoms in an elderly Asian cohort. *J Neurol Neurosurg Psychiatry* **88**, 7-11 (2017).
114. F. E. de Leeuw *et al.*, Prevalence of cerebral white matter lesions in elderly people: a population based magnetic resonance imaging study. The Rotterdam Scan Study. *J Neurol Neurosurg Psychiatry* **70**, 9-14 (2001).
115. M. M. Poels *et al.*, Prevalence and risk factors of cerebral microbleeds: an update of the Rotterdam scan study. *Stroke* **41**, S103-106 (2010).

116. Z. Wang, Q. Chen, J. Chen, N. Yang, K. Zheng, Risk factors of cerebral small vessel disease: A systematic review and meta-analysis. *Medicine (Baltimore)* **100**, e28229 (2021).
117. Y. Shi, J. M. Wardlaw, Update on cerebral small vessel disease: a dynamic whole-brain disease. *Stroke Vasc Neurol* **1**, 83-92 (2016).
118. R. Lemmens *et al.*, Novel COL4A1 mutations cause cerebral small vessel disease by haploinsufficiency. *Hum Mol Genet* **22**, 391-397 (2013).
119. K. H. Chou *et al.*, Classification differentiates clinical and neuroanatomic features of cerebral small vessel disease. *Brain Commun* **3**, fcab107 (2021).
120. R. N. Kalaria, C. Ballard, Overlap between pathology of Alzheimer disease and vascular dementia. *Alzheimer Dis Assoc Disord* **13 Suppl 3**, S115-123 (1999).
121. W. D. Brenowitz, P. T. Nelson, L. M. Besser, K. B. Heller, W. A. Kukull, Cerebral amyloid angiopathy and its co-occurrence with Alzheimer's disease and other cerebrovascular neuropathologic changes. *Neurobiol Aging* **36**, 2702-2708 (2015).
122. S. Kocahan, Z. Dogan, Mechanisms of Alzheimer's Disease Pathogenesis and Prevention: The Brain, Neural Pathology, N-methyl-D-aspartate Receptors, Tau Protein and Other Risk Factors. *Clin Psychopharmacol Neurosci* **15**, 1-8 (2017).
123. J. P. Vonsattel *et al.*, Cerebral amyloid angiopathy without and with cerebral hemorrhages: a comparative histological study. *Ann Neurol* **30**, 637-649 (1991).
124. M. O. McCarron, J. A. Nicoll, Cerebral amyloid angiopathy and thrombolysis-related intracerebral haemorrhage. *Lancet Neurol* **3**, 484-492 (2004).
125. N. Liu *et al.*, The dynamic change of phenotypic markers of smooth muscle cells in an animal model of cerebral small vessel disease. *Microvasc Res* **133**, 104061 (2021).
126. C. Banerjee, M. I. Chimowitz, Stroke Caused by Atherosclerosis of the Major Intracranial Arteries. *Circ Res* **120**, 502-513 (2017).
127. G. L. Baumbach, D. D. Heistad, Regional, segmental, and temporal heterogeneity of cerebral vascular autoregulation. *Ann Biomed Eng* **13**, 303-310 (1985).
128. F. M. Faraci, D. D. Heistad, Regulation of large cerebral arteries and cerebral microvascular pressure. *Circ Res* **66**, 8-17 (1990).
129. Z. Springo *et al.*, Aging impairs myogenic adaptation to pulsatile pressure in mouse cerebral arteries. *J Cereb Blood Flow Metab* **35**, 527-530 (2015).
130. T. Tarumi *et al.*, Cerebral hemodynamics in normal aging: central artery stiffness, wave reflection, and pressure pulsatility. *J Cereb Blood Flow Metab* **34**, 971-978 (2014).
131. C. Iadecola, R. L. Davisson, Hypertension and cerebrovascular dysfunction. *Cell Metab* **7**, 476-484 (2008).

132. X. Xu *et al.*, Age-related Impairment of Vascular Structure and Functions. *Aging Dis* **8**, 590-610 (2017).
133. J. Duncombe *et al.*, Chronic cerebral hypoperfusion: a key mechanism leading to vascular cognitive impairment and dementia. Closing the translational gap between rodent models and human vascular cognitive impairment and dementia. *Clin Sci (Lond)* **131**, 2451-2468 (2017).
134. L. J. Ignarro, Endothelium-derived nitric oxide: actions and properties. *FASEB J* **3**, 31-36 (1989).
135. Q. Gao *et al.*, S100B and ADMA in cerebral small vessel disease and cognitive dysfunction. *J Neurol Sci* **354**, 27-32 (2015).
136. S. Munoz Maniega *et al.*, Integrity of normal-appearing white matter: Influence of age, visible lesion burden and hypertension in patients with small-vessel disease. *J Cereb Blood Flow Metab* **37**, 644-656 (2017).
137. C. E. Zhang *et al.*, Blood-brain barrier leakage is more widespread in patients with cerebral small vessel disease. *Neurology* **88**, 426-432 (2017).
138. Y. Li *et al.*, Compromised Blood-Brain Barrier Integrity Is Associated With Total Magnetic Resonance Imaging Burden of Cerebral Small Vessel Disease. *Front Neurol* **9**, 221 (2018).
139. J. Walsh *et al.*, Microglial activation and blood-brain barrier permeability in cerebral small vessel disease. *Brain* **144**, 1361-1371 (2021).
140. S. M. Wong *et al.*, Blood-brain barrier impairment and hypoperfusion are linked in cerebral small vessel disease. *Neurology* **92**, e1669-e1677 (2019).
141. R. M. Rajani *et al.*, Blood brain barrier leakage is not a consistent feature of white matter lesions in CADASIL. *Acta Neuropathol Commun* **7**, 187 (2019).
142. E. L. Bailey, C. Smith, C. L. Sudlow, J. M. Wardlaw, Pathology of lacunar ischemic stroke in humans--a systematic review. *Brain Pathol* **22**, 583-591 (2012).
143. L. Cucullo, M. Hossain, V. Puvenna, N. Marchi, D. Janigro, The role of shear stress in Blood-Brain Barrier endothelial physiology. *BMC Neurosci* **12**, 40 (2011).
144. M. Mancuso *et al.*, Monogenic cerebral small-vessel diseases: diagnosis and therapy. Consensus recommendations of the European Academy of Neurology. *Eur J Neurol* **27**, 909-927 (2020).
145. S. K. Narayan, G. Gorman, R. N. Kalaria, G. A. Ford, P. F. Chinnery, The minimum prevalence of CADASIL in northeast England. *Neurology* **78**, 1025-1027 (2012).
146. J. W. Rutten *et al.*, The effect of NOTCH3 pathogenic variant position on CADASIL disease severity: NOTCH3 EGFr 1-6 pathogenic variant are associated with a more severe phenotype and lower survival compared with EGFr 7-34 pathogenic variant. *Genet Med* **21**, 676-682 (2019).
147. H. Chabriat, A. Joutel, M. Dichgans, E. Tournier-Lasserve, M. G. Bousser, Cadasil. *Lancet Neurol* **8**, 643-653 (2009).

148. S. Hosseini-Alghaderi, M. Baron, Notch3 in Development, Health and Disease. *Biomolecules* **10** (2020).
149. V. Domenga *et al.*, Notch3 is required for arterial identity and maturation of vascular smooth muscle cells. *Genes Dev* **18**, 2730-2735 (2004).
150. A. Joutel *et al.*, Strong clustering and stereotyped nature of Notch3 mutations in CADASIL patients. *Lancet* **350**, 1511-1515 (1997).
151. N. Peters *et al.*, Spectrum of mutations in biopsy-proven CADASIL: implications for diagnostic strategies. *Arch Neurol* **62**, 1091-1094 (2005).
152. M. Duering *et al.*, Co-aggregate formation of CADASIL-mutant NOTCH3: a single-particle analysis. *Hum Mol Genet* **20**, 3256-3265 (2011).
153. A. Ishiko *et al.*, Notch3 ectodomain is a major component of granular osmiophilic material (GOM) in CADASIL. *Acta Neuropathol* **112**, 333-339 (2006).
154. M. Baudrimont, F. Dubas, A. Joutel, E. Tournier-Lasserve, M. G. Bousser, Autosomal dominant leukoencephalopathy and subcortical ischemic stroke. A clinicopathological study. *Stroke* **24**, 122-125 (1993).
155. A. Joutel *et al.*, The ectodomain of the Notch3 receptor accumulates within the cerebrovasculature of CADASIL patients. *J Clin Invest* **105**, 597-605 (2000).
156. K. Coupland, U. Lendahl, H. Karlstrom, Role of NOTCH3 Mutations in the Cerebral Small Vessel Disease Cerebral Autosomal Dominant Arteriopathy With Subcortical Infarcts and Leukoencephalopathy. *Stroke* **49**, 2793-2800 (2018).
157. J. W. Rutten *et al.*, Hypomorphic NOTCH3 alleles do not cause CADASIL in humans. *Hum Mutat* **34**, 1486-1489 (2013).
158. T. Mizuno, I. Mizuta, A. Watanabe-Hosomi, M. Mukai, T. Koizumi, Clinical and Genetic Aspects of CADASIL. *Front Aging Neurosci* **12**, 91 (2020).
159. E. Cognat, S. Cleophax, V. Domenga-Denier, A. Joutel, Early white matter changes in CADASIL: evidence of segmental intramyelinic oedema in a pre-clinical mouse model. *Acta Neuropathol Commun* **2**, 49 (2014).
160. F. Dabertrand *et al.*, Potassium channelopathy-like defect underlies early-stage cerebrovascular dysfunction in a genetic model of small vessel disease. *Proc Natl Acad Sci U S A* **112**, E796-805 (2015).
161. C. Capone *et al.*, Reducing Timp3 or vitronectin ameliorates disease manifestations in CADASIL mice. *Ann Neurol* **79**, 387-403 (2016).
162. M. Monet-Lepretre *et al.*, Abnormal recruitment of extracellular matrix proteins by excess Notch3 ECD: a new pathomechanism in CADASIL. *Brain* **136**, 1830-1845 (2013).
163. K. Brew, H. Nagase, The tissue inhibitors of metalloproteinases (TIMPs): an ancient family with structural and functional diversity. *Biochim Biophys Acta* **1803**, 55-71 (2010).
164. F. Dabertrand *et al.*, PIP2 corrects cerebral blood flow deficits in small vessel disease by rescuing capillary Kir2.1 activity. *Proc Natl Acad Sci U S A* **118** (2021).

165. B. C. Suh, B. Hille, PIP2 is a necessary cofactor for ion channel function: how and why? *Annu Rev Biophys* **37**, 175-195 (2008).
166. F. Dabertrand *et al.*, PIP(2) corrects cerebral blood flow deficits in small vessel disease by rescuing capillary Kir2.1 activity. *Proc Natl Acad Sci U S A* **118** (2021).
167. A. Mughal, O. F. Harraz, A. L. Gonzales, D. Hill-Eubanks, M. T. Nelson, PIP2 Improves Cerebral Blood Flow in a Mouse Model of Alzheimer's Disease. *Function (Oxf)* **2**, zqab010 (2021).
168. T. Fukutake, K. Hirayama, Familial young-adult-onset arteriosclerotic leukoencephalopathy with alopecia and lumbago without arterial hypertension. *Eur Neurol* **35**, 69-79 (1995).
169. K. Hara *et al.*, Association of HTRA1 mutations and familial ischemic cerebral small-vessel disease. *N Engl J Med* **360**, 1729-1739 (2009).
170. H. Nozaki *et al.*, Distinct molecular mechanisms of HTRA1 mutants in manifesting heterozygotes with CARASIL. *Neurology* **86**, 1964-1974 (2016).
171. T. Oide *et al.*, Extensive loss of arterial medial smooth muscle cells and mural extracellular matrix in cerebral autosomal recessive arteriopathy with subcortical infarcts and leukoencephalopathy (CARASIL). *Neuropathology* **28**, 132-142 (2008).
172. K. Arima, S. Yanagawa, N. Ito, S. Ikeda, Cerebral arterial pathology of CADASIL and CARASIL (Maeda syndrome). *Neuropathology* **23**, 327-334 (2003).
173. T. Fukutake, Cerebral autosomal recessive arteriopathy with subcortical infarcts and leukoencephalopathy (CARASIL): from discovery to gene identification. *J Stroke Cerebrovasc Dis* **20**, 85-93 (2011).
174. T. Clausen, M. Kaiser, R. Huber, M. Ehrmann, HTRA proteases: regulated proteolysis in protein quality control. *Nat Rev Mol Cell Biol* **12**, 152-162 (2011).
175. A. C. Cabrera *et al.*, HtrA1 activation is driven by an allosteric mechanism of inter-monomer communication. *Sci Rep* **7**, 14804 (2017).
176. Y. Nishimoto *et al.*, A novel mutation in the HTRA1 gene causes CARASIL without alopecia. *Neurology* **76**, 1353-1355 (2011).
177. C. Oka *et al.*, HtrA1 serine protease inhibits signaling mediated by Tgfbeta family proteins. *Development* **131**, 1041-1053 (2004).
178. M. J. Goumans, Z. Liu, P. ten Dijke, TGF-beta signaling in vascular biology and dysfunction. *Cell Res* **19**, 116-127 (2009).
179. T. H. Lan, X. Q. Huang, H. M. Tan, Vascular fibrosis in atherosclerosis. *Cardiovasc Pathol* **22**, 401-407 (2013).
180. A. Shiga *et al.*, Cerebral small-vessel disease protein HTRA1 controls the amount of TGF-beta1 via cleavage of proTGF-beta1. *Hum Mol Genet* **20**, 1800-1810 (2011).
181. M. Shi *et al.*, Latent TGF-beta structure and activation. *Nature* **474**, 343-349 (2011).

182. S. Launay *et al.*, HtrA1-dependent proteolysis of TGF-beta controls both neuronal maturation and developmental survival. *Cell Death Differ* **15**, 1408-1416 (2008).
183. J. R. Graham *et al.*, Serine protease HTRA1 antagonizes transforming growth factor-beta signaling by cleaving its receptors and loss of HTRA1 in vivo enhances bone formation. *PLoS One* **8**, e74094 (2013).
184. S. Lanfranconi, H. S. Markus, COL4A1 mutations as a monogenic cause of cerebral small vessel disease: a systematic review. *Stroke* **41**, e513-518 (2010).
185. D. S. Kuo, C. Labelle-Dumais, D. B. Gould, COL4A1 and COL4A2 mutations and disease: insights into pathogenic mechanisms and potential therapeutic targets. *Hum Mol Genet* **21**, R97-110 (2012).
186. E. Poschl *et al.*, Collagen IV is essential for basement membrane stability but dispensable for initiation of its assembly during early development. *Development* **131**, 1619-1628 (2004).
187. D. B. Gould, J. K. Marchant, O. V. Savinova, R. S. Smith, S. W. John, Col4a1 mutation causes endoplasmic reticulum stress and genetically modifiable ocular dysgenesis. *Hum Mol Genet* **16**, 798-807 (2007).
188. M. Jeanne *et al.*, COL4A2 mutations impair COL4A1 and COL4A2 secretion and cause hemorrhagic stroke. *Am J Hum Genet* **90**, 91-101 (2012).
189. D. S. Kuo *et al.*, Allelic heterogeneity contributes to variability in ocular dysgenesis, myopathy and brain malformations caused by Col4a1 and Col4a2 mutations. *Hum Mol Genet* **23**, 1709-1722 (2014).
190. A. Fribley, K. Zhang, R. J. Kaufman, Regulation of apoptosis by the unfolded protein response. *Methods Mol Biol* **559**, 191-204 (2009).
191. N. Chaudhari, P. Talwar, A. Parimisetty, C. Lefebvre d'Hellencourt, P. Ravanan, A molecular web: endoplasmic reticulum stress, inflammation, and oxidative stress. *Front Cell Neurosci* **8**, 213 (2014).
192. L. S. Murray *et al.*, Chemical chaperone treatment reduces intracellular accumulation of mutant collagen IV and ameliorates the cellular phenotype of a COL4A2 mutation that causes haemorrhagic stroke. *Hum Mol Genet* **23**, 283-292 (2014).
193. D. H. Perlmutter, Chemical chaperones: a pharmacological strategy for disorders of protein folding and trafficking. *Pediatr Res* **52**, 832-836 (2002).
194. G. Hayashi, C. Labelle-Dumais, D. B. Gould, Use of sodium 4-phenylbutyrate to define therapeutic parameters for reducing intracerebral hemorrhage and myopathy in Col4a1 mutant mice. *Dis Model Mech* **11** (2018).
195. M. Jeanne, J. Jorgensen, D. B. Gould, Molecular and Genetic Analyses of Collagen Type IV Mutant Mouse Models of Spontaneous Intracerebral Hemorrhage Identify Mechanisms for Stroke Prevention. *Circulation* **131**, 1555-1565 (2015).

196. M. Mao *et al.*, Identification of fibronectin 1 as a candidate genetic modifier in a Col4a1 mutant mouse model of Gould syndrome. *Dis Model Mech* **14** (2021).
197. M. Mao, C. Labelle-Dumais, S. F. Tufa, D. R. Keene, D. B. Gould, Elevated TGFbeta signaling contributes to ocular anterior segment dysgenesis in Col4a1 mutant mice. *Matrix Biol* **110**, 151-173 (2022).
198. E. Plaisier *et al.*, COL4A1 mutations and hereditary angiopathy, nephropathy, aneurysms, and muscle cramps. *N Engl J Med* **357**, 2687-2695 (2007).
199. J. D. Parkin *et al.*, Mapping structural landmarks, ligand binding sites, and missense mutations to the collagen IV heterotrimers predicts major functional domains, novel interactions, and variation in phenotypes in inherited diseases affecting basement membranes. *Hum Mutat* **32**, 127-143 (2011).
200. S. Alamowitch *et al.*, Cerebrovascular disease related to COL4A1 mutations in HANAC syndrome. *Neurology* **73**, 1873-1882 (2009).
201. E. Plaisier *et al.*, Novel COL4A1 mutations associated with HANAC syndrome: a role for the triple helical CB3[IV] domain. *Am J Med Genet A* **152A**, 2550-2555 (2010).
202. E. Verdura *et al.*, Disruption of a miR-29 binding site leading to COL4A1 upregulation causes pontine autosomal dominant microangiopathy with leukoencephalopathy. *Ann Neurol* **80**, 741-753 (2016).
203. X. Q. Ding *et al.*, MRI features of pontine autosomal dominant microangiopathy and leukoencephalopathy (PADMAL). *J Neuroimaging* **20**, 134-140 (2010).
204. H. S. Markus, Genes, endothelial function and cerebral small vessel disease in man. *Exp Physiol* **93**, 121-127 (2008).
205. A. L. Gonzales, Z. I. Garcia, G. C. Amberg, S. Earley, Pharmacological inhibition of TRPM4 hyperpolarizes vascular smooth muscle. *Am J Physiol Cell Physiol* **299**, C1195-1202 (2010).
206. S. Earley, B. J. Waldron, J. E. Brayden, Critical role for transient receptor potential channel TRPM4 in myogenic constriction of cerebral arteries. *Circ Res* **95**, 922-929 (2004).
207. H. J. Knot, N. B. Standen, M. T. Nelson, Ryanodine receptors regulate arterial diameter and wall [Ca2+] in cerebral arteries of rat via Ca2+-dependent K+ channels. *J Physiol* **508 (Pt 1)**, 211-221 (1998).
208. A. L. Gonzales, G. C. Amberg, S. Earley, Ca2+ release from the sarcoplasmic reticulum is required for sustained TRPM4 activity in cerebral artery smooth muscle cells. *Am J Physiol Cell Physiol* **299**, C279-288 (2010).
209. A. Malo, B. Kruger, B. Goke, C. H. Kubisch, 4-Phenylbutyric acid reduces endoplasmic reticulum stress, trypsin activation, and acinar cell apoptosis while increasing secretion in rat pancreatic acini. *Pancreas* **42**, 92-101 (2013).

210. M. E. Meuwissen *et al.*, The expanding phenotype of COL4A1 and COL4A2 mutations: clinical data on 13 newly identified families and a review of the literature. *Genet Med* **17**, 843-853 (2015).
211. A. K. Kraeuter, P. C. Guest, Z. Sarnyai, The Y-Maze for Assessment of Spatial Working and Reference Memory in Mice. *Methods Mol Biol* **1916**, 105-111 (2019).
212. H. A. T. Pritchard *et al.*, Microtubule structures underlying the sarcoplasmic reticulum support peripheral coupling sites to regulate smooth muscle contractility. *Sci Signal* **10** (2017).
213. P. Launay *et al.*, TRPM4 is a Ca2+-activated nonselective cation channel mediating cell membrane depolarization. *Cell* **109**, 397-407 (2002).
214. S. Earley, S. V. Straub, J. E. Brayden, Protein kinase C regulates vascular myogenic tone through activation of TRPM4. *Am J Physiol Heart Circ Physiol* **292**, H2613-2622 (2007).
215. J. Schleifenbaum *et al.*, Stretch-activation of angiotensin II type 1a receptors contributes to the myogenic response of mouse mesenteric and renal arteries. *Circ Res* **115**, 263-272 (2014).
216. N. Yasuda *et al.*, Conformational switch of angiotensin II type 1 receptor underlying mechanical stress-induced activation. *EMBO Rep* **9**, 179-186 (2008).
217. P. S. McPherson *et al.*, The brain ryanodine receptor: a caffeine-sensitive calcium release channel. *Neuron* **7**, 17-25 (1991).
218. S. Wray, T. Burdyga, Sarcoplasmic reticulum function in smooth muscle. *Physiol Rev* **90**, 113-178 (2010).
219. T. Iannitti, B. Palmieri, Clinical and experimental applications of sodium phenylbutyrate. *Drugs R D* **11**, 227-249 (2011).
220. M. T. Nelson, J. M. Quayle, Physiological roles and properties of potassium channels in arterial smooth muscle. *Am J Physiol* **268**, C799-822 (1995).
221. J. G. McCarron, J. W. Craig, K. N. Bradley, T. C. Muir, Agonist-induced phasic and tonic responses in smooth muscle are mediated by InsP(3). *J Cell Sci* **115**, 2207-2218 (2002).
222. A. Shmygol, S. Wray, Modulation of agonist-induced Ca2+ release by SR Ca2+ load: direct SR and cytosolic Ca2+ measurements in rat uterine myocytes. *Cell Calcium* **37**, 215-223 (2005).
223. A. B. Parekh, J. W. Putney, Jr., Store-operated calcium channels. *Physiol Rev* **85**, 757-810 (2005).
224. R. A. Fernandez *et al.*, Upregulated expression of STIM2, TRPC6, and Orai2 contributes to the transition of pulmonary arterial smooth muscle cells from a contractile to proliferative phenotype. *Am J Physiol Cell Physiol* **308**, C581-593 (2015).
225. V. Krishnan *et al.*, STIM1-dependent peripheral coupling governs the contractility of vascular smooth muscle cells. *Elife* **11** (2022).

226. M. Potier *et al.*, Evidence for STIM1- and Orai1-dependent store-operated calcium influx through ICRAC in vascular smooth muscle cells: role in proliferation and migration. *FASEB J* **23**, 2425-2437 (2009).
227. R. Bravo-Sagua *et al.*, Sarcoplasmic reticulum and calcium signaling in muscle cells: Homeostasis and disease. *Int Rev Cell Mol Biol* **350**, 197-264 (2020).
228. M. Schroder, R. J. Kaufman, The mammalian unfolded protein response. *Annu Rev Biochem* **74**, 739-789 (2005).
229. P. F. Lebeau, K. Platko, J. H. Byun, R. C. Austin, Calcium as a reliable marker for the quantitative assessment of endoplasmic reticulum stress in live cells. *J Biol Chem* **296**, 100779 (2021).
230. W. R. Yamamoto *et al.*, Endoplasmic reticulum stress alters ryanodine receptor function in the murine pancreatic beta cell. *J Biol Chem* **294**, 168-181 (2019).
231. J. Favor *et al.*, Type IV procollagen missense mutations associated with defects of the eye, vascular stability, the brain, kidney function and embryonic or postnatal viability in the mouse, Mus musculus: an extension of the Col4a1 allelic series and the identification of the first two Col4a2 mutant alleles. *Genetics* **175**, 725-736 (2007).
232. N. Pallast *et al.*, Processing Pipeline for Atlas-Based Imaging Data Analysis of Structural and Functional Mouse Brain MRI (AIDAmri). *Front Neuroinform* **13**, 42 (2019).
233. H. W. Dong, *Allen reference atlas : a digital color brain atlas of the C57Black/6J male mouse* (Wiley, Hoboken, N.J., 2008), pp. ix, 366 p.
234. A. L. Gonzales, G. C. Amberg, S. Earley, Ca2+ release from the sarcoplasmic reticulum is required for sustained TRPM4 activity in cerebral artery smooth muscle cells. *American journal of physiology Cell physiology* **299**, C279-288 (2010).
235. M. Dichgans, D. Leys, Vascular Cognitive Impairment. *Circ Res* **120**, 573-591 (2017).
236. C. Labelle-Dumais *et al.*, COL4A1 Mutations Cause Neuromuscular Disease with Tissue-Specific Mechanistic Heterogeneity. *Am J Hum Genet* **104**, 847-860 (2019).
237. M. D. Shoulders, R. T. Raines, Collagen structure and stability. *Annu Rev Biochem* **78**, 929-958 (2009).
238. S. Zagaglia *et al.*, Neurologic phenotypes associated with COL4A1/2 mutations: Expanding the spectrum of disease. *Neurology* **91**, e2078-e2088 (2018).
239. M. Jeanne, D. B. Gould, Genotype-phenotype correlations in pathology caused by collagen type IV alpha 1 and 2 mutations. *Matrix Biol* **57-58**, 29-44 (2017).
240. B. Nilius *et al.*, The Ca2+-activated cation channel TRPM4 is regulated by phosphatidylinositol 4,5-biphosphate. *EMBO J* **25**, 467-478 (2006).

241. Z. Zhang, H. Okawa, Y. Wang, E. R. Liman, Phosphatidylinositol 4,5-bisphosphate rescues TRPM4 channels from desensitization. *J Biol Chem* **280**, 39185-39192 (2005).
242. B. Nilius *et al.*, Voltage dependence of the Ca2+-activated cation channel TRPM4. *J Biol Chem* **278**, 30813-30820 (2003).
243. P. Arullampalam *et al.*, Species-Specific Effects of Cation Channel TRPM4 Small-Molecule Inhibitors. *Front Pharmacol* **12**, 712354 (2021).
244. L. C. Ozhathil *et al.*, Identification of potent and selective small molecule inhibitors of the cation channel TRPM4. *Br J Pharmacol* **175**, 2504-2519 (2018).
245. A. L. Gonzales, S. Earley, Endogenous cytosolic Ca(2+) buffering is necessary for TRPM4 activity in cerebral artery smooth muscle cells. *Cell Calcium* **51**, 82-93 (2012).
246. S. Ali *et al.*, Nitric Oxide Signals Through IRAG to Inhibit TRPM4 Channels and Dilate Cerebral Arteries. *Function (Oxf)* **2**, zqab051 (2021).
247. J. Xie, Q. Li, X. Ding, Y. Gao, GSK1059615 kills head and neck squamous cell carcinoma cells possibly via activating mitochondrial programmed necrosis pathway. *Oncotarget* **8**, 50814-50823 (2017).
248. L. Zhang, F. Zhou, P. ten Dijke, Signaling interplay between transforming growth factor-beta receptor and PI3K/AKT pathways in cancer. *Trends Biochem Sci* **38**, 612-620 (2013).
249. G. J. Inman *et al.*, SB-431542 is a potent and specific inhibitor of transforming growth factor-beta superfamily type I activin receptor-like kinase (ALK) receptors ALK4, ALK5, and ALK7. *Mol Pharmacol* **62**, 65-74 (2002).
250. S. Earley, D. Kleinfeld, PIP2 as the "coin of the realm" for neurovascular coupling. *Proc Natl Acad Sci U S A* **118** (2021).
251. A. Hamidi *et al.*, TGF-beta promotes PI3K-AKT signaling and prostate cancer cell migration through the TRAF6-mediated ubiquitylation of p85alpha. *Sci Signal* **10** (2017).
252. J. Ratelade *et al.*, Reducing Hypermuscularization of the Transitional Segment Between Arterioles and Capillaries Protects Against Spontaneous Intracerebral Hemorrhage. *Circulation* **141**, 2078-2094 (2020).
253. J. Ratelade *et al.*, Severity of arterial defects in the retina correlates with the burden of intracerebral haemorrhage in COL4A1-related stroke. *J Pathol* **244**, 408-420 (2018).
254. C. F. Wenceslau *et al.*, Guidelines for the measurement of vascular function and structure in isolated arteries and veins. *American journal of physiology. Heart and circulatory physiology* 10.1152/ajpheart.01021.2020 (2021).
255. R. A. Corriveau *et al.*, The Science of Vascular Contributions to Cognitive Impairment and Dementia (VCID): A Framework for Advancing Research Priorities in the Cerebrovascular Biology of Cognitive Decline. *Cell Mol Neurobiol* **36**, 281-288 (2016).

256. J. M. Wardlaw, C. Smith, M. Dichgans, Mechanisms of sporadic cerebral small vessel disease: insights from neuroimaging. *Lancet Neurol* **12**, 483-497 (2013).
257. S. Debette, S. Schilling, M. G. Duperron, S. C. Larsson, H. S. Markus, Clinical Significance of Magnetic Resonance Imaging Markers of Vascular Brain Injury A Systematic Review and Meta-analysis. *Jama Neurol* **76**, 81-94 (2019).
258. L. E. Evans *et al.*, Cardiovascular comorbidities, inflammation, and cerebral small vessel disease. *Cardiovasc Res* **117**, 2575-2588 (2021).
259. M. van Dinther *et al.*, Extracerebral microvascular dysfunction is related to brain MRI markers of cerebral small vessel disease: The Maastricht Study. *Geroscience* **44**, 147-157 (2022).
260. A. Jokumsen-Cabral, A. Aires, S. Ferreira, E. Azevedo, P. Castro, Primary involvement of neurovascular coupling in cerebral autosomal-dominant arteriopathy with subcortical infarcts and leukoencephalopathy. *J Neurol* **266**, 1782-1788 (2019).
261. M. Jeanne, D. B. Gould, Genotype-phenotype correlations in pathology caused by collagen type IV alpha 1 and 2 mutations. *Matrix Biol* **57-58**, 29-44 (2017).
262. M. Mao, M. V. Alavi, C. Labelle-Dumais, D. B. Gould, Type IV Collagens and Basement Membrane Diseases: Cell Biology and Pathogenic Mechanisms. *Curr Top Membr* **76**, 61-116 (2015).
263. D. S. Kuo, C. Labelle-Dumais, D. B. Gould, COL4A1 and COL4A2 mutations and disease: insights into pathogenic mechanisms and potential therapeutic targets. *Hum Mol Genet* **21**, R97-R110 (2012).
264. H. Girouard *et al.*, Astrocytic endfoot Ca2+ and BK channels determine both arteriolar dilation and constriction. *Proc Natl Acad Sci U S A* **107**, 3811-3816 (2010).
265. G. C. Petzold, D. F. Albeanu, T. F. Sato, V. N. Murthy, Coupling of neural activity to blood flow in olfactory glomeruli is mediated by astrocytic pathways. *Neuron* **58**, 897-910 (2008).
266. C. Iadecola, M. Nedergaard, Glial regulation of the cerebral microvasculature. *Nat Neurosci* **10**, 1369-1376 (2007).
267. P. J. Drew, C. Mateo, K. L. Turner, X. Yu, D. Kleinfeld, Ultra-slow Oscillations in fMRI and Resting-State Connectivity: Neuronal and Vascular Contributions and Technical Confounds. *Neuron* **107**, 782-804 (2020).
268. L. Kaplan, B. W. Chow, C. H. Gu, Neuronal regulation of the blood-brain barrier and neurovascular coupling. *Nat Rev Neurosci* **21**, 416-432 (2020).
269. C. L. Huang, S. Feng, D. W. Hilgemann, Direct activation of inward rectifier potassium channels by PIP2 and its stabilization by Gbetagamma. *Nature* **391**, 803-806 (1998).
270. S. B. Hansen, X. Tao, R. MacKinnon, Structural basis of PIP2 activation of the classical inward rectifier K+ channel Kir2.2. *Nature* **477**, 495-U152 (2011).

271. S. Hilal *et al.*, Prevalence, risk factors and consequences of cerebral small vessel diseases: data from three Asian countries. *J Neurol Neurosurg Psychiatry* **88**, 669-674 (2017).
272. H. J. Knot, P. A. Zimmermann, M. T. Nelson, Extracellular K(+)-induced hyperpolarizations and dilatations of rat coronary and cerebral arteries involve inward rectifier K(+) channels. *J Physiol* **492 (Pt 2)**, 419-430 (1996).
273. H. Girouard *et al.*, Astrocytic endfoot Ca2+ and BK channels determine both arteriolar dilation and constriction. *P Natl Acad Sci USA* **107**, 3811-3816 (2010).
274. L. Park *et al.*, Age-dependent neurovascular dysfunction and damage in a mouse model of cerebral amyloid angiopathy. *Stroke* **45**, 1815-1821 (2014).
275. S. Tarantini *et al.*, Pharmacologically-induced neurovascular uncoupling is associated with cognitive impairment in mice. *J Cerebr Blood F Met* **35**, 1871-1881 (2015).
276. M. Ohno *et al.*, BACE1 deficiency rescues memory deficits and cholinergic dysfunction in a mouse model of Alzheimer's disease. *Neuron* **41**, 27-33 (2004).
277. H. Oakley *et al.*, Intraneuronal beta-amyloid aggregates, neurodegeneration, and neuron loss in transgenic mice with five familial Alzheimer's disease mutations: Potential factors in amyloid plaque formation. *J Neurosci* **26**, 10129-10140 (2006).
278. A. K. Swonger, R. H. Rech, Serotonergic and cholinergic involvement in habituation of activity and spontaneous alternation of rats in a Y maze. *J Comp Physiol Psychol* **81**, 509-522 (1972).
279. Z. Sarnyai *et al.*, Impaired hippocampal-dependent learning and functional abnormalities in the hippocampus in mice lacking serotonin(1A) receptors. *Proc Natl Acad Sci U S A* **97**, 14731-14736 (2000).
280. S. Suer, A. Sickmann, H. E. Meyer, F. W. Herberg, L. M. Heilmeyer, Jr., Human phosphatidylinositol 4-kinase isoform PI4K92. Expression of the recombinant enzyme and determination of multiple phosphorylation sites. *Eur J Biochem* **268**, 2099-2106 (2001).
281. A. Balla, T. Balla, Phosphatidylinositol 4-kinases: old enzymes with emerging functions. *Trends Cell Biol* **16**, 351-361 (2006).
282. T. Gehrmann *et al.*, Functional expression and characterisation of a new human phosphatidylinositol 4-kinase PI4K230. *Biochim Biophys Acta* **1437**, 341-356 (1999).
283. O. F. Harraz, T. A. Longden, F. Dabertrand, D. Hill-Eubanks, M. T. Nelson, Endothelial GqPCR activity controls capillary electrical signaling and brain blood flow through PIP2 depletion. *P Natl Acad Sci USA* **115**, E3569-E3577 (2018).
284. A. V. Bakin, A. K. Tomlinson, N. A. Bhowmick, H. L. Moses, C. L. Arteaga, Phosphatidylinositol 3-kinase function is required for transforming growth

factor beta-mediated epithelial to mesenchymal transition and cell migration. *Journal of Biological Chemistry* **275**, 36803-36810 (2000).
285. I. Shin, A. V. Bakin, U. Rodeck, A. Brunet, C. L. Arteaga, Transforming growth factor beta enhances epithelial cell survival via Akt-dependent regulation of FKHRL1. *Mol Biol Cell* **12**, 3328-3339 (2001).
286. K. Branyan *et al.*, Elevated TGFbeta Signaling Contributes to Cerebral Small Vessel Disease in Mouse Models of Gould Syndrome. *Matrix Biol* 10.1016/j.matbio.2022.11.007 (2022).
287. R. Mishra, H. Patel, S. Alanazi, M. K. Kilroy, J. T. Garrett, PI3K Inhibitors in Cancer: Clinical Implications and Adverse Effects. *Int J Mol Sci* **22** (2021).
288. N. Verzijl *et al.*, Effect of collagen turnover on the accumulation of advanced glycation end products. *J Biol Chem* **275**, 39027-39031 (2000).
289. R. Nissen, G. J. Cardinale, S. Udenfriend, Increased turnover of arterial collagen in hypertensive rats. *Proc Natl Acad Sci U S A* **75**, 451-453 (1978).
290. P. K. Mays, R. J. McAnulty, J. S. Campa, G. J. Laurent, Age-related changes in collagen synthesis and degradation in rat tissues. Importance of degradation of newly synthesized collagen in regulating collagen production. *Biochem J* **276 (Pt 2)**, 307-313 (1991).
291. R. P. Boot-Handford, M. Kurkinen, D. J. Prockop, Steady-state levels of mRNAs coding for the type IV collagen and laminin polypeptide chains of basement membranes exhibit marked tissue-specific stoichiometric variations in the rat. *J Biol Chem* **262**, 12475-12478 (1987).
292. J. P. Annes, J. S. Munger, D. B. Rifkin, Making sense of latent TGFbeta activation. *J Cell Sci* **116**, 217-224 (2003).
293. P.-E. Gleizes, R. C. Beavis, R. Mazzieri, B. Shen, D. B. Rifkin, Identification and Characterization of an Eight-cysteine Repeat of the Latent Transforming Growth Factor-β Binding Protein-1 that Mediates Bonding to the Latent Transforming Growth Factor-β1*. *Journal of Biological Chemistry* **271**, 29891-29896 (1996).
294. K. Miyazono, A. Olofsson, P. Colosetti, C. H. Heldin, A role of the latent TGF-beta 1-binding protein in the assembly and secretion of TGF-beta 1. *EMBO J* **10**, 1091-1101 (1991).
295. T. Mizuguchi *et al.*, Heterozygous TGFBR2 mutations in Marfan syndrome. *Nat Genet* **36**, 855-860 (2004).
296. B. L. Loeys *et al.*, A syndrome of altered cardiovascular, craniofacial, neurocognitive and skeletal development caused by mutations in TGFBR1 or TGFBR2. *Nat Genet* **37**, 275-281 (2005).
297. H. Pannu *et al.*, Mutations in transforming growth factor-beta receptor type II cause familial thoracic aortic aneurysms and dissections. *Circulation* **112**, 513-520 (2005).
298. X. Chen *et al.*, Integrin-mediated type II TGF-beta receptor tyrosine dephosphorylation controls SMAD-dependent profibrotic signaling. *J Clin Invest* **124**, 3295-3310 (2014).

299. A. Ahmadi, M. Najafi, B. Farhood, K. Mortezaee, Transforming growth factor-beta signaling: Tumorigenesis and targeting for cancer therapy. *J Cell Physiol* **234**, 12173-12187 (2019).
300. M. K. Brown, N. Naidoo, The endoplasmic reticulum stress response in aging and age-related diseases. *Front Physiol* **3**, 263 (2012).
301. P. K. Mays, R. J. McAnulty, J. S. Campa, G. J. Laurent, Age-related changes in collagen synthesis and degradation in rat tissues. Importance of degradation of newly synthesized collagen in regulating collagen production. *Biochem J* **276 (Pt 2)**, 307-313 (1991).
302. E. Giorgio *et al.*, Two families with novel missense mutations in COL4A1: When diagnosis can be missed. *J Neurol Sci* **352**, 99-104 (2015).
303. C. del Corsso *et al.*, Effects of aging on Ca2+ signaling in murine mesenteric arterial smooth muscle cells. *Mech Ageing Dev* **127**, 315-323 (2006).
304. C. Georgeon-Chartier, C. Menguy, A. Prevot, J. L. Morel, Effect of aging on calcium signaling in C57Bl6J mouse cerebral arteries. *Pflugers Arch* **465**, 829-838 (2013).
305. A. Mughal, O. F. Harraz, A. L. Gonzales, D. Hill-Eubanks, M. T. Nelson, PIP(2) Improves Cerebral Blood Flow in a Mouse Model of Alzheimer's Disease. *Function (Oxf)* **2**, zqab010 (2021).
306. K. P. Doyle, E. Cekanaviciute, L. E. Mamer, M. S. Buckwalter, TGFbeta signaling in the brain increases with aging and signals to astrocytes and innate immune cells in the weeks after stroke. *J Neuroinflammation* **7**, 62 (2010).
307. K. Tominaga, H. I. Suzuki, TGF-beta Signaling in Cellular Senescence and Aging-Related Pathology. *Int J Mol Sci* **20** (2019).